OCTOBER–DECEMBER 2025 VOL. 17 № 4 (67)

ISSN 2075-8251

ActaNaturae

Targeted Radionuclide Detection of Malignant Tumors Using Affibody

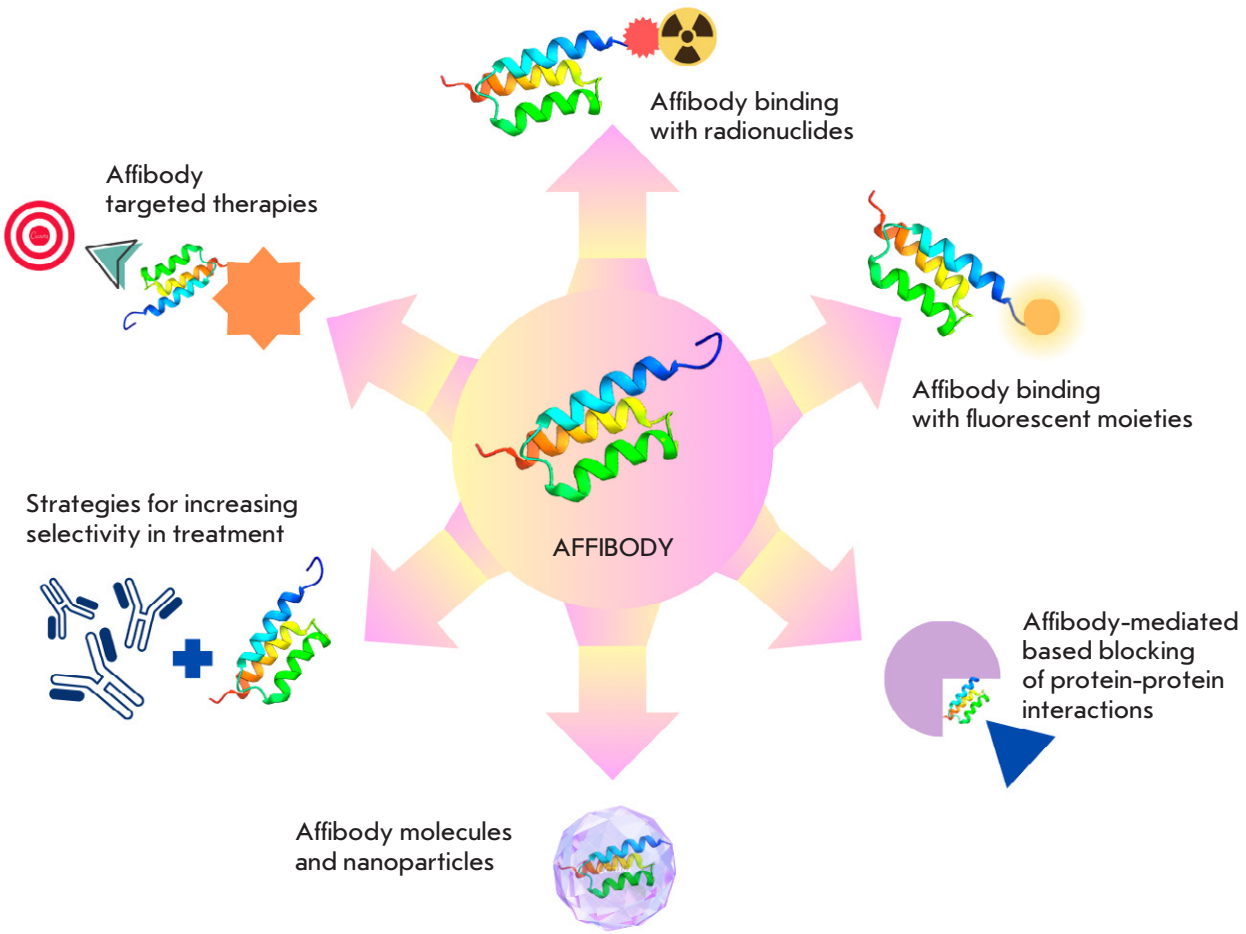

Dimephosphon Radioprotective Properties on the Model of Radiation Injury *In Vivo*

D. A. Kiseleva, M. A. Melchenko, O. I. Yarovaya, N. V. Basov, A. D. Rogachev, A. G. Pokrovsky, N. F. Salakhutdinov, T. G. Tolstikova

The search for effective radioprotective agents remains one of the primary goals of radiation oncology and radiobiology. The radioprotective properties of the drug Dimephosphon, which possesses anti-acidotic, antitumor, and antioxidant properties, were studied in animals with experimental radiation injury. It has been shown that administration of the drug exerts a local radioprotective effect, reducing the severity of the radiation-induced damage to the intestinal epithelium and splenic capsule.

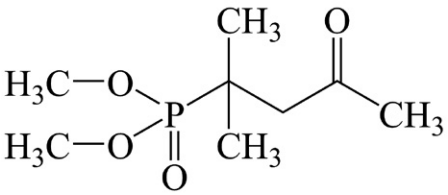

The structural formula of the active substance of Dimephosphon

Recombinant Production, Species-Specific Activity at the TRPA1 Channel, and Significance of the N-Terminal Residue of ProTx-I Toxin from *Thrixopelma Pruriens* Tarantula Venom

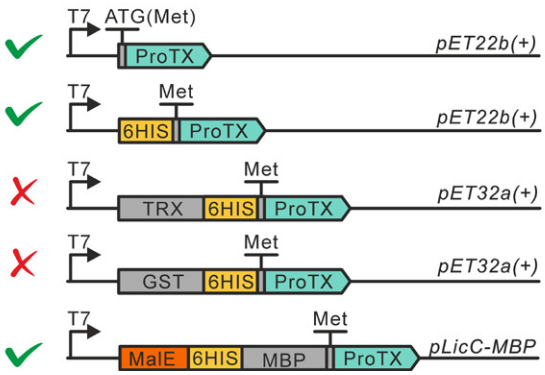

Design of expression vectors for ProTx-I production in *E. coli* cells

M. A. Shulepko, M. Zhang, E. A. Zhivov, D. S. Kulbatskii, A. S. Paramonov, Yu. Che, A. V. Kuznetsov, A. V. Popov, M. P. Kirpichnikov, Z. O. Shenkarev, E. N. Lyukmanova

The ProTx-I toxin (from the *Thrixopelma pruriens* tarantula) inhibits Na_V and TRPA1 channels and can serve as a model for developing new analgesics. The inhibitory cystine knot motif complicates the recombinant production of ProTx-I. Testing various approaches to the bacterial production of disulfide-containing proteins enabled obtaining ProTx-I with a native structure through renaturation from cytoplasmic inclusion bodies and by secretion into the periplasm as a fusion with maltose-binding protein. ProTx-I is more active against rat TRPA1 than human, and modification of the *N*-terminal sequence attenuates ProTx-I activity.

The Potential of the Peptide Drug Semax and Its Derivative for Correcting Pathological Impairments in the Animal Model of Alzheimer's Disease

A. I. Radchenko, E. V. Kuzubova, A. A. Apostol, V. A. Mitkevich, L. A. Andreeva, S. A. Limborska, Yu. V. Stepenko, V. S. Shmigerova, A. V. Solin, M. V. Korokin, M. V. Pokrovskii, N. F. Myasoedov, A. A. Makarov

Alzheimer's disease is currently among the most common neurodegenerative diseases. The present study assessed the effect of the known neuroprotective peptide Semax and its derivative on the behavioral characteristics and development of amyloidosis in transgenic APPswe/PS1dE9/Blg mice acting as a model of Alzheimer's disease. These findings demonstrate the high potential of Semax and its derivatives when used to develop therapeutic and corrective strategies for Alzheimer's disease.

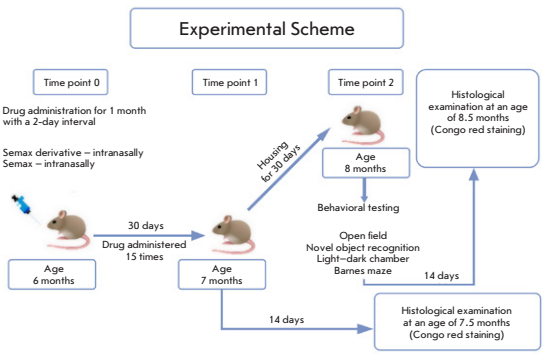

The experiment design in the study investigating the effects of Semax and the Heptapeptide on APP/PS1 mice

ActaNaturae
OCTOBER–DECEMBER 2025 VOL. 17 № 4 (67)
since april 2009, 4 times a year

Founders
Acta Naturae, Ltd,
National Research University
Higher School of Economics

Adress: 101000, Moscow, Myasnitskaya Ulitsa, 13, str. 4
Phone/Fax: +7 (495) 727 38 60
E-mail: actanaturae@gmail.com

Номер подписан в печать 30 декабря 2025 г.
Тираж 15 экз. Цена свободная.
Отпечатано в типографии: НИУ ВШЭ,
г. Москва, Измайловское шоссе, 44, стр. 2

Founder and Chairman
of the Editorial Board (from 2009 to 2023)
of the journal Acta Naturae
Academician Grigoriev Anatoly Ivanovich

Indexed in PubMed, Web of Science, Scopus, and RISC

Impact Factor: 2.0 (WOS); 3.5 (Scopus)

CONTENTS

REVIEWS

RESEARCH ARTICLES

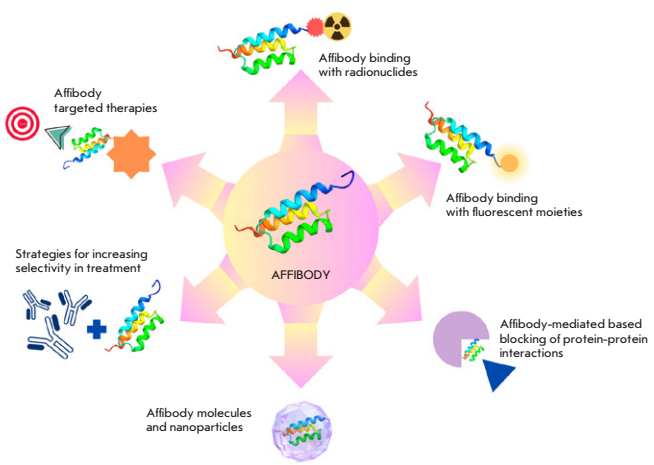

IMAGE ON THE COVER PAGE
(see the article by Bragina et al.)

Targeted Radionuclide Detection of Malignant Tumors Using Affibody

O. D. Bragina[1,2], A. A. Nesynov[1*], E. Yu. Sitnikova[3], S. V. Patalyak[1,3], S. M. Deyev[2,4]
[1]Tomsk National Research Medical Center of the Russian Academy of Sciences, Tomsk, 634009 Russia
[2]National Research Tomsk Polytechnic University, Tomsk, 634050 Russia
[3]Siberian State Medical University, Tomsk, 634050 Russia
[4]Shemyakin-Ovchinnikov Institute of Biorganic Chemistry of the Russian Academy of Sciences, Moscow, 117997 Russia
[*]E-mail: nesynov.alex@mail.ru
Received April 22, 2025; in final form, August 06, 2025
DOI: 10.32607/actanaturae.27677

ABSTRACT **This review examines the potential applications of affibody molecules in various fields of biotechnology and clinical medicine. Consideration is given to the high affinity and specificity of affibody molecules for selected molecular targets, as well as their potential for the *in vivo* visualization of various malignant tumors. Significant attention is paid to preclinical and clinical studies of affibody conjugates with various radioisotopes for targeted radionuclide tumor imaging, which is particularly relevant in addressing challenges encountered during the diagnosis and treatment of these patients. Clinical trials demonstrate that radiopharmaceuticals are well-tolerated and effective for the assessment of tumor process prevalence and the determination of HER2/neu status in breast cancer patients, supporting further research.**
KEYWORDS **Malignant tumors, theranostics, targeted radionuclide diagnostics, alternative scaffold proteins, affibodies.**
ABBREVIATIONS **MT – malignant tumor; IHC – immunohistochemistry; RPH – radiopharmaceutical; ASP – alternative scaffold proteins; RPD – radiopharmaceutical drug; SPECT – single-photon emission computed tomography; PET – positron emission tomography; HCC – hepatocellular carcinoma; FDG – fluorodeoxyglucose; FISH – fluorescence in situ hybridization.**

INTRODUCTION

The International Agency for Research on Cancer (IARC) indicates that approximately 20 million new cancer cases are diagnosed annually around the globe, with 9.7 million deaths reported in 2022. A trend of annual increases at these rates has been observed. Population forecasts suggest that by 2050, the incidence of malignant tumors (MT) will reach 35 million cases [1]. In the Russian Federation, 674,000 instances of MT were documented in 2023, representing an 8% increase over the figures for 2022 [2]. Given the significant prevalence and socioeconomic impact of cancer, research into the development of more targeted MT diagnostic methods, novel drugs, and strategies to overcome antitumor therapy resistance is essential [3–5].

The critical step in oncology diagnostics involves acquiring tumor tissue for subsequent histological confirmation. This stage significantly influences subsequent therapeutic strategies, prognosis, and the necessity for supplementary investigations, including a molecular genetic analysis [6]. Tumor samples may be acquired through core biopsy and excisional biopsy, with the latter entailing complete tumor removal via diagnostic surgery [7, 8]. The methodologies employed are uniformly invasive and potentially distressing, with some instances necessitating patient recovery and rehabilitation, this entailing supplementary financial expenditures. Hence, thoracoscopic and laparoscopic manipulations require patient hospitalization and anesthesia, and they do not preclude the potential for procedural failure stemming from

the tumor's anatomical site, the presence of numerous metastatic foci, and the patient's unwillingness to undergo the manipulation [9, 10]. The issue of whether immunohistochemical analysis of additional tumor structures is necessary, considering potential receptor status differences from the primary tumor and the limitations of routine application, requires further investigation.

Furthermore, several difficulties are inherent in the histological and immunohistochemistry (IHC) analyzes of tumor tissues, stemming from the complexities of determining tumor cell origins in poorly differentiated and anaplastic lesions [13], as well as the subjective nature of parameter assessment [14]. Analysis of statistical data reveals that the rate of disagreement in diagnoses among pathologists could be as high as 30%, which can be attributed to diagnostic challenges, human factors, and the use of additional staining procedures [15, 16].

The limitations of conventional radiological and morphological techniques, the necessity of invasive interventions, a substantial economic burden, and potential challenges in results interpretation and reproducibility necessitate the development and adoption of supplementary diagnostic approaches. This adjustment aims to broaden diagnostic and therapeutic possibilities for individuals afflicted with malignant neoplasms, thereby fostering enhanced longevity and improved quality of life. The evolution of new methodologies utilizing small molecules, specifically those exhibiting antibody-like characteristics and tumor antigen tropism, is considered to be of significant importance.

MALIGNANCY THERANOSTICS

With the developments in fundamental oncology, it has become crucial to determine the molecular genetic parameters of the tumor. This enables new points of application of drug therapy to be identified, bringing us closer to the concept of personalized medicine, i.e., to the determination of treatment based on the biological features of the tumor of each patient with maximum efficiency [17]. Theranostics, a rapidly evolving field in personalized medicine, integrates diagnostic procedures, such as identifying tumor cell molecular targets and therapy indications, with targeted therapeutic interventions based on previously detected tumor growth markers in the patient. Adoption of the theranostics approach on a larger scale has the potential to improve therapy response rates, lower the incidence of adverse events, increase both overall and relapse-free survival, enhance patient quality of life, and lessen the economic burden on healthcare provision [18].

In 1998, John Funkhouser, then the CEO of PharmaNetics, used the term "theranostics" for the first time to refer to the business strategy of his company, which centered on the creation of diagnostic panels for the subsequent prescription of targeted pharmaceutical treatments [19]. But the concept of employing a single molecule for both cancer diagnosis and treatment had been established some decades earlier. A significant advancement in the development of theranostics was the discovery and widespread application of radioactive iodine in the treatment of thyroid cancer [20]. The pretreatment imaging of the tumor with the iodine-123 isotope aided in improved treatment strategy planning for radioiodotherapy. Thus, the combination of iodine-123 and iodine-131 was the first radioisotope pair used in theranostics. Progress in this area has been significantly impacted by advances in radiochemistry and enhanced instrumental investigation techniques [21]. It is important to acknowledge that the journal Theranostics (www.thno.org) has been providing summaries of pertinent data in this domain for over ten years. This field has experienced a recent surge in development, attributable to the use of radionuclides.

Classification includes photo-, sono-, chemo-, nano- and radiotherapy, contingent on diagnostic methods and therapeutic agents [22]. Targeted radionuclide diagnostics has potential as the only area of theranostics implemented in clinical practice. This approach is based on radioisotope-labeled "targeting" molecules that selectively attach themselves to receptors present on the surface of tumor cells. The recording of isotope radiation using specialized equipment can facilitate both the anatomical and molecular evaluation of tumor presence in patients with malignant neoplasms, eliminating the need for further invasive procedures, and enabling repeated examinations at the stages of primary diagnosis and treatment [23–25].

Radiopharmaceuticals (RPHs) incorporate diverse molecular structures as targeting modules, such as full-size monoclonal antibodies, antibody fragments, and synthetic framework molecules/alternative scaffold proteins (ASPs), with the latter exhibiting significant potential in radionuclide diagnostics [26–29].

Alternative scaffold proteins

The accelerated evolution of technologies for the clonal selection of polypeptides via binding from substantial libraries has enabled the development of a new class of binding proteins, employing protein engineering approaches. In order to reduce immunogenicity, these structures were designed using various scaffolds which differ in both size and structural organization from the original immunoglobulin. A range

of non-immunoglobulin affinity proteins have been documented, based on several surface-located amino acid residues present in secondary structure elements or unstructured loops, subsequently selected through different display platforms [30].

The structure of these compounds typically comprises a constant scaffold part (constant region) and a variable region. The first component contains a pair of α-helices or β-sheets forming a rigid tertiary structure and maintains the conformational stability inherent in protein scaffolds. The second component comprises several open loops or residues within rigid secondary structures that permit specific binding to different target molecules through structural ligand-receptor pairing or chemical interactions [31].

The biodistribution and tumor penetration capabilities of ASP are primarily determined by their compact size (4–15 kDa). This results in a significant reduction in the time interval between the administration of the radiopharmaceutical medicinal product (RPhMP) and the start of imaging study, improves the degree of drug accumulation in the tumor, and influences the choice of a radioisotope suitable for specific research goals and timing. ASPs are also typically known for their robust ability to withstand environmental conditions. The absence of disulfide bridges in the ASP structure, typical for antibodies, as well as a sufficiently dense structure, determines its high thermal stability, stability in acidic and alkaline conditions, and resistance to proteolysis. Furthermore, additional structures can be introduced into protein scaffolds through chemical synthesis for conjugation with pharmaceuticals or diagnostic agents. The solubility and robust physicochemical stability of small protein scaffolds are typically advantageous for *in vivo* application. Given the aforementioned characteristics, scaffold proteins can be regarded as versatile compounds for modification and production [32].

Currently, representatives of the alternative scaffold protein class include affibody molecules, affilins, anticalins, avimers, DARPins, Kunitz-type inhibitor domains, and albumin-binding domains (e.g., ADAPTs), among others. Each of these is at various stages of investigation, with an ongoing search for potential points of future clinical application.

AFFIBODY IN BIOTECHNOLOGY AND CLINICAL MEDICINE

Affibody, a synthetic molecule, is an example of an alternative protein framework with a domain structure. The affibody molecule has a Z-domain at its core, which is the peptide domain of protein A of *Staphylococcus aureus* [33]. The spatial structure of the Z-domain, which comprises 58 amino acid residues and has a relatively low molecular mass (~6.5 kDa), is formed by three alpha-helices that create a bundle. Affibody molecules exhibit good structural stability, resistance to proteolysis, high temperatures (around 90°C), and acidic and alkaline conditions (pH from 2.5 to 11) [34]. Affibody combinatorial libraries can be generated by randomly modifying genes that encode 13 amino acid residues in the first and second helices of the Z-domain. For this purpose, phage, cellular, ribosomal and mRNA displays are used. Libraries are combined with the target antigen to facilitate the selection of molecules, which are subsequently washed to eliminate unbound ligands, leaving only those peptides bound to the ligand. The primary targeting molecules obtained can be subjected to further re-randomization to increase their affinity for a particular target [35]. Variants of interest can be produced in bacterial, yeast, and cell systems. Moreover, due to their small size, affibodies can also be created via peptide synthesis methods [36]. Introducing a functionalizing group at the N- or C-terminus of a peptide enables the acquisition of a molecule with the properties required for a specific application, such as radioisotope labeling for radionuclide diagnostics or a cytotoxic group for targeted treatment [37, 38].

The unique properties of affibody molecules make them of considerable interest in diagnostic and clinical medicine, as well as diverse biomedical applications (*Fig. 1*).

Consequently, the possibility of employing affibody molecules conjugated with fluorescent fragments for the bioluminescent detection of malignant lesions is actively being explored. This method offers several key advantages: high sensitivity, the absence of toxicity and the avoidance of invasive procedures, as well as cost-effectiveness [39].

Affibody molecules can also function as a barrier between interacting proteins, offering a novel approach to treating diseases caused by these interactions. Viral diseases can serve as an example. Viral spike proteins are important targets for vaccine and antiviral drug development. For instance, an affibody molecule has been shown to have high specificity and affinity for the RBMFP protein (a product synthesized from the SARS-CoV-2 protein), and the interaction of the affibody molecule with the Receptor Binding Motif (RBM) leads to the neutralization of the SARS-CoV-2 pseudovirus infection [40].

Conjugates of affibody molecules with various types of nanoparticles are considered promising agents for the therapy and imaging of malignant neoplasms [41]. For example, an affibody conjugate with the contrast agent nanobullbe is used for binding HER2 and IR783 and developing a method for

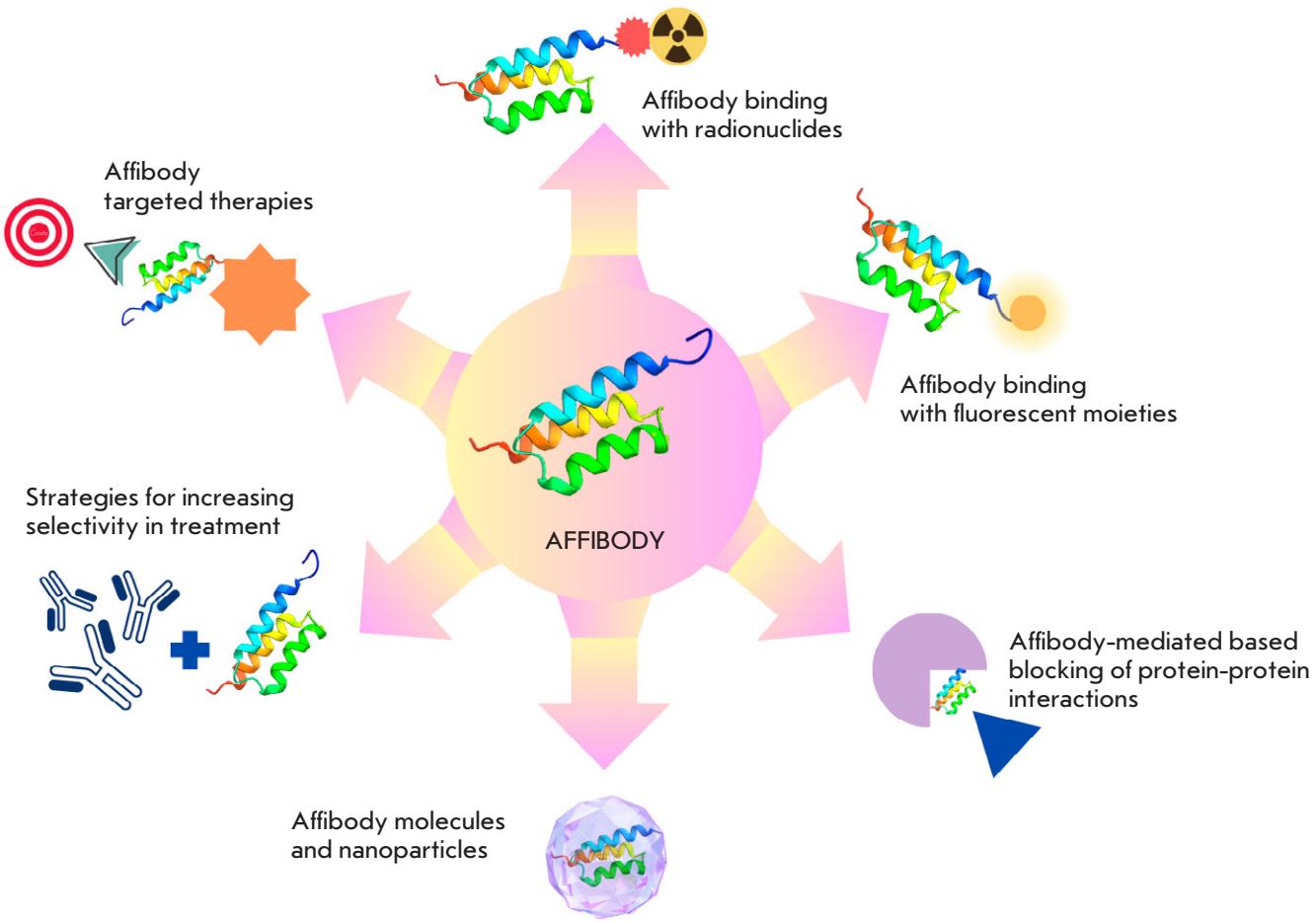

Fig. 1. Biotechnological and clinical applications of affibody molecules

ultrasound detection of HER2-positive breast cancer [42]. The potential therapeutic effect of high-affinity probes such as Gd@C-dots-Cys-ZEGFR:1907 against EGFR in the therapy of non-small cell lung cancer and PFH/AGM-CBA/HSV-TK/liposome (PAHL)-affibody in the therapy of HER2-positive breast cancer is being studied [43, 44].

Of particular importance is the development of affibody-based targeting drugs. A Phase III clinical trial of Izokibep®, an IL-17 inhibitor, was initiated in 2022 to examine its effects on numerous complement-dependent diseases such as psoriatic arthritis, uveitis, ankylosing spondylitis, and hidradenitis suppurativa [45, 46].

Affibody for targeted radionuclide diagnostics of malignancies

The studies predominantly explore the potential of using affibody as a basis for radiopharmaceuticals for the targeted imaging of malignant neoplasms of various localizations. The selection of the imaging method is crucial for the radionuclide diagnosis of malignancies. This is due to the unique characteristics of each radioisotope, among which are the half-life ($T_{1/2}$), the type of radiation (positron or gamma radiation), and the method of production (generator or cyclotron) [47, 48]. Currently, single-photon emission computed tomography (SPECT) and positron emission tomography (PET) are used for radiation detection, with the choice depending on the isotope incorporated into the radiopharmaceutical preparation (RPH) (*Table 1*). Presently, the radionuclides most frequently used in conjunction with affibody molecules encompass ^{68}Ga ($T_{1/2}$ = 68 min), ^{99m}Tc ($T_{1/2}$ = 6.02 h), ^{18}F ($T_{1/2}$ = 109.8 min), among others. The long-lived radionuclides used are ^{66}Ga ($T_{1/2}$ = 9.9 h), ^{64}Cu ($T_{1/2}$ = 12.7 h), ^{188}Re ($T_{1/2}$ = 17 h),

^{89}Zr ($T_{1/2}$ = 78.4 h), ^{111}In ($T_{1/2}$ = 2.81 days), ^{177}Lu ($T_{1/2}$ = 6.7 days), ^{125}I ($T_{1/2}$ = 60 days), ^{57}Co ($T_{1/2}$ = 271.8 days) [49].

Radioconjugates are synthesized to target receptors that are overexpressed on the surface of tumor cells in many malignant pathologies. These receptors are not only involved in the pathogenesis of malignant tumors but also represent additional therapeutic options for cancer patients. For instance, preclinical studies are currently underway on radioconjugates targeting the ligand of the programmed cell death receptor PD-L1. This receptor is a transmembrane protein that regulates the cellular immune response, and the expression of PD-L1 by tumor cells or cells of the tumor microenvironment leads to the inhibition of the cellular immune response. This allows tumor cells to evade apoptosis associated with the cytotoxic action of T-lymphocytes. PD-L1 expression has been detected in various tumors, including melanoma, lung cancer, breast cancer, bladder cancer, pancreatic cancer, and ovarian cancer [50–52].

For example, Liang et al. [53] assessed the pharmacokinetics of [^{99m}Tc]Tc-PDA-affibody, its toxicity profile, and the potential for *in vivo* imaging of PD-L1-positive tumors via SPECT at 30, 60, and 120 min post-injection. The tumor was observed to exhibit a fairly rapid accumulation of RPH after 30 min. Nevertheless, an imaging interval of 1–2 h was considered optimal, given the overall drug distribution. The disadvantages associated with this pharmaceutical agent include poor SPECT resolution, substantial drug concentration in the kidneys, thyroid, and gastrointestinal tract, attributed to the binding of unconjugated technetium-99m oxide.

Another promising target for targeted imaging is the B7-H3 (CD276) receptor, a transmembrane protein from the immune checkpoint molecule family that has a co-activating or co-inhibitory effect on T-lymphocytes. In normal tissues, this protein is expressed at a rather low level, but overexpression of this protein has been observed in some tumors [54]. These include prostate cancer, renal cell and urothelial cancer, ovarian cancer, and others. Within tumor tissue, this protein exerts a pro-oncogenic effect by suppressing the antitumor immune response. Given the active development of immunotherapy, this receptor is considered a viable target, thereby making the development of specific diagnostics for B7-H3 overexpression in tumor tissue a priority [55].

Oroujeni et al. [56] investigated the drug [^{99m}Tc]Tc-AC12-GGGC in ovarian and breast cancer cell lines. A Ramos lymphoma cell line lacking B7-H3 expression served as a negative control. The B7-H3-positive xenograft cells demonstrated a six-fold increase in drug accumulation compared to the control group. However, a minimal absolute amount of drug accumulation was observed in the tumor. SPECT imaging, conducted four hours after RPH injection, demonstrated visualization of the xenografted B7-H3-positive tumor, while in the negative control group the tumor was not visualized. High accumulation of [^{99m}Tc]Tc-AC12-GGGC was also noted in tissues such as the kidneys and liver.

Oroujeni et al. [57] also investigated the possibility of improving the detection of B7-H3 overexpression with the radiopharmaceutical preparation [^{99m}Tc]Tc-AC12-GGGC by increasing the affinity of the affibody molecule. After they were generated via phage display, three daughter molecules were labeled with technetium-99m and evaluated in mouse models, along with the original AC12 molecule. As a result, the SYNT-179 molecule was selected, as it possesses superior characteristics: higher tumor accumulation, lower accumulation in normal tissues with an improved tumor-to-organ ratio, and lower RPH accumulation in the liver. The study demonstrated that affinity maturation improved molecular biodistribution and imaging performance, and that the optimized Affibody protein exhibited enhanced performance in targeting B7-H3 overexpression.

Table 1. Radioisotopes for radionuclide diagnostics using PET or SPECT

Radioisotope	$T_{1/2}$	Emission type	Production method
^{68}Ga	68 min	β^+, γ	Generator
^{99m}Tc	6.02 h	γ	Generator
^{18}F	109.8 min	β^+	Cyclotron
^{66}Ga	9.9 h	β^+, γ	Cyclotron
^{64}Cu	12.7 h	β^+, β^-, γ	Cyclotron
^{188}Re	17 h	β^-, γ	Generator
^{89}Zr	78.4 h	β^+	Cyclotron
^{111}In	2.81 days	γ	Cyclotron
^{177}Lu	6.7 days	β^-, γ	Cyclotron
^{125}I	60 days	γ	Cyclotron
^{57}Co	271.8 days	γ	Cyclotron

Table 2. Affibody-based radiopharmaceuticals in various stages of clinical and preclinical trials

RPH	Imaging method	Target receptor	Research phase	Authors, year
[^{99m}Tc]Tc-PDA-Affibody	SPECT	PD-L1	Preclinical	Liang et al., 2022 [53]
[^{99m}Tc]Tc-AC12-GGGC	SPECT	B7-H3	Preclinical	Oroujeni et al., 2022 [56]
[^{99m}Tc]Tc-SYNT-179	SPECT	B7-H3	Preclinical	Oroujeni et al., 2023 [57]
[^{68}Ga]Ga-DOTA-Z_{TRI}	PET	PDGFRβ	Preclinical	Cai et al., 2023 [58]
[^{18}F]AlF-NOTA-HER2	PET	HER2	Preclinical	Han et al., 2022 [64]
[^{99m}Tc]Tc-$(HE)_3Z_{HER2:V2}$	SPECT	HER2	Preclinical	Hu et al., 2024 [68]
[^{111}In]In-ABY-002	SPECT	HER2	Clinical (Phase I)	Baum et al., 2010 [72]
[^{68}Ga]Ga-ABY-002	PET	HER2	Clinical (Phase I)	Baum et al., 2010 [72]
[^{111}In]In-ABY-025	SPECT	HER2	Clinical (Phase I)	Sörensen et al., 2014 [73]
[^{68}Ga]Ga-ABY-025	PET	HER2	Clinical (Phase I)	Sörensen et al., 2016 [74]
[^{68}Ga]Ga-NOTA-Mal-Cys-MZHer342	PET	HER2	Clinical (Phase I)	Miao et al., 2022 [75]
[^{68}Ga]Ga-ABY-025	PET	HER2	Clinical (Phase II)	Alhuseinalkhudhur et al., 2023 [76]
[^{68}Ga]Ga-ABY-025	PET	HER2	Clinical (Phase II)	Altena et al., 2024 [77]
[^{99m}Tc]Tc-ZHER2:41071	SPECT	HER2	Clinical (Phase I)	Bragina et al., 2023 [78]

In a preclinical study, Cai et al. [58] investigated the use of a trimeric affibody molecule labeled with ^{68}Ga([^{68}Ga]Ga-DOTA-Z_{TRI}) for PET diagnostics of hepatocellular carcinoma (HCC). [^{68}Ga]Ga-DOTA-Z_{TRI} exhibits high affinity for platelet-derived growth factor receptor type beta (PDGFRβ), which is expressed on the surface of pericytes, cells found within the walls of small blood vessels. In normal blood vessels, pericytes are covered by an intact endothelium. However, in tumors, the architecture of the vascular walls is disrupted, resulting in areas of pericytes not covered by endothelium, which renders PDGFRβ on their surface accessible for detection [59]. Therefore, it was hypothesized that PDGFRβ could serve as a potential biomarker for HCC, which is a highly vascularized neoplasm, suggesting that this receptor could be overexpressed in HCC compared to normal liver tissue.

In the initial stage, PDGFRβ was validated as a biomarker for HCC and the trimeric affibody Z_{TRI} was found to have high affinity for PDGFRβ. In addition, the PET data indicated that the accumulation of [^{68}Ga]Ga-DOTA-Z_{TRI} correlated directly with PDGFRβ expression by tumor cells; therefore, the drug actively accumulated in PDGFRβ-positive HCC cells in laboratory animals. At the same time, no accumulation of [^{68}Ga]Ga-DOTA-Z_{TRI} was detected in healthy liver tissues. Thus, the high potential of the radiopharmaceutical preparation [^{68}Ga]Ga-DOTA-Z_{TRI} for PET diagnostics of HCC and the rationale for its further study and implementation in clinical practice were demonstrated.

Affibody for the detection of HER2-positive malignancies

Targeted therapy for malignant diseases often focuses on human epidermal growth factor receptor type 2 (HER2/neu), a tyrosine kinase receptor that is key to cell differentiation, proliferation, and apoptosis. HER2 overexpression, primarily attributed to ERBB2 gene amplification, has been identified in breast, gastric, pancreatic, lung, endometrial, ovarian, bladder, colorectal cancer, and various other tumor localizations [60].

Current approaches for determining HER2 status include IHC and fluorescence *in situ* hybridization (FISH) techniques. As per the 2023 ASCO/CAP guidelines, a HER2/neu expression result is deemed negative in the absence of staining or with faint, sporadic membrane staining (0 and 1+) and is considered positive with intense, complete circumferential membrane staining in more than 10% of tumor cells (3+). For ambiguous cases (2+), the result is confirmed via

amplification of the HER2 gene using FISH and an ERBB2(17q12)/SE17 DNA probe (Kreatech, USA) [61].

The scientific community is currently directing its attention toward investigating targeted radionuclide detection using affibody to evaluate HER2/neu receptor expression in gastric and ovarian cancers. This is due to the unique anatomical challenges and the pursuit of supplementary therapeutic strategies within these oncological contexts. Gastric cancer is often diagnosed at late stages when surgical treatment is not feasible, requiring the molecular biological parameters of the tumor to be determined for selecting a systemic therapy option. HER2 expression is detected in 17–20% of gastric cancer cases. However, a very high level of heterogeneity in HER2 expression is observed (14–79% by IHC and 23–54% by IHC + FISH). Furthermore, the HER2 status of a tumor can change during anti-HER2 therapy, causing difficulties in assessing the effectiveness of the ongoing treatment, as performing multiple biopsies is associated with risks of complications and is not always an option [62, 63].

Han et al. [64] researched the possibility of targeted detection using the [^{18}F]AlF-NOTA-HER2 preparation. The HER2-positive cell line was NCI-N87, whereas the HER2-negative cell line was MKN74. *In vitro* studies demonstrated the accumulation of the RPH in question in HER2-expressing cells. *In vivo*, [^{18}F]AlF-NOTA-HER2 was found to rapidly accumulate in HER2-positive xenografts and to be quickly eliminated from the blood, primarily by the kidneys. Within normal tissues, the highest accumulation was observed in bones and kidneys, which was a significant drawback of this molecule, as the high level of absorbed radioactivity requires nephroprotection. The comparison of [^{18}F]AlF-NOTA-HER2 and ^{68}Ga-NOTA-HER2 demonstrated a benefit in using fluorine-18 over gallium-68, due to its longer half-life (109.8 min vs. 67.7 min, respectively), which provided more time for the study. Additionally, the shorter positron diffusion range of fluorine-18 results in improved resolution in PET imaging.

Ovarian cancer presents multiple diagnostic and therapeutic challenges attributable to its high recurrence and distant metastasis rates, in addition to the large proportion of cases diagnosed in advanced stages [65, 66]. Until recently, anti-HER2 therapy was not used to treat tumors of this type, owing to adverse outcomes with trastuzumab. Nonetheless, research in this area has been resumed due to the development of monoclonal antibody conjugates with cytostatics. For example, the *DESTINY-PanTumor02* study investigating the efficacy of trastuzumab-deruxtecan therapy in various solid tumors reported objective response rates (ORR) in 63-64% of patients with HER2-positive ovarian cancer, which makes it promising in determining the HER2 status in this oncopathology [67].

Hu et al. conducted a feasibility study on affibody molecules in ovarian cancer utilizing [^{99m}Tc]Tc-$(HE)_3Z_{HER2:V2}$ [68]. The results demonstrated elevated compound accumulation in HER2/neu-overexpressing tumors, whereas tumors lacking HER2/neu expression did not exhibit drug accumulation. A disadvantage of [^{99m}Tc]Tc-$(HE)_3Z_{HER2:V2}$ discovered during the study was its high accumulation in the kidneys, which could potentially lead to nephrotoxicity. However, it is assumed that this shortcoming may be remedied through enhanced patient hydration in clinical settings.

Affibody for diagnosing HER2-positive breast cancer

Overexpression of the HER2 receptor occurs in 15–20% of breast cancer (BC) cases and has traditionally been associated with a more aggressive course and, consequently, a worse prognosis. Nevertheless, the use of targeted anti-HER2 therapy has improved the overall survival of patients with HER2-positive cancer, approaching the prognosis observed in more favorable molecular genetic subtypes [69]. Currently employed in clinical practice are drugs including trastuzumab, pertuzumab, and lapatinib, in addition to a new class: conjugates of monoclonal antibodies and cytostatics (trastuzumab-emtansine and trastuzumab-deruxtecan) [70, 71].

To date, multiple trials have been performed using affibody as a targeting agent for radionuclide diagnosis of HER2/neu status in individuals with operable, locally advanced and metastatic breast cancer.

In 2005, Baum et al. [72] performed the first clinical study of the indium-111- and gallium-68-labeled affibody molecule ABY-002 to evaluate safety, pharmacokinetics, and the feasibility of imaging tumor foci in breast cancer patients. Following administration, [^{111}In]In-ABY-002 and [^{68}Ga]Ga-ABY-002 demonstrated swift clearance from the circulation, enabling SPECT and PET imaging to commence within 2–3 h post-injection. It was also shown that these drugs were effective in radionuclide tumor imaging: all patients demonstrated an accumulation of the investigated compounds in HER2-positive tumors. Additionally, in one case, [^{68}Ga]Ga-ABY-002 allowed muscle metastasis (quadriceps) to be detected, which was not identified by ^{18}F-FDG PET. Notwithstanding the favorable outcomes, [^{111}In]In-ABY-002 and [^{68}Ga]Ga-ABY-002 present drawbacks, including elevated accumulation in the liver and kidneys, thereby substantially impeding tissue visualization within those areas. For example, it proved impossible to detect liver metastasis in one patient and an adrenal gland metastasis in another.

The next stage involved studying a second-generation affibody molecule (ABY-025). The study by Sörensen et al. [73] included seven patients with metastatic breast cancer: five with the HER2-positive and two with the HER2-negative disease. As in the study with ABY-002, the administration of [^{111}In]In-ABY-025 was safe and not associated with adverse events. According to SPECT data, in addition to clear visualization of HER2-positive tumors, weak accumulation of the studied drug was observed in HER2-negative foci, attributable to the presence of a certain amount of the HER2 receptor on the surface of tumor cells. During the study, metastatic foci in the liver, not detected using the ABY-002 molecule, were visualized. An interesting finding of this analysis was the detection of a brain tumor metastasis, previously undetected by ^{18}F-FDG-PET, as well as the identification of a HER2-negative tumor metastasis in a patient with a positive HER2 status of the primary breast tumor. The primary limitation observed was the failure to identify metastatic nodes below 1 cm.

Since the low visualization of small tumor foci could be due to the low resolution of SPECT, a study of the [^{68}Ga]Ga-ABY-025 drug using PET was conducted. An analysis of 16 patients with metastatic BC, conducted by Sörensen et al. [74], demonstrated good visualization of small-sized foci, enabling the detection of breast cancer metastases in the liver, bones, lymph nodes, brain, and other organs. Furthermore, in two patients after the [^{68}Ga]Ga-ABY-025 study, the HER2 status in the primary breast tumor was changed from negative to positive. In most cases, differences in HER2 expression between the primary tumor and metastatic foci were found.

Miao et al. [75] investigated the usage of the gallium-68-labeled affibody molecule NOTA-Mal-Cys-MZHer342 in a clinical trial that included 24 BC patients. An important component of the analysis included the utilization of PET/CT scans "on demand" by oncologists to address complex diagnostic issues. This approach was used in six patients to differentiate between metastases and two concurrent breast cancers, or concurrent MT of a different origin. In all cases, the SUVmax of [^{68}Ga]Ga-NOTA-Mal-Cys-MZHer342 [^{68}Ga]Ga-NOTA-Mal-Cys-MZHer342 in tumor foci was compared with the results of immunohistochemical examination. According to the analysis, [^{68}Ga]Ga-NOTA-Mal-Cys-MZHer342 usage allowed researchers to detect HER2 overexpression in tumor tissue with a 91.7% specificity and to detect negative HER2 expression with an 84.6% specificity, with a conversion of HER2/neu status from positive to negative observed in seven patients.

A Phase II study conducted by Alhuseinalkhudhur et al. [76] included 19 patients with primary stage II–III BC scheduled for neoadjuvant therapy with dual targeted anti-HER2 blockade, and 21 patients with metastatic breast cancer undergoing systemic therapy. The premise for this analysis was the assumption that the accumulation of [^{68}Ga]Ga-ABY-025 could be a predictor of an early tumor response to ongoing anti-HER2 therapy. According to the study design, patients underwent ^{18}F-FDG-PET/CT before and after two courses of chemo/targeted therapy to assess early metabolic response, and [^{68}Ga]Ga-ABY-025 before treatment.

A repeat biopsy was performed in all cases on a tumor focus to evaluate the HER2 status relative to the treatment. In a cohort of 12 patients, a comparison of PET imaging with [^{68}Ga]Ga-ABY-025 and biopsy data uncovered a discrepancy in HER2/neu status, which was ascribed to several factors. These encompassed challenges in tumor material acquisition, such as the observed prevalence of negative HER2 expression in positive PET scans when samples originated from the liver or bone, intratumoral heterogeneity, and drug binding impediments to HER2 receptors, which garnered specific attention due to the association between a positive biopsy result with diminished [^{68}Ga]Ga-ABY-025 accumulation and a poorer prognosis within the metastatic breast cancer cohort. Furthermore, the study revealed an inverse relationship between the number of prior treatment lines and the metabolic response to the current therapy: increased prior treatment lines corresponded to a higher RPH accumulation threshold for a metabolic response. However, given that this correlation was observed in only 30% of cases and that no significant concordance was found between PET with Affibody and biopsy results, a phase III study with [^{68}Ga]Ga-ABY-025 was deemed unwarranted.

Altena et al. [77] performed the initial clinical trial involving [^{68}Ga]Ga-ABY-025, which explored the potential to visualize metastatic breast cancer with HER2-low tumors. The study included eight patients with negative (IHC 1+) and an equivocal (IHC 2+, FISH negative) HER2 status, as well as two patients with no HER2 expression (IHC 0), previously determined based on primary breast tumor biopsy results. In one patient, the absence of HER2 expression was accompanied by minimal accumulation of [^{68}Ga]Ga-ABY-025, which correlated with the IHC results. In another case, the drug accumulation was higher and did not correspond to the status determined by HER2 biopsy. A detailed study of the tumor focus revealed heterogeneity of HER2 expression with higher RPH accumulation at the periphery and low

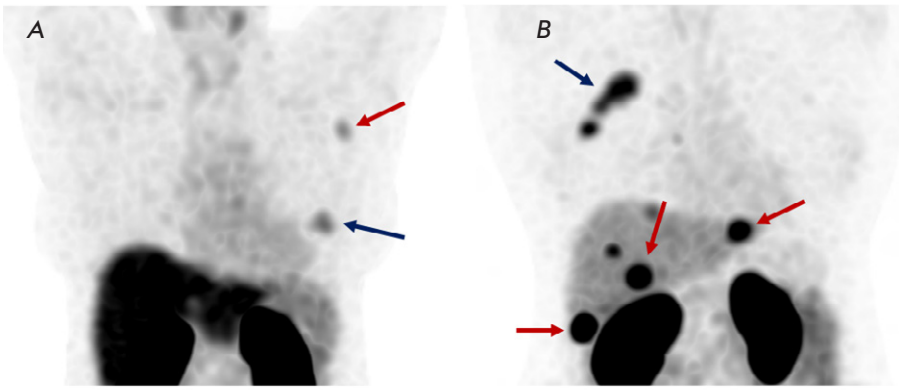

Fig. 2. Accumulation of [^{99m}Tc]Tc-ZHER2:41071 in breast cancer patients 2 h after its administration at a dose of 1,000 μg: (*A*) – patient with HER2-negative breast cancer (blue arrow indicates breast tumor; red – metastatic axillary lymph node); (*B*) – patient with HER2-positive breast cancer (blue arrow indicates breast tumor; red – liver metastases)

accumulation in the center. Therefore, it is probable that the biopsy sample originated from the central, "cold" region, whereas the primary tumor exhibited a HER2-low status. In two other cases, high accumulation was observed in previously unverified foci, which could indicate HER2 overexpression and the potential for prescribing first-line anti-HER2 therapy. In the remaining eight cases, proportional accumulation of [^{68}Ga]Ga-ABY-025 according to HER2 status was noted, consistent with the results of numerous studies of this RPH. Thus, PET using [^{68}Ga]Ga-ABY-025 can serve as an additional diagnostic tool for selecting patients eligible for therapy with antibody-drug conjugates.

In the Russian Federation, Bragina et al. were the first to implement a clinical trial utilizing the radiopharmaceutical [^{99m}Tc]Tc-ZHER2:41071 [78] for the targeted radionuclide diagnostics of HER2-positive breast cancer, using affibody molecules. The research involved 31 BC patients without prior local or systemic therapies. In all patients, the safety, tolerability, and pharmacokinetics of the drug were assessed, with the accumulation of the RPH by the tumor compared with the results of IHC/FISH. The patients were divided into three cohorts depending on the administered dose of [^{99m}Tc]Tc-ZHER2:41071: 500, 1,000 and 1,500 μg. All patients showed good tolerability of RPH at all stages of dynamic follow-up. Additionally, at a dose of 1,000 μg, the drug exhibited enhanced pharmacokinetic properties two hours after administration, along with superior breast tumor separation rates contingent upon HER2/neu status. The [^{99m}Tc]Tc-ZHER2:41071 preparation exhibited a low level of accumulation in normal liver tissue, thereby enabling the visualization of a liver metastasis in one patient, which was later verified through contrast-enhanced computed tomography. A clinical example of the use of RPH is shown in *Fig. 2*.

CONCLUSION

Worldwide, the incidence and mortality rates of malignant tumors are notably high. In this context, the diagnostic stage, involving the investigation of clinical-instrumental, morphologic, and molecular parameters, is of particular importance in identifying the optimal strategies for local and systemic treatment [6]. Given the challenges involved in one-step assessment of tumor process prevalence, the necessity of numerous invasive interventions, the financial implications, and the possibility of subjective interpretation, of significant relevance is the introduction of supplementary patient examination methods for those with malignant conditions. Targeted radionuclide imaging shows great potential, because it enables both anatomical staging and the analysis of tumor nodule molecular characteristics, ultimately leading to improved examinations and fewer invasive procedures [23, 24].

This review highlights the potential for affibodies to be used as beneficial agents in biotechnology and clinical medicine, especially in the context of bioluminescent ultrasound imaging and in developing antiviral and targeted therapies [38–40]. At present, most studies focus on radio conjugates of affibody with varied isotopes for targeted imaging of malignant tumors in various locations. Preclinical trials have consistently demonstrated a strong affinity of Affibody

for molecular targets like epidermal growth factor receptor type 2 (HER2/neu) [59], programmed cell death receptor ligand (PD-L1) [52], B7-H3 receptor (CD276) [58], platelet-derived growth factor receptor type beta (PDGFRβ), and other receptors, as well as suitability for tumor imaging using PET and SPECT techniques.

The findings from several inpatient clinical trials of affibody for HER2-positive breast cancer are compelling [71–75], demonstrating excellent radiopharmaceutical tolerability and no adverse effects throughout dynamic monitoring. The clinical significance of visualizing breast tumor structures, regional lymph nodes, and distant organs and tissues, alongside HER2/neu expression, is notable, with results comparable to immunohistochemical and FISH analyses [76, 77]. The analysis performed clearly demonstrates the high potential of using alternative non-immunoglobulin framework proteins, like affibody molecules, in clinical applications. ●

This study was financially supported by the Russian Science Foundation (grant No. 075-15-2024-536).

REFERENCES

1. Bray F, Laversanne M, Sung H, et al. Global cancer statistics 2022: GLOBOCAN estimates of incidence and mortality worldwide for 36 cancers in 185 countries. *CA Cancer J Clin.* 2024;74(3):229-263. doi: 10.3322/caac.21834
2. Kaprin AD, Starinskii VV, Shakhzadova AO, eds. *Zlokachestvennye novoobrazovaniia v Rossii v 2023 godu (zabolevaemost i smertnost)* [Malignant neoplasms in Russia in 2023 (morbidity and mortality)]. P.A. Gertsen Moscow Oncology Research Institute; 2024.
3. Cai A, Chen Y, Wang LS, Cusick JK, Shi Y. Depicting Biomarkers for HER2-Inhibitor Resistance: Implication for Therapy in HER2-Positive Breast Cancer. *Cancers (Basel).* 2024;16(15):2635. doi: 10.3390/cancers16152635
4. Cai M, Song XL, Li XA, et al. Current therapy and drug resistance in metastatic castration-resistant prostate cancer. *Drug Resist Updat.* 2023;68:100962. doi: 10.1016/j.drup.2023.100962
5. Wang L, Wang X, Zhu X, et al. Drug resistance in ovarian cancer: from mechanism to clinical trial. *Mol Cancer.* 2024;23(1):66. doi: 10.1186/s12943-024-01967-3
6. Passaro A, Al Bakir M, Hamilton EG, et al. Cancer biomarkers: Emerging trends and clinical implications for personalized treatment. *Cell.* 2024;187(7):1617-1635. doi: 10.1016/j.cell.2024.02.041
7. Chae KJ, Hong H, Yoon SH, et al. Non-diagnostic Results of Percutaneous Transthoracic Needle Biopsy: A Meta-analysis. *Sci Rep.* 2019;9(1):12428. doi: 10.1038/s41598-019-48805-x
8. Laurent F, Montaudon M, Latrabe V, Bégueret H. Percutaneous biopsy in lung cancer. *Eur J Radiol.* 2003;45(1):60-68. doi: 10.1016/s0720-048x(02)00286-3
9. Kemeny MM, Busch-Devereaux E, Merriam LT, O'Hea BJ. Cancer surgery in the elderly. *Hematol Oncol Clin North Am.* 2000;14(1):169-192. doi: 10.1016/s0889-8588(05)70283-5
10. Nicolò E, Serafini MS, Munoz-Arcos L, et al. Real-time assessment of HER2 status in circulating tumor cells of breast cancer patients: Methods of detection and clinical implications. *J Liq Biopsy.* 2023;2:100117. doi: 10.1016/j.jlb.2023.100117
11. Hou Y, Nitta H, Li Z. HER2 Intratumoral Heterogeneity in Breast Cancer, an Evolving Concept. *Cancers (Basel).* 2023;15(10):2664. doi: 10.3390/cancers15102664
12. Hamilton E, Shastry M, Shiller SM, Ren R. Targeting HER2 heterogeneity in breast cancer. *Cancer Treat Rev.* 2021;100:102286. doi: 10.1016/j.ctrv.2021.102286
13. Laprovitera N, Riefolo M, Ambrosini E, Klec C, Pichler M, Ferracin M. Cancer of Unknown Primary: Challenges and Progress in Clinical Management. *Cancers (Basel).* 2021;13(3):451. doi: 10.3390/cancers13030451
14. Harms PW, Frankel TL, Moutafi M, et al. Multiplex Immunohistochemistry and Immunofluorescence: A Practical Update for Pathologists. *Mod Pathol.* 2023;36(7):100197. doi: 10.1016/j.modpat.2023.100197
15. Lino-Silva LS, Gamboa-Domínguez A, Zúñiga-Tamayo D, López-Correa P. Interobserver variability in colorectal cancer and the 2016 ITBCC concensus. *Mod Pathol.*

2019;32(1):159-160. doi: 10.1038/s41379-018-0027-5
16. Wu Q, Xu L. Challenges in HER2-low breast cancer identification, detection, and treatment. *Transl Breast Cancer Res.* 2024;5:3. doi: 10.21037/tbcr-23-48
17. Rulten SL, Grose RP, Gatz SA, Jones JL, Cameron AJM. The Future of Precision Oncology. *Int J Mol Sci.* 2023;24(16):12613. doi:10.3390/ijms241612613
18. Langbein T, Weber WA, Eiber M. Future of Theranostics: An Outlook on Precision Oncology in Nuclear Medicine. *J Nucl Med.* 2019;60(S2):13S-19S. doi: 10.2967/jnumed.118.220566
19. Idée JM, Louguet S, Ballet S, Corot C. Theranostics and contrast-agents for medical imaging: a pharmaceutical company viewpoint. *Quant Imaging Med Surg.* 2013;3(6):292-297. doi: 10.3978/j.issn.2223-4292.2013.12.06
20. Klain M, Nappi C, Zampella E, et al. Ablation rate after radioactive iodine therapy in patients with differentiated thyroid cancer at intermediate or high risk of recurrence: a systematic review and a meta-analysis. *Eur J Nucl Med Mol Imaging.* 2021;48(13):4437-4444. doi: 10.1007/s00259-021-05440-x
21. Bauckneht M, Ciccarese C, Laudicella R, et al. Theranostics revolution in prostate cancer: Basics, clinical applications, open issues and future perspectives. *Cancer Treat Rev.* 2024;124:102698. doi: 10.1016/j.ctrv.2024.102698
22. Kasi PB, Mallela VR, Ambrozkiewicz F, Trailin A, Liška V, Hemminki K. Theranostics Nanomedicine Applications for Colorectal Cancer and Metastasis: Recent Advances. *Int J Mol Sci.* 2023;24(9):7922. doi: 10.3390/ijms24097922
23. Song Y, Zou J, Castellanos EA, et al. Theranostics — a sure cure for cancer after 100 years? *Theranostics.* 2024;14(6):2464-2488. doi: 10.7150/thno.96675
24. Burkett BJ, Bartlett DJ, McGarrah PW, et al. A Review of Theranostics: Perspectives on Emerging Approaches and Clinical Advancements. *Radiol Imaging Cancer.* 2023;5(4):e220157. doi: 10.1148/rycan.220157
25. Bodei L, Herrmann K, Schöder H, Scott AM, Lewis JS. Radiotheranostics in oncology: current challenges and emerging opportunities. *Nat Rev Clin Oncol.* 2022;19(8):534-550. doi: 10.1038/s41571-022-00652-y
26. Wei Z, Li B, Wen X, et al. Engineered Antibodies as Cancer Radiotheranostics. *Adv Sci (Weinh).* 2024;11(30):e2402361. doi: 10.1002/advs.202402361
27. Bragina OD, Chernov VI, Garbukov EYu, et al. Possibilities of radionuclide diagnostics of Her2-positive breast cancer using technetium-99m-labeled target molecules: the first experience of clinical use. *Bull Sib Med.* 2021;20(1):23-30. doi: 10.20538/1682-0363-2021-1-23-30
28. Tolmachev V, Vorobyeva A. Radionuclides in Diagnostics and Therapy of Malignant Tumors: New Development. *Cancers (Basel).* 2022;14(2):297. doi: 10.3390/cancers14020297
29. Bragina OD, Deyev SM, Chernov VI, Tolmachev VM. The Evolution of Targeted Radionuclide Diagnosis of HER2-Positive Breast Cancer. *Acta Naturae.* 2022;14(2):4-15. doi: 10.32607/actanaturae.11611
30. Luo R, Liu H, Cheng Z. Protein scaffolds: antibody alternatives for cancer diagnosis and therapy. *RSC Chem Biol.* 2022;3(7):830-847. doi: 10.1039/d2cb00094f
31. Tolmachev V, Orlova A, Sörensen J. The emerging role of radionuclide molecular imaging of HER2 expression in breast cancer. *Semin Cancer Biol.* 2021;72:185-197. doi: 10.1016/j.semcancer.2020.10.005
32. Shipunova VO, Deyev SM. Artificial Scaffold Polypeptides As an Efficient Tool for the Targeted Delivery of Nanostructures In Vitro and In Vivo. *Acta Naturae.* 2022;14(1):54-72. doi: 10.32607/actanaturae.11545
33. Liu J, Cui D, Jiang Y, et al. Selection and characterization of a novel affibody peptide and its application in a two-site ELISA for the detection of cancer biomarker alpha-fetoprotein. *Int J Biol Macromol.* 2021;166:884-892. doi: 10.1016/j.ijbiomac.2020.10.245
34. Zhu J, Kamara S, Cen D, et al. Correction: Generation of novel affibody molecules targeting the EBV LMP2A N-terminal domain with inhibiting effects on the proliferation of nasopharyngeal carcinoma cells. *Cell Death Dis.* 2020;11(6):494. doi: 10.1038/s41419-020-2692-9
35. Liu S, Gao C, Tong Z, et al. A highly sensitive electrochemiluminescence method for abrin detection by a portable biosensor based on a screen-printed electrode with a phage display affibody as specific labeled probe. *Anal Bioanal Chem.* 2022;414(2):1095-1104. doi: 10.1007/s00216-021-03735-4
36. Barozzi A, Lavoie RA, Day KN, Prodromou R, Menegatti S. Affibody-Binding Ligands. *Int J Mol Sci.* 2020;21(11):3769. doi: 10.3390/ijms21113769
37. DiRusso CJ, Dashtiahangar M, Gilmore TD. Scaffold proteins as dynamic integrators of biological processes. *J Biol Chem.* 2022;298(12):102628. doi: 10.1016/j.jbc.2022.102628
38. Ståhl S, Gräslund T, Eriksson Karlström A, Frejd FY, Nygren PÅ, Löfblom J. Affibody Molecules in Biotechnological and Medical Applications. *Trends Biotechnol.* 2017;35(8):691-712. doi: 10.1016/j.tibtech.2017.04.007
39. Hersh J, Yang YP, Roberts E, et al. Targeted Bioluminescent Imaging of Pancreatic Ductal Adenocarcinoma Using Nanocarrier-Complexed EGFR-Binding Affibody-Gaussia Luciferase Fusion Protein. *Pharmaceutics.* 2023;15(7):1976. doi: 10.3390/pharmaceutics15071976
40. Du W, Jiang P, Li Q, et al. Novel Affibody Molecules Specifically Bind to SARS-CoV-2 Spike Protein and Efficiently Neutralize Delta and Omicron Variants. *Microbiol Spectr.* 2023;11(1):e0356222. doi: 10.1128/spectrum.03562-22
41. Gabriele F, Palerma M, Ippoliti R, Angelucci F, Pitari G, Ardini M. Recent Advances on Affibody- and DARPin-Conjugated Nanomaterials in Cancer Therapy. *Int J Mol Sci.* 2023;24(10):8680. doi: 10.3390/ijms24108680
42. Cai W, Lv W, Meng L, Duan Y, Zhang L. The Combined Effect of Nanobubble-IR783-HPPH-Affibody Complex and Laser on HER2-Positive Breast Cancer. *Int J Nanomedicine.* 2023;18:339-351. doi: 10.2147/IJN.S387409
43. Wu Y, Li H, Yan Y, et al. Affibody-Modified Gd@C-Dots with Efficient Renal Clearance for Enhanced MRI of EGFR Expression in Non-Small-Cell Lung Cancer. *Int J Nanomedicine.* 2020;15:4691-4703. doi: 10.2147/IJN.S244172
44. Zhou H, Liu H, Zhang Y, et al. "PFH/AGM-CBA/HSV-TK/LIPOSOME-Affibody": Novel Targeted Nano Ultrasound Contrast Agents for Ultrasound Imaging and Inhibited the Growth of ErbB2-Overexpressing Gastric Cancer Cells. *Drug Des Devel Ther.* 2022;16:1515-1530. doi: 10.2147/DDDT.S351623
45. Pinto Salgueiro G, Yilmaz O, Nogueira M, Torres T. Interleukin-17 Inhibitors in the Treatment of Hidradenitis Suppurativa. *BioDrugs.* 2025;39(1):53-74. doi: 10.1007/s40259-024-00687-w
46. Kerschbaumer A, Smolen JS, Ferreira RJO, et al. Efficacy and safety of pharmacological treatment of psoriatic arthritis: a systematic literature research informing

the 2023 update of the EULAR recommendations for the management of psoriatic arthritis. *Ann Rheum Dis.* 2024;83(6):760-774. doi: 10.1136/ard-2024-225534
47. Ahmadzadehfar H, Seifert R, Afshar-Oromieh A, Kratochwil C, Rahbar K. Prostate Cancer Theranostics With ^{177}Lu-PSMA. *Semin Nucl Med.* 2024;54(4):581-590. doi: 10.1053/j.semnuclmed.2024.02.007
48. Salih S, Alkatheeri A, Alomaim W, Elliyanti A. Radiopharmaceutical Treatments for Cancer Therapy, Radionuclides Characteristics, Applications, and Challenges. *Molecules.* 2022;27(16):5231. doi: 10.3390/molecules27165231
49. Zhang L, Zhang H. Recent advances of affibody molecules in biomedical applications. *Bioorg Med Chem.* 2024;113:117923. doi: 10.1016/j.bmc.2024.117923
50. Rouanne M, Radulescu C, Adam J, Allory Y. PD-L1 testing in urothelial bladder cancer: essentials of clinical practice. *World J Urol.* 2021;39(5):1345-1355. doi: 10.1007/s00345-020-03498-0
51. Mucileanu A, Chira R, Mircea PA. PD-1/PD-L1 expression in pancreatic cancer and its implication in novel therapies. *Med Pharm Rep.* 2021;94(4):402-410. doi: 10.15386/mpr-2116
52. Lin KX, Istl AC, Quan D, Skaro A, Tang E, Zheng X. PD-1 and PD-L1 inhibitors in cold colorectal cancer: challenges and strategies. *Cancer Immunol Immunother.* 2023;72(12):3875-3893. doi: 10.1007/s00262-023-03520-5
53. Liang Z, Hu X, Hu H, Wang P, Cai J. Novel small ^{99m}Tc-labeled affibody molecular probe for PD-L1 receptor imaging. *Front Oncol.* 2022;12:1017737. doi: 10.3389/fonc.2022.1017737
54. Zhao B, Li H, Xia Y, et al. Immune checkpoint of B7-H3 in cancer: from immunology to clinical immunotherapy. *J Hematol Oncol.* 2022;15(1):153. doi: 10.1186/s13045-022-01364-7
55. Getu AA, Tigabu A, Zhou M, Lu J, Fodstad Ø, Tan M. New frontiers in immune checkpoint B7-H3 (CD276) research and drug development. *Mol Cancer.* 2023;22(1):43. doi: 10.1186/s12943-023-01751-9
56. Oroujeni M, Bezverkhniaia EA, Xu T, et al. Evaluation of an Affibody-Based Binder for Imaging of Immune Check-Point Molecule B7-H3. *Pharmaceutics.* 2022;14(9):1780. doi: 10.3390/pharmaceutics14091780
57. Oroujeni M, Bezverkhniaia EA, Xu T, et al. Evaluation of affinity matured Affibody molecules for imaging of the immune checkpoint protein B7-H3. *Nucl Med Biol.* 2023;124-125:108384. doi: 10.1016/j.nucmedbio.2023.108384
58. Cai H, Li Z, Shi Q, et al. Preclinical evaluation of ^{68}Ga-radiolabeled trimeric affibody for PDGFRβ-targeting PET imaging of hepatocellular carcinoma. *Eur J Nucl Med Mol Imaging.* 2023;50(10):2952-2961. doi: 10.1007/s00259-023-06260-x
59. Papadopoulos N, Lennartsson J. The PDGF/PDGFR pathway as a drug target. *Mol Aspects Med.* 2018;62:75-88. doi: 10.1016/j.mam.2017.11.007
60. Ivanova M, Porta FM, D'Ercole M, et al. Standardized pathology report for HER2 testing in compliance with 2023 ASCO/CAP updates and 2023 ESMO consensus statements on HER2-low breast cancer. *Virchows Arch.* 2024;484(1):3-14. doi: 10.1007/s00428-023-03656-w
61. Wolff AC, Somerfield MR, Dowsett M, et al. Human Epidermal Growth Factor Receptor 2 Testing in Breast Cancer: ASCO-College of American Pathologists Guideline Update. *J Clin Oncol.* 2023;41(22):3867-3872. doi: 10.1200/JCO.22.02864
62. Giugliano F, Carnevale Schianca A, Corti C, et al. Unlocking the Resistance to Anti-HER2 Treatments in Breast Cancer: The Issue of HER2 Spatial Distribution. *Cancers (Basel).* 2023;15(5):1385. doi: 10.3390/cancers15051385
63. Schrijver WAME, Suijkerbuijk KPM, van Gils CH, van der Wall E, Moelans CB, van Diest PJ. Receptor Conversion in Distant Breast Cancer Metastases: A Systematic Review and Meta-analysis. *J Natl Cancer Inst.* 2018;110(6):568-580. doi: 10.1093/jnci/djx273
64. Han J, Chen Y, Zhao Y, et al. Pre-Clinical Study of the [^{18}F]AlF-Labeled HER2 Affibody for Non-Invasive HER2 Detection in Gastric Cancer. *Front Med (Lausanne).* 2022;9:803005. doi: 10.3389/fmed.2022.803005
65. Stewart D, Cristea M. Antibody-drug conjugates for ovarian cancer: current clinical development. *Curr Opin Obstet Gynecol.* 2019;31(1):18-23. doi: 10.1097/GCO.0000000000000515
66. Luo H, Xu X, Ye M, Sheng B, Zhu X. The prognostic value of HER2 in ovarian cancer: A meta-analysis of observational studies. *PLoS One.* 2018;13(1):e0191972. doi: 10.1371/journal.pone.0191972
67. Murciano-Goroff YR, Suehnholz SP, Drilon A, Chakravarty D. Precision Oncology: 2023 in Review. *Cancer Discov.* 2023;13(12):2525-2531. doi: 10.1158/2159-8290.CD-23-1194
68. Hu X, Hu H, Li D, Wang P, Cai J. Affibody-based molecular probe ^{99m}Tc-$(HE)_3Z_{HER2:V2}$ for non-invasive HER2 detection in ovarian and breast cancer xenografts. *Open Med (Wars).* 2024;19(1):20241027. doi: 10.1515/med-2024-1027
69. Swain SM, Shastry M, Hamilton E. Targeting HER2-positive breast cancer: advances and future directions. *Nat Rev Drug Discov.* 2023;22(2):101-126. doi: 10.1038/s41573-022-00579-0
70. Dowling GP, Keelan S, Toomey S, Daly GR, Hennessy BT, Hill ADK. Review of the status of neoadjuvant therapy in HER2-positive breast cancer. *Front Oncol.* 2023;13:1066007. doi: 10.3389/fonc.2023.1066007
71. Zimmerman BS, Esteva FJ. Next-Generation HER2-Targeted Antibody-Drug Conjugates in Breast Cancer. *Cancers (Basel).* 2024;16(4):800. doi: 10.3390/cancers16040800
72. Baum RP, Prasad V, Müller D, et al. Molecular imaging of HER2-expressing malignant tumors in breast cancer patients using synthetic 111In- or 68Ga-labeled affibody molecules. *J Nucl Med.* 2010;51(6):892-897. doi: 10.2967/jnumed.109.073239
73. Sörensen J, Sandberg D, Sandström M, et al. First-in-human molecular imaging of HER2 expression in breast cancer metastases using the 111In-ABY-025 affibody molecule. *J Nucl Med.* 2014;55(5):730-735. doi: 10.2967/jnumed.113.131243
74. Sörensen J, Velikyan I, Sandberg D, et al. Measuring HER2-Receptor Expression In Metastatic Breast Cancer Using [68Ga]ABY-025 Affibody PET/CT. *Theranostics.* 2016;6(2):262-271. doi: 10.7150/thno.13502
75. Miao H, Sun Y, Jin Y, Hu X, Song S, Zhang J. Application of a Novel ^{68}Ga-HER2 Affibody PET/CT Imaging in Breast Cancer Patients. *Front Oncol.* 2022;12:894767. doi: 10.3389/fonc.2022.894767
76. Alhuseinalkhudhur A, Lindman H, Liss P, et al. Human Epidermal Growth Factor Receptor 2-Targeting [^{68}Ga]Ga-ABY-025 PET/CT Predicts Early Metabolic Response in Metastatic Breast Cancer. *J Nucl Med.* 2023;64(9):1364-1370. doi: 10.2967/jnumed.122.265364
77. Altena R, Burén SA, Blomgren A, et al. Human Epider-

mal Growth Factor Receptor 2 (HER2) PET Imaging of HER2-Low Breast Cancer with [^{68}Ga]Ga-ABY-025: Results from a Pilot Study. *J Nucl Med.* 2024;65(5):700-707. doi: 10.2967/jnumed.123.266847

78. Bragina O, Chernov V, Larkina M, et al. Phase I clinical evaluation of ^{99m}Tc-labeled Affibody molecule for imaging HER2 expression in breast cancer. *Theranostics.* 2023;13(14):4858-4871. doi: 10.7150/thno.86770

mRNA-Based Personalized Cancer Vaccines: Opportunities, Challenges and Outcomes

A. A. Ibragimova[1], A. A. Fedorov[1], K. M. Kirilenko[2], E. L. Choynzonov[1], E. V. Denisov[1], M. R. Patysheva[1*]

[1]Cancer Research Institute, Tomsk National Research Medical Center, Russian Academy of Sciences, Tomsk, 634009 Russia

[2]Center for Systems Bioinformatics, Tomsk National Research Medical Center, Russian Academy of Sciences, Tomsk, 634050 Russia

*E-Mail: patysheva_mr@onco.tnimc.ru

Received: May 31, 2025; in final form, August 06, 2025

DOI: 10.32607/actanaturae.27707

ABSTRACT **mRNA-based cancer vaccines represent an innovative approach to cancer treatment. Cancer mRNA vaccines are structurally based on specific tumor antigens, a technique which enables the patient's immune system to become activated against cancer cells. Clinical trials of mRNA vaccines against various types of tumors, including melanoma, lung cancer, pancreatic carcinoma, breast cancer and others, are currently underway. Because of their favorable safety profile and adaptability, these therapeutics hold considerable promise in efforts to enhance cancer treatment efficacy and prolong patient life. This review outlines steps in the development of manufacturing technologies for mRNA-based therapeutics, describes the algorithm used to design personalized anti-tumor mRNA vaccines, discusses their practical implementation, and summarizes current clinical trials in cancer immunotherapy.**

KEYWORDS **mRNA vaccine, cancer, immunotherapy, neoantigens, liposomes, clinical trials.**

ABBREVIATIONS **APCs – antigen-presenting cells; LNPs – lipid nanoparticles; LPPs – lipopolyplexes; PEG – polyethylene glycol; CpG-ODNs – CpG-oligodeoxynucleotides; BDMPs – biotechnology-derived medicinal preparations; CTLA-4 – cytotoxic T-lymphocyte antigen-4; PD-1 – programmed cell death receptor; PD-L1 – programmed cell death receptor ligand.**

INTRODUCTION

Cancer is a leading cause of death and disability worldwide, which justifies its status as a top medical and societal concern. Despite decades of innovation, solid tumors remain among the leading causes of cancer-related mortality worldwide, owing to their high incidence and the complexity of achieving effective intervention [1]. Even with refined treatment protocols, long-term survival remains hard to achieve: in lung cancer – the most frequently diagnosed cancer – more than 50% of patients do not survive beyond 3.5 years post-diagnosis [2].

Novel therapeutic strategies are urgently needed to enhance treatment efficacy and improve both survival and the quality of life of cancer patients. In this regard, modulation of the anti-tumor immune response holds particular promise. The inclusion of immunotherapy with immune checkpoint inhibitors in clinical guidelines has significantly improved treatment efficacy with melanoma, lung cancer, breast cancer, ovarian cancer, and other types of solid tumors [3, 4]. Nucleic-acid–based anti-tumor vaccines, particularly those utilizing DNA or mRNA platforms, represent a promising frontier in cancer immunotherapy.

mRNA-based anti-tumor vaccines exploit the natural protein synthesis machinery of antigen-presenting cells (APCs): by delivering transcripts encoding tumor antigens into the cytoplasm, mRNA enables endogenous production and immunogenic presentation of the target antigen. Following processing, proteins associated with the target antigen (epitopes) can appear on the surface of APCs by binding to the molecules of the major histocompatibility complex classes I and II – MHC I and MHC II, respectively (*Fig. 1*). The resulting immune activation engages both of the arms of adaptive immunity: CD4+ T helper cells and B cells (for antibody production), as well as CD8+ cytotoxic T lymphocytes, which are capable of directly

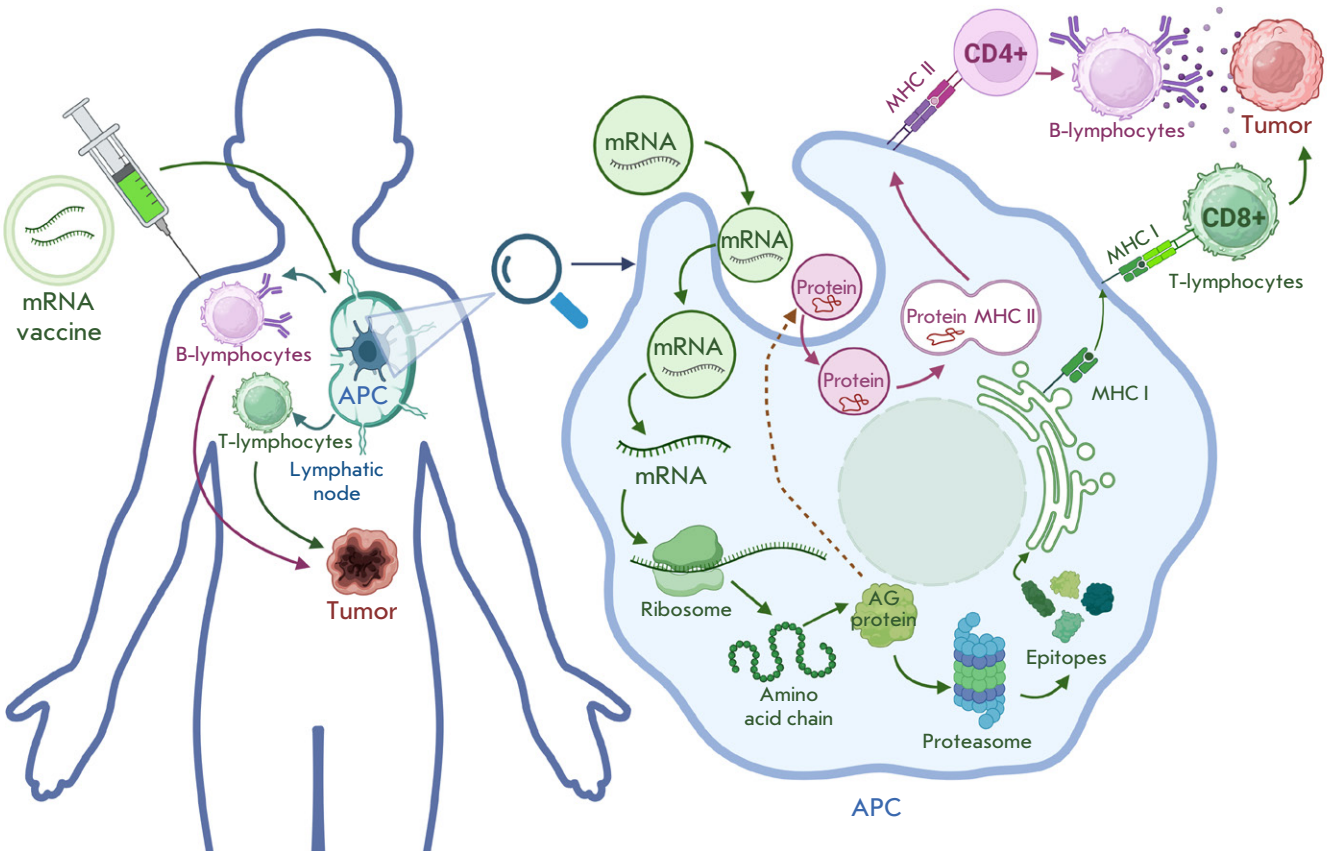

Fig. 1. Anti-tumor mRNA vaccine mechanism. mRNA – messenger ribonucleic acid, APCs – antigen-presenting cells, AG protein – antigenic protein

eliminating target cells [5]. mRNA-based vaccine platforms offer advantages such as:

1) Enhanced stability and translational efficiency. Advances in nucleotide modification and delivery technologies have rendered mRNA more resistant to degradation and significantly improved its protein expression in target cells [6].
2) Intrinsic immunostimulatory properties. The mRNA molecule itself can activate the innate immune system, thereby acting as a built-in adjuvant that enhances vaccine efficacy [7].
3) Favorable safety profile. Unlike DNA vaccines or viral vectors, mRNA remains extranuclear and does not integrate into the host genome, thereby eliminating the risk of insertional mutagenesis [8].
4) Economical and scalable production pipeline. The development of personalized mRNA vaccines relies on the synthesis of a single DNA template, followed by enzymatic *in vitro* transcription to yield large quantities of mRNA – a streamlined process that is substantially less resource-intensive than the complex manufacturing required for viral vector or plasmid DNA vaccines.

This review critically assesses the promise of mRNA-based therapeutic vaccines in solid malignancies, addressing key aspects, including mRNA design and production, delivery systems for efficient targeting of APCs, and the status of ongoing and completed clinical trials.

KEY MILESTONES IN THE EVOLUTION OF mRNA TECHNOLOGIES

Despite the discovery of mRNA and transcription in the 1960s, the therapeutic potential of synthetic mRNA was not immediately understood. A pivotal shift occurred in 1984, when researchers demonstrated that *in vitro*–transcribed mRNA could direct functional protein expression in cells, laying the foundation for mRNA-based gene regulation and therapy [9] (*Fig. 2*). Early progress in mRNA therapeutics was hampered by the molecule's susceptibility to degradation and inefficient cellular delivery [10]. This chal-

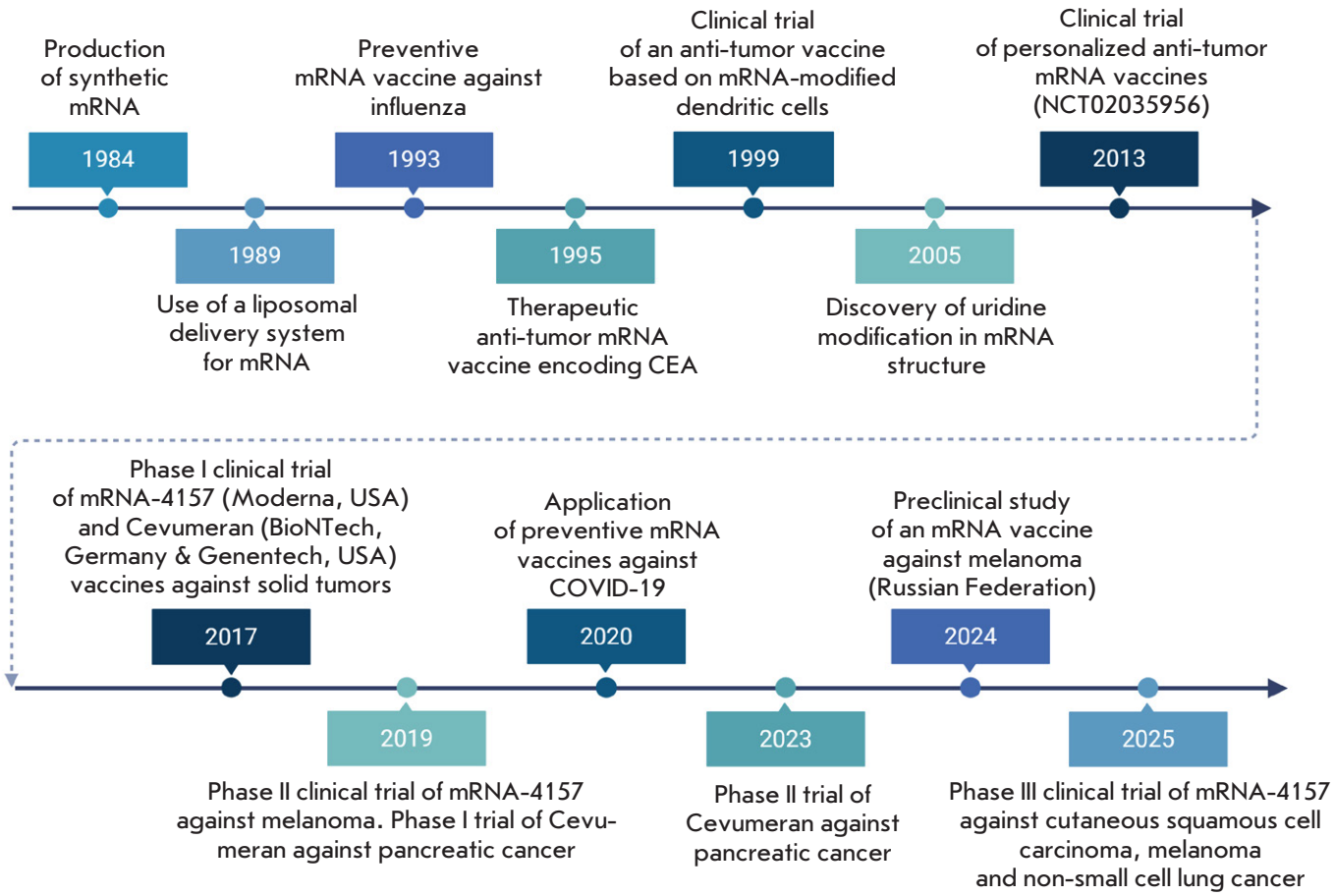

Fig. 2. Development history of mRNA-based vaccine production and application technologies. CEA – carcinoembryonic antigen, DC – dendritic cells, mRNA – messenger ribonucleic acid

lenge was first overcome in 1989, with the successful delivery of synthetic Photinus pyralis luciferase mRNA into murine cells via liposomes formulated with the cationic lipid DOTMA (N-[1-(2,3-dioleoyloxy) propyl]-N,N,N-trimethylammonium chloride) [11]. In the 1990s, most companies that had pursued mRNA vaccine development redirected their investments elsewhere, as the production of stable liposomal mRNA formulations remained prohibitively expensive. Nevertheless, research continued: as early as 1990, a landmark study demonstrated that synthetic mRNA could be expressed *in vivo* following direct injection into mice [12, 13]. In 1993, researchers synthesized the first prophylactic mRNA vaccine, designed to express the nucleoprotein of the influenza virus and demonstrated its ability to activate antigen-specific cytotoxic T lymphocytes in murine models [14].

The first evidence of anti-tumor immunity induced by mRNA vaccination was reported in 1995, following intramuscular delivery of a mRNA-encoding carcinoembryonic antigen (CEA) into mice [15]. Subsequently, in 1999, using a mouse melanoma model, it was demonstrated that the introduction of gp100 mRNA, which encodes the melanosome matrix glycoprotein, into the spleen inhibits tumor growth [16]. Meanwhile, a Phase 1 clinical trial was initiated to activate antigen presentation in autologous dendritic cells from prostate cancer patients by means of synthetic mRNA encoding prostate-specific antigen (PSA) [17]. In 2000, Ingmar Hoerr et al. discovered that direct injections of mRNA can induce an immune response in mice and, then, with the promising development of mRNA vaccines in mind, CureVac (Germany) was incorporated, a company that remains one of the leading developers of mRNA-based vaccines to this day [18, 19].

The seminal work of Katalin Karikó and Drew Weissman laid the groundwork for modern mRNA

therapeutics. During early efforts to develop an mRNA-based HIV vaccine in the late 1990s, they discovered that unmodified mRNA activated innate immune pathways – specifically through Toll-like receptors (TLR3, TLR7, TLR8) – eliciting a robust inflammatory response in murine models [20]. A pivotal advance happened in 2005, when Karikó and Weissman reported and patented the incorporation of pseudouridine, in place of uridine, within mRNA. This chemical modification prevented recognition by innate immune sensors, thereby suppressing inflammatory responses and markedly improving translational efficiency – a discovery that underpins the development of modern mRNA vaccines [21, 22]. In 2023, Katalin Karikó and Drew Weissman were awarded the Nobel Prize in Physiology or Medicine for their discovery that nucleoside-modified mRNA can suppress innate immune activation – a breakthrough that enabled the development of effective mRNA vaccines [23].

Improvements in mRNA-based technology have enabled pharmaceutical companies such as Moderna and Pfizer-BioNTech to develop effective mRNA vaccines against COVID-19 [6]. The successful and expanded clinical use of mRNA vaccines has driven the rapid advancement and optimization of the entire mRNA manufacturing pipeline [24]. Moreover, mRNA technologies are suitable for creating preparations not only against infectious diseases (rabies, influenza, Epstein-Barr virus, Zika virus, Nipah virus, etc.), but also against oncological diseases, such as prostate cancer, hepatocellular carcinoma, melanoma, and non-small cell lung cancer, thereby attracting the attention of scientists and biotechnology and pharmaceutical companies in Russia, the United States, Germany, China, and other countries [24]. Against this background, the first clinical trial of a personalized mRNA-based vaccine against melanoma (NCT02035956) was initiated in 2013 [25].

Personalized therapy represents the most promising strategy in modern oncology. mRNA-based anti-tumor vaccines targeting tumor neoantigens – unique antigens arising from somatic mutations in malignant cells – have demonstrated high efficacy. Neoantigens are broadly classified into two categories: shared (or common) neoantigens, which occur across multiple patients and are absent from the normal genome, and personalized (or private) neoantigens, which are unique to an individual's tumor mutanome [26, 27]. Shared neoantigens represent promising targets for "off-the-shelf" therapeutic cancer vaccines with broad applicability, whereas personalized neoantigens – though patient-specific – have demonstrated remarkable therapeutic efficacy in clinical settings [28–32]. Production of a personalized anti-tumor mRNA vaccine involves a sequential workflow: (1) comprehensive profiling of the patient's tumor neoantigen repertoire, (2) computational design of the mRNA construct, (3) synthesis of the DNA template, (4) *in vitro* transcription to generate mRNA, and (5) formulation into a delivery vehicle, such as lipid nanoparticles.

Identification of tumor neoantigens

The identification of neoantigens, defined as patient-unique tumor antigens generated by somatic mutations, represents the cornerstone of personalized mRNA vaccine design. This process involves a multimodal genomic analysis including whole-exome sequencing (WES), whole-genome sequencing (WGS), and transcriptome profiling, coupled with advanced computational algorithms to predict and rank neoantigens based on immunogenicity and expression levels [33, 34]. At the same time, DNA sequencing makes it possible to identify somatic mutations (missense, nonsense, deletions, insertions, etc.) that potentially encode neoepitopes, while RNA sequencing confirms their expression status, which serves as an important criterion for selecting neoantigens [35]. Additionally, the use of RNA sequencing allows for the false positives detected in a DNA sequencing analysis but not actually expressed to be excluded [35]. Actually, comparing DNA and RNA sequencing data in practice yields more reliable results when forming a pool of potential neoantigens [34].

Once the "raw" data has been collected, it undergoes preliminary processing, including quality control (using FastQC[1]), filtering and trimming of incorrect sections (Trimmomatic or Cutadapt), and alignment of reads to the reference genome (Bowtie 2) [36–38]. The subsequent step involves identifying somatic mutations in the tumor as compared to normal samples, using tools such as MuTect2 (from the GATK pipeline), Strelka, or VarScan2 [39–41]. In addition, the variant allele frequency (VAF) is calculated, reflecting the proportion of mutations in the tumor cell genome [42]. Simultaneously, RNA sequencing data is analyzed using STAR + RSEM, the Salmon or Kallisto pipeline which allows quantitative expression metrics to be collected – TPM (Transcripts Per Million) and FPKM (Fragments Per Kilobase of transcript per Million mapped reads) [43–46]. Such normalization approaches incorporate both the transcript length and sequencing depth, allowing for re-

[1] *Andrews S. FastQC: A Quality Control Tool for High Throughput Sequence Data. In: Babraham Bioinformatics [Internet]. Cambridge: Babraham Institute; 2004-. [cited 2024 Dec 15]. Available at: https://www.bioinformatics.babraham.ac.uk/projects/fastqc/*

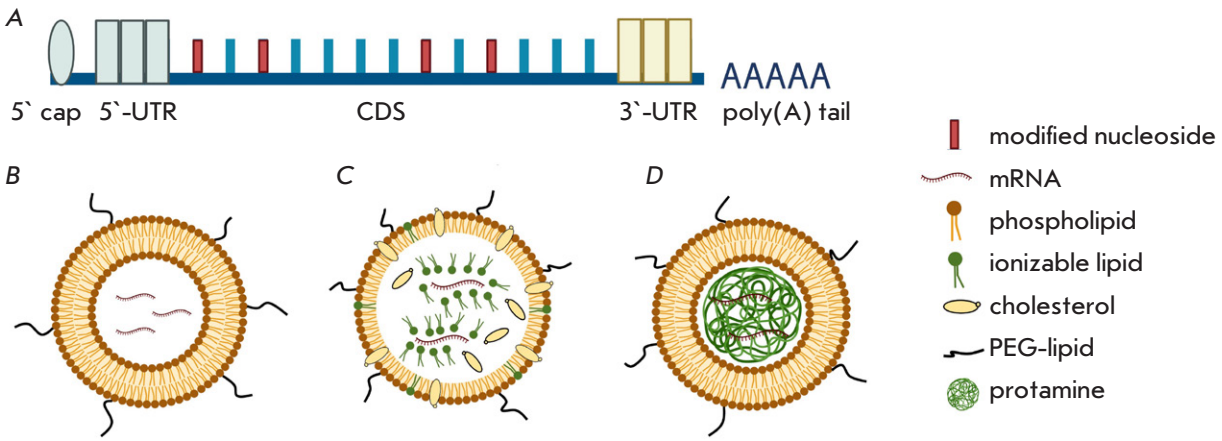

Fig. 3. Structural components of mRNA vaccine. (*A*) – mRNA molecule composition; (*B*) – liposome structure; (*C*) – lipid nanoparticle structure; (*D*) – lipoliplex structure. 5′ cap – cap, 5′-UTR and 3′-UTR – untranslated regions, CDS – coding sequence

liable cross-sample and cross-transcript expression quantification, which is essential in prioritizing immunogenic neoantigens [34].

The next stage involves running computational predictions of neoepitopes and an assessment of the likelihood that they would elicit a T-cell-mediated immune response. Determination of the patient's HLA genotype using, for example, the OptiType algorithm is particularly significant [47]. The binding affinity of mutant peptides to MHC I/II molecules is also assessed using various tools, the most popular of which are NetMHC and NetMHCpan, MHCflurry, and IEDB [48–50]. With these tools, the IC_{50}, or percentile rank, is calculated, allowing epitopes with a high predicted binding affinity (IC_{50} < 500 nM) to be sampled. Today's neoantigen prioritization strategies incorporate multiple biological and computational parameters: the expression level of the mutant allele, variant allele frequency (VAF), dissimilarity of the mutant peptide from its wild-type counterpart, and the thermodynamic stability of the peptide-MHC complex [34]. Although *in silico* neoantigen screening is standard in personalized mRNA vaccine pipelines because of its efficiency, immunopeptidomics-mass spectrometry-based identification of naturally presented peptide–MHC complexes offers definitive validation of surface presentation [51, 52].

While predicting which neoepitopes will elicit a strong immune response is far from a perfect approach, the synergy of multi-omics data and intelligent computational models now offers a powerful and increasingly reliable strategy for designing personalized mRNA vaccines with real therapeutic potential [34].

Key structural elements of mRNA

Modern mRNA vaccines are engineered with an optimized molecular architecture to enhance stability, maximize protein expression, and minimize unintended immune activation [53]. The mRNA molecule has several essential elements (5'-cap, 5'-UTR, coding sequence, 3'-UTR, and poly(A)-tail), each of which plays a key role (*Fig. 3A*) [53].

The rational engineering of therapeutic mRNA now relies heavily on advanced bioinformatic software capable of predicting higher order RNA structures. Secondary and tertiary folding patterns – key determinants of mRNA stability, innate immune activation, and protein yield in APCs – are modeled using tools such as RNAfold, NUPACK, and mfold. These platforms facilitate the identification of structurally optimal regions where to incorporate modified nucleosides, thereby fine-tuning vaccine efficacy and safety [54–56].

The 5′ Cap is the most critical structural element of mRNA, as it protects the transcript from exonucleolytic degradation and facilitates the initiation of translation (*Fig. 3A*). Several types of caps are classified: Cap0, Cap1, Cap2, m6Am Cap. Modern technologies, such as CleanCap, enable a capping efficiency of up to 99%, which is critical for the synthesis of target proteins in APCs [53]. Modified nucleosides (pseudouri-

dine, 5-methylcytidine, N1-methylpseudouridine) are often involved in mRNA production, which increases expression levels and reduces innate immunogenicity. The cap is followed by a 5'-untranslated region (5'-UTR) which affects the stability and efficiency of translation.

The coding sequence (CDS), located in the central part of the molecule, contains information about the target antigen. In mRNA-based antitumor vaccines, these may be tumor-associated antigens (TAAs) or tumor-specific antigens (TSAs). Multiple antigens can be encoded simultaneously, which enhances the immune response [57, 58]. Codons optimization improves the speed and accuracy of translation, thereby enhancing vaccine efficacy [57]. The 3′ end of mRNA comprises the 3′-untranslated region (3′-UTR) and a polyadenylated tail, which together modulate mRNA decay kinetics, subcellular localization, and translational persistence (*Fig. 3A*) [53].

In addition to linear mRNA molecules, self-replicating mRNAs are being developed that include viral replication elements which increase their copy number in cells and thereby reduce the required dose of the mRNA preparation [53]. Circular mRNAs with a closed structure are an alternative, allowing mRNAs to remain in the body over a longer period of time and ensuring more prolonged antigen expression [58]. Both areas are being actively researched, with account of the potential to improve the efficacy and safety of mRNA-based vaccines [53, 58].

Delivery systems for mRNA-based cancer vaccines

The mRNA molecule that has been administered to the patient must be delivered to the APCs without it losing its integrity. Selecting the optimal mRNA delivery system is an important step in the production of mRNA-based vaccines. The most commonly used mRNA-based delivery systems include lipid platforms, which comprise liposomes, lipid nanoparticles (LNPs), and lipopolyplexes (LPPs). They all differ in structure and functional characteristics (*Fig. 3B–D*).

Liposomes consist of a bilipid layer forming an outer shell inside which mRNA is encapsulated. The surface of liposomes may contain polyethylene glycol (PEG) molecules, which provide steric stabilization and increase circulation time in the blood. LNPs are more complex optimized structures that include ionizable lipids, phospholipids, cholesterol, and PEG-lipids, which not only effectively encapsulate mRNA but also protect it from degradation and ensure that it is delivered into the cells' cytoplasm [59]. LNPs are successfully utilized in antitumor mRNA-based vaccines, in which they demonstrate high stability and delivery efficiency [53, 60].

The efficiency of lipid delivery platforms is affected by a variety of factors, such as size, charge, lipid composition, membrane phase state, antigen localization method, and the presence of immunomodulatory components.

The size of mRNA delivery vehicles dictates their biodistribution and the immunological outcome. Small nanoparticles – typically $\leqslant$ 100 nm for lipid nanoparticles (LNPs) and < 200 nm for conventional liposomes – readily access lymphoid tissues, engage resident dendritic cells, and are associated with Th2-polarized responses. In contrast, larger particles (> 100 nm for LNPs; > 500 nm for liposomes) exhibit prolonged retention at the injection site, creating an antigen deposit that supports Th1-type immunity [60–63].

Particle charge also plays a significant role: cationic particles, for example, based on dioctadecyl dimethylammonium bromide (DDA), are actively absorbed by APCs, promote cross-presentation and the activation of CD8+ T-lymphocytes, whereas neutral and anionic liposomes predominantly induce humoral immunity [64, 65]. In LNPs, ionizable lipids acquire a positive charge at low pH values in endosomes, facilitating the release of mRNA into the cytoplasm [66].

The phase state of the bilipid layer determines the ability of liposomes to fuse with cell membranes and release antigen intracellularly. Liquid-crystalline liposomes facilitate cross-presentation via MHC I, whereas more rigid liposomes induce a pronounced Th1 response *in vivo* [66–68]. Cholesterol, which is part of the membrane, increases the stability of liposomes and may enhance or reduce complement activation depending on its charge and size [66, 69].

The addition of immunomodulatory components such as Toll-like receptor ligands, e.g. CpG-oligodeoxynucleotides (CpG-ODNs), poly(I:C), synthetic glycolipids and cytokines, allows the immune response to be directed towards the desired type of inflammation. Specifically, CpG-ODNs recognized by TLR9 and trehalose-6,6'-dibeheneate (TDB) promote the induction of a Th1 response accompanied by IFN-γ production [70–73]. Poly(I:C), which mimics viral double-stranded RNA and activates TLR3, enhances the cross-presentation of antigen and stimulates the development of a cytotoxic T-lymphocyte response [74, 75]. Additionally, the combination of TDB with lipids such as DDA may lead to the activation of the Th17 response and the production of IL-17 [67, 76–78].

Encapsulated antigens have been demonstrated to efficiently enter the intracellular compartments of APCs, where they are processed and presented via both class I and class II MHC molecules, enabling the

activation of CD8+ and CD4+ T-lymphocytes [68]. At the same time, antigens associated with the surface of liposomes have a lower capacity for intracellular processing but may be accessible for direct recognition by B-lymphocytes via BCR receptors, contributing to the formation of a humoral response [68, 79].

Lipopolyplexes (LPPs) are hybrid systems that combine cationic lipids, such as DOTAP (1,2-dioleoyl-3-trimethylammonium-propane), and polymers, such as protamine, to form stable complexes with mRNA [80]. Lipids protect mRNA and facilitate its delivery across cell membranes, while polymers enhance mRNA compaction, increasing the stability of the complex. LPPs are highly stable *in vitro* and effectively deliver mRNA, including self-replicating mRNA, to dendritic cells, eliciting a strong immune response. LPPs used to deliver mRNA encoding neoantigens have been demonstrated to induce potent T-cell responses and exhibit anti-tumor activity in mouse models [80].

Beyond lipid-based systems, alternative mRNA delivery strategies for targeting APCs include polymeric nanoparticles, dendrimers, peptide-based complexes, physical methods such as jet injection and electroporation, and engineered viral vectors.

Polymeric nanoparticles, such as poly(β-amino-esters), are biodegradable polymers containing amino and ether groups in their structure, which enables them to bind mRNA through electrostatic interactions. The flexibility in modifying polymer nanoparticles provides the ability to vary the molecular weight, degree of branching, and polymer chemical composition, optimizing the charge, particle size, and their ability to protect mRNA from enzymatic degradation [53].

Dendrimers are highly branched polymer molecules with a tree-like structure. Dendrimers feature a compact central core – typically a small molecule or ion – serving as the focal point for the iterative, layer-by-layer growth of branched monomeric units, resulting in a well-defined, tree-like nanostructure. Functional groups such as amines or hydroxyl groups are located on the outer surface of the dendrimer, which confers the ability to bind and protect mRNA [53]. Peptide complexes consist of mRNA bound to cationic peptides such as protamine, which form dense nanoparticles as a result of electrostatic interactions between positively charged peptides and negatively charged mRNA, protecting it from degradation and facilitating its penetration into cells [53].

Jet injection allows researchers to deliver "naked" mRNA without carriers using jet injectors such as PharmaJet or Bioject. The devices have no needles and use high pressure (up to 1,000 bar) to push mRNA through the skin into the subcutaneous fat or muscle tissue. An mRNA penetration mechanism into cells is based on a temporary disruption of cell membrane integrity as a result of mechanical stress caused by a high-speed jet, which allows mRNA to reach the cytoplasm of APCs [81]. Studies show that introducing mRNA using this method can trigger an innate immune response comparable to that induced by LNPs [81].

Electroporation is primarily used for *ex vivo* delivery of mRNA into dendritic cells or other immune cells which are subsequently administered to the body. This method involves the use of electrical pulses to temporarily increase the permeability of cell membranes, facilitating penetration by the mRNA. Electroporation is effective for activating the immune response, but its use *in vivo* remains limited as a consequence of the risk of tissue damage and the complexity of implementation [53].

Viral vectors, more commonly used to deliver self-replicating mRNA, consist of a modified viral genome containing mRNA or self-replicating mRNA, as well as a protein capsid or lipid envelope that enables cell penetration. Adenoviruses, lentiviruses, or alphaviruses modified to express tumor antigens are often used. Self-replicating mRNA includes viral replication elements that enhance antigen translation in cells, reducing the required dose of the mRNA vaccine and enhancing the immune response. Vaccines utilizing viral vectors are being actively explored as immunotherapeutic agents against multiple cancer types, with particularly promising results in preclinical studies with HPV-driven tumors [82].

Storage and transportation of mRNA-based therapeutics

Immunobiological medicinal preparations, which include all known vaccines, are stored at a temperature between +2°C and +8°C[1]. The exception is mRNA-based vaccines, which are classified as biotechnology-derived medicinal preparations (BDMPs) with specific storage and transportation requirements[2]. As an example, Pfizer's mRNA vaccine is stable for 6 months at −80°C and only 5 days at +2 to

[1] *General Pharmacopoeia Article (GPA) 1.7.1.0018.18, approved by Order of the Ministry of Health of Russia No. 749 dated 31 October 2018. Available at: https://pharmacopoeia.regmed.ru/pharmacopoeia/izdanie-14/1/1-7/1-7-1/ [Accessed: February 25, 2024].*

[2] *Resolution of the Government of the Russian Federation No. 213 of February 24, 2025. "About biotechnological medicinal preparations intended for use in accordance with individual medical prescriptions and specially manufactured for a specific patient directly in the medical organization where such biotechnological medicinal preparations are used, containing compounds synthesized based on the results of genetic studies of material obtained from the patient for whom such biotechnological medicinal preparations are manufactured." Available at: http://government.ru/docs/all/157884/ [Accessed: February 25, 2024].*

+8°C. Moderna's vaccine can be stored for 6 months at −20°C but 30 days at 2–8°C [83].

Storage and transportation of mRNA vaccines requires strict temperature control as specified by the manufacturer and special equipment such as refrigerators and freezers, refrigerated boxes, and vaccine carriers that can be stored at −80°C and meet the performance standards as defined by the World Health Organization (WHO) [84].

One of the newest methods of delivery of mRNA into a patient's body is the use of micro-needle chips [84]. This method allows the mRNA preparation to be stored and transported at room temperature for several months. To date, this method has been applied exclusively to anti-infective mRNA vaccines; the technical intricacies and scalability limitations of chip-based production systems render it poorly suited to personalized cancer vaccine development.

All of the above-mentioned transportation issues lead to certain difficulties in the further implementation of mRNA vaccines; however, they do not make their use impossible in clinical practice. One way to resolve this issue could be to manufacture and use the preparation within a single institution, which is currently being done in the Russian Federation through Resolution No. 213 dated February 24, 2025, related to BDMPs intended for use in accordance with individual medical prescriptions.

Administration strategies for therapeutic mRNA cancer vaccines

Selecting an appropriate route of administration is essential in maximizing the therapeutic potential of mRNA vaccines while minimizing off-target effects and systemic toxicity. Administration routes have different characteristics and influence the distribution of the vaccine in the body, the type of immune cells activated, and, consequently, the strength and duration of the response. mRNA-based vaccines can be administered intradermally, subcutaneously, intranasally, intranodally, intraperitoneally, intramuscularly, and intravenously. In modern clinical trials, intravenous, intramuscular, and subcutaneous administration of mRNA vaccines are the most commonly practiced protocols.

In intravenous administration, the preparation penetrates the systemic bloodstream, spreading throughout organs and tissues, and rapidly reaches the APCs. This method allows for the administration of significant volumes of the vaccine and repeated runs to ensure a high level of anti-tumor immunity [58]. Data from clinical trials of BioNTech SE's intravenous vaccine Cevumeran have confirmed its safety, good tolerability, and effectiveness in stimulating an immune response against cancer cells [32, 85]. This method of administration may, however, cause the development of a generalized febrile syndrome and flu-like symptoms, and there is also a risk of systemic toxicity, which is important to consider when planning studies. As a consequence of the specific structure of the liver's vascular network and the mechanism of receptor-mediated uptake of mRNA vaccines by hepatocytes, these vaccines have an increased tropism for this organ, which can lead to immune-mediated hepatitis or hepatotoxicity [86]. With this method of preparation administration, it is essential to conduct a risk-benefit analysis of the treatment, and this puts restrictions on mRNA vaccine treatment.

Intramuscular administration of vaccines is better tolerated compared to intravenous administration. As a result of the muscle tissue's good vascularization and the presence of APCs precursors that migrated during ontogenesis and converged to the injection site, intramuscular administration is sufficient to induce an anti-tumor immune response. The additional advantages of this method include flexibility in selecting the dose administered, the possibility of repeated administration to maintain anti-tumor immune activity, and a reduced risk of adverse reactions at the injection site [87]. The only side effects as relates to this method may be fever and flu-like symptoms, which can be treated with anti-inflammatory preparations. Moderna's mRNA-4157 vaccine, encapsulated in lipid nanoparticles, was administered intramuscularly in all clinical trials, demonstrating sufficient safety and eliciting clinical responses in patients with melanoma and solid tumors [88, 89]. Considering its numerous advantages, the intramuscular route is widely used for the administration of already-approved anti-infective mRNA-based vaccines, including prophylactic preparations against SARS-CoV-2 [90–93].

Intradermal and subcutaneous methods of mRNA administration may be implemented using either the traditional syringe method, microchips, or jet injection [81, 84]. Intradermal administration of mRNA-based vaccines stimulates a Th1-type immune response, which is explained by the high concentration of APCs in the dermis and epidermis layers and the favorable microenvironment for antigen transfer [94]. Whilst this method provides an opportunity to use smaller volumes of the preparation, it often leads to local adverse reactions, such as swelling, soreness, hyperemia, and itching [95, 96]. As opposed to this, the subcutaneous method of administration is characterized by a lower number of APCs in the subcutaneous adipose tissue, which requires an increase in dosage and the use of multiple injection sites. A slow absorption rate following subcutaneous administration, however, may contribute to mRNA degradation, reducing treatment

efficacy [97]. Nevertheless, this route of administration has been used in mRNA-based vaccine trials before and is actively used in clinical trials conducted in China (NCT03908671, NCT05949775, NCT05761717) [80, 98, 99].

The intranasal route delivers the mRNA molecule to the APCs of peripheral lymphatic vessels, while the intranodal route delivers it to lymphatic APCs. At the same time, the implementation of these methods is complex and has limitations in terms of the volume of administered preparation [100]. The intraperitoneal method has similar limitations and is more commonly used to deliver mRNA-based vaccines encoding co-stimulatory immune molecules [101].

In selecting the administration method, the type of mRNA-based vaccine should be taken into consideration. As an example, to ensure the efficiency of native mRNA delivery *in vivo*, intradermal or intranodal methods are more commonly used due to the assumption that immature dendritic cells located in the dermis and lymph nodes are capable of absorbing mRNA through micro-pinocytosis [102].

Lipid nanoparticles, as a popular delivery tool, are compatible with virtually all known methods of administration. Intramuscular and intradermal administration, however, results in the longest mRNA transmission, with a half-life of more than 20 h, while intravenous administration results in a half-life of only 7 h [103]. A comparison of the anti-tumor effect and immunogenicity of intramuscular, intradermal, and subcutaneous administration of LPP-CT26 in CT26-luc mice with lung metastases was undertaken to evaluate the optimal method of vaccine delivery [80]. Mice that received the preparation subcutaneously had fewer metastatic lesions in the lungs, showed increased IFN-γ secretion, and greater anti-tumor efficacy when the number of injection sites was increased without a change in the dose, compared with the other two groups. This further illustrates the impact of optimizing the method of mRNA vaccine administration versus the anti-tumor response.

In summary, the method used to administer the mRNA-based vaccine is one of the key factors determining its efficacy and safety. All routes of administration have their advantages and disadvantages, which affect the distribution of the preparation in the body, the activation of immune cells and, as a result, the strength and duration of the immune response. Intravenous administration ensures systemic distribution, but it carries the risk of toxicity and high tropism for the liver. Intramuscular administration, due to its simplicity and safety, remains the most popular, providing flexibility in dosage and the possibility of repeated injections. Intradermal administration stimulates a potent Th1-type immune response but may cause local reactions. Subcutaneous administration, to the contrary, requires an increase in dosage due to slow absorption. Optimization of the method, dose, and frequency of administration, with consideration as to the type of mRNA-based vaccine and delivery system, is a prerequisite for achieving maximum anti-tumor efficacy and minimizing adverse reactions. Further studies in this area will enable the development of personalized vaccination strategies aimed at achieving a clinical response and minimizing adverse reactions.

CURRENT STATUS OF CLINICAL TRIALS OF mRNA-BASED CANCER VACCINES

Therapeutic mRNA vaccines targeting cancer are being developed globally, and most have transitioned successfully from preclinical validation into clinical evaluation *(Table 1)*. Regulatory authorization as an oncology treatment requires the successful completion of three sequential clinical trial phases, with Phase III – focused on efficacy in large patient cohorts – representing the lengthiest and most complex stage (*Fig. 4*).

Preclinical trials of mRNA-based vaccines include an assessment of safety and immunological properties *in vitro* and/or *ex vivo* and *in vivo* in animal models. The success of preclinical trials opens an opportunity to proceed to Phase I clinical trials, where the therapeutic dose is determined and the preliminary efficacy of the preparation in treating patients is evaluated. This phase is usually undertaken on healthy volunteers, but in the case of anti-tumor mRNA-based vaccines, studies commence directly with target patients, resulting in the combination of phases I and IIa (NCT06307431, NCT06305767), as well as the emergence of dose escalation and expansion stages [104, 105]. Phase II can be divided into a pilot phase IIa, which evaluates short-term safety, establishes a dosing regimen, determines the dose-response relationship, and defines efficacy assessment criteria, and a more extensive controlled Phase IIb, which is necessary to determine the efficacy, safety, and optimal dosage of the preparation, as well as to make a decision about whether to proceed to the next phase. In the second stage, a comparison group receiving standard therapy is required. The most time-consuming and costly Phase III is a randomized, controlled, double-blind, multicenter study with a mandatory control group, which allows researchers to evaluate the efficacy and safety in a large number of patients. Successful completion of this stage leads to the preparation dossier being submitted to the authorized body for registra-

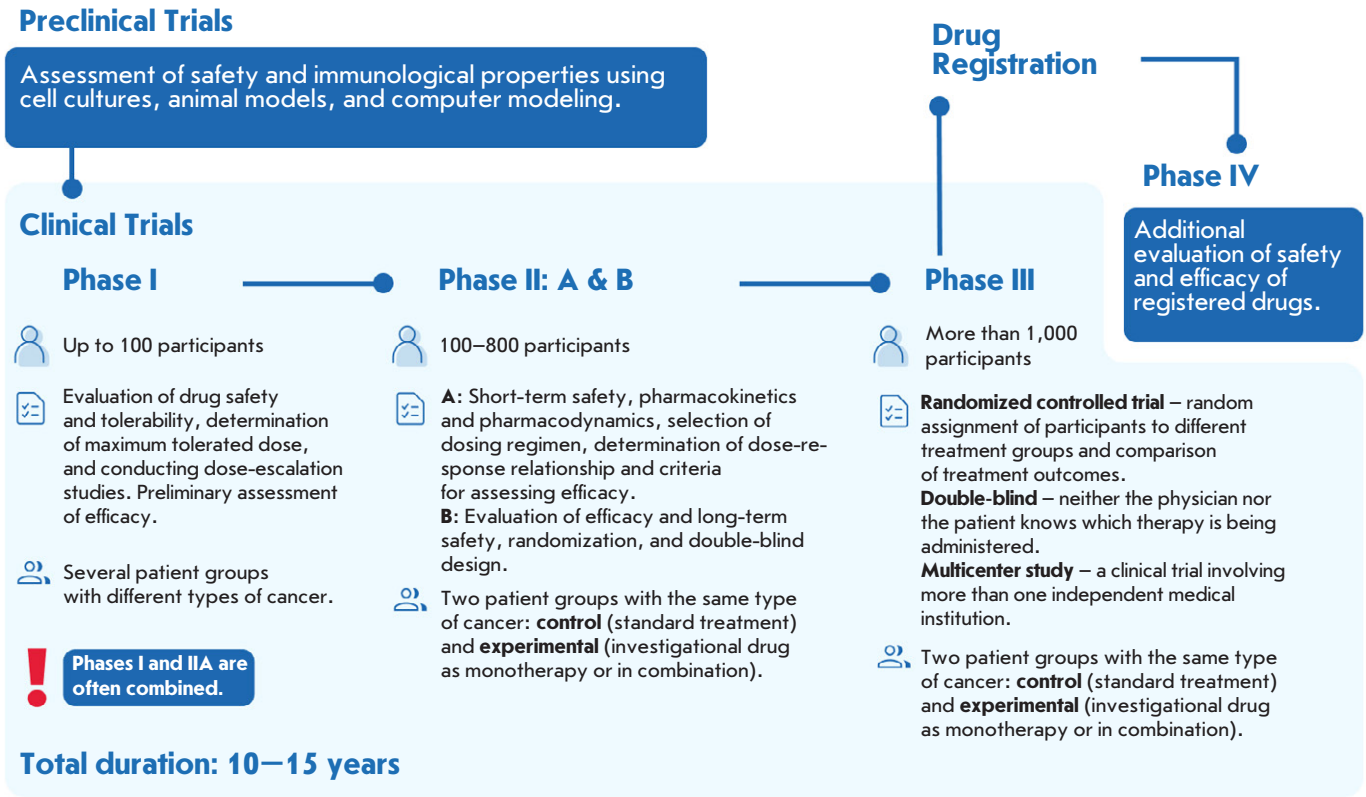

Fig. 4. Anti-tumor mRNA vaccine trials stages required for preparation registration

tion. In the case of personalized mRNA-based vaccines, it is not each specific preparation that is registered, but rather the technology used to produce it. Furthermore, in the Russian Federation, clinical trials of personalized anti-tumor mRNA-based vaccines related to BDMPs are permitted after their efficacy and safety have been proven and without the need for clinical studies[1].

Personalized mRNA-based vaccines are currently used in combination with immune checkpoint inhibitors (ICIs) in clinical trials, as they help activated T-lymphocytes recognize tumor cell neoantigens and implement a full anti-tumor immune response. A class of preparations known as ICIs, which is quite common in oncology practice, includes monoclonal antibodies against cytotoxic T-lymphocyte antigen-4 (CTLA-4), a programmed cell death receptor (PD-1) and its ligand (PD-L1) (*Table 2*). CTLA-4, PD-1, and PD-L1 are surface receptors on T-cells that are necessary for their negative regulation [106]. Tumor cells use these molecules to deplete T-cells and "escape" the immune response. ICIs are designed to block this mechanism and restore the immune response suppressed by the tumor [107, 108].

ICIs monotherapy serves as a comparison group in studies of mRNA-based vaccines combined with ICIs (NCT03897881, NCT05933577, NCT03289962, NCT03815058), or mRNA vaccine monotherapy (NCT03289962, NCT05192460, NCT05359354, NCT06541639). A comparison of mRNA vaccine monotherapy with groups receiving standard conventional therapy appropriate for the selected cancer type is also available (NCT06295809, NCT04486378, NCT06026800). Expectations of potential success are high in combining ICIs with mRNA-based vaccines in clinical trials conducted on patients in the terminal-stage of a disease for whom traditional treatments have proven ineffective (NCT03815058, NCT03289962, NCT05949775, NCT05192460, NCT05359354, NCT06541639).

[1] *Resolution of the Government of the Russian Federation No. 213 of February 24, 2025 "About biotechnological medicinal preparations intended for use in accordance with individual medical prescriptions and specially manufactured for a specific patient directly in the medical organization where such biotechnological medicinal preparations are used, containing compounds synthesized based on the results of genetic studies of material obtained from the patient for whom such biotechnological medicinal preparations are manufactured Available at: http://government.ru/docs/all/157884/ [Accessed: February 25, 2024].*

Table 1. Clinical trials of personalized anti-tumor mRNA vaccines from 2021 to 2025

Drug name	Country, Sponsors	NCT ID	Phase	Status, Study Years	Tumor Localization	Treatment	Study Results
mRNA-4157 (V940)	USA, Moderna, MSD	NCT03313778 (KEYNOTE-603)	I	Open, recruiting 2017–2025	Any malignant tumors with MSI-H or other dMMR	Three groups: mRNA-4157 monotherapy, combination mRNA-4157 + pembrolizumab, combination mRNA-4157 + pembrolizumab + chemotherapy.	Neoantigen-specific T-cell responses were detected in all patients (n = 33); no adverse events of grade ⩾3 were observed.
		NCT03897881 (KEYNOTE-942)	II	Open, recruiting 2019–2029	High-risk melanoma (stages IIIB–D or IV)	Two groups: combination mRNA-4157 + pembrolizumab, pembrolizumab monotherapy (control group).	With a median follow-up of 18 months, recurrence-free survival was 79% in the combination therapy group (n = 107) versus 62% in the monotherapy group (n = 50).
		NCT06307431 (INTerpath-004)	I–II	Open, recruiting 2024–2032	Renal cell carcinoma after surgical resection	Three groups: mRNA-4157 monotherapy, combination mRNA-4157 + pembrolizumab, pembrolizumab monotherapy (control group).	No results posted
		NCT06305767 (INTerpath-005)	I–II	Open, recruiting 2024–2031	Muscle-invasive urothelial carcinoma after surgical resection	Three groups: combination mRNA-4157 + pembrolizumab, pembrolizumab monotherapy (control group), combination mRNA-4157 + pembrolizumab + enfortumab vedotin + surgery.	No results posted
		NCT06295809 (INTerpath-007)	III	Open, recruiting 2024–2033	Resectable locally advanced operable cutaneous squamous cell carcinoma	Three groups: combination mRNA-4157 + pembrolizumab + surgery, surgery + radiotherapy, pembrolizumab monotherapy + surgery.	No results posted
		NCT05933577 (INTerpath-001)	III	Active, not recruiting 2023–2030	Melanoma stages II–IV	Two groups: combination mRNA-4157 + pembrolizumab, pembrolizumab monotherapy (control group).	No results posted
		NCT06077760 (INTerpath-002)	III	Open, recruiting 2023–2035	Resected non-small cell lung cancer, stages II, IIIA, IIIB (N2)		No results posted

Drug name	Country, Sponsors	NCT ID	Phase	Status, Study Years	Tumor Localization	Treatment	Study Results
Cevumeran (RO7198457)	USA, Memorial Sloan Kettering Cancer Center, Genentech	NCT04161755	I	Active, not recruiting 2019–2025	Pancreatic cancer after surgical resection	Sequential treatment: cevumeran, atezolizumab, followed by chemotherapy mFOLFIRINOX.	Treatment response was observed in 50% of patients (n = 8). Recurrence-free survival in 75% of responders (n = 6) exceeded 38 months. The median recurrence-free survival in non-responders (n = 8) was 13.4 months.
	USA, BioNTech Genentech	NCT03289962 (GO39733)	I	Active, not recruiting 2017–2025	Locally advanced or metastatic solid tumors	Two groups: pembrolizumab monotherapy, combination mRNA-4157 + atezolizumab.	Neoantigen-specific T-cell responses were recorded in 71% of patients; 90% of patients receiving monotherapy and 92% receiving combination therapy experienced no adverse events of grade ⩾3.
		NCT03815058 (IMCODE001)	II	Active, not recruiting 2019–2025	Metastatic or unresectable locally advanced melanoma stage IIIC/D	Two groups: combination Cevumeran + pembrolizumab, pembrolizumab monotherapy (control group).	No results posted
		NCT05968326 (IMCODE003)	II	Open, recruiting 2023–2029	Ductal pancreas adenocarcinoma after surgical resection	Two groups: combination Cevumeran + pembrolizumab + chemotherapy mFOLFIRINOX, chemotherapy mFOLFIRINOX.	No results posted
		NCT06534983 (IMCODE004)	II	Open, recruiting 2024–2034	High-risk muscle-invasive urothelial carcinoma after surgical resection	Two groups: combination Cevumeran + nivolumab, nivolumab monotherapy.	No results posted
		NCT04486378 (BNT122-01)	II	Open, recruiting 2021–2030	Rectal cancer stage II/III or colon cancer stage II/III	Two groups: Cevumeran monotherapy, no treatment (watchful waiting).	No results posted
STZD-1801	China, Stemirna Therapeutics	NCT03908671	I	Open, recruiting 2019–2025	Advanced esophageal cancer (stage IIIc, IV) and non-small cell lung cancer (stages IIIB–IV)	mRNA vaccine monotherapy.	No results posted
SW1115C3		NCT05198752 (SWP1001-06)	I	Unknown status 2022–2024	Advanced solid tumors		All patients (n = 2) showed a treatment response. Recurrence-free survival was 8.4 months for the first patient and over 12 months for the second.
2020-06-mRNA-COM		NCT05949775	Not Applicable	Active, not recruiting 2023–2026	Advanced solid tumors	Combination mRNA vaccine + sintilimab.	No results posted
2021-10-mRNA-COM		NCT05761717	Not Applicable	Active, not recruiting 2023–2025	Hepatocellular carcinoma with postoperative recurrence	Combination mRNA vaccine + sintilimab.	No results posted

Drug name	Country, Sponsors	NCT ID	Phase	Status, Study Years	Tumor Localization	Treatment	Study Results
PGV002	China, NeoCura	NCT05192460 (XKY-1005)	Early I	Open, recruiting 2022–2025	Advanced gastric, esophageal, or liver cancer	Two groups: mRNA vaccine monotherapy, combination mRNA vaccine + PD-1/L1 antibody.	No results posted
Personalized neoantigen tumor vaccine		NCT05359354 (XKY-1007)	Not Applicable		Advanced solid tumors		No results posted
iNeo-Vac-R01	China, Hangzhou Neoantigen Therapeutics Co., Ltd.	NCT06019702 (SRRSH2023-755-01)	I	Open, recruiting 2023–2027	Advanced malignancies of the gastrointestinal system	mRNA vaccine monotherapy	No results posted
		NCT06026800 (SRRSH2023-755-02)				First-line standard therapy, followed by mRNA vaccine monotherapy.	
		NCT06026774 (SRRSH2023-755-03)				Combination mRNA vaccine + standard adjuvant therapy.	No results posted
EVM16	China, Everest Medicines	NCT06541639 (EVM16CX01)	I	Open, recruiting 2023–2027	Any advanced or recurrent solid tumors	Two groups: mRNA vaccine monotherapy, combination mRNA vaccine + tislelizumab.	No results posted
SJ-Neo006	China, Jiangsu Synthgene Biotechnology	NCT06326736	Early I	Open, recruiting 2024-2026	Resectable ductal adenocarcinoma of the pancreas	Combination mRNA vaccine + camrelizumab + chemotherapy.	No results posted
mRNA tumor vaccines	China, Shanghai Regenelead Therapies	NCT06156267	Early I	Active, not recruiting 2024–2027	Adenocarcinoma of the pancreas after surgical resection	Combination mRNA vaccine + adebrelimab + mFOLFIRINOX chemotherapy.	No results posted
		NCT06735508 (NSCLC-IIT-RGL)	Early I	Active, not recruiting 2025–2026	Non-small cell lung cancer after surgical resection	Combination mRNA vaccine + adebrelimab.	No results posted
XP-004 Personalized mRNA Tumor Vaccine	China, Shanghai Xinpu BioTechnology Company Limited	NCT06496373 (2023PCV004)	I	Open, recruiting 2024–2027	Recurrent pancreatic cancer	Combination mRNA vaccine + PD-1 antibody.	No results posted

Table 2. Immune checkpoint inhibitors used in clinical practice

Molecule targeted by the preparation	International name of the preparation	Trade name of the preparation	Oncologic ailments
CTLA-4	Ipilimumab	Yervoy	Unresectable or metastatic melanoma, renal cell carcinoma, colorectal cancer, hepatocellular carcinoma, non-small cell lung cancer
	Tremelimumab	Imjudo	
	Nurulimab	Nurdati	
PD-1	Prolgolimab	Forteca	Melanoma, non-small cell lung cancer, pancreatic cancer, oesophageal cancer, gastric cancer, breast cancer, prostate cancer, head and neck tumors, ovarian cancer
	Pembrolizumab	Keytruda Pembroria	
	Nivolumab	Opdivo	
	Camrelizumab	Areima	
PD-L1	Atezolizumab	Tecentriq	Bladder cancer, non-small cell lung cancer, breast cancer, hepatocellular carcinoma, metastatic melanoma, Merkel cell carcinoma, urothelial and renal cell carcinoma
	Avelumab	Bavencio	
	Durvalumab	Imfinzi	

Clinical studies performed in the European Union and the United States

mRNA-4157 vaccine. In 2017, Moderna (USA) initiated a Phase I clinical trial of the personalized mRNA-4157 vaccine (NCT03313778) (*Fig. 2*). In the first stage, patients with resected (part A) and unresectable (part B) solid tumors received four doses of mRNA-4157 monotherapy intramuscularly or combination therapy with pembrolizumab based on dose escalation regimens ranging from 0.04 to 1 mg. During the dose escalation stage, the group was divided into three parts: participants with unresectable, locally advanced or metastatic solid tumors (parts B and C) and resected cutaneous melanoma (part D). The patients were advised to use 1 mg of mRNA-4157, in combination with pembrolizumab and/or chemotherapy. In 2019, the first results were published, confirming the safety of the preparation by the absence of short-term severe adverse reactions (⩾ grade 3) in all 33 patients, and its immunogenicity by the presence of multifunctional neoantigen-specific T-cells in response to target neoantigens in each patient. Among the 13 patients who received adjuvant monotherapy with mRNA-4157, 92.3% showed no evidence of disease at a median follow-up time length of 8 months. The remaining 20 patients received combination therapy consisting of a mRNA vaccine and pembrolizumab, and 14 of them responded to combination therapy: in half of the cases, partial remission or stabilization of the disease was observed, while in the other half, disease progression or immunosuppression was observed. Consequently, mRNA-4157 proved safe and well tolerated at all tested dose levels. These results confirmed the efficacy of the target neoantigen selection algorithm and highlighted the promising clinical application of the personalized neoantigen mRNA vaccine therapy strategy, which made possible for mRNA-4157 to advance to Phase II clinical trials [109].

At the Society for Immunotherapy of Cancer conference (San Diego, California, USA) held in November 2023, the results obtained with mRNA-4157 use were supplemented: In evaluating safety and tolerability, all patients experienced ⩾ 1 adverse event during treatment; no dose-limiting adverse events of grade 4 or 5 severity had been observed. The most common adverse events were fatigue (67%), fever (60%), and pain at the injection spot (40%). T-cell responses were observed in all patients, 85% of which were identified as *de novo* responses. The highest frequency of these responses was achieved after the beginning of combination therapy with pembrolizumab. It was also observed that a high percentage of immune responses to the combination of mRNA-4157 with pembrolizumab in patients was associated with an activated T-cell phenotype, while a low percentage was associated with the prevalence of a naive T-cell phenotype [89]. The mRNA-4157 study is ongoing and forms the basis for phases involving groups of patients with tumors in other locations.

In 2019, the KEYNOTE-942 (Phase II) study was initiated to evaluate the efficacy of the personalized mRNA-4157 vaccine in patients with stage IIIB-D and IV melanoma after complete surgical resection with a high risk of recurrence (NCT03897881). Patients received combination therapy with mRNA-4157 and

pembrolizumab (n = 107) or pembrolizumab monotherapy (n = 50). The mRNA-4157 vaccine (1 mg) was administered intramuscularly nine times at three-week intervals, and pembrolizumab (200 mg) was administered intravenously every three weeks for 18 cycles. With a minimum follow-up period of 14 months in the group of patients who completed the full course of treatment, adverse outcomes (relapse or death) were observed in 22% (24/107) of the patients in the combination therapy group and in 40% (20/50) of patients who received monotherapy. Recurrence-free survival was better in the combination therapy group than in the monotherapy group (83% versus 77% at 12 months and 79% versus 62% at 18 months). Cases of distant recurrence or death after 24 months were observed in 8% of patients after combination therapy and 24% of patients under monotherapy [110].

Encouraging results from Moderna and Merck & Co's (USA) mRNA-4157 vaccine have resulted in the initiation of the studies NCT06307431 and NCT06305767, which began in 2024. It is anticipated that mRNA-4157 therapy in combination with pembrolizumab will be more efficient than pembrolizumab monotherapy in renal cell carcinoma (NCT06307431) and standard treatment in muscle-invasive urothelial carcinoma (NCT06305767). These trials cover between 8 and 15 countries and will continue until 2031–2032. In addition, in early 2025, Moderna, in partnership with Merck & Co (USA), initiated Phase III clinical trials of the mRNA-4157 vaccine, in combination with pembrolizumab, for the treatment of squamous cell skin carcinoma (NCT06295809), melanoma (NCT05933577), and non-small cell lung cancer (NCT06077760). Each study involves between 20 and 33 countries and between 868 and 1,089 patients.

Cevumeran. In 2017, BioNTech (Germany) and Genentech (USA) initiated Phase I clinical trials of the mRNA preparation Cevumeran (NCT03289962) intended for the treatment of patients with melanoma, head and neck cancer, colorectal cancer, non-small cell lung cancer, bladder cancer, and other progressive solid tumors (*Fig. 2*). The safety, immunogenicity, and preliminary efficacy of monotherapy (n = 30) and in combination with atezolizumab (n = 183) were evaluated in patients who had received prior therapy. According to safety data, 9 out of 30 patients receiving Cevumeran monotherapy and 47 out of 183 patients receiving combination therapy with atezolizumab discontinued treatment as a result of ailment expansion. Side effects were noted in 90% of the patients receiving Cevumeran monotherapy: in 3 patients, they were classified as grade 3, and in the remaining 24 patients they were classified as grade 1 or 2. One case of dose-limiting toxicity grade 3 was observed during monotherapy with 100 μg of Cevumeran, but after the side effects had dissipated, the patient continued to participate in the study at a reduced dose until ailment progression on day 82. Three grade 4 or 5 adverse events were recorded during the combined use of Cevumeran and atezolizumab; subsequently, 11 patients discontinued treatment as a result of adverse immune-mediated reactions, predominantly in the atezolizumab monotherapy group. The remaining participants experienced minimal side effects, the most common of which were infusion reactions (56.7% and 59.6% for monotherapy and combination therapy, respectively), cytokine release syndrome (30% and 20.8%), and flu-like symptoms (3.3% and 12.6%). In the preliminary efficacy assessment, 71% of the patients demonstrated a polyepitope neoantigen-specific response involving $CD4^+$ and/or $CD8^+$ T-cells, which persisted for up to 23 months. At the same time, $CD8^+$ T-cells specific to several neoantigens constituted an average of 7.3% of the circulating pool of $CD8^+$ T-cells and were also detected in tumor foci, comprising up to 7.2% of the total number of tumor-infiltrating T-cells. No statistically significant results about a correlation between the clinical effect and immune response were obtained due to the limited volume and heterogeneity of the samples for each tumor type. A patient with microsatellite-stable rectal cancer (low PD-L1 expression) demonstrated a complete response to combination therapy with autologous Cevumeran (9 doses of 38 mcg) and atezolizumab for 8.2 months. A patient with highly differentiated breast cancer (high PD-L1 level) due to tumor progression against a background of experimental treatment with nivolumab was transferred to autologous Cevumeran at a dose of 38 mcg and atezolizumab, which led to a partial response with a reduction in the size of metastases in the lungs over a period of 9.9 months. These results justified further study of Cevumeran and became the basis for new phase I–II clinical trials [111].

In 2019, BioNTech (Germany) and Genentech (USA) jointly initiated Phase I clinical trials of Cevumeran against resected pancreatic adenocarcinoma (NCT04161755). The study included 16 patients who received atezolizumab and Cevumeran after surgery, 15 of whom then underwent chemotherapy with mFOLFIRINOX. The safety profile was assessed based on the number and severity of adverse reactions, and preliminary efficacy was assessed based on T-cell specificity to the vaccine neoantigens, recurrence-free survival, and overall survival at 18 months. In 15 of the 16 patients, autologous Cevumeran was tolerated without grade 3–5 adverse reactions; one

patient experienced fever and hypertension, which were assessed as a grade 3 adverse reaction. The appearance of neoantigen-specific T cells was noted in 8 out of the 16 patients, accounting for up to 10% of all blood T-cells The cells retained functionality and produced IFN-γ. Even after chemotherapy and were reactivated upon administration of a booster dose of the vaccine. They also included up to 2.5% of multifunctional neoantigen-specific effector $CD8^+$ T-cells that persisted for 2 years after the surgery. During 18 months of follow-up, the median overall and recurrence-free survival in eight patients with a T-cell response to the vaccine exceeded 18 months, while in eight non-responders, the median recurrence-free survival time was 13.4 months. Since T-cell activity in patients with resected pancreatic adenocarcinoma correlated with delayed recurrence, a global randomized phase II trial was initiated [30].

Although initial results were published in 2023, long-term follow-up of Phase I participants remained ongoing, leading to updated findings from the NCT04161755 trial in 2025. With a median follow-up period of 3.2 years (2.3–4.0 years), all eight patients who responded to therapy remained recurrence-free. Consequently, six out of eight respondents remained in remission, while seven out of eight who did not respond to therapy experienced a relapse. Additionally, the origin and lifespan of specific T-cell clones were studied. It has been revealed that Cevumeran induces $CD8^+$ T-cell clones with an average lifespan of 7 years. At the same time, vaccine-induced clones are not observed in tissues prior to vaccination, and 86% of them retain the cytotoxic, tissue-resident state of memory T-cells for 3 years after vaccination, while preserving neoantigen-specific effector function. This observation led to the conclusion that there is a consistent correlation between the response to the vaccine and progression-free survival for 3.6 years [32].

In 2023, a randomized phase II trial of the preparation Cevumeran (NCT05968326) was initiated. The treatment regimen for patients with pancreatic ductal adenocarcinoma following surgical resection included a combination of Cevumeran, atezolizumab, and mFOLFIRINOX chemotherapy versus single-agent chemotherapy. In addition, as part of Phase II trials, the preparation Cevumeran, in combination with ICIs, was being administered to patients with melanoma (NCT03815058) and muscle-invasive urothelial carcinoma (NCT06534983), and as monotherapy to patients with rectal or colon cancer (NCT04486378). The NCT03815058 study was completed in January 2025, but the results are not yet available. The completion of the other studies should not be expected before 2029.

Clinical studies performed in China

A total of 14 early Phase I and II trials listed on clinicaltrials.gov are underway in China as of January 2025, and five in the United States (*Table 1*). Chinese companies such as Stemirna Therapeutics, NeoCura, Everest Medicines, Hangzhou Neoantigen Therapeutics, Jiangsu Synthgene Biotechnology, Shanghai Regenelead Therapies, and Shanghai Xinpu BioTechnology are active in the development of mRNA-based vaccines.

In October 2024, the results of preclinical studies of the Chinese anti-tumor vaccine SW1115C3 [112] were published. The preparation proved to be efficient in mouse models of CT26, MC38, and B16F10 tumors by activating neoantigen-specific cytotoxic T-cells and inducing the secretion of cytotoxic cytokines. This encouraged the move to Phase I clinical trials on two patients. The first patient with advanced stomach cancer, multifocal metastases, and a low mutation burden, achieved a recurrence-free survival period of 8.4 months and partial remission after receiving a combination of SW1115C3 with vedolizumab and pembrolizumab. The second patient with type B luminal breast cancer after neoadjuvant therapy and mRNA vaccine treatment evinced a persistent T-cell response to 11 out of 20 neoantigens. One year after surgery, she shows no evidence of recurrence or metastasis, and monitoring continues.

Stemirna Therapeutics has initiated studies to evaluate the efficacy of STZD-1801 monotherapy in patients with esophageal cancer and non-small cell lung cancer (NCT03908671), as well as combination therapy with a mRNA-based vaccine and stintilumab for advanced solid tumors (NCT05949775) and hepatocellular carcinoma (NCT05761717) [80]. NeoCura has initiated a study of the efficacy of mRNA-based monotherapy and combination therapy with ICIs in patients with advanced solid tumors (NCT05359354), with a separate study focusing on patients with gastric, esophageal, or liver cancer (NCT05192460). The anti-tumor mRNA-based vaccine iNeo-Vac-R01 from Hangzhou Neoantigen Therapeutics (China) targets common neoplasms of the digestive system and is being studied in three parallel trials to select the most effective treatment strategy (NCT06019702, NCT06026800, NCT06026774). The EVM16 mRNA-based vaccine from Everest Medicines is in Phase I clinical trials, including patients with recurrent or advanced solid tumors receiving monotherapy with the vaccine or combination therapy with tislelizumab (NCT06541639). The efficacy of various combinations of anti-tumor mRNA-based vaccines with chemotherapy and ICIs is being evaluated in studies initiated by Jiangsu Synthgene Biotechnology,

Shanghai Regenelead Therapies, and Shanghai Xinpu BioTechnology Company Limited. The study groups include patients with pancreatic cancer (NCT06326736, NCT06156267, NCT06496373) and non-small cell lung cancer (NCT06735508). The results of all these studies, however, have not yet been published.

Studies performed in the Russian Federation

In September 2024, the National Research Center for Epidemiology and Microbiology named after Honorary Academician N.F. Gamaleya of the Ministry of Health of the Russian Federation announced the completion of preclinical trials of a domestic mRNA-based vaccine against melanoma, developed jointly with the National Medical Research Radiological Centre of the Ministry of Health of the Russian Federation[1] (*Fig. 2*). According to the official website of the N.N. Blokhin National Medical Research Centre of Oncology, patient enrollment for Phase I clinical trials is not expected until the second half of 2025[2].

A scientific and technological center for the development of mRNA technologies has been established in accordance with Decree No. 195-r of the Government of the Russian Federation dated February 3, 2025. The functions of this leading scientific organization are entrusted to the Federal State Budgetary Institution "National Research Center for Epidemiology and Microbiology named after Honorary Academician N.F. Gamaleya" of the Ministry of Health of the Russian Federation[3].

CONCLUSION

mRNA-based vaccines designed to encode defined tumor antigens have shown robust clinical activity, either alone or in synergy with immune checkpoint inhibitors (ICIs), in multiple oncological indications. The platform's versatility, embodied in broad target selection (notably neoantigens), tunable mRNA constructs, and interchangeable delivery systems, points to its capacity for rapid development and implementation in real-world oncology settings. ●

This study was conducted as part of the state assignment of the Ministry of Science and Higher Education of the Russian Federation No. 075-00490-25-04 (project registration number 125042105351-3).

[1] *ria.ru [Internet]. Russian cancer vaccine has passed preclinical trials. 2014–2025. Available from: https://ria.ru/20240906/vaktsina-1971091162.html [Accessed: September 6, 2024].*

[2] *www.ronc.ru [Internet]. N.N. Blokhin National Medical Research Center of Oncology: key facts about the anti-tumour mRNA-based vaccine. 2024–2025. Available from: https://www.ronc.ru/about/press-tsentr/glavnoe-oprotivoopukholevoy-mrnk-vaktsine/ [Accessed: February 5, 2025].*

[3] *Decree of the Government of the Russian Federation No. 195-r dated February 3, 2025 "About the founding of a centre for the development of mRNA technologies." Available from: http://government.ru/docs/54127/ [Accessed: February 5, 2025].*

REFERENCES

1. Kaprin AD, Starinsky VV, Shakhzadova AO. The state of oncological care for the population of Russia in 2022. P. Herzen Moscow Oncology Research Institute – the branch of the FSBI «National Medical Research Radiology Center» of the Ministry of Health of the Russian Federation; 2023.
2. Shah A, Apple J, Belli AJ, et al. Real-world study of disease-free survival & patient characteristics associated with disease-free survival in early-stage non-small cell lung cancer: a retrospective observational study. *Cancer Treat Res Commun.* 2023;36:100742. doi: 10.1016/j.ctarc.2023.100742
3. Garg P, Pareek S, Kulkarni P, Horne D, Salgia R, Singhal SS. Next-Generation Immunotherapy: Advancing Clinical Applications in Cancer Treatment. *J Clin Med.* 2024;13(21):6537. doi: 10.3390/jcm13216537
4. Parvez A, Choudhary F, Mudgal P, et al. PD-1 and PD-L1: architects of immune symphony and immunotherapy breakthroughs in cancer treatment. *Front Immunol.* 2023;14:1296341. doi: 10.3389/fimmu.2023.1296341
5. Yuan Y, Gao F, Chang Y, Zhao Q, He X. Advances of mRNA vaccine in tumor: a maze of opportunities and challenges. *Biomark Res.* 2023;11(1):6. doi: 10.1186/s40364-023-00449-w
6. Fang E, Liu X, Li M, et al. Advances in COVID-19 mRNA vaccine development. *Signal Transduct Target Ther.* 2022;7(1):94. doi: 10.1038/s41392-022-00950-y
7. Mu X, Hur S. Immunogenicity of in vitro-transcribed RNA. *Acc Chem Res.* 2021;54(21):4012–4023. doi: 10.1021/acs.accounts.1c00521
8. Gao M, Zhang Q, Feng XH, Liu J. Synthetic modified messenger RNA for therapeutic applications. *Acta Biomater.* 2021;131:1–15. doi: 10.1016/j.actbio.2021.06.020
9. Melton DA, Krieg PA, Rebagliati MR, Maniatis T, Zinn K, Green MR. Efficient in vitro synthesis of biologically active RNA and RNA hybridization probes from plasmids containing a bacteriophage SP6 promoter. *Nucleic Acids Res.* 1984;12(18):7035–7056. doi: 10.1093/nar/12.18.7035
10. Gómez-Aguado I, Rodríguez-Castejón J, Vicente-Pascual M, Rodríguez-Gascón A, Solinís MÁ, Del Pozo-Rodríguez A. Nanomedicines to deliver mRNA: State of the Art and Future Perspectives. *Nanomaterials (Basel).* 2020;10(2):364 doi: 10.3390/nano10020364
11. Malone RW, Felgner PL, Verma IM. Cationic liposome-mediated RNA transfection. *Proc Natl Acad Sci USA.* 1989;86(16):6077–6081. doi: 10.1073/pnas.86.16.6077
12. Wolff JA, Malone RW, Williams P, et al. Direct gene

transfer into mouse muscle in vivo. *Science*. 1990;247(4949 Pt 1):1465–1468. doi: 10.1126/science.1690918
13. Jirikowski GF, Sanna PP, Maciejewski-Lenoir D, Bloom FE. Reversal of diabetes insipidus in Brattleboro rats: intrahypothalamic injection of vasopressin mRNA. *Science*. 1992;255(5047):996–998. doi: 10.1126/science.1546298
14. Martinon F, Krishnan S, Lenzen G, et al. Induction of virus-specific cytotoxic T lymphocytes in vivo by liposome-entrapped mRNA. *Eur J Immunol*. 1993;23(7):1719–1722. doi: 10.1002/eji.1830230749
15. Conry RM, LoBuglio AF, Wright M, et al. Characterization of a messenger RNA polynucleotide vaccine vector. *Cancer Res*. 1995;55(7):1397–1400.
16. Zhou WZ, Hoon DS, Huang SK, et al. RNA melanoma vaccine: induction of antitumor immunity by human glycoprotein 100 mRNA immunization. *Hum Gene Ther*. 1999;10(16):2719–2724. doi: 10.1089/10430349950016762
17. Heiser A, Coleman D, Dannull J, et al. Autologous dendritic cells transfected with prostate-specific antigen RNA stimulate CTL responses against metastatic prostate tumors. *J Clin Invest*. 2002;109(3):409–417. doi: 10.1172/jci14364
18. Hoerr I, Obst R, Rammensee HG, Jung G. In vivo application of RNA leads to induction of specific cytotoxic T lymphocytes and antibodies. *Eur J Immunol*. 2000;30(1):1–7. doi: 10.1002/1521-4141(200001)30:1<1::AID-IMMU1>3.0.CO;2-#
19. Probst J, Weide B, Scheel B, et al. Spontaneous cellular uptake of exogenous messenger RNA in vivo is nucleic acid-specific, saturable and ion dependent. *Gene Ther*. 2007;14(15):1175–1180. doi: 10.1038/sj.gt.3302964
20. Karikó K, Kuo A, Barnathan E. Overexpression of urokinase receptor in mammalian cells following administration of the in vitro transcribed encoding mRNA. *Gene Ther*. 1999;6(6):1092–1100. doi: 10.1038/sj.gt.3300930
21. Karikó K, Ni H, Capodici J, Lamphier M, Weissman D. mRNA is an endogenous ligand for Toll-like receptor 3. *J Biol Chem*. 2004;279(13):12542–12550. doi: 10.1074/jbc.M310175200
22. Karikó K, Buckstein M, Ni H, Weissman D. Suppression of RNA recognition by Toll-like receptors: the impact of nucleoside modification and the evolutionary origin of RNA. *Immunity*. 2005;23(2):165–175. doi: 10.1016/j.immuni.2005.06.008
23. Krammer F, Palese P. Profile of Katalin Karikó and Drew Weissman: 2023 Nobel laureates in Physiology or Medicine. *Proc Natl Acad Sci USA*. 2024;121(9):e2400423121. doi: 10.1073/pnas.2400423121
24. Szabó GT, Mahiny AJ, Vlatkovic I. COVID-19 mRNA vaccines: Platforms and current developments. *Mol Ther*. 2022;30(5):1850–1868. doi: 10.1016/j.ymthe.2022.02.016
25. Sahin U, Derhovanessian E, Miller M, et al. Personalized RNA mutanome vaccines mobilize poly-specific therapeutic immunity against cancer. *Nature*. 2017;547(7662):222–226. doi: 10.1038/nature23003
26. Sahin U, Türeci Ö. Personalized vaccines for cancer immunotherapy. *Science*. 2018;359(6382):1355–1360. doi: 10.1126/science.aar7112
27. Schumacher TN, Schreiber RD. Neoantigens in cancer immunotherapy. *Science*. 2015;348(6230):69–74. doi: 10.1126/science.aaa4971
28. Zhao W, Wu J, Chen S, Zhou Z. Shared neoantigens: ideal targets for off-the-shelf cancer immunotherapy. *Pharmacogenomics*. 2020;21(9):637–645. doi: 10.2217/pgs-2019-0184
29. Klebanoff CA, Wolchok JD. Shared cancer neoantigens: Making private matters public. *J Exp Med*. 2018;215(1):5–7. doi: 10.1084/jem.20172188
30. Rojas LA, Sethna Z, Soares KC, et al. Personalized RNA neoantigen vaccines stimulate T cells in pancreatic cancer. *Nature*. 2023;618(7963):144–150. doi: 10.1038/s41586-023-06063-y
31. Weber JS, Luke JJ, Carlino MS, et al. INTerpath-001: Pembrolizumab with V940 (mRNA-4157) versus pembrolizumab with placebo for adjuvant treatment of high-risk stage II-IV melanoma. *J Clin Oncol*. 2024;42(16S):TPS9616. doi: 10.1200/JCO.2024.42.16_suppl.TPS9616
32. Sethna Z, Guasp P, Reiche C, et al. RNA neoantigen vaccines prime long-lived CD8+ T cells in pancreatic cancer. *Nature*. 2025;639(8056):1042–1051. doi: 10.1038/s41586-024-08508-4
33. Chan TA, Yarchoan M, Jaffee E, et al. Development of tumor mutation burden as an immunotherapy biomarker: utility for the oncology clinic. *Ann Oncol*. 2019;30(1):44–56. doi: 10.1093/annonc/mdy495
34. Richters MM, Xia H, Campbell KM, Gillanders WE, Griffith OL, Griffith M. Best practices for bioinformatic characterization of neoantigens for clinical utility. *Genome Med*. 2019;11(1):56. doi: 10.1186/s13073-019-0666-2
35. Nguyen BQT, Tran TPD, Nguyen HT, et al. Improvement in neoantigen prediction via integration of RNA sequencing data for variant calling. *Front Immunol*. 2023;14:1251603. doi: 10.3389/fimmu.2023.1251603
36. Bolger AM, Lohse M, Usadel B. Trimmomatic: a flexible trimmer for Illumina sequence data. *Bioinformatics*. 2014;30(15):2114–2120. doi: 10.1093/bioinformatics/btu170
37. Martin M. Cutadapt removes adapter sequences from high-throughput sequencing reads. *EMBnet J*. 2011;17(1):10–12. doi: 10.14806/ej.17.1.200
38. Langmead B, Salzberg SL. Fast gapped-read alignment with Bowtie 2. *Nat Methods*. 2012;9(4):357–359. doi: 10.1038/nmeth.1923
39. Benjamin D, Sato T, Cibulskis K, et al. Calling Somatic SNVs and Indels with Mutect2. *bioRxiv*. 2019. doi: 10.1101/861054
40. Saunders CT, Wong WSW, Swamy S, Becq J, Murray LJ, Cheetham RK. Strelka: accurate somatic small-variant calling from sequenced tumor-normal sample pairs. *Bioinformatics*. 2012;28(14):1811–1817. doi: 10.1093/bioinformatics/bts271
41. Koboldt DC, Zhang Q, Larson DE, et al. VarScan 2: somatic mutation and copy number alteration discovery in cancer by exome sequencing. *Genome Res*. 2012;22(3):568–576. doi: 10.1101/gr.129684.111
42. Wood DE, White JR, Georgiadis A, et al. A machine learning approach for somatic mutation discovery. *Sci Transl Med*. 2018;10(457):eaar7939. doi: 10.1126/scitranslmed.aar7939
43. Dobin A, Davis CA, Schlesinger F, et al. STAR: ultrafast universal RNA-seq aligner. *Bioinformatics*. 2013;29(1):15–21. doi: 10.1093/bioinformatics/bts635
44. Li B, Dewey CN. RSEM: accurate transcript quantification from RNA-Seq data with or without a reference genome. *BMC Bioinformatics*. 2011;12:323. doi: 10.1186/1471-2105-12-323
45. Patro R, Duggal G, Love MI, Irizarry RA, Kingsford C. Salmon provides fast and bias-aware quantification of transcript expression. *Nat Methods*. 2017;14(4):417–419. doi: 10.1038/nmeth.4197
46. Bray NL, Pimentel H, Melsted P, Pachter L. Near-opti-

mal probabilistic RNA-seq quantification. *Nat Biotechnol.* 2016;34(5):525–527. doi: 10.1038/nbt.3519
47. Szolek A, Schubert B, Mohr C, Sturm M, Feldhahn M, Kohlbacher O. OptiType: precision HLA typing from next-generation sequencing data. *Bioinformatics.* 2014;30(23):3310–3316. doi: 10.1093/bioinformatics/btu548
48. Andreatta M, Nielsen M. Gapped sequence alignment using artificial neural networks: application to the MHC class I system. *Bioinformatics.* 2016;32(4):511–517. doi: 10.1093/bioinformatics/btv639
49. O'Donnell TJ, Rubinsteyn A, Bonsack M, Riemer AB, Laserson U, Hammerbacher J. MHCflurry: Open-Source Class I MHC Binding Affinity Prediction. *Cell Syst.* 2018;7(1):129–132.e4. doi: 10.1016/j.cels.2018.05.014
50. Fleri W, Paul S, Dhanda SK, et al. The Immune Epitope Database and Analysis Resource in Epitope Discovery and Synthetic Vaccine Design. *Front Immunol.* 2017;8:278. doi: 10.3389/fimmu.2017.00278
51. Abelin JG, Keskin DB, Sarkizova S, et al. Mass Spectrometry Profiling of HLA-Associated Peptidomes in Mono-allelic Cells Enables More Accurate Epitope Prediction. *Immunity.* 2017;46(2):315–326. doi: 10.1016/j.immuni.2017.02.007
52. Yu W, Yu H, Zhao J, et al. NeoDesign: a computational tool for optimal selection of polyvalent neoantigen combinations. *Bioinformatics.* 2024;40(10):btae585. doi: 10.1093/bioinformatics/btae585
53. Lu RM, Hsu HE, Perez SJLP, et al. Current landscape of mRNA technologies and delivery systems for new modality therapeutics. *J Biomed Sci.* 2024;31(1):89. doi: 10.1186/s12929-024-01080-z
54. Lorenz R, Bernhart SH, Höner Zu Siederdissen C, et al. ViennaRNA Package 2.0. *Algorithms Mol Biol.* 2011;6:26. doi: 10.1186/1748-7188-6-26
55. Zadeh JN, Steenberg CD, Bois JS, et al. NUPACK: Analysis and design of nucleic acid systems. *J Comput Chem.* 2011;32(1):170–173. doi: 10.1002/jcc.21596
56. Zuker M. Mfold web server for nucleic acid folding and hybridization prediction. *Nucleic Acids Res.* 2003;31(13):3406–3415. doi: 10.1093/nar/gkg595
57. Ni L. Advances in mRNA-Based Cancer Vaccines. *Vaccines (Basel).* 2023;11(10):1599. doi: 10.3390/vaccines11101599
58. Fu Q, Zhao X, Hu J, et al. mRNA vaccines in the context of cancer treatment: from concept to application. *J Transl Med.* 2025;23(1):12. doi: 10.1186/s12967-024-06033-6
59. Kraft JC, Freeling JP, Wang Z, Ho RJY. Emerging research and clinical development trends of liposome and lipid nanoparticle drug delivery systems. *J Pharm Sci.* 2014;103(1):29–52. doi: 10.1002/jps.23773
60. Tenchov R, Bird R, Curtze AE, Zhou Q. Lipid Nanoparticles – From Liposomes to mRNA Vaccine Delivery, a Landscape of Research Diversity and Advancement. *ACS Nano.* 2021;15(11):16982–17015. doi: 10.1021/acsnano.1c04996
61. Bartlett S, Skwarczynski M, Toth I. Lipids as activators of innate immunity in peptide vaccine delivery. *Curr Med Chem.* 2020;27(17):2887–2901. doi: 10.2174/0929867325666181026100849
62. Brewer JM, Pollock KGJ, Tetley L, Russell DG. Vesicle size influences the trafficking, processing, and presentation of antigens in lipid vesicles. *J Immunol.* 2004;173(10):6143–6150. doi: 10.4049/jimmunol.173.10.6143
63. Ghaffar KA, Giddam AK, Zaman M, Skwarczynski M, Toth I. Liposomes as nanovaccine delivery systems. *Curr Top Med Chem.* 2014;14(9):1194–1208. doi: 10.2174/1568026614666140329232757
64. Henriksen-Lacey M, Christensen D, Bramwell VW, et al. Liposomal cationic charge and antigen adsorption are important properties for the efficient deposition of antigen at the injection site and ability of the vaccine to induce a CMI response. *J Control Release.* 2010;145(2):102–108. doi: 10.1016/j.jconrel.2010.03.027
65. Miller CR, Bondurant B, McLean SD, McGovern KA, O'Brien DF. Liposome-cell interactions in vitro: effect of liposome surface charge on the binding and endocytosis of conventional and sterically stabilized liposomes. *Biochemistry.* 1998;37(37):12875–12883. doi: 10.1021/bi980096y
66. Swetha K, Kotla NG, Tunki L, et al. Recent advances in the lipid nanoparticle-mediated delivery of mRNA vaccines. *Vaccines (Basel).* 2023;11(3):658. doi: 10.3390/vaccines11030658
67. Christensen D, Henriksen-Lacey M, Kamath AT, et al. A cationic vaccine adjuvant based on a saturated quaternary ammonium lipid have different in vivo distribution kinetics and display a distinct CD4 T cell-inducing capacity compared to its unsaturated analog. *J Control Release.* 2012;160(3):468–476. doi: 10.1016/j.jconrel.2012.03.016
68. Tanaka Y, Taneichi M, Kasai M, Kakiuchi T, Uchida T. Liposome-coupled antigens are internalized by antigen-presenting cells via pinocytosis and cross-presented to CD8 T cells. *PLoS One.* 2010;5(12):e15225. doi: 10.1371/journal.pone.0015225
69. Szebeni J, Baranyi L, Savay S, et al. The interaction of liposomes with the complement system: in vitro and in vivo assays. *Methods Enzymol.* 2003;373:136–154. doi: 10.1016/S0076-6879(03)73010-9
70. Hemmi H, Takeuchi O, Kawai T, et al. A Toll-like receptor recognizes bacterial DNA. *Nature.* 2000;408(6813):740–745. doi: 10.1038/35047123
71. Henriksen-Lacey M, Devitt A, Perrie Y. The vesicle size of DDA:TDB liposomal adjuvants plays a role in the cell-mediated immune response but has no significant effect on antibody production. *J Control Release.* 2011;154(2):131–137. doi: 10.1016/j.jconrel.2011.05.019
72. Lee Y, Lee YS, Cho SY, Kwon HJ. Perspective of peptide vaccine composed of epitope peptide, CpG-DNA, and liposome complex without carriers. *Adv Protein Chem Struct Biol.* 2015;99:75–97. doi: 10.1016/bs.apcsb.2015.03.004
73. Vabulas RM, Pircher H, Lipford GB, Häcker H, Wagner H. CpG-DNA activates in vivo T cell epitope presenting dendritic cells to trigger protective antiviral cytotoxic T cell responses. *J Immunol.* 2000;164(5):2372–2378. doi: 10.4049/jimmunol.164.5.2372
74. Schulz O, Diebold SS, Chen M, et al. Toll-like receptor 3 promotes cross-priming to virus-infected cells. *Nature.* 2005;433(7028):887–892. doi: 10.1038/nature03326
75. Zaks K, Jordan M, Guth A, et al. Efficient immunization and cross-priming by vaccine adjuvants containing TLR3 or TLR9 agonists complexed to cationic liposomes. *J Immunol.* 2006;176(12):7335–7345. doi: 10.4049/jimmunol.176.12.7335
76. Jin B, Sun T, Yu XH, et al. Immunomodulatory effects of dsRNA and its potential as vaccine adjuvant. *J Biomed Biotechnol.* 2010;2010:690438. doi: 10.1155/2010/690438
77. Liu Y, Janeway CA Jr. Microbial induction of co-stimulatory activity for CD4 T-cell growth. *Int Immunol.* 1991;3(4):323–332. doi: 10.1093/intimm/3.4.323
78. Werninghaus K, Babiak A, Gross O, et al. Adjuvanticity of a synthetic cord factor analogue for subunit Mycobacterium tuberculosis vaccination requires FcRγ-Syk-Card9-dependent innate immune activation. *J Exp Med.*

2009;206(1):89–97. doi: 10.1084/jem.20081445
79. Hou X, Zaks T, Langer R, Dong Y. Lipid nanoparticles for mRNA delivery. *Nat Rev Mater.* 2021;6(12):1078–1094. doi: 10.1038/s41578-021-00358-0
80. Fan T, Xu C, Wu J, et al. Lipopolyplex-formulated mRNA cancer vaccine elicits strong neoantigen-specific T cell responses and antitumor activity. *Sci Adv.* 2024;10(41):eadn9961. doi: 10.1126/sciadv.adn9961
81. Kisakov DN, Karpenko LI, Kisakova LA, et al. Jet injection of naked mRNA encoding the RBD of the SARS-CoV-2 spike protein induces a high level of a specific immune response in mice. *Vaccines (Basel).* 2025;13(1):65. doi: 10.3390/vaccines13010065
82. Ramos da Silva J, Bitencourt Rodrigues K, Formoso Pelegrin G, et al. Single immunizations of self-amplifying or non-replicating mRNA-LNP vaccines control HPV-associated tumors in mice. *Sci Transl Med.* 2023;15(686):eabn3464. doi: 10.1126/scitranslmed.abn3464
83. Cao Y, Gao GF. mRNA vaccines: a matter of delivery. *EClinicalMedicine.* 2021;32:100746. doi: 10.1016/j.eclinm.2021.100746
84. Pambudi NA, Sarifudin A, Gandidi IM, Romadhon R. Vaccine cold chain management and cold storage technology to address the challenges of vaccination programs. *Energy Rep.* 2022;8:955–972. doi: 10.1016/j.egyr.2021.12.039
85. Schmidt M, Vogler I, Derhovanessian E, et al. 88MO T-cell responses induced by an individualized neoantigen specific immune therapy in post (neo)adjuvant patients with triple negative breast cancer. *Ann Oncol.* 2020;31(S4):S276. doi: 10.1016/j.annonc.2020.08.209
86. Chen J, Ye Z, Huang C, et al. Lipid nanoparticle-mediated lymph node-targeting delivery of mRNA cancer vaccine elicits robust CD8+ T cell response. *Proc Natl Acad Sci USA.* 2022;119(34):e2207841119. doi: 10.1073/pnas.2207841119
87. Ols S, Yang L, Thompson EA, et al. Route of vaccine administration alters antigen trafficking but not innate or adaptive immunity. *Cell Rep.* 2020;30(12):3964–3971.e7. doi: 10.1016/j.celrep.2020.02.111
88. Weber JS, Carlino MS, Khattak A, et al. Individualised neoantigen therapy mRNA-4157 (V940) plus pembrolizumab versus pembrolizumab monotherapy in resected melanoma (KEYNOTE-942): a randomised, phase 2b study. *Lancet.* 2024;403(10427):632–644. doi: 10.1016/S0140-6736(23)02268-7
89. Gainor JF, Patel MR, Weber JS, et al. T-cell responses to individualized neoantigen therapy mRNA-4157 (V940) alone or in combination with pembrolizumab in the phase 1 KEYNOTE-603 study. *Cancer Discov.* 2024;14(11):2209–2223. doi: 10.1158/2159-8290.CD-24-0158
90. Cafri G, Gartner JJ, Zaks T, et al. mRNA vaccine-induced neoantigen-specific T cell immunity in patients with gastrointestinal cancer. *J Clin Invest.* 2020;130(11):5976–5988. doi: 10.1172/JCI134915
91. Islam MA, Rice J, Reesor E, et al. Adjuvant-pulsed mRNA vaccine nanoparticle for immunoprophylactic and therapeutic tumor suppression in mice. *Biomaterials.* 2021;266:120431. doi: 10.1016/j.biomaterials.2020.120431
92. Wang QT, Nie Y, Sun SN, et al. Tumor-associated antigen-based personalized dendritic cell vaccine in solid tumor patients. *Cancer Immunol Immunother.* 2020;69(7):1375–1387. doi: 10.1007/s00262-020-02496-w
93. Thomas KS. Intramuscular injections for COVID-19 vaccinations. *J Nucl Med Technol.* 2021;49(1):11–12. doi: 10.2967/jnmt.121.262049
94. Persano S, Guevara ML, Li Z, et al. Lipopolyplex potentiates anti-tumor immunity of mRNA-based vaccination. *Biomaterials.* 2017;125:81–89. doi: 10.1016/j.biomaterials.2017.02.019
95. Rini BI, Stenzl A, Zdrojowy R, et al. IMA901, a multipeptide cancer vaccine, plus sunitinib versus sunitinib alone, as first-line therapy for advanced or metastatic renal cell carcinoma (IMPRINT): a multicentre, open-label, randomised, controlled, phase 3 trial. *Lancet Oncol.* 2016;17(11):1599–1611. doi: 10.1016/S1470-2045(16)30408-9
96. Wang B, Pei J, Xu S, Liu J, Yu J. Recent advances in mRNA cancer vaccines: meeting challenges and embracing opportunities. *Front Immunol.* 2023;14:1246682. doi: 10.3389/fimmu.2023.1246682
97. Gradel AKJ, Porsgaard T, Lykkesfeldt J, et al. Factors affecting the absorption of subcutaneously administered insulin: effect on variability. *J Diabetes Res.* 2018;2018(1):1205121. doi: 10.1155/2018/1205121
98. Oberli MA, Reichmuth AM, Dorkin JR, et al. Lipid nanoparticle assisted mRNA delivery for potent cancer immunotherapy. *Nano Lett.* 2017;17(3):1326–1335. doi: 10.1021/acs.nanolett.6b03329
99. Ott PA, Hu Z, Keskin DB, et al. An immunogenic personal neoantigen vaccine for patients with melanoma. *Nature.* 2017;547(7662):217–221. doi: 10.1038/nature22991
100. Lorentzen CL, Haanen JB, Met Ö, Svane IM. Clinical advances and ongoing trials on mRNA vaccines for cancer treatment. *Lancet Oncol.* 2022;23(10):e450–e458. doi: 10.1016/S1470-2045(22)00372-2
101. Haabeth OAW, Blake TR, McKinlay CJ, et al. Local delivery of Ox40l, Cd80, and Cd86 mRNA kindles global anticancer immunity. *Cancer Res.* 2019;79(7):1624–1634. doi: 10.1158/0008-5472.CAN-18-2867
102. Diken M, Kreiter S, Selmi A, et al. Selective uptake of naked vaccine RNA by dendritic cells is driven by macropinocytosis and abrogated upon DC maturation. *Gene Ther.* 2011;18(7):702–708. doi: 10.1038/gt.2011.17
103. Pardi N, Hogan MJ, Porter FW, Weissman D. mRNA vaccines – a new era in vaccinology. *Nat Rev Drug Discov.* 2018;17(4):261–279. doi: 10.1038/nrd.2017.243
104. Choueiri TK, Powles T, Braun D, et al. 45 INTerpath-004: a phase 2, randomized, double-blind study of pembrolizumab with V940 (mRNA-4157) or placebo in the adjuvant treatment of renal cell carcinoma. *Oncologist.* 2024;29(S1):S15. doi: 10.1093/oncolo/oyae181.022
105. Sonpavde GP, Valderrama BP, Chamie K, et al. Phase 1/2 INTerpath-005 study: V940 (mRNA-4157) plus pembrolizumab with or without enfortumab vedotin (EV) for resected high-risk muscle-invasive urothelial carcinoma (MIUC). *J Clin Oncol.* 2025;43(5S):TPS893. doi: 10.1200/JCO.2025.43.5_suppl.TPS893
106. Sadeghi Rad H, Monkman J, Warkiani ME, et al. Understanding the tumor microenvironment for effective immunotherapy. *Med Res Rev.* 2021;41(3):1474–1498. doi: 10.1002/med.21765
107. Seidel JA, Otsuka A, Kabashima K. Anti-PD-1 and anti-CTLA-4 therapies in cancer: mechanisms of action, efficacy, and limitations. *Front Oncol.* 2018;8:86. doi: 10.3389/fonc.2018.00086
108. Shiravand Y, Khodadadi F, Kashani SMA, et al. Immune checkpoint inhibitors in cancer therapy. *Curr Oncol.* 2022;29(5):3044–3060. doi: 10.3390/curroncol29050247
109. Burris HA, Patel MR, Cho DC, et al. A phase I multicenter study to assess the safety, tolerability, and immu-

nogenicity of mRNA-4157 alone in patients with resected solid tumors and in combination with pembrolizumab in patients with unresectable solid tumors. *J Clin Oncol.* 2019;37(15S):2523. doi: 10.1200/JCO.2019.37.15_suppl.2523
110. Khattak A, Weber JS, Meniawy TM, et al. Distant metastasis-free survival results from the randomized, phase 2 mRNA-4157-P201/KEYNOTE-942 trial. *J Clin Oncol.* 2023;41(17S):LBA9503. doi: 10.1200/JCO.2023.41.17_suppl.LBA9503
111. Lopez J, Powles T, Braiteh F, et al. Autogene cevumeran with or without atezolizumab in advanced solid tumors: a phase 1 trial. *Nat Med.* 2025;31(1):152–164. doi: 10.1038/s41591-024-03334-7
112. Chen JK, Eisenberg E, Krutchkoff DJ, Katz RV. Changing trends in oral cancer in the United States, 1935 to 1985: a Connecticut study. *J Oral Maxillofac Surg.* 1991;49(11):1152–1158. doi: 10.1016/0278-2391(91)90406-C

Gut Microbiota and Short-Chain Fatty Acids in the Pathogenesis of Necrotizing Enterocolitis in Very Preterm Infants

E. N. Kukaev[1,2*], A. O. Tokareva[1], O. A. Krogh-Jensen[1,3], A. A. Lenyushkina[1], N. L. Starodubtseva[1,4]

[1]National Medical Research Center for Obstetrics Gynecology and Perinatology Named after Academician V.I. Kulakov of the Ministry of Healthcare of Russian Federation, Moscow, 117997 Russia

[2]V.L. Talrose Institute for Energy Problems of Chemical Physics, N.N. Semenov Federal Research Center for Chemical Physics, Russian Academy of Sciences, Moscow, 119991 Russia

[3]Federal State Autonomous Educational Institution of Higher Education I.M. Sechenov First Moscow State Medical University of the Ministry of Health of the Russian Federation (Sechenov University), Moscow, 119048 Russia

[4]Moscow Institute of Physics and Technology, Dolgoprudny, Moscow region, 141701 Russia

*E-mail: e_kukaev@oparina4.ru

Received January 29, 2025; in final form, June 25, 2025

DOI: 10.32607/actanaturae.27623

ABSTRACT **The development of a symbiotic gut ecosystem is a crucial step in postnatal adaptation. The gut microbiome of very preterm infants is characterized by an overall instability, reduced microbial diversity, and a predominance of Gram-negative Proteobacteria, all factors associated with an increased risk of necrotizing enterocolitis (NEC). Short-chain fatty acids (SCFAs) are the key bacterial metabolites that are essential for maintaining intestinal homeostasis, supporting immune development, enhancing intestinal barrier integrity, and reducing inflammation. This review examines the role of gut microbiota and SCFAs in neonatal NEC, with a focus on potential diagnostic and therapeutic strategies. Clinical studies have consistently demonstrated a significant decrease in total SCFA levels and individual bacterial metabolites in preterm infants with NEC. This finding has been corroborated by various experimental models. Clarification of the role of SCFAs in NEC pathogenesis, determination of their diagnostic utility, and assessment of the feasibility of developing comprehensive pro- and postbiotic formulations require multi-center, multi-omics investigations that include a large cohort of very preterm infants.**

KEYWORDS **necrotizing enterocolitis, very premature infants, diagnostics, gas chromatography-mass spectrometry, short-chain fatty acids, gut microbiota.**

ABBREVIATIONS **GC – gas-chromatography; LC – liquid-chromatography; SCFA – short-chain fatty acids; MS – mass-spectrometry; NEC – necrotizing enterocolitis; NICU – neonatal intensive care unit; PCR – polymerase chain reaction.**

INTRODUCTION

Necrotizing enterocolitis (NEC) is a severe gastrointestinal disease that affects newborns. It is characterized by marked inflammation of the intestinal wall, followed by necrosis and potential perforation. NEC is a significant gastrointestinal complication that primarily affects premature infants, with rare instances reported in infants born after 32 weeks gestation [1]. The primary factors that predispose to excessive gut inflammation include gastrointestinal immaturity, impaired bacterial colonization, and the lack of enteral feeding with breast milk [2]. The incidence of NEC is inversely proportional to gestational age, ranging from 2% to 10% in very preterm infants (28–32 weeks of gestation) and reaching 55% among extremely preterm newborns [3].

Notwithstanding the progress achieved in modern medicine, the incidence of NEC has not changed substantially over time in very low birth weight (VLBW) infants and constitutes a major cause of adverse outcomes in this cohort. The need for surgical intervention due to intestinal perforation or suspicion thereof in NEC ranges from 20% to 52%. Mortality rates for VLBW infants with surgical NEC in developed coun-

tries average 30%, reaching 50–72% among extremely low birth weight (ELBW) newborns [4, 5]. According to clinical observations, the progression of NEC is especially unfavorable in cases with concurrent congenital pneumonia, hemodynamically significant patent ductus arteriosus, and ELBW [6]. Between 22.7% and 35% of newborns who survive the surgical stage of NEC will develop intestinal failure syndrome, a condition with a reduction in gut function below the level necessary for the absorption of macronutrients and/or water and electrolytes [7]. Not only does the occurrence of NEC have implications for the gastrointestinal tract, but it also substantially increases the chances of adverse neurological outcomes. Due to the large surface area, considerable vascularization, and high concentration of immune cells, inflammation in the intestine can lead both to intestinal wall perforation and development of systemic effects that impact other tissues and organs [8]. Prospective cohort studies examining the long-term outcomes of NEC reveal that 37.6–56.8% of preterm infants weighing less than 1,000 g at birth experience delayed neuropsychiatric development, a percentage significantly greater than in those without NEC [9].

Given the high prevalence of NEC and the significant risk of adverse outcomes, the development of innovative predictive and diagnostic tools is a priority in the study of this disease. Identifying early specific biomarkers of NEC opens the possibility of detecting excessive inflammatory processes in the gut even before the onset of clinical symptoms [10]. Such an approach would allow for the timely identification of high-risk groups, which, in turn, would ensure early initiation of conservative treatment and the prospective implementation of targeted innovative therapies. Particularly important is the use of noninvasive predictive and diagnostic methods that eliminate phlebotomy losses and painful stimuli, which is critical for VLBW newborns. One such method is the determination of fecal calprotectin levels as a potential early biomarker of NEC in preterm infants. However, its diagnostic value remains a subject of scientific debate [11].

Over the past twenty years, the gut microbiome has been the focus of considerable research, owing to its significance in maintaining health and its connection to diverse diseases like diabetes mellitus, asthma, and inflammatory bowel diseases, including NEC [12]. The reduced frequency of inflammatory diseases in individuals with an abundance of SCFA-producing bacteria and higher SCFA concentrations has stimulated active research in this field [13]. The analysis of gut microbiota composition involves costly and time-consuming tools, such as 16S rRNA sequencing, which generates extensive and complex datasets that are difficult for clinicians to interpret. Therefore, quantitative analysis of microbial metabolic activity via fecal SCFA levels using gas chromatography-mass spectrometry (GC-MS) merits particular consideration [14, 15]. GC-MS affords rapid, accurate, and non-invasive analysis, making it ideal for neonatal intensive care units (NICUs), notably for very premature infants at elevated risk of NEC.

This review aims to summarize and analyze current data on the pathogenetic role of SCFAs, key metabolites of the gut microbiota, in the development of NEC in very preterm infants (less than 32 weeks of gestation). This avenue appears promising both for understanding the pathogenesis of the disease and for developing novel diagnostic and preventive strategies.

GUT MICROBIOTA IN THE PATHOGENESIS OF NEC

The bacterial community of the gastrointestinal tract is a vast population of microorganisms (approximately 10^{12}–10^{14} cells), representing between 100 and 1,000 various species. Because of the ability to influence various bodily functions by releasing thousands of substances into the bloodstream, this ecosystem is frequently referred to as the "second genome" or even the "second brain" [14].

The microbiome of a newborn develops from birth, affected by factors such as the method of delivery (vaginal delivery or cesarean section), feeding regimen (breast or formula feeding), and the environment [16]. Initially highly plastic and variable, the composition of the neonatal microbiota stabilizes in early childhood [17]. Prolonged hospitalization, antibiotic therapy, feeding via oro- or nasogastric tubes, lack of contact with maternal microflora, and a deficiency of breast milk are key factors influencing the specific development of gut microbiota in preterm infants, the microbial profile of which differs from that of full-term newborns [18]. Gastrointestinal tract colonization in infants within neonatal intensive care units (NICU) is thought to result in a reduced alpha-diversity of the microbial community with simultaneous enrichment in genes responsible for antibiotic resistance [19–22].

In very preterm infants, the gut is mostly populated by opportunistic facultative anaerobes, such as Proteobacteria and Firmicutes representatives. This coincides with a reduction in the prevalence of commensal bacteria, including Actinobacteria and Bacteroidota [23, 24]. A significantly increased relative abundance is observed of bacteria of the Enterobacteriaceae family, which comprises *Enterobacter*, *Escherichia*, and *Klebsiella* (phylum Proteobacteria). In contrast, beneficial bacteria of the

genus *Bifidobacterium* (phylum Actinobacteria) are markedly underrepresented compared to full-term infants [23, 24]. Of particular interest is the observation that during the development of the microbial community in very preterm infants a transition from the dominance of one genus of bacteria to another occurs, reflecting the high dynamism and instability of the microbiota in such infants [22, 25, 26]. These changes could be associated with external influences, including antibiotic administration and feeding specifics [22]. Due to the significant instability in the gut microbiome of preterm infants, coupled with the small study group sizes, it is challenging to pinpoint the specific bacteria linked to the onset of NEC [26].

Prior research indicated decreased gut microbiome diversity in very preterm infants, with an even more substantial reduction observed in infants diagnosed with NEC [27]. It should be noted that the reduction in commensal bacteria, specifically representatives of the genera *Bifidobacterium* (phylum Actinobacteria) and *Bacteroides* (phylum Bacteroidota), and the increase in opportunistic microorganisms of the phylum Proteobacteria (especially the family Enterobacteriaceae) and Firmicutes (genera *Staphylococcus*, *Clostridium*, *Streptococcus*, and *Blautia*) become increasingly pronounced [27–31]. A correlation between Gammaproteobacteria, particularly the Enterobacteriaceae family, and NEC development was demonstrated in a major longitudinal study of preterm infants with a birth weight under 1,500 g [31]. An increase in the abundance of potentially pathogenic Gammaproteobacteria with a simultaneous decrease in Bacteroides abundance prior to NEC manifestation has also been confirmed in other works [27, 32, 33].

Stewart C.J. et al. (2016) suggested that the etiology of NEC in very preterm infants should be interpreted in terms of the instability of the developing intestinal microbiome rather than specific microorganisms as potential pathogens [25]. This instability is manifested in frequent transitions between dominant bacterial communities. A longitudinal investigation into the gut microbiome of 35 very preterm infants demonstrated that NEC was only observed when bacteria from the genera *Klebsiella* and *Escherichia* (family Enterobacteriaceae, phylum Proteobacteria), or *Staphylococcus* and *Enterococcus* (phylum Firmicutes), predominate. Moreover, NEC did not occur in the presence of a more diverse bacterial community with a high relative abundance of *Bifidobacterium*. These data suggest that, in the pathogenesis of NEC, one should consider not only (and not primarily) the factor of colonization by a specific pathogenic bacterial species, but more broadly, the factor of microbiome stability and diversity, which underscores the multifactorial nature of this pathology [25].

The immature gut of very preterm infants exhibits impaired epithelial cell differentiation, fewer Paneth cells, and a reduction in the synthesis of protective mucus [34]. Insufficient formation of intestinal mucus, immature gut immunity, and reduced endogenous production of antimicrobial factors can lead to increased bacterial adhesion and heightened exposure to bacterial endotoxin (lipopolysaccharide, LPS) from Gram-negative bacteria (specifically the phylum Proteobacteria prevalent in such children). This stimulates Toll-like receptors 4 (TLR4) on epithelial cells, leading to their apoptosis and the disruption of intestinal epithelial barrier integrity, as well as triggering a pronounced inflammatory reaction mediated by TNFα, IL-1β, and other pro-inflammatory cytokines [35]. Ultimately, these processes increase the risk of developing neonatal sepsis or a local inflammation (*Fig. 1*) [6, 36, 37].

In NEC, a pathogen may not always be identified [25]. Diagnosis is established through clinical and radiological indicators, negating the need for microorganism isolation. However, examining the contribution of microbiome dysregulation to the etiology of NEC is essential in integrating the microbiome analysis into clinical application. Early detection of bacterial overgrowth, particularly of species associated with NEC and late-onset sepsis, as well as analysis of changes in the structure of the microbiome over time could be a promising avenue in treating very preterm infants [36]. Particular emphasis is placed on the microbiological analysis of mucosal secretions from the upper respiratory and gastrointestinal tracts within the first 24 h of life in identifying early neonatal sepsis and NEC risk factors in very preterm infants [38]. Yet incorporating data on the gut microbiota and its changes into daily clinical practice is hindered by several obstacles, encompassing the substantial diversity and intricacy of microbiota composition, as well as the absence of standardized analytical methodologies and procedures. These factors complicate the interpretation of the data obtained and require further research.

Conventional methods used to study microbiota involve culturing microorganisms in various nutrient media. These methods facilitate a thorough examination of live bacterial cultures and functional assessments, like antibiotic sensitivity. However, such methods have significant limitations: only a small percentage of gut microorganisms can be cultured in a laboratory setting, and the culturing process can be time-consuming. Consequently, culture-based methods reflect the species composition of the microbiota to a

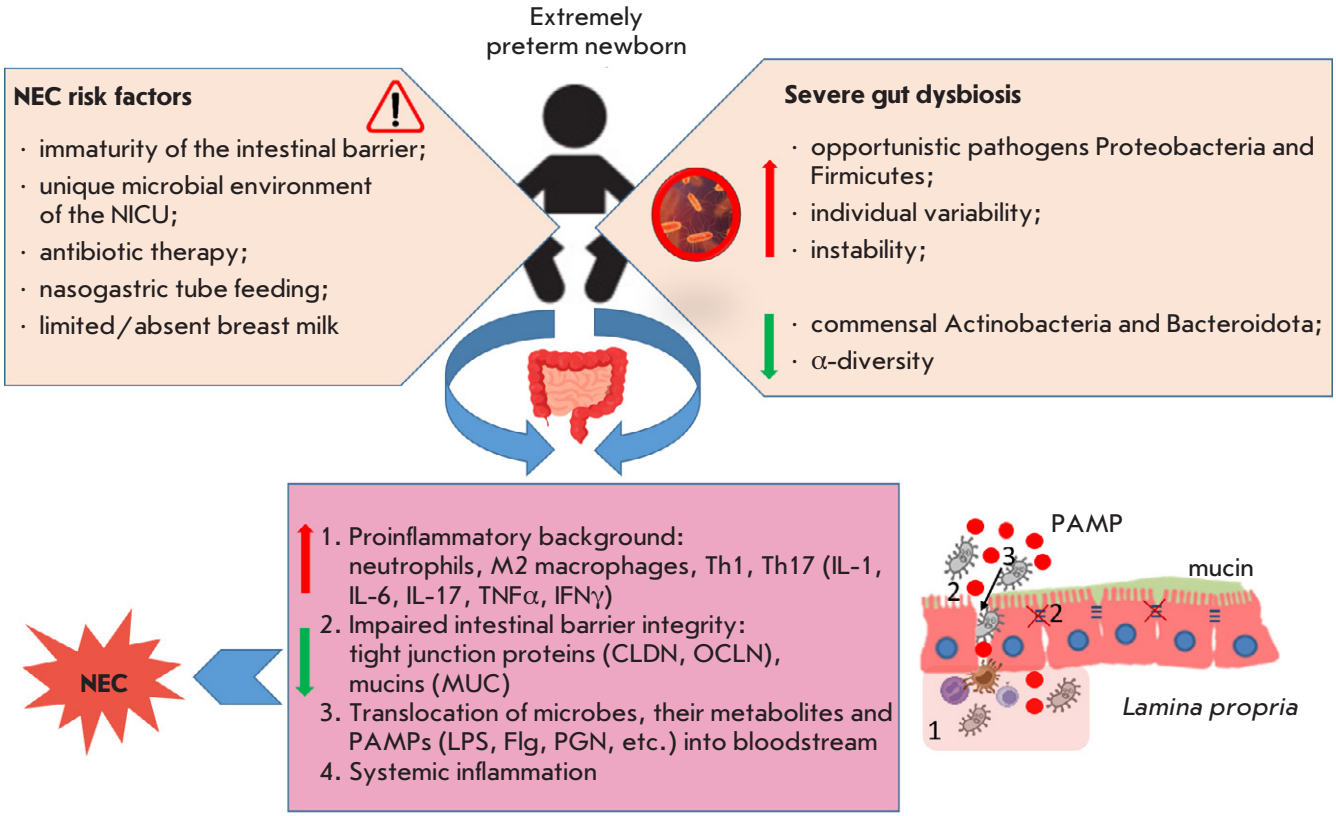

Fig. 1. Scheme of NEC pathogenesis in very preterm infants

limited extent and provide qualitative, rather than quantitative, data [39].

Polymerase chain reaction (PCR), a potent and extremely sensitive molecular technique, is employed to amplify and identify specific DNA segments to rapidly detect particular microorganisms. However, PCR is primarily employed to detect known species and does not facilitate an assessment of species diversity and richness within microbiota composition [40].

The use of next-generation sequencing (NGS) of 16S rRNA has become widespread in microbiota studies, because it allows for the analysis of the genetic material of both culturable and non-culturable microorganisms [40]. This method allows one to identify bacterial species, estimate their relative abundance, and evaluate their potential metabolic activity. However, 16S rRNA NGS has its drawbacks, such as the difficulty in differentiating closely related species, a lack of detailed information on the functional aspects of bacterial communities, high cost and time requirements for the analysis, and the complexity of data processing and interpretation (*Table 1*) [41].

Despite providing comprehensive data on microbial community composition and genetic profiles, 16S rRNA sequencing does not fully elucidate the functional role of each species within the microbiome. Microorganisms are capable of adapting by altering enzyme synthesis levels and activity, allowing them to influence the environment, community members, cells, and the host organism itself. Multi-omics approaches integrating metagenomics, metatranscriptomics, proteomics, and metabolomics are being developed to address these challenges. These methods can provide more comprehensive data concerning the intensity of gut dysbiosis, interaction dynamics, and the metabolic functions of the microbial community, which could be especially beneficial in clinical research and in managing complex diseases linked to changes in the microbiome [42].

SHORT-CHAIN FATTY ACIDS ARE KEY METABOLITES OF THE GUT MICROBIOTA

Bacteria are capable of synthesizing approximately 15,000 molecules unique to the human host, for which

Table 1. Comparison of major methods for investigating microbiota composition: advantages and limitations

Method	Advantages	Limitations
Culture-based methods	Obtaining live cultures; Conducting functional assessments, including antibiotic sensitivity tests.	Limited number of culturable species; Labor-intensive and time-consuming process; Primarily qualitative data [39].
PCR	High sensitivity; Rapid detection of established microorganisms.	The detection is limited to established microorganisms; The total species diversity cannot be estimated [40].
16S rRNA sequencing	Analysis of culturable and non-culturable species; Assessment of relative abundance; Microbiota profiling.	The lack of discrimination between closely related species; Limited functional data; High cost; Interpretation challenges [40, 41].

immune and intestinal cells express specific receptors [43]. Bacterial metabolites can penetrate the intestinal barrier and exert systemic effects [44, 45]. Notable among these bioactive compounds of microbial origin are antimicrobial peptides, conjugated linoleic acid, gamma-aminobutyric acid (GABA), and short-chain fatty acids (SCFAs) [45].

In the human body, these compounds perform a multitude of important functions, including inhibiting the synthesis of pro-inflammatory cytokines, maintaining the integrity of the intestinal epithelial barrier, and stimulating the proliferation and differentiation of colonocytes [45]. SCFAs serve as universal energy substrates for various cells, with butyric acid acting as the preferred energy source for colonocytes, providing 60–70% of their energy requirements [46]. Compared to individual microorganisms or their combinations, SCFAs, the end products of bacterial metabolism, offer a more insightful indication of gut status. Understanding the mechanisms of action of these metabolites is fundamental in identifying potential NEC biomarkers and developing new therapeutic targets.

Of the SCFAs produced in the gut, only 5% are detected in feces, as colonocytes absorb the majority [47]. The average concentration of SCFAs in feces ranges from units to tens of mmol/kg [48]. Only a small fraction (approximately 1%) of SCFA is absorbed into the portal vein as salts [49]. Acetic acid (acetate) is a key end product of glycolysis in a multitude of commensal microorganisms, including representatives of *Lactobacillus*, *Clostridium*, *Blautia* (phylum Firmicutes), *Bacteroides* and *Prevotella* (phylum Bacteroidota), as well as *Bifidobacterium* (phylum Actinobacteria) [30]. Propionic acid (propionate) is synthesized by a limited number of gut bacteria via the metabolism of succinate, acrylate, and propanediol. These microorganisms include representatives of the genera *Clostridium*, *Veillonella* (phylum Firmicutes), *Propionibacterium* (phylum Actinobacteria), and *Bacteroides* (phylum Bacteroidota) [4]. Bacteria producing butyric acid (butyrate) mainly belong to the phylum *Firmicutes*, including the families Ruminococcaceae, Lachnospiraceae, Erysipelotrichaceae, and Clostridiaceae [50]. Butyrate production is notably high in species belonging to the class Clostridia [51]. Additionally, the gut microbiota includes bacteria that employ the metabolic byproducts of other microorganisms to produce butyric acid, thereby inhibiting the buildup of lactate and acetate [5]. For example, acetate produced by *Bifidobacterium* is converted into butyrate by bacteria of the class Clostridia [52].

Acetic acid functions as a fatty acid biosynthesis substrate, is involved in the Krebs cycle [53], and demonstrates anti-inflammatory activity [54]. Propionate contributes to the improvement of barrier function and intestinal epithelial integrity and also plays an important role in regulating glucose and lipid homeostasis in the liver [55]. Butyric acid (butyrate) is a key energy source for the epithelial and immune cells of the large intestine [56, 57], increases the expression of tight junction proteins, thereby promoting the maintenance of gut barrier integrity [56], and exhibits a pronounced anti-inflammatory effect [58].

Establishing the relationship between gut microbiota and health requires reliable quantitative tools for determining metabolite concentrations in various biological matrices, such as plasma, serum, urine, and feces. Contemporary research uses such techniques as capillary electrophoresis (CE), nuclear magnetic resonance (NMR), and liquid and gas chromatography

Table 2. Comparative characteristics of methods for the quantitative determination of SCFAs in feces

Analysis method	Principle	Advantages	Limitations
Capillary electrophoresis [61]	Separation of ions in an electric field within a capillary	– Method simplicity – Low reagent consumption – Possibility of analyzing multiple compounds simultaneously	– Low sensitivity – Requires a high degree of sample purification
NMR spectroscopy [62]	Registers magnetic properties of atomic nuclei	– Non-destructive method – Simultaneous analysis of many metabolites – No need for derivatization	– Low sensitivity – High equipment cost
LC–MS [60, 63, 65, 66]	Separation of compounds in the liquid phase followed by ion analysis	– High sensitivity and specificity – Wide range of detectable SCFAs – Possibility of isotopic normalization	– Multi-step sample preparation – Need for derivatization and/or use of internal standards – Volatile compound issues
GC–MS [59, 62, 64, 69, 71]	Separation of volatile compounds in gas phase and their mass spectrometric analysis	– High accuracy and sensitivity – Suitable for the analysis of volatile SCFAs – Possibility of analysis without derivatization (under optimal conditions)	– Time-consuming sample preparation – Need for derivatization for non-volatile compounds – Variable reproducibility when analyzing neonatal feces

coupled with mass spectrometry (LC-MS and GC-MS) [59–64]. Mass spectrometry is the method of choice for the quantitative analysis of low-molecular-weight compounds owing to its high sensitivity and specificity [59, 60, 63–66]. However, the application of these methods to the analysis of SCFAs in feces is not without some challenges. Firstly, the high lipid content in feces reduces the extraction efficiency of water-soluble compounds. Secondly, the volatile and partially hydrophilic properties of SCFAs significantly complicate their analysis via LC-MS, which requires multistep sample preparation, including extraction and derivatization stages [67]. Besides making the analysis more complex and time-consuming, it also elevates the technical variation [68]. GC-MS is a reliable method for the quantitative determination of low-molecular-weight compounds [64, 69, 70]. Due to the volatile nature of SCFAs, their analysis via GC-MS can be performed without derivatization if one uses chromatographic columns with highly polar phases and specific liquid-liquid extraction conditions [59, 69].

The precision and reliability of quantitative assessments could be compromised when examining infant fecal samples relative to adult samples. This is attributable to the significant fluctuations in water content, challenges in standardizing sample weight, the application of diapers and defecation stimulants within the NICU, and the scarcity of available biological material.

Table 2 presents a comparative analysis of the most commonly employed analytical methods for determining SCFAs in fecal matter. The predominant methodologies employed in clinical and research environments are presented, with particular attention to their relevance in the context of neonatal fecal sample analysis. Special attention is paid to parameters such as sensitivity, specificity, sample preparation requirements, and the potential limitations of each method. Considering the instability of SCFAs, GC-MS, when appropriately configured, may be the superior option, notwithstanding sample preparation needs.

MECHANISMS OF ACTION OF SCFAs

The primary function of SCFAs involves providing energy to intestinal cells, including colonocytes and cells of the immune system, thereby stimulating their metabolism, proliferation, and differentiation [72, 73]. Butyric acid (butyrate), one of the key SCFAs, reverses mitochondrial respiration deficits and prevents autophagy in energy-deprived germ-free colonocytes [74].

SCFAs play a crucial role in maintaining intestinal barrier integrity, preventing the development of increased intestinal permeability syndrome, known as "leaky gut." This syndrome facilitates bacterial translocation, intensifies inflammatory processes, and may cause systemic complications [75]. Adding butyrate to neuroglioma epithelial cells (H4) and including it in the diet of mice increases local oxygen consumption, which stabilizes the hypoxia-inducible factor (HIF). As a result, the transcription of the genes involved in the synthesis of key tight junction components, such as mucin (MUC20), claudins (CLDN2, 4, 11, and 15), and occludin (OCLN), is activated [76]. These alterations contribute to the fortification of intercellular

connections, thus impeding the passage of pathogens through the intestinal barrier.

SCFAs play a key role in the regulation of the immune response in the gut, making them important mediators of the interaction between the microbiota and the immune system [45]. Butyrate induces colonocytes to synthesize the anti-inflammatory cytokine IL-18, which not only enhances mucin production but also stimulates the synthesis of antimicrobial peptides, including defensins and cathelicidins, which are effective against numerous pathogens [77]. Concurrently, the bacterial metabolite inhibits IL-1-induced expression of pro-inflammatory genes, such as IL-6, CX3CL1, and CXCL5, thus regulating microbiota composition and preventing dysbiosis [78, 79].

SCFAs, acting as ligands for G-protein-coupled receptors (GPR43/FFAR2, GPR41/FFAR3), play a role in the activation and differentiation of cells in both innate and adaptive immunity [58, 80]. Butyrate guides macrophage differentiation toward the M2 immunosuppressive phenotype, which contributes to the suppression of inflammation and the preservation of tissue homeostasis [81]. Acetic acid reduces intestinal inflammation by activating the GPR43/FFAR2 receptor on granulocytes, contributing to a reduction in their inflammatory activity [82].

SCFAs influence gene expression levels in immune cells via epigenetic mechanisms. For example, butyrate and propionate inhibit histone deacetylases (HDACs), which promotes chromatin decondensation and the activation of transcription for the genes responsible for immunoregulation [72, 83]. Through HDAC inhibition, butyrate directs T-cell differentiation into Foxp3+ regulatory T cells (Tregs) [84]. Tregs play a central role in suppressing excessive immune responses to commensal microorganisms and preventing the development of chronic inflammation. In addition, the activation of GPR43 and GPR109A receptors on dendritic cells by butyrate enhances Treg differentiation through the upregulation of the anti-inflammatory cytokine IL-10 [85].

SCFAs are also known to affect how B-cell functions. Kim M. et al. (2016) demonstrated that SCFAs, particularly acetate, directly stimulate bacterial differentiation of B cells into IgA-producing cells [86]. The secretion of immunoglobulin A (IgA) provides protection to the intestinal mucosa, preventing the overgrowth of pathogenic microorganisms and protecting commensals [86].

SCFAs inhibit the growth and colonization of pathogenic intestinal microflora, including the microorganisms of the family Enterobacteriaceae, such as *E. coli*, *K. pneumoniae*, and *P. aeruginosa* [87]. They alter intracellular pH levels in pathogens, creating unfavorable conditions for their survival. This is attributable to the capacity of SCFAs to permeate the bacterial cell in a non-ionized state, subsequently dissociating, thereby decreasing intracellular pH and compromising metabolic functions within pathogen cells [88].

In colonocytes, butyrate activates the peroxisome proliferator-activated receptor-gamma (PPARγ), which plays an important role in regulating fatty acid metabolism. The activation of PPARγ stimulates β-oxidation, resulting in heightened oxygen consumption by colonocytes, consequently diminishing oxygen availability within the intestinal lumen. The change in the oxygen environment hinders the growth of aerobic pathogenic microorganisms, especially those of the *Enterobacteriaceae* family, which need oxygen for proliferation [89].

Thus, SCFAs, particularly butyric acid, act not only as universal energy substrates for intestinal cells but also as potent regulators of local immunity, barrier function, and microbial homeostasis (*Fig. 2*). The impact of SCFAs is of particular significance for very preterm infants. This is due to an elevated risk of colonization by pathogenic microorganisms stemming from the underdeveloped intestinal barrier and immune system. This results in metabolites being key factors in the prevention and treatment of conditions such as NEC.

SCFAs IN THE PATHOGENESIS OF NEC

Gut dysbiosis is recognized as one of the key factors in the pathogenesis of NEC [90]. Numerous studies conducted on model organisms have confirmed the significance of the microbiota and its metabolites in the development of this disease [91, 92]. In particular, the colonization of germ-free mice with bacteria isolated from the feces of NEC patients provokes NEC-like intestinal injury [15].

Gut dysbiosis leads to impaired SCFA synthesis, which is particularly relevant for very preterm infants [93], whose minimal SCFA levels at birth gradually increase with post-conceptional age in the absence of NEC [94–97]. However, SCFA metabolism in very preterm infants remains poorly understood.

Clinical research on the gut microbiota and generated SCFAs in very premature infants with NEC is still limited. Data from 16S rRNA sequencing in studies from 2021 to 2023 (*Table 3*) [15, 30, 98–100] validated the finding that Proteobacteria is the dominant bacteria in the immature gut microbiota, which has been linked to the development of NEC [27–29, 31]. Concurrently, a marked reduction in Firmicutes representatives, including major butyrate-producing strains, was observed prior to the onset of disease clinical manifestations [30].

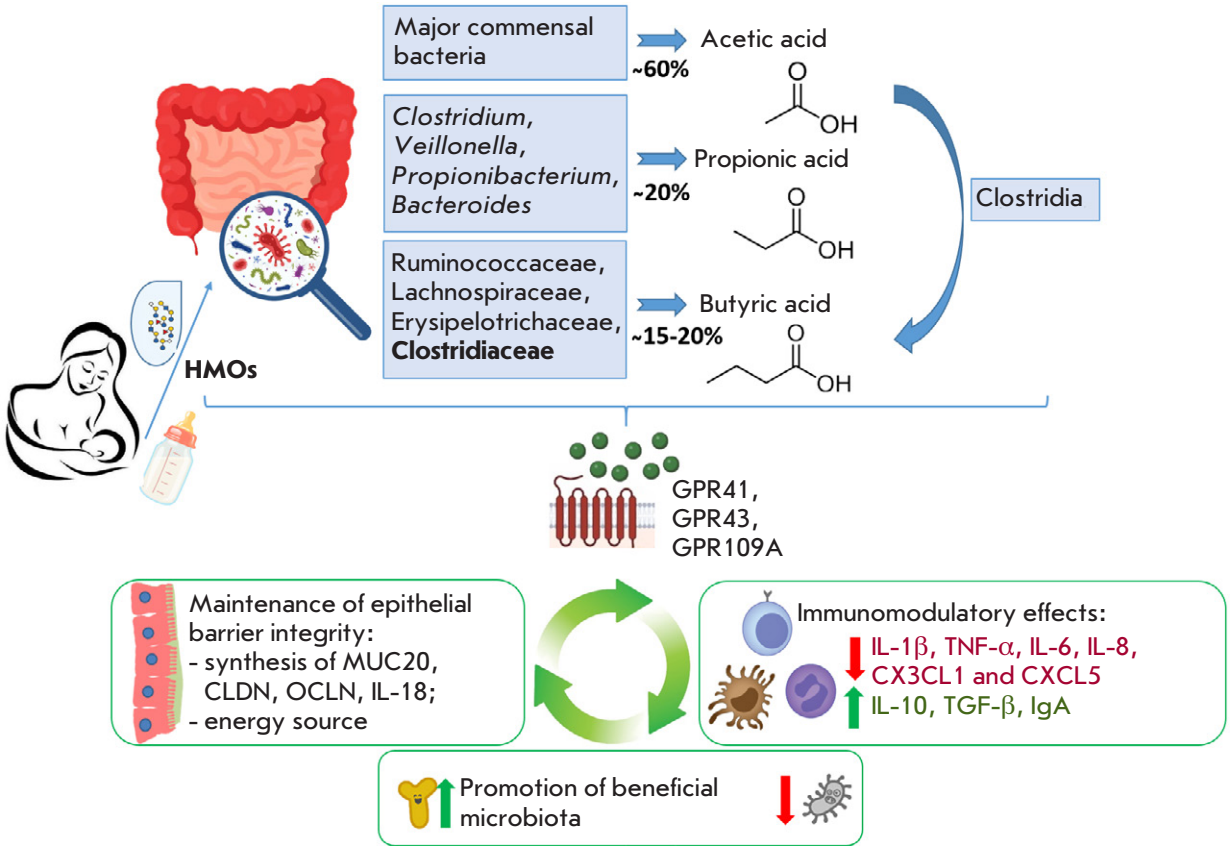

Fig. 2. Protective mechanisms of SCFAs in the neonatal gut

A significant reduction in SCFA levels ($p < 0.05$) was found in newborns with NEC, especially formic, propionic, butyric, isovaleric, and caproic acids [15, 30, 98, 100]. Notably, in extremely preterm infants receiving expressed breast milk, fecal SCFA concentrations were significantly higher than in formula-fed infants [101]. While further investigation is needed to establish a direct causal relationship between SCFA levels and the onset of NEC, the results suggest that these metabolites may offer protection by preserving gut barrier integrity and regulating the inflammatory response.

However, significant variability in absolute SCFA concentrations has been revealed. For example, Liu X.C. et al. (2022) identified the mean fecal butyrate level in the control group as 41 μg/g [30], while in the study by He Y. et al. (2021), this figure was found to reach 225 μg/g [15]. These inconsistencies may be attributed to variances in the analytical techniques employed, the characteristics of the cohort, and the procedures for biomaterial collection and storage.

According to the reviews by Alsharairi N.A. et al. (2023) and Cifuentes M.P. et al. (2024), the function of butyrate in the development of neonatal NEC is still being debated [93, 102]. However, a detailed analysis of clinical works (*Table 3*) demonstrates a pronounced decrease in fecal butyrate levels in extremely preterm infants one week prior to the appearance of clinical NEC symptoms and at the onset of the disease, confirming its potential diagnostic value [15, 30]. For adults, butyric acid has also been linked to a lower chance of developing inflammatory bowel diseases, including ulcerative colitis and Crohn's disease [103, 104]. Studies focusing on experiments highlight that butyrate improves the function of the intestinal barrier and lowers the inflammatory reactions of immune cells.

At the same time, a number of model experiments have revealed a negative role for butyrate in NEC [92, 105–108]. Incomplete carbohydrate digestion in the small intestine leads to their fermentation in the colon with the formation of SCFAs, lactate, and gases such as carbon dioxide, methane, and hydrogen [109]. In preterm piglets modeling NEC, excessive formation of bacterial metabolites due to high levels of undigested lactose can trigger an inflammatory reaction [108].

Table 3. Characteristics of the gut microbiome and SCFAs in NEC in preterm infants

References	Clinical groups	Gestational age, weeks	Day of NEC onset	Predominant microorganisms, phylum and share (%, control vs NEC)	SCFAs, direction of change and fold change
Liu X.C. et al., 2022 [30]	NEC 7.0 ± 7.6 days prior (n = 17) and at manifestation (n = 12)	30.5 ± 2.1	30.2 ± 15.9	Proteobacteria ↑ (from 40 to 53%) Firmicutes ↓ (from 55 to 35%) Actinobacteriota ↑ (from 5 to 10%) Bacteroidota ↑ (from 0.5 to 4%)	*Acetic 1.8↓ **Propionic 1.2↓ **Butyric 1.1↓ **Isovaleric 2.3↓ *Total SCFAs 2.4↓
	Control (n = 17)	30.5 ± 1.9	–		
He Y. et al., 2021 [15]	NEC (n = 81)	31.0 (29.4–33.7)	15 (12–19)	***Proteobacteria ↑ (from 27 to 55%) ***Firmicutes ↓ (from 57 to 37%) ***Actinobacteriota ↓ (from 4 to 1%) ***Bacteroidota ↓ (from 10 to 3%)	**Butyric 1.4↓
	Control (n = 81)	31.1 (29.3–33.2)	–		
Xiong J., 2022 [98]	NEC (n = 22)	35.5 ± 2.2	11.6 (6.8–16.0)	Proteobacteria ↓ (from 50 to 37%) Firmicutes ↑ (from 45 to 57%) *Actinobacteriota↑ (from 3 to 5%) **Bacteroidota ↓ (from 4 to 1%)	**Acetic 1.5↓ **Propionic 2.3↓ **Butyric 2.7↓ **Isovaleric 2.0↓ **Caproic 2.7↑ **Total SCFAs 1.6↓
	FPIAP (n = 21)	36.5 ± 1.4	15.2 (11.0–22.0)		
Casaburi G. et al., 2023 [100]	NEC (n = 3)	~29	–	Proteobacteria ↑	*Formic 6.7↑
	Control (n = 10)	~29	–		
	NEC, treatment (n = 3)	~29	after 3 weeks of treatment	Proteobacteria ↓ Bacteroidetes ↑ compared to NEC onset	–
Huang H., 2022 [99]	NEC (n = 9)	31.6 (28.35–37.45)		Proteobacteria ↑ (from 30 to 65%) Firmicutes ↓ (from 65 to 30%) Actinobacteriota ↓ (from 5 to 1%) Bacteroidota ↑ (from 0 to 5%)	Not performed
	Control (n = 10)	37.75 (32.03–39.05)			
Pourcyrous M. et al., 2014 [101]	Formula (n = 9)	27	–	Not performed	**Total SCFAs 1.9↑ **Acetate 3.1↑ **Propionate 3.4↑
	Expressed milk (n = 10)	27	–		

Note: Bold text indicates changes of more than 2-fold in fecal SCFA levels in the NEC group compared to the control group. * – $p < 0.05$, ** – $p < 0.01$, *** – $p < 0.001$ – for paired comparison of the NEC group and the control or comparison group.

The diverse effects of butyrate may be accounted for by its dose-related activity, as previously noted by Lin et al. (2002) [106]. Later, high concentrations of butyrate (greater than 16 mM) were confirmed to stimulate the synthesis of the pro-inflammatory cytokine IL-6, while low doses exert a protective effect by reducing IL-6 and NF-kB expression and enhancing the synthesis of the tight junction protein claudin-7 [57, 110]. Using a neonatal mouse NEC model, it was shown that an optimal level of butyric acid exists at which the risk of developing NEC is minimized [111].

The inconsistencies in data comparison across studies stem from the diversity of analytical methodologies, limited sample sizes of very premature infants, and the heterogeneity of NEC experimental models. Multicenter randomized trials using a unified method-

ology for biomaterial collection and analysis of microbiological and metabolic data may help clarify the role of SCFAs in NEC pathogenesis, as well as to determine optimal therapeutic doses for these metabolites. At the same time, GC-MS application for quantifying SCFAs in feces provides an accurate, noninvasive, rapid, and cost-effective method that can be readily implemented in routine neonatal practice for early diagnosis and monitoring of metabolic activity within the intestinal microflora of very preterm infants [102].

CONCLUSION

A crucial step in the successful adaptation to life of a newborn child is the development of a symbiotic gut ecosystem. The formation of a dysbiotic microbial signature is influenced by several factors: birth at a low gestational age, congenital immaturity of the gut, frequent cesarean sections, extended stays in intensive care, antibiotic treatment, absence of contact with maternal microflora, and the lack or insufficiency of breast milk. The gut microbiome of very preterm infants is characterized by a predominance of Gram-negative bacteria of the phylum Proteobacteria, reduced microbial diversity, and overall instability. Research has correlated these alterations with an increased risk of life-threatening conditions, such as NEC.

Recent findings emphasize the critical role of microbiota metabolites, such as SCFAs, in maintaining the metabolic and immune homeostasis of the gut. However, the majority of the data has been obtained using murine models and cell lines. Moreover, accumulating evidence indicates that the SCFA metabolism operates within a dynamic equilibrium, and imbalances, whether elevated or diminished, can detrimentally affect health.

A more thorough understanding of the function of SCFAs and the microbiome in the development of NEC necessitates multicenter research encompassing a suitable number of cases of this rare disease. The incorporation of multi-omics techniques, encompassing metagenomic sequencing, transcriptomics, and targeted metabolomics, is necessary to identify particular microbial communities and metabolic biomarkers, including SCFAs. The improvement of rapid and non-invasive methods for functional microbiome profiling for clinical settings will lead to the creation of a system for assessing the risk of NEC development in very preterm infants. The correlation between neonatal pathologies and microbial metabolites presents opportunities for developing intricate pro- and postbiotic formulations. ●

This study was supported by the Russian Science Foundation (grant No. 24-25-00068): https://rscf.ru/project/24-25-00068/.

REFERENCES

1. Neu J, Mshvildadze M, Mai V. A roadmap for understanding and preventing necrotizing enterocolitis. *Curr Gastroenterol Rep.* 2008;10(5):450–457. doi: 10.1007/s11894-008-0084-x
2. Ahearn-Ford S, Berrington JE, Stewart CJ. Development of the gut microbiome in early life. *Exp Physiol.* 2022;107(5):415–421. doi: 10.1113/EP089919
3. Thänert R, Sawhney SS, Schwartz DJ, Dantas G. The resistance within: Antibiotic disruption of the gut microbiome and resistome dynamics in infancy. *Cell Host Microbe.* 2022;30(5):675–683. doi: 10.1016/j.chom.2022.03.013
4. Reichardt N, Duncan SH, Young P, et al. Phylogenetic distribution of three pathways for propionate production within the human gut microbiota. *ISME J.* 2014;8(6):1323–1335. doi: 10.1038/ismej.2014.14
5. Scheiman J, Luber JM, Chavkin TA, et al. Meta-omic analysis of elite athletes identifies a performance-enhancing microbe that functions via lactate metabolism. *Nat Med.* 2019;25(7):1104–1109. doi: 10.1038/s41591-019-0485-4
6. Nikitina IV, Lenyushkina AA, Krogh-Jensen OA, et al. Recurrent necrotizing enterocolitis: predictors, biological markers, diagnostic signs, and therapeutic approaches – a year-long case study. *Neonatology.* 2024;12(3):66–77. doi: 10.33029/2308-2402-2024-12-3-66-77
7. Jones IH, Hall NJ. Contemporary Outcomes for Infants with Necrotizing Enterocolitis – A Systematic Review. *J Pediatr.* 2020;220:86–92.e3. doi: 10.1016/j.jpeds.2019.11.011
8. Scheese DJ, Sodhi CP, Hackam DJ. New insights into the pathogenesis of necrotizing enterocolitis and the dawn of potential therapeutics. *Semin Pediatr Surg.* 2023;32(3):151309. doi: 10.1016/j.sempedsurg.2023.151309
9. Zhou Q, Niño DF, Yamaguchi Y, et al. Necrotizing enterocolitis induces T lymphocyte–mediated injury in the developing mammalian brain. *Sci Transl Med.* 2021;13(575):eaay6621. doi: 10.1126/scitranslmed.aay6621
10. Fullerton BS, Hong CR, Velazco CS, et al. Severe neurodevelopmental disability and healthcare needs among survivors of medical and surgical necrotizing enterocolitis: A prospective cohort study. *J Pediatr Surg.* 2018;53(1):101–107. doi: 10.1016/j.jpedsurg.2017.10.029
11. Pupysheva AF, Savelyeva EI, Piskunova VV, et al. Fecal Calprotectin Levels Dynamics in Newborns with High-Risk of Necrotizing Enterocolitis. *Pediatr Pharmacol.* 2023;20(1):51–55. doi: 10.15690/pf.v20i1.2529
12. Thakkar HS, Lakhoo K. Necrotizing enterocolitis. *Surgery (Oxf).* 2022;40(11):713–716. doi: 10.1016/j.mpsur.2022.09.007
13. Hsu CY, Khachatryan LG, Younis NK, et al. Microbiota-derived short chain fatty acids in pediatric health and diseases: from gut development to neuroprotection. *Front Microbiol.* 2024;15:1456793. doi: 10.3389/fmicb.2024.1456793
14. Facchin S, Bertin L, Bonazzi E, et al. Short-Chain Fatty Acids and Human Health: From Metabolic Path-

ways to Current Therapeutic Implications. *Life (Basel).* 2024;14(5):559. doi: 10.3390/life14050559
15. He Y, Du W, Xiao S, et al. Colonization of fecal microbiota from patients with neonatal necrotizing enterocolitis exacerbates intestinal injury in germfree mice subjected to necrotizing enterocolitis-induction protocol via alterations in butyrate and regulatory T cells. *J Transl Med.* 2021;19(1):510. doi: 10.1186/s12967-021-03109-5
16. Bäckhed F, Roswall J, Peng Y, et al. Dynamics and stabilization of the human gut microbiome during the first year of life. *Cell Host Microbe.* 2015;17(5):690–703. doi: 10.1016/j.chom.2015.04.004
17. Cuna A, Morowitz MJ, Ahmed I, Umar S, Sampath V. Dynamics of the preterm gut microbiome in health and disease. *Am J Physiol Gastrointest Liver Physiol.* 2021;320(4):G411–G419. doi: 10.1152/ajpgi.00399.2020
18. Yao Y, Cai X, Ye Y, Wang F, Chen F, Zheng C. The Role of Microbiota in Infant Health: From Early Life to Adulthood. *Front Immunol.* 2021;12:708472. doi: 10.3389/fimmu.2021.708472
19. Olm MR, Brown CT, Brooks B, et al. Identical bacterial populations colonize premature infant gut, skin, and oral microbiomes & exhibit different in situ growth rates. *Genome Res.* 2017;27(4):601–612. doi: 10.1101/gr.213256.116
20. Gibson MK, Wang B, Ahmadi S, et al. Developmental dynamics of the preterm infant gut microbiota and antibiotic resistome. *Nat Microbiol.* 2016;1:16024. doi: 10.1038/nmicrobiol.2016.24
21. Gasparrini AJ, Wang B, Sun X, et al. Metagenomic signatures of early life hospitalization and antibiotic treatment in the infant gut microbiota and resistome persist long after discharge. *Nat Microbiol.* 2016;4(12):2285–2297. doi: 10.1038/s41564-019-0550-2
22. Wandro S, Osborne S, Enriquez C, Bixby C, Arrieta A, Whiteson K. The Microbiome and Metabolome of Preterm Infant Stool Are Personalized and Not Driven by Health Outcomes, Including Necrotizing Enterocolitis and Late-Onset Sepsis. *mSphere.* 2018;3(3):e00104–18. doi: 10.1128/msphere.00104-18
23. Young GR, van der Gast CJ, Smith DL, Berrington JE, Embleton ND, Lanyon C. Acquisition and Development of the Extremely Preterm Infant Microbiota Across Multiple Anatomical Sites. *J Pediatr Gastroenterol Nutr.* 2020;70(1):12–19. doi: 10.1097/MPG.0000000000002549
24. Patel AL, Mutlu EA, Sun Y, et al. Longitudinal Survey of Microbiota in Hospitalized Preterm Very Low Birth Weight Infants. *J Pediatr Gastroenterol Nutr.* 2016;62(2):292–303. doi: 10.1097/MPG.0000000000000913
25. Stewart CJ, Embleton ND, Marrs ECL, et al. Temporal bacterial and metabolic development of the preterm gut reveals specific signatures in health and disease. *Microbiome.* 2016;4(1):67. doi: 10.1186/s40168-016-0216-8
26. Unger S, Stintzi A, Shah P, Mack D, O'Connor DL. Gut microbiota of the very-low-birth-weight infant. *Pediatr Res.* 2015;77(1–2):205–213. doi: 10.1038/pr.2014.162
27. Wang Y, Hoenig JD, Malin KJ, et al. 16S rRNA gene-based analysis of fecal microbiota from preterm infants with and without necrotizing enterocolitis. *ISME J.* 2009;3(8):944–954. doi: 10.1038/ismej.2009.37
28. Lemme-Dumit JM, Song Y, Lwin HW, et al. Altered Gut Microbiome and Fecal Immune Phenotype in Early Preterm Infants With Leaky Gut. *Front Immunol.* 2022;13:815046. doi: 10.3389/fimmu.2022.815046
29. Torrazza RM, Ukhanova M, Wang X, et al. Intestinal microbial ecology and environmental factors affecting necrotizing enterocolitis. *PLoS One.* 2013;8(12):e83304. doi: 10.1371/journal.pone.0083304
30. Liu XC, Du TT, Gao X, et al. Gut microbiota and short-chain fatty acids may be new biomarkers for predicting neonatal necrotizing enterocolitis: A pilot study. *Front Microbiol.* 2022;13:969656. doi: 10.3389/fmicb.2022.969656
31. Warner PBB, Deych E, Zhou Y, et al. Gut bacteria dysbiosis and necrotising enterocolitis in very low birthweight infants: a prospective case-control study. *Lancet.* 2017;387(10031):1928–1936. doi: 10.1016/S0140-6736(16)00081-7
32. Morrow AL, Lagomarcino AJ, Schibler KR, et al. Early microbial and metabolomic signatures predict later onset of necrotizing enterocolitis in preterm infants. *Microbiome.* 2013;1(1):13. doi: 10.1186/2049-2618-1-13
33. Olm MR, Bhattacharya N, Crits-Christoph A, et al. Necrotizing enterocolitis is preceded by increased gut bacterial replication, Klebsiella, and fimbriae-encoding bacteria. *Sci Adv.* 2019;5(12):eaax5727. doi: 10.1126/sciadv.aax5727
34. Salzman NH, Underwood MA, Bevins CL. Paneth cells, defensins, and the commensal microbiota: A hypothesis on intimate interplay at the intestinal mucosa. *Semin Immunol.* 2007;19(2):70–83. doi: 10.1016/j.smim.2007.04.002
35. Mih B, Good M. Impact of Toll-like receptor 4 signaling in necrotizing enterocolitis: The state of the science. Clin Perinatol. 2019;46(1):145–157. doi: 10.1016/j.clp.2018.09.007
36. Healy DB, Ryan CA, Ross RP, Stanton C, Dempsey EM. Clinical implications of preterm infant gut microbiome development. *Nat Microbiol.* 2022;7(1):22–33. doi: 10.1038/s41564-021-01025-4
37. Nikitina IV, Donnikov AE, Krogh-Jensen OA, et al. Genetic predictors of necrotizing enterocolitis in neonates. *Akush Ginekol (Russian Fed).* 2020;(12):150–158. doi: 10.18565/aig.2020.12.150-158
38. Krogh-Jensen OA, Nikitina IV, Bragina ON, et al. Body surface cultures in preterm neonates on the first day of life: clinical usefulness. *Akush Ginekol (Russian Fed).* 2022;(8):108–123. doi: 10.18565/aig.2022.8.108-123
39. Gupta S, Mortensen MS, Schjørring S, et al. Amplicon sequencing provides more accurate microbiome information in healthy children compared to culturing. *Commun Biol.* 2019;2:291. doi: 10.1038/s42003-019-0540-1
40. Deurenberg RH, Bathoorn E, Chlebowicz MA, et al. Application of next generation sequencing in clinical microbiology and infection prevention. J Biotechnol. 2017;243:16–24. doi: 10.1016/j.jbiotec.2016.12.022
41. Woo PCY, Lau SKP, Teng JLL, Tse H, Yuen KY. Then and now: Use of 16S rDNA gene sequencing for bacterial identification and discovery of novel bacteria in clinical microbiology laboratories. *Clin Microbiol Infect.* 2008;14(10):908–934. doi: 10.1111/j.1469-0691.2008.02070.x
42. Sher Y, Olm MR, Raveh-Sadka T, et al. Combined analysis of microbial metagenomic and metatranscriptomic sequencing data to assess in situ physiological conditions in the premature infant gut. *PLoS One.* 2020;15(3):e0229537. doi: 10.1371/journal.pone.0229537
43. Wishart DS, Oler E, Peters H, et al. MiMeDB: the Human Microbial Metabolome Database. *Nucleic Acid Res.* 2023;51(D1):D611–D620. doi: 10.1093/nar/gkac868
44. Liu M, Lu Y, Xue G, et al. Role of short-chain fatty acids in host physiology. *Animal Model Exp Med.* 2024;7(5):641–652. doi: 10.1002/ame2.12464
45. Takeuchi T, Nakanishi Y, Ohno H. Microbial Metabolites and Gut Immunology. *Annu Rev Immunol.* 2024;42(1):153–178. doi: 10.1146/annurev-immunol-090222-102035

46. Martin-Gallausiaux C, Marinelli L, Blottière HM, Larraufie P, Lapaque N. SCFA: Mechanisms and functional importance in the gut. *Proc Nutr Soc.* 2021;80(1):37–49. doi: 10.1017/S0029665120006916
47. den Besten G, van Eunen K, Groen AK, Venema K, Reijngoud DJ, Bakker BM. The role of short-chain fatty acids in the interplay between diet, gut microbiota, and host energy metabolism. *J Lipid Res.* 2013;54(9):2325–2340. doi: 10.1194/jlr.R036012
48. Morrison DJ, Preston T. Formation of short chain fatty acids by the gut microbiota and their impact on human metabolism. *Gut Microbes.* 2016;7(3):189–200. doi: 10.1080/19490976.2015.1134082
49. Tan J, McKenzie C, Potamitis M, Thorburn AN, Mackay CR, Macia L. The Role of Short-Chain Fatty Acids in Health and Disease. *Adv Immunol.* 2014:121:91–119. doi: 10.1016/B978-0-12-800100-4.00003-9
50. Barcenilla A, Pryde SE, Martin JC, et al. Phylogenetic relationships of butyrate-producing bacteria from the human gut. *Appl Environ Microbiol.* 2000;66(4):1654–1661. doi: 10.1128/AEM.66.4.1654-1661.2000
51. Louis P, Young P, Holtrop G, Flint HJ. Diversity of human colonic butyrate-producing bacteria revealed by analysis of the butyryl-CoA:acetate CoA-transferase gene. *Environ Microbiol.* 2010;12(2):304–314. doi: 10.1111/j.1462-2920.2009.02066.x
52. Turroni F, Milani C, Duranti S, Mahony J, van Sinderen D, Ventura M. Glycan Utilization and Cross-Feeding Activities by Bifidobacteria. *Trends Microbiol.* 2018;26(4):339–350. doi: 10.1016/j.tim.2017.10.001
53. Liu L, Fu C, Li F. Acetate affects the process of lipid metabolism in rabbit liver, skeletal muscle and adipose tissue. *Animals (Basel).* 2019;9(10):799. doi: 10.3390/ani9100799
54. Ma J, Liu Z, Gao X, et al. Gut microbiota remodeling improves natural aging-related disorders through Akkermansia muciniphila and its derived acetic acid. *Pharmacol Res.* 2023;189:106687. doi: 10.1016/j.phrs.2023.106687
55. Langfeld LQ, Du K, Bereswill S, Heimesaat MM. A review of the antimicrobial and immune-modulatory properties of the gut microbiota-derived short chain fatty acid propionate – What is new? *Eur J Microbiol Immunol (Bp).* 2021;11(2):50–56. doi: 10.1556/1886.2021.00005
56. Rivière A, Selak M, Lantin D, Leroy F, De Vuyst L. Bifidobacteria and butyrate-producing colon bacteria: Importance and strategies for their stimulation in the human gut. *Front Microbiol.* 2016;7:979. doi: 10.3389/fmicb.2016.00979
57. Liu J, Zhu H, Li B, et al. Beneficial effects of butyrate in intestinal injury. *J Pediatr Surg.* 2020;55(6):1088–1093. doi: 10.1016/j.jpedsurg.2020.02.036
58. Liu P, Wang Y, Yang G, et al. The role of short-chain fatty acids in intestinal barrier function, inflammation, oxidative stress, and colonic carcinogenesis. *Pharmacol Res.* 2021;165:105420. doi: 10.1016/j.phrs.2021.105420
59. Yao L, Davidson EA, Shaikh MW, Forsyth CB, Prenni JE, Broeckling CD. Quantitative analysis of short-chain fatty acids in human plasma and serum by GC-MS. *Anal Bioanal Chem.* 2022;414(15):4391–4399. doi: 10.1007/s00216-021-03785-8
60. Saha S, Day-Walsh P, Shehata E, Kroon PA. Development and validation of a lc-ms/ms technique for the analysis of short chain fatty acids in tissues and biological fluids without derivatisation using isotope labelled internal standards. *Molecules.* 2021;26(21):6444. doi: 10.3390/molecules26216444
61. Garcia A, Olmo B, Lopez-Gonzalvez A, Cornejo L, Rupérez FJ, Barbas C. Capillary electrophoresis for short chain organic acids in faeces. Reference values in a Mediterranean elderly population. *J Pharm Biomed Anal.* 2008;46(2):356–361. doi: 10.1016/j.jpba.2007.10.026
62. Cai J, Zhang J, Tian Y, et al. Orthogonal Comparison of GC–MS and 1 H NMR Spectroscopy for Short Chain Fatty Acid Quantitation. *Anal Chem.* 2017;89(15):7900–7906. doi: 10.1021/acs.analchem.7b00848
63. Zheng J, Zheng SJ, Cai WJ, Yu L, Yuan BF, Feng YQ. Stable isotope labeling combined with liquid chromatography-tandem mass spectrometry for comprehensive analysis of short-chain fatty acids. *Anal Chim Acta.* 2019;1070:51–59. doi: 10.1016/j.aca.2019.04.021
64. Hoving LR, Heijink M, van Harmelen V, van Dijk KW, Giera M. GC-MS analysis of short-chain fatty acids in feces, cecum content, and blood samples. *Methods Mol Biol.* 2018;1730:247–256. doi: 10.1007/978-1-4939-7592-1_17
65. Dei Cas M, Paroni R, Saccardo A, et al. A straightforward LC-MS/MS analysis to study serum profile of short and medium chain fatty acids. *J Chromatogr B Analyt Technol Biomed Life Sci.* 2020;1154:121982. doi: 10.1016/j.jchromb.2020.121982
66. Trivedi N, Erickson HE, Bala V, Chhonker YS, Murry D. A Concise Review of Liquid Chromatography-Mass Spectrometry-Based Quantification Methods for Short Chain Fatty Acids as Endogenous Biomarkers. *Int J Mol Sci.* 2022;23(21):13486. doi: 10.3390/ijms232113486
67. Primec M, Mičetić-Turk D, Langerholc T. Analysis of short-chain fatty acids in human feces: A scoping review. *Anal Biochem.* 2017;526:9–21. doi: 10.1016/j.ab.2017.03.007
68. Tumanov S, Bulusu V, Gottlieb E, Kamphorst JJ. A rapid method for quantifying free and bound acetate based on alkylation and GC-MS analysis. *Cancer Metab.* 2016;4(1):17. doi: 10.1186/s40170-016-0157-5
69. Kim KS, Lee Y, Chae W, Cho JY. An Improved Method to Quantify Short-Chain Fatty Acids in Biological Samples Using Gas Chromatography–Mass Spectrometry. *Metabolites.* 2022;12(6):525. doi: 10.3390/metabo12060525
70. Zhang C, Tang P, Xu H, Weng Y, Tang Q, Zhao H. Analysis of Short-Chain Fatty Acids in Fecal Samples by Headspace-Gas Chromatography. *Chromatographia.* 2018;81:1317–1323. doi: 10.1007/s10337-018-3572-7
71. Kukaev E, Kirillova E, Tokareva A, et al. Impact of Gut Microbiota and SCFAs in the Pathogenesis of PCOS and the Effect of Metformin Therapy. *Int J Mol Sci.* 2024;25(19):10636. doi: 10.3390/ijms251910636
72. Luu M, Visekruna A. Short-chain fatty acids: Bacterial messengers modulating the immunometabolism of T cells. *Eur J Immunol.* 2019;49(6):842–848. doi: 10.1002/eji.201848009
73. Moffett JR, Puthillathu N, Vengilote R, Jaworski DM, Namboodiri AM. Acetate Revisited: A Key Biomolecule at the Nexus of Metabolism, Epigenetics and Oncogenesis – Part 1: Acetyl-CoA, Acetogenesis and Acyl-CoA Short-Chain Synthetases. *Front Physiol.* 2020;11:580167. doi: 10.3389/fphys.2020.580167
74. Donohoe DR, Collins LB, Wali A, Bigler R, Sun W, Bultman SJ. The Warburg Effect Dictates the Mechanism of Butyrate Mediated Histone Acetylation and Cell Proliferation. *Mol Cell.* 2012;48(4):611–626. doi: 10.1016/j.molcel.2012.08.033
75. Baldassarre ME, Di Mauro A, Capozza M, et al. Dysbiosis and prematurity: Is there a role for probiotics?

Nutrients. 2019;11(6):1273. doi: 10.3390/nu11061273
76. Zhao J, Hu J, Ma X. Sodium caprylate improves intestinal mucosal barrier function and antioxidant capacity by altering gut microbial metabolism. *Food Funct*. 2021;12(20):9750–9762. doi: 10.1039/d1fo01975a
77. Levy M, Thaiss CA, Zeevi D, et al. Microbiota-modulated metabolites shape the intestinal microenvironment by regulating NLRP6 inflammasome signaling. *Cell*. 2015;163(6):1428–1443. doi: 10.1016/j.cell.2015.10.048
78. Tian P, Yang W, Guo X, et al. Early life gut microbiota sustains liver-resident natural killer cells maturation via the butyrate-IL-18 axis. *Nat Commun*. 2023;14(1):1710. doi: 10.1038/s41467-023-37419-7
79. Beisner J, Filipe Rosa L, Kaden-Volynets V, Stolzer I, Günther C, Bischoff SC. Prebiotic Inulin and Sodium Butyrate Attenuate Obesity-Induced Intestinal Barrier Dysfunction by Induction of Antimicrobial Peptides. *Front Immunol*. 2021;12:678360. doi: 10.3389/fimmu.2021.678360
80. van der Hee B, Wells JM. Microbial Regulation of Host Physiology by Short-chain Fatty Acids. *Trends Microbiol*. 2021;29(8):700–712. doi: 10.1016/j.tim.2021.02.001
81. Schulthess J, Pandey S, Capitani M, et al. The Short Chain Fatty Acid Butyrate Imprints an Antimicrobial Program in Macrophages. *Immunity*. 2019;50(2):432–445.e7. doi: 10.1016/j.immuni.2018.12.018
82. Maslowski KM, Vieira AT, Ng A, et al. Regulation of inflammatory responses by gut microbiota and chemoattractant receptor GPR43. *Nature*. 2009;461(7268):1282–1286. doi: 10.1038/nature08530
83. Thomas SP, Denu JM. Short-chain fatty acids activate acetyltransferase p300. *Elife*. 2021;10:e72171. doi: 10.7554/eLife.72171
84. Furusawa Y, Obata Y, Fukuda S, et al. Commensal microbe-derived butyrate induces the differentiation of colonic regulatory T cells. *Nature*. 2013;504(7480):446–450. doi: 10.1038/nature12721
85. Sun M, Wu W, Chen L, et al. Microbiota-derived short-chain fatty acids promote Th1 cell IL-10 production to maintain intestinal homeostasis. *Nat Commun*. 2018;9(1):3555. doi: 10.1038/s41467-018-05901-2
86. Kim M, Qie Y, Park J, Kim CH. Gut Microbial Metabolites Fuel Host Antibody Responses. *Cell Host Microbe*. 2016;20(2):202–214. doi: 10.1016/j.chom.2016.07.001
87. Kumar M, Singh P, Murugesan S, et al. Microbiome as an Immunological Modifier. *Methods Mol Biol*. 2020;2055:595–638. doi: 10.1007/978-1-4939-9773-2_27
88. Sorbara MT, Dubin K, Littmann ER, et al. Inhibiting antibiotic-resistant Enterobacteriaceae by microbiota-mediated intracellular acidification. *J Exp Med*. 2019;216(1):84–98. doi: 10.1084/jem.20181639
89. Byndloss MX, Olsan EE, Rivera-Chávez F, et al. Microbiota-activated PPAR-γ signaling inhibits dysbiotic Enterobacteriaceae expansion. *Science*. 2017;357(6351):570–575. doi: 10.1126/science.aam9949
90. Fundora JB, Guha P, Shores DR, Pammi M, Maheshwari A. Intestinal dysbiosis and necrotizing enterocolitis: assessment for causality using Bradford Hill criteria. *Pediatr Res*. 2020;87(2):235–248. doi: 10.1038/s41390-019-0482-9
91. Jilling T, Simon D, Lu J, et al. The Roles of Bacteria and TLR4 in Rat and Murine Models of Necrotizing Enterocolitis. *J Immunol*. 2006;177(5):3273–3282. doi: 10.4049/jimmunol.177.5.3273
92. Waligora-Dupriet AJ, Dugay A, Auzeil N, Huerre M, Butel MJ. Evidence for clostridial implication in necrotizing enterocolitis through bacterial fermentation in a gnotobiotic quail model. *Pediatr Res*. 2005;58(4):629–635. doi: 10.1203/01.PDR.0000180538.13142.84
93. Alsharairi NA. Therapeutic Potential of Gut Microbiota and Its Metabolite Short-Chain Fatty Acids in Neonatal Necrotizing Enterocolitis. *Life (Basel)*. 2023;13(2):561. doi: 10.3390/life13020561
94. Athalye-Jape G, Esvaran M, Patole S, et al. Effect of single versus multistrain probiotic in extremely preterm infants: a randomised trial. *BMJ Open Gastroenterol*. 2022;9(1):e000811. doi: 10.1136/bmjgast-2021-000811
95. Neumann CJ, Mahnert A, Kumpitsch C, et al. Clinical NEC prevention practices drive different microbiome profiles and functional responses in the preterm intestine. *Nat Commun*. 2023;14(1):1349. doi: 10.1038/s41467-023-36825-1
96. Frau A, Lett L, Slater R, et al. The stool volatile metabolome of pre-term babies. *Molecules*. 2021;26(11):3341. doi: 10.3390/molecules26113341
97. Wang C, Shoji H, Sato H, et al. Effects of oral administration of Bifidobacterium breve on fecal lactic acid and short-chain fatty acids in low birth weight infants. *J Pediatr Gastroenterol Nutr*. 2007;44(2):252–257. doi: 10.1097/01.mpg.0000252184.89922.5f
98. Xiong J, Liao XS, Yin T, Liu XC, Bao L, Li LQ. Alterations of the gut microbiota and short chain fatty acids in necrotizing enterocolitis and food protein-induced allergic protocolitis infants: A prospective cohort study. *Front Cell Infection Microbiol*. 2022;12:1030588. doi: 10.3389/fcimb.2022.1030588
99. Huang H, Peng Q, Zhang Y, et al. Abnormalities in microbial composition and function in infants with necrotizing enterocolitis: A single-center observational study. *Front Pediatr*. 2022;10:963345. doi: 10.3389/fped.2022.963345
100. Casaburi G, Wei J, Kazi S, et al. Metabolic model of necrotizing enterocolitis in the premature newborn gut resulting from enteric dysbiosis. *Front Pediatr*. 2022;10:893059. doi: 10.3389/fped.2022.893059
101. Pourcyrous M, Nolan VG, Goodwin A, Davis SL, Buddington RK. Fecal short-chain fatty acids of very-low-birth-weight preterm infants fed expressed breast milk or formula. *J Pediatr Gastroenterol Nutr*. 2014;59(6):725–731. doi: 10.1097/MPG.0000000000000515
102. Cifuentes MP, Chapman JA, Stewart CJ. Gut microbiome derived short chain fatty acids: Promising strategies in necrotising enterocolitis. *Curr Res Microb Sci*. 2024;6:100219. doi: 10.1016/j.crmicr.2024.100219
103. Frank DN, St Amand AL, Feldman RA, Boedeker EC, Harpaz N, Pace N. Molecular-phylogenetic characterization of microbial community imbalances in human inflammatory bowel diseases. *Proc Natl Acad Sci U S A*. 2007;104(34):13780–13785. doi: 10.1073/pnas.0706625104
104. Sokol H, Seksik P, Furet JP, et al. Low counts of faecalibacterium prausnitzii in colitis microbiota. *Inflamm Bowel Dis*. 2009;15(8):1183–1189. doi: 10.1002/ibd.20903
105. Waligora-Dupriet AJ, Dugay A, Auzeil N, et al. Short-chain fatty acids and polyamines in the pathogenesis of necrotizing enterocolitis: Kinetics aspects in gnotobiotic quails. *Anaerobe*. 2009;15(4):138–144. doi: 10.1016/j.anaerobe.2009.02.001
106. Lin J, Nafday SM, Chauvin SN, et al. Variable effects of short chain fatty acids and lactic acid in inducing intestinal mucosal injury in newborn rats. *J Pediatr Gastroenterol Nutr*. 2002;35(4):545–550. doi: 10.1097/00005176-200210000-00016

107. Nafday SM, Chen W, Peng L, Babyatsky MW, Holzman IR, Lin J. Short-chain fatty acids induce colonic mucosal injury in rats with various postnatal ages. *Pediatr Res.* 2005;57(2):201–204. doi: 10.1203/01.PDR.0000150721.83224.89
108. Thymann T, Møller HK, Stoll B, et al. Carbohydrate maldigestion induces necrotizing enterocolitis in preterm pigs. *Am J Physiol Gastrointest Liver Physiol.* 2009;297(6):G1115–G1125. doi: 10.1152/ajpgi.00261.2009
109. Kien CL. Digestion, absorption, and fermentation of carbohydrates in the newborn. *Clin Perinatol.* 1996;23(2):211–228. doi: 10.1016/s0095-5108(18)30239-2
110. Peng L, He Z, Chen W, Holzman IR, Lin J. Effects of butyrate on intestinal barrier function in a caco-2 cell monolayer model of intestinal barrier. *Pediatr Res.* 2007;61(1):37–41. doi: 10.1203/01.pdr.0000250014.92242.f3
111. Vieira ELM, Leonel AJ, Sad AP, et al. Oral administration of sodium butyrate attenuates inflammation and mucosal lesion in experimental acute ulcerative colitis. J Nutr Biochem. 2012;23(5):430–436. doi: 10.1016/j.jnutbio.2011.01.007

The Role of EPFL Peptides in Plant Development and Stress Responses

A. D. Maiboroda[1], A. A. Makeeva[1], R. A. Azarkina[1], A. S. Barashkova[1,2], A. S. Mamaeva[1*]
[1]Shemyakin–Ovchinnikov Institute of Bioorganic Chemistry, Russian Academy of Sciences, Moscow, 117997 Russia
[2]All-Russian Institute of Plant Protection, St. Petersburg, Pushkin, 196608 Russia
*E-mail: AnnetteSt@yandex.ru
Received April 18, 2025; in final form, July 01, 2025
DOI: 10.32607/actanaturae.27675

ABSTRACT **Cysteine-rich peptides belonging to the EPF/EPFL (epidermal patterning factor/epidermal patterning factor-like) family are common in many plants, from mosses to angiosperms. EPF/EPFL play an important role in morphogenesis: they regulate stomatal patterning, the functioning of the shoot apical and lateral meristems, inflorescence architecture, vascular development, growth of leaf margin, as well as the development of flowers and fruits. Recent studies have indicated that EPFL may be involved in plant adaptation to biotic and abiotic stress. This review examines the structure, phylogenetic distribution, mechanisms of signal transduction, and functions of the EPF/EPFL peptide family.**
KEYWORDS **plant regulatory peptides; cysteine-rich peptides; EPF/EPFL.**
ABBREVIATIONS **EPF – epidermal patterning factor; EPFL – epidermal patterning factor-like; ABA – abscisic acid; MAPK – mitogen-activated protein kinase; MDA – malondialdehyde; MMC – megaspore mother cell.**

INTRODUCTION

As sessile organisms, plants adapt to environmental changes through a flexible system that regulates physiological processes. A crucial role in this adaptation is played by signal peptides, which control a broad range of responses, including growth and development, sexual reproduction, intercellular communication, senescence, symbiosis, as well as resistance to pathogens and abiotic stress [1, 2]. The first identified plant regulatory peptide, systemin, was isolated from tomato leaves in 1991 [3]. Numerous peptide families, originating either from the processing of precursor proteins or via translation of short open reading frames, have been described since then [1, 4].

Peptides derived from precursor proteins are classified into three functionally and structurally distinct groups: post-translationally modified peptides [5], cysteine-rich peptides, and unmodified peptides without cysteine residues [6, 7]. Cysteine-rich peptides carry an even number of cysteine residues that form disulfide bonds, a disposition that ensures the stability of their spatial structure. Antimicrobial peptides were the first members of this group to be discovered and described [8]. It was originally believed that the functions of cysteine-rich peptides were limited to defense against pathogens [4, 9]. However, subsequent research demonstrated that cysteine-rich peptides have a much broader range of functions, encompassing the regulation of stomatal initiation, symbiosis, reproductive processes, and stress responses [10–12].

The cysteine-rich peptides EPF/EPFL were first identified as key regulators of stomatal development in *Arabidopsis thaliana* (Arabidopsis) [10, 13–15]. Further research revealed that these peptides are involved in the regulation of the size of shoot apical meristem, inflorescence development, and stress adaptation. Although the body of experimental data on the subject continues to grow, there are currently no systematic reviews that summarize information about this family. Our study has endeavored to consolidate the data on EPF/EPFL peptides, including their structure, evolutionary diversity, and biological functions.

THE STRUCTURE AND SIGNAL TRANSDUCTION

Cysteine-rich plant peptides can be roughly divided into defensive (antimicrobial) and regulatory peptides and comprise several families, including the EPF/EPFL one [16]. The structure of defensive peptides has been the one studied most thoroughly: NMR analyses have been performed for many of these pep-

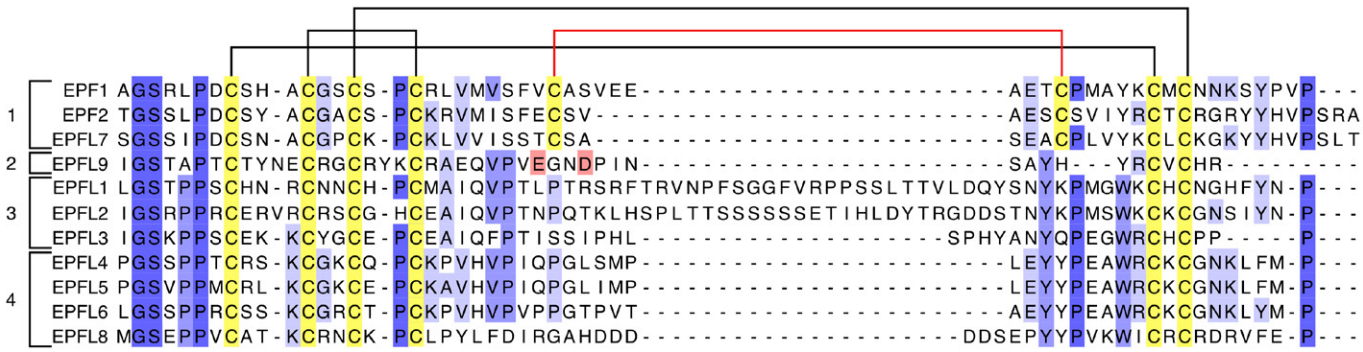

Fig. 1. Multiple alignment of mature peptides belonging to the EPF/EPFL family in *A. thaliana* conducted using the Muscle algorithm. (1–4) clades of peptides; cysteine amino acid residues are highlighted in yellow. Three conservative disulfide bonds are indicated with black brackets; the fourth disulfide bond, specific to the EPF1/EPF2/EPFL7 clade, is indicated with red bracket. Glu28 and Asp31 amino acid residues in EPFL9 are highlighted in pink. UniProt ID: EPF1: Q8S8I4; EPF2: Q8LC53; EPFL7: C4B8C5; EPFL9: Q9SV72; EPFL1: Q9LFT5; EPFL2: Q9T068; EPFL3: C4B8C4; EPFL4: Q2V3I3; EPFL5: Q9LUH9; EPFL6: Q1PEY6; EPFL8: Q1G3V9

tides, and the structural determinants of their antimicrobial activity have been identified [17, 18]. The structural features of cysteine-rich signal peptides in plants, including the EPF/EPFL family, have been investigated less thoroughly; however, the primary and spatial structures of the EPFL9 peptide isolated from the *A. thaliana* apoplast have been determined [19, 20]. Furthermore, structural data on peptide-receptor interactions for several peptides belonging to this family has been obtained [21]. Eleven peptides have been identified in *A. thaliana*, the classical model organism that is most commonly used to study this peptide family: EPF1–2 and EPFL1–9, including EPFL9/Stomagen [22]. EPF1 and EPF2 were the first to be characterized, followed by other EPF1 paralogs named EPFL [23]. The EPF/EPFL peptides were divided into four clades by phylogenetic analysis (*Fig. 1*). Members of two of these clades, EPF1–EPF2–EPFL7 and EPFL9, have been the most thoroughly studied.

Like most peptide hormones and antimicrobial peptides in plants, members of the EPF/EPFL family are synthesized as precursor proteins consisting of an N-terminal signal peptide, a prodomain, and a mature peptide (*Fig. 2A*) [24]. The signal peptide guides the precursor to the endoplasmic reticulum, where it is then cleaved off and degraded by peptidases. The prodomain is subsequently removed, and a mature peptide capable of interacting with receptor complexes is released [25].

The primary structure of EPF/EPFL peptides is rich in cysteine residues; six of them are conserved across the entire family, and two additional residues occur only in the EPF1/EPF2/EPFL7 clade (*Fig. 1*). All the peptides belonging to this family carry the Gly-Ser motif in the N-terminal region. This motif is known to be critical in peptides binding to their receptors [21]. A conserved Pro residue is also present in the N-terminal region. This residue probably helps maintain the spatial conformation of the peptide by bending the polypeptide chain.

The NMR spectroscopy data garnered for EPFL9 suggest that the three-dimensional structure of EPF/EPFL peptides consists of two antiparallel β-sheets (a scaffold) connected by a loop region and stabilized by disulfide bonds (*Fig. 2B*). The loop region is more variable than the scaffold and plays a crucial role in the specificity of the binding to receptors [19]. The spatial structures of other family members have been determined via homology modeling.

Conserved cysteine residues are involved in the formation of disulfide bonds, whose number and arrangement affect the functional activity and conformation of the peptide. Thus, the ability to stimulate stomatal initiation was lost after cysteine residues had been replaced with serine in the EPFL9 molecule [19]. Conversely, variable regions can be responsible for the functional specificity of the peptides. Thus, EPF1/2 peptides act as negative regulators of stomatal development, whereas EPFL9 is a positive regulator [20]. The diversity in physiological responses are probably a result of structural differences in the loop region of these peptides [21].

Thus, replacing the EPF2 loop with the corresponding sequence from EPFL9 converted the peptide's function from inhibition to promotion of stomatal development. Meanwhile, a chimeric peptide carrying the EPF2 loop and the EPFL9 scaffold exhibited an inhibitory activity [19]. The ERECTA family (ERf) kinases, which belong to the leucine-rich repeat receptor-like kinases (LRR-RLK) clade XIII, act as receptors for EPFL peptides. In Arabidopsis, this family includes the ERECTA (ER), ERECTA-LIKE 1 (ERL1), and ERECTA-LIKE 2 (ERL2) proteins. The combined signaling pathway involves the MAPK (mitogen-activated protein kinase) cascade, which consists of MAPKKK YODA, MKK4/5, and the terminal kinases MPK3/6 in Arabidopsis [27]. The peptide–receptor interaction depends on whether the receptor is part of a complex with LRR–RLP (leucine-rich repeat receptor-like protein) TMM (Too Many Mouths). Interestingly, EPF1/2 bind only to the ERf–TMM complex, while EPFL4 interacts with each of three ERf in the absence of TMM [21].

PHYLOGENETIC DIVERSITY IN PLANTS

The EPF and EPFL peptides have been identified only in terrestrial plants, but they are not found in algae [28, 29]. This indicates that this peptide family evolved after plants had colonized the land and may have played an important role in their adaptation to terrestrial life. There is a hypothesis holding that the key genetic components ensuring the formation of the stomatal apparatus, including EPF/EPFL, originated at the early stages of the evolution of terrestrial plants [30].

Peptide sequences are conserved across different taxa: *Pp*EPF1, a homolog of *At*EPF1 and *At*EPF2, was identified in moss *Physcomitrium patens*. Phylogenetic analysis shows that *Pp*EPF1 is closer to *At*EPF1 and *At*EPF2 than *At*EPFL9 [28]. This is rather interesting, since the stomatal apparatus of mosses differs from that of angiosperms, and yet their developmental mechanisms seem to be similar [31, 32]. In addition to *Pp*EPF1, ten EPFL peptides have been identified in moss; their functions are still to be characterized [28]. In angiosperms, the genes encoding EPF/EPFL peptides are unevenly distributed across chromosomes, which may be a result of genetic duplication events [33, 34]

This peptide family in Arabidopsis is phylogenetically subdivided into four clades: EPF1–EPF2–EPFL7, EPFL9, EPFL1–3, and EPFL4–6–EPFL8 (*Fig. 1*) [28, 34]. These groups differ in both structure and putative functions. Thus, members of the EPF1–EPF2–EPFL7 clade carry four conserved disulfide bonds, one located in the loop region, whereas the peptides from the other clades carry three disulfide bonds. This feature affects the ability of the peptides to bind to receptor complexes [21, 28].

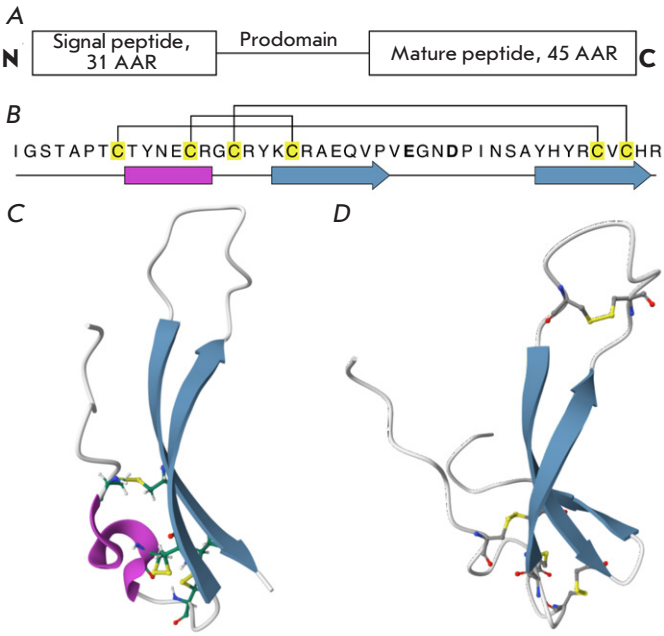

Fig. 2. The structure of EPFL9 peptide. (*A*) The structure of preproprotein [20]. (*B*) The primary structure of peptide [19]. β-sheets are shown with blue arrows; the 3_{10}-helix is shown with a pink rectangle; Cys residues are highlighted in yellow; disulfide bonds are shown with brackets. Negatively charged amino acid residues Glu28 and Asp31 in the loop region are highlighted in bold. (*C*) The spatial structure of EPFL9 (PDB ID: 2LIY). (*D*) The structural model of EPFL7 peptide in *A. thaliana*, generated using the AlphaFold3 algorithm [26]

The EPFL9 peptide was found in all the studied vascular plants, from lycophytes (*Selaginella moellendorffii*) and gymnosperms to angiosperms [28]. However, it was not identified in moss *P. patens*, although a EPF1/EPF2 homolog is present in that plant. Notably, the emergence of EPFL9, which activates stomatal development, coincides with an abrupt rise in stomatal density on leaf surfaces in the Late Devonian period, when megaphylls – large leaves with a well-developed vascular system – evolved [28, 35].

The number of sequenced plant genomes has recently increased, thus substantially facilitating the search for and subsequent validation of homologs. The genomes of a large number of agricultural flowering plants have been analyzed using bioinformat-

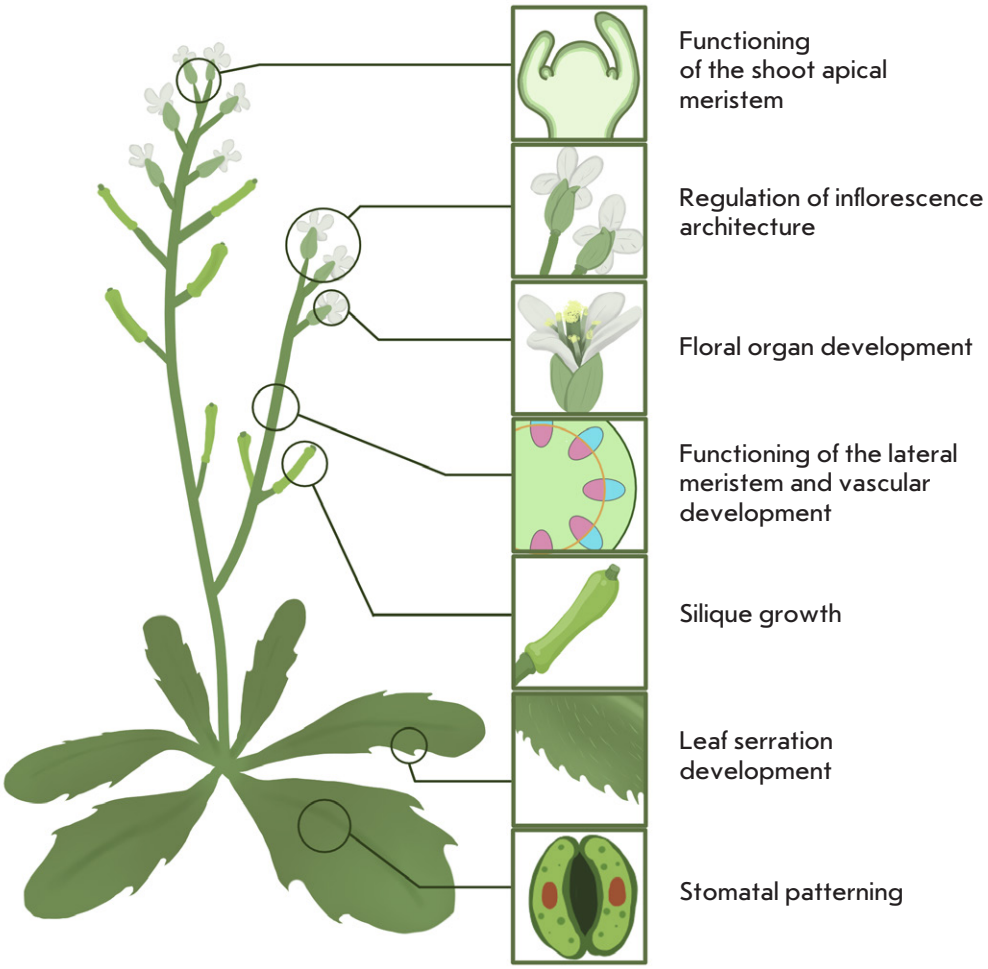

Fig. 3. Morphogenetic processes regulated by peptides of the EPF/EPFL family in *Arabidopsis thaliana*

ic tools. A total of 132 *EPF/EPFL* genes have been identified in the four cotton plant genomes: 20 and 24 genes in diploid species, and 44 genes in each of the tetraploid species [34]. Fourteen genes have been identified in potato plants [36]; and 27 genes, in rapeseed [37]. Fifteen *EPF/EPFL* genes have been identified in the black cottonwood *Populus trichocarpa* [38], while 14 genes have been in the Euphrates poplar *P. euphratica* [33]. *EPFL* genes were also discovered in monocots: 12 genes were identified in rice, sorghum, and rye [39–41]; 18 genes, in maize [42]; and 35 genes, in wheat [43]. The considerable abundance of the *EPF/EPFL* genes across different evolutionary lineages of angiosperms and other plants underscores their importance in adaptation to terrestrial environments, while the functions of many recently identified homologs remain unclear, requiring further experimental research.

STOMATAL INITIATION

EPF/EPFL peptides are known to orchestrate a broad spectrum of morphogenetic programs; regulation of stomatal patterning was the first function of these peptides to be discovered (*Fig. 3*, *Table 1*) [10].

In Arabidopsis, *EPF1* is expressed in young leaves; namely, in stomatal precursor cells. *EPF1* overexpression reduces the stomatal density, while *EPF1* knockout increases the stomatal density and clustering [10]. The EPF1 homolog, EPF2, also inhibits stomatal development: plants that overexpress the *EPF2* gene are characterized by a reduced stomatal density, whereas *EPF2*-knockout plants demonstrate an increased stomatal density but do not form clusters [13]. Both peptides enforce the “one-cell spacing rule” dictating that at least one intervening nonstomatal epidermal cell should separate two stomata [10, 13, 14]. *EPF2* is expressed in stomatal precursors earlier than *EPF1*.

Table 1. Functions of the EPF/EPFL peptides in *A. thaliana*

Peptide	Function	Reference
*At*EPF1/2	Inhibition of stomatal formation	[10, 13, 15, 23, 44]
*At*EPFL9 (STOMAGEN)	Stimulation of stomatal formation	[11, 15, 44, 45]
	Silique elongation	[46]
*At*EPFL2	Leaf serration development	[47]
	Regular ovule spacing and increased ovule number per silique	[46]
*At*EPFL1/2/4/6	Regulation of functioning of the apical meristem	[48–51]
	Enhancement of pathogen resistance	[52]
	Elongation of inflorescences and pedicels	[53]
	Formation of a single megaspore mother cell	[54]
*At*EPFL1–6	Envelopment of the nucellus by integuments	[55]
*At*EPFL4–6	Stamen filament elongation due to cell proliferation	[56, 57]

Thus, EPF2 regulates the initiation of stomatal differentiation, while EPF1 controls further development [10, 14, 15]. Contrariwise, the EPFL9 peptide promotes stomatal development: *EPFL9* overexpression increases stomatal density and causes clustering, whereas silencing of *EPFL9* inhibits stomatal development [45]. Both the EPF1–2 and EPFL9 peptides have been shown to bind to the ER receptor; EPFL9 competitively displaces EPF1–2 from this complex [44]. The EPF1/2 peptides are expressed in stomatal cells, bind to ER and ERL1, and inhibit stomatal differentiation, whereas EPFL9 is expressed in mesophyll cells, competes with EPF2 for binding to ER, and promotes stomatal formation [15, 44]. Hence, EPF1/2 and EPFL9 act as antagonists in the stomatal density control [44].

The role of EPF peptides are best studied in Arabidopsis; however, their involvement in the regulation of stomatal development has been demonstrated for other plants as well. For example, overexpression of poplar *Pe*EPF2, a homolog of *At*EPF2, in *At*EPF2 knockout Arabidopsis plants reduced the stomatal density on leaves and rescued the mutant phenotype [33]. Orthologs of *AtEPF2* and *AtEPFL9* involved in the regulation of stomatal development in Arabidopsis have been detected in the genomes of the monocots *Triticum aestivum* and *Brachypodium distachyon* [58]. These peptides also exert an opposing effect on stomatal development.

It has been demonstrated that the EPF/TMM/ERECTA module is a rather ancient regulator of stomatal development: its components control stomatal patterning in early terrestrial plants, in moss *P. patens* in particular [59]. In *P. patens*, stomata form on the sporophyte; *Pp*EPF1, a homolog of Arabidopsis *EPF1/2*, negatively regulates their development. However, *Pp*EPF1 overexpression cannot restore the normal stomatal density in the Arabidopsis mutant *epf2*. Meanwhile, *P. patens* lacks an *At*EPFL9 ortholog and *At*EPFL9 overexpression does not affect its stomatal density, an indication that competitive regulation of stomatal patterning emerged at later stages of terrestrial plant evolution [59].

Hence, EPFL peptides are conserved and ancient regulators of stomatal development in terrestrial plants.

FUNCTIONING OF THE SHOOT APICAL MERISTEM

The shoot apical meristem is a key structure that ensures the development of plant aerial organs. Its spatial organization, size, and activity are tightly regulated by a network of signaling cascades: EPFL peptides also participate in the process.

In *A. thaliana*, the EPFL1, EPFL2, EPFL4, and EPFL6 peptides are preferentially expressed in the periphery of the shoot apical meristem and within the boundary region between the meristem and leaf primordia [48]. Meanwhile, the ER, ERL1, and ERL2 receptors are active in the central zone of the meristem, suggesting that they are involved in the spatial regulation of meristem cell division and differentiation. The *EPFL1/2/4/6* and *ERf* knockout mutants share a phenotype: a larger meristem, fewer leaf primordia, and a reduced overall plant biomass [48]. These data support the hypothesis that EPFL peptides and ER receptors are functionally redundant when regulating the size of the shoot apical meristem and initiating leaf growth [60].

EPFL2 knockout mutants exhibit disrupted symmetry and irregular organ spacing, as well as changes in the auxin maxima number in the shoot apical meristem [49]. That is consistent with the results of another study that reported that *epfl2* mutants showed impaired shape of leaves and cotyledons due to change in auxin maxima number [50].

Furthermore, it has been demonstrated that treatment with synthetic EPFL4 and EPFL6 peptides ERf-dependently limits the lateral growth of the meristem by downregulating the expression of the key apical meristem regulators CLV3 (CLAVATA3) and WUS (WUSCHEL) [51]. The interaction between these pep-

tides and their receptors determines both the meristem size and its boundaries, thus contributing to the regulation of the number of initiated organs and ensuring normal plant development.

Hence, EPFL peptides play a pivotal role in the spatiotemporal regulation of the activity of the shoot apical meristem.

REGULATION OF THE LATERAL MERISTEM AND VASCULAR DEVELOPMENT

Regulation of lateral meristems and vascular tissue initiation are the key processes responsible for the proper development of both vegetative and reproductive organs. The receptor kinases ER and ERL1 participate in the regulation of lateral meristems in the hypocotyls and inflorescence of Arabidopsis [61–63]. Thus, expression of the *ER* and *ERL1* genes – but not *ERL2* – was detected in the central cylinder of the hypocotyl [61]. In comparison with wild-type plants, *er erl1* double mutants have thickened hypocotyls caused by excessive xylem development; this xylem has a higher proportion of cells with lignified cell walls [61]. In other words, ER and ERL1 prevent excessive xylem development in hypocotyls.

The ER and ERL1 kinases also regulate procambium development in inflorescence stems [62, 63]. The vascular bundle structure was impaired in *er erl1* double mutants: the procambium layer was discontinuous, and direct contact between xylem and phloem frequently occurred. It has been demonstrated that *ER* and *ERL1* are expressed in the xylem and phloem, phloem-specific expression of the *ER* gene being crucial for the regulation of the anatomical structure of the inflorescence stem [62]. It is hypothesized that the EPFL4 and EPFL6 peptides, which are expressed in the endodermis and bind to ER, are involved in this process. However, the *epfl4 epfl6* double mutant does not seem to have a disrupted vascular bundle structure. Therefore, it still remains an open question which EPFL peptides are involved in the regulation of the lateral meristem function.

Hence, it has been demonstrated that the ER and ERL1 receptors – and presumably their ligands – participate in the regulation of the formation and function of lateral meristems, as well as vascular tissue initiation.

DEVELOPMENT OF THE SERRATED LEAF MARGIN

Another role of EPFL peptides is the development of leaf margin serration [47]. In Arabidopsis, this process is regulated by the EPFL2 peptide, together with the ER and ERL1/2 receptors. *EPFL2* knockout mutants, as well as ERf double mutants, have no serrated leaf margin. Moreover, the interaction between EPFL2 and each of the three ERf has been confirmed by co-immunoprecipitation [47]. The *EPFL2* gene is expressed in growing leaves, except for the serrated tips and developing veins [47]. Interestingly, the *ERL2* expression contrasts with that of *EPFL2*: it has been detected on the serrated tips and in the veins, while *ER* and *ERL1* are expressed in the entire leaf blade. Hence, the EPFL2–ERf regulatory module suppresses the auxin response, confining it to a few cells on the tip of the developing serration.

THE DEVELOPMENT OF REPRODUCTIVE ORGANS

Angiosperms have evolutionarily developed complex and diverse reproductive structures, with EPF/EPFL peptides playing a crucial role in the formation of these structures, from regulating the inflorescence architecture to seed formation.

EPFL4/6, and to a lesser extent EPFL1/2 together with ERf, stimulate the elongation of inflorescences and pedicels in *A. thaliana* [53]. EPFL4/6, which act as ER ligands, are expressed in endodermal cells, while the *ER* gene is expressed in the epidermis, phloem, and xylem. However, signal reception in the phloem is essential for the development of a normal inflorescence architecture, since *ER* expression under the phloem-specific *SUC1* promoter restores the phenotype of *er* mutants. This effect has not been observed for *ER* expression under promoters active in the xylem and epidermis [53]. Hence, EPFL4/6 peptides are expressed in endodermal cells in plant inflorescences and transported to the phloem, where they bind to the ER and stimulate the growth of the inflorescence stem and pedicels [53]. Transcriptomic data demonstrate that many differentially expressed genes in *A. thaliana er-2* and *epfl4/6* mutants are components of the auxin and gibberellin response pathways. In particular, the expression of ARGOS, which promotes the growth of aerial organs [64], is suppressed, as well as the expression of the transcription factor WRKY15 [53].

The role played by EPFL peptides in the regulation of the inflorescence architecture has also been demonstrated in rice. Thus, *Os*EPFL5–9 regulate the panicle architecture and grain size. *Os*EPFL6–9 decrease the number of spikelets per panicle, while *Os*EPFL5 increase it, acting as an antagonist [65]. Further signaling in *Os*EPFL6–9 proceeds via the *Os*ER1 receptor and the MAPK cascade comprising *Os*MKKK10–*Os*MKK4–*Os*MPK6 [65, 66].

Peptides belonging to the EPFL family control not only the overall development of inflorescences, but also the development of male and female reproductive organs and the resulting fruits. In Arabidopsis plants, EPFL4/5/6 promote stamen filament elongation

by regulating cell proliferation [56, 57]. Impaired self-pollination and male sterility are observed in *epfl4/5/6* triple mutants, since stamens become significantly shorter than the pistil [57]. At lower temperatures, self-pollination is already impaired for the mutant carrying a single *epfl6* mutation [56]. ER mediates the elongation of both the stamens and the pistil [56].

EPFL1 in *T. aestivum* and EPFL6 in *Brassica napus* also appear to regulate the morphology of floral organs. Their overexpression in *A. thaliana* plants reduces the number of stamens and the stamen-to-pistil length ratio [67, 68].

EPFL peptides can also regulate *A. thaliana* silique development. EPFL9 recognized by ER promotes silique elongation, whereas *EPFL2* expressed in inter-ovule spaces increases the number of ovules per silique and ensures regular ovule spacing by interacting with the ERL2 and ERL1 receptors [46]. Interestingly, EPFL9 and EPFL2 may act as antagonists, since the *EPFL9* expression under the *EPFL2* promoter produce a phenotype similar to that of the *epfl2* mutant [46].

EPFL1/2/4/6 also control the initial stages of female gametophyte development. These peptides are needed for differentiation of a single megaspore mother cell (MMC), preventing both the initiation of multiple MMCs and their absence [54].

At later stages of ovule development, EPFL1–6 ensure proper envelopment of the nucellus by integuments [55]. The EPFL1–6, ER, and ERL1/2 genes are expressed at different ovule developmental stages, while mutations in these genes disrupt integument formation. In this process, SERK1/2/3 function as coreceptors: the interaction between SERK and ERf kinases is enhanced in the presence of exogenous EPFL4/6 peptides [55].

EPF/EPFL peptides control the awn development, an important agricultural trait of rice. In wild rice (*Oryza rufipogon*) the *EPFL1* gene is actively expressed in developing inflorescences and ensures the formation of longer awns and fewer grains per panicle [69]. Mutations altering the number of cysteine residues in *OsEPFL1* were detected in most awnless cultivars of rice *O. sativa*, and introduction of the *EPFL1* allele from African rice cultivar (*O. glaberrima*) leads to awned seeds in *O. sativa ssp. japonica* [69]. In the *O. sativa ssp. aus* cv. Kasalath, other *EPF/EPFL* genes are responsible for the awned phenotype: the *osepfl1* single mutant retains awns, whereas the *osepfl2* mutant is awnless and displays shorter grains, lower grain weights, and a decreasing number of cells along the longitudinal axis. *OsEPF2*, *OsEPFL7*, *OsEPFL9*, and *OsEPFL10* also contribute to awn development. Both the *OsEPFL1/GAD1/RAE2* and *OsEPFL2/9/10* genes are believed to have undergone selection during rice domestication [39, 69].

The functions of EPFL peptides in the reproductive development of plants are extremely diverse. The members of this family orchestrate the inflorescence architecture, growth of floral organs, and proper formation of the female gametophyte.

ABIOTIC STRESS

In recent years, multiple studies have concentrated on the identification of EPF/EPFL genes in various crop species. The promoter regions of these genes have been often found to contain the *cis*-regulatory elements associated with responses to stress factors and phytohormones [33, 34, 36, 40, 41]. Moreover, it has been experimentally verified that these factors regulate the expression of individual EPF/EPFL genes. This suggests that EPF/EPFL peptides may contribute to plant tolerance to environmental stress.

For example, *EPFL8* expression is upregulated after treatment of maize plants with abscisic acid (ABA), methyl jasmonate, and salicylic acid, while expression of a number of other *EPFL* genes is downregulated under the same conditions [34]. Furthermore, water deficit can simultaneously alter the expression of several *EPFL* genes, indirectly demonstrating that they are possibly involved in the regulation of the drought response [34, 70]. Rye has both osmotic stress-induced and osmotic stress-repressed *EPFL* genes, as well as two heat-inducible *EPFL* genes [40]. A significant decline in the expression of seven *EPF* genes in rapeseed in response to salt stress was demonstrated in [37]. *EPFL* genes differentially expressed in response to osmotic stress have also been identified in sorghum, potato, poplar, and apple [33, 36, 41, 71].

EPF1/2 are known to inhibit stomatal formation in *A. thaliana*, while *EPFL9* promotes it [10, 13, 45]. Stomatal density and transpiration intensity are responsible for the drought resistance of a plant. Comparison of the expression of *EPF/EPFL* genes in drought-tolerant and drought-sensitive apple (*Malus domestica*) cultivars has demonstrated that the expression of *MdEPF2*, an *AtEPF2* ortholog, is more strongly induced by drought in the leaves of tolerant cultivar [71]. Treatment with abscisic acid (ABA), a key regulator of the osmotic stress response, also induces *MdEPF2* expression. Tomato plants overexpressing *MdEPF2* were shown to exhibit enhanced tolerance to osmotic stress. Under drought conditions, these plants were characterized by greater biomass, higher photosynthetic rates and relative water content, lower levels of malondialdehyde (MDA, a marker of oxidative stress) and hydrogen peroxide, as well as higher activity of antioxidant enzymes compared to

that in wild-type plants [71]. The primary morphological effect of *MdEPF2* overexpression consisted in a decline in stomatal density, which can be considered a key reason behind the greater osmotic stress tolerance observed in these plants.

The physiological role of the *AtEPF2* ortholog, PdEPF2, identified in the poplar genome was studied previously [72]. Expression of *PdEPF2* is induced by drought and ABA. Arabidopsis plants overexpressing *PdEPF2* showed enhanced drought tolerance: their proline level and photosynthetic intensity were increased under osmotic stress conditions.

Four *EPF/EPFL* genes respond to drought in potato: *EPF4* is downregulated, while the other three genes are upregulated [36]. Plants with either *EPF4* knockdown or *EPF4* overexpression were generated. Knockdown of this gene increased drought tolerance. Under drought stress these plants had a higher relative water content, proline level, and displayed activity of antioxidant enzymes (SOD, POD, and CAT), along with a lower MDA level than in wild-type plants. Conversely, the opposite effects were observed under drought conditions in plants overexpressing *EPF4* [36]. Altered *EPF4* expression affected the stomatal density, which was lower in *EPF4* knockdown plants and higher in plants overexpressing *EPF4*. The negative role of EPF4 in the regulation of the osmotic stress response can possibly be associated with its effect on stomatal formation.

Taken together genomic and physiological data obtained for various agricultural crops, it can be concluded that *EPF/EPFL* peptides are potentially involved in plant responses to abiotic stresses, primarily to drought. Regulation of stomatal density and transpiration are the most frequently proposed mechanisms of action for these peptides; however, other mechanisms cannot be ruled out. Different members of this family can play both a positive and negative regulatory role, which underscores the functional diversity of EPF/EPFL peptides and suggests that further research into their specific functions across different physiological contexts is needed.

BIOTIC STRESS

Differential expression of various EPF/EPFL members was shown in several plant species upon infection by phytopathogenic fungi. Thus, infection of moss *P. patens* with the pathogenic fungus *Botrytis cinerea* significantly downregulates expression of the six genes encoding the predicted EPFL peptides [73]. It was demonstrated that the expression of the *EPFL1–6* and *EPFL9* genes in *A. thaliana* increases after inoculation with *Sclerotinia sclerotiorum*, while the expression of other members of the *EPF/EPFL* family remains unaltered [52]. Meanwhile, biotic stress appeared to have different effects on the expression of the *EPF/EPFL* genes in tomato *Solanum lycopersicum* plants. Thus, infection with the phytopathogen *Fusarium oxysporum* f. sp. *lycopersici* induces the expression of *SlEPF7* and decreases the expression of *SlEPF1/5*. Treatment with elicitors from a non-pathogenic for tomato *F. sambicinum* strain increases *SlEPF6/7* expression and decreases that of *SlEPF3/5* [74].

Simultaneous changes in the expression level of several *EPF/EPFL* genes upon interaction with phytopathogens suggest that peptides belonging to this family can coordinately regulate plant defense mechanisms. Thus, the growth of *S. sclerotiorum* and H_2O_2 generation were shown to increase significantly in Arabidopsis *epfl1,2,4,6* multiple mutants, whereas single mutants did not differ from wild-type plants [52]. Furthermore, pathogen-induced expression of the genes belonging to the *YODA DOWNSTREAM (YDD)* group was significantly reduced in the *epfl1,2,4,6* mutants. *YDD* is a group of genes positively regulated in constitutively active *YODA* mutants [52]. On the other hand, inducible *EPF1/2* expression in *A. thaliana* did not enhance plant resistance to the necrotrophic fungus *Plectosphaerella cucumerina* [75]. Many pathogens are known to penetrate into plant tissues through stomata; therefore, the weakened resistance of *ERf* mutants can plausibly be attributed to the increased stomatal density. Thus, treatment with EPFL9 increases the stomatal density and exacerbates the symptoms of infection [76].

Hence, data on the involvement of *EPF/EPFL* peptides in the regulation of the biotic stress response are extremely sparse. Meanwhile, it has been repeatedly demonstrated that receptors and components of the *EPF/EPFL* peptide signaling pathway are involved in ensuring phytopathogen resistance. Thus, *er* mutants were characterized by reduced resistance to the bacterium *Ralstonia solanacearum* [77], oomycete *Pythium irregulare* [78], as well as the pathogenic fungi *Verticillium longisporum* [79], *S. sclerotiorum* [80], and *P. cucumerina* [81, 82]. Additional knockout of the *ERL1/2* and *TMM* genes exacerbated infection symptoms [75, 80].

However, the reduced resistance to *R. solanacearum* after inoculation through damaged roots [77] indicates that the susceptibility of *er* mutants may be caused not only by the increased stomatal density but also by an impaired defense response. This is further supported by the downregulated expression of the pathogen-inducible genes *WRKY33*, *WRKY53*, *CYP79B2*, and *CYP81F2* in *er*, *bak1*, and *er bak1* mutants [75].

Meanwhile, the activity of ER was shown to have no effect on the expression of the genes induced by flg22, a 22-amino acid flagellin-derived epitope [75]. Furthermore, *er* mutants were no less resistant to infection by *B. cinerea*, *F. oxysporum* f. sp. *conglutinans*, and *Peronospora parasitica* than wild-type plants [81]. Therefore, ER is not always required for pathogen resistance. This can be associated with the functional redundancy of EPFL receptors.

ER regulates the Arabidopsis response to *S. sclerotiorum* infection via affecting binding between the WRKY33 transcription factor and promoters of the *YDD* genes [80]. This process involves the chromatin remodeling complex SWR1 and the ER–MPK6–WRKY33 regulatory module. SWR1 promotes the binding of the W-box transcription factor WRKY33 to promoters and activates expression of the YDD genes, which are necessary for resistance to *S. sclerotiorum* infection [80, 83].

Since EPF/EPFL peptides are primarily known as regulators of stomatal development, their role in stress adaptation is often attributed to their impact on stomatal density. However, the role of this peptide family under stress conditions appears to be broader and needs further investigation.

CONCLUSIONS

Despite significant progress in understanding EPF/EPFL peptides functions, knowledge gaps still remain. Thus, the vast majority of functional studies on EPF/EPFL have been conducted on the model plant *A. thaliana*. Furthermore, although homologs of the *EPF/EPFL* genes have been identified across different groups of angiosperms, their function need more comprehensive investigation. This issue is particularly relevant in the context of the plant phylogenetic diversity, since the results obtained for Arabidopsis may not fully represent the range of biological functions of EPFL peptides in other plant species.

Additional challenges arise from the functional redundancy of these peptides: multiple EPF/EPFL family members can partially compensate for each other, thus complicating the assessment of individual contributions. So, much of the research analyzes receptor mutants, which are also partially redundant, but their number is significantly smaller.

It has been demonstrated so far that *EPFL* expression can be altered in response to biotic and abiotic stresses; however, the association between peptide-mediated regulation and plant adaptive responses still needs to be fully elucidated.

Modulating the activity of EPFL peptides and their receptors may be used to optimize morphogenesis, enhance stress tolerance, and, therefore, improve cultivated crops. ●

This work was supported by the Russian Science Foundation (project No. 23-74-10048).

REFERENCES

1. Fukuda H, Hardtke CS. Peptide Signaling Pathways in Vascular Differentiation. *Plant Physiol.* 2020;182(4):1636–1644. doi: 10.1104/pp.19.01259
2. Mamaeva A, Makeeva A, Ganaeva D. The Small Key to the Treasure Chest: Endogenous Plant Peptides Involved in Symbiotic Interactions. *Plants (Basel).* 2025;14(3):378. doi: 10.3390/plants14030378
3. Pearce G, Strydom D, Johnson S, Ryan CA. A Polypeptide from Tomato Leaves Induces Wound-Inducible Proteinase Inhibitor Proteins. *Science.* 1991;253(5022):895–897. doi: 10.1126/science.253.5022.895
4. Tavormina P, De Coninck B, Nikonorova N, De Smet I, Cammue BP. The Plant Peptidome: An Expanding Repertoire of Structural Features and Biological Functions. *Plant Cell.* 2015;27(8):2095–2118. doi: 10.1105/tpc.15.00440
5. Stintzi A, Schaller A. Biogenesis of post-translationally modified peptide signals for plant reproductive development. *Curr Opin Plant Biol.* 2022;69:102274. doi: 10.1016/j.pbi.2022.102274
6. Feng YZ, Zhu QF, Xue J, Chen P, Yu Y. Shining in the dark: the big world of small peptides in plants. *aBIOTECH.* 2023;4(3):238–256. doi: 10.1007/s42994-023-00100-0
7. Gancheva MS, Malovichko YV, Poliushkevich LO, Dodueva IE, Lutova LA. Plant Peptide Hormones. *Russ J Plant Physiol.* 2019;66:171–189. doi: 10.1134/S1021443719010072
8. Okada T, Yoshizumi H, Terashima Y. A Lethal Toxic Substance for Brewing Yeast in Wheat and Barley: Part I. Assay of Toxicity on Various Grains, and Sensitivity of Various Yeast StrainsPart II. Isolation and Some Properties of Toxic Principle. *J Agric Biol Chem.* 1970;34(7):1084–1094. doi: 10.1080/00021369.1970.10859736
9. van der Weerden NL, Bleackley MR, Anderson MA. Properties and mechanisms of action of naturally occurring antifungal peptides. *Cell Mol Life Sci.* 2013;70(19):3545–3570. doi: 10.1007/s00018-013-1260-1
10. Hara K, Kajita R, Torii KU, Bergmann DC, Kakimoto T. The secretory peptide gene EPF1 enforces the stomatal one-cell-spacing rule. *Genes Dev.* 2007;21(14):1720–1725. doi: 10.1101/gad.1550707
11. Sugano SS, Shimada T, Imai Y, et al. Stomagen positively regulates stomatal density in Arabidopsis. *Nature.* 2010;463(7278):241–244. doi: 10.1038/nature08682

12. Maróti G, Downie JA, Kondorosi É. Plant cysteine-rich peptides that inhibit pathogen growth and control rhizobial differentiation in legume nodules. *Curr Opin Plant Biol.* 2015;26:57–63. doi: 10.1016/j.pbi.2015.05.031
13. Hunt L, Gray JE. The Signaling Peptide EPF2 Controls Asymmetric Cell Divisions during Stomatal Development. *Curr Biol.* 2009;19(10):864–869. doi: 10.1016/j.cub.2009.03.069
14. Richardson LGL, Torii KU. Take a deep breath: peptide signalling in stomatal patterning and differentiation. *J Exp Bot.* 2013;64(17):5243–5251. doi: 10.1093/jxb/ert246
15. Lee JS, Kuroha T, Hnilova M, et al. Direct interaction of ligand–receptor pairs specifying stomatal patterning. *Genes Dev.* 2012;26(2):126–136. doi: 10.1101/gad.179895.111
16. Silverstein KAT, Moskal WA Jr, Wu HC, et al. Small cysteine-rich peptides resembling antimicrobial peptides have been under-predicted in plants. *Plant J.* 2007;51(2):262–280. doi: 10.1111/j.1365-313X.2007.03136.x
17. Finkina EI, Melnikova DN, Bogdanov IV, Ovchinnikova TV. Peptides of the innate immune system of plants. Part I. Structure, biological activity and mechanisms of action. *Rus J Bioorgan Chem.* 2019;45(1):3–16. doi: 10.1134/S013234231901007X
18. Finkina EI, Melnikova DN, Bogdanov IV, Ovchinnikova TV. Peptides of the innate immune system of plants. Part II. Biosynthesis, biological functions, and possible practical applications. *Rus J Bioorgan Chem.* 2019;45(2):55–65. doi: 10.1134/S1068162019020043
19. Ohki S, Takeuchi M, Mori M. The NMR structure of stomagen reveals the basis of stomatal density regulation by plant peptide hormones. *Nat Commun.* 2011;2:512. doi: 10.1038/ncomms1520
20. Kondo T, Kajita R, Miyazaki A, et al. Stomatal Density is Controlled by a Mesophyll-Derived Signaling Molecule. *Plant Cell Physiol.* 2010;51(1):1–8. doi: 10.1093/pcp/pcp180
21. Lin G, Zhang L, Han Z, et al. A receptor-like protein acts as a specificity switch for the regulation of stomatal development. *Genes Dev.* 2017;31(9):927–938. doi: 10.1101/gad.297580.117
22. Rowe MH, Bergmann DC. Complex signals for simple cells: the expanding ranks of signals and receptors guiding stomatal development. *Curr Opin Plant Biol.* 2010;13(5):548–555. doi: 10.1016/j.pbi.2010.06.002
23. Hara K, Yokoo T, Kajita R, et al. Epidermal cell density is autoregulated via a secretory peptide, EPIDERMAL PATTERNING FACTOR 2 in Arabidopsis leaves. *Plant Cell Physiol.* 2009;50(6):1019–1031. doi: 10.1093/pcp/pcp068
24. Tabata R, Sawa S. Maturation processes and structures of small secreted peptides in plants. *Front Plant Sci.* 2014;5:311. doi: 10.3389/fpls.2014.00311
25. Olsson V, Joos L, Zhu S, Gevaert K, Butenko MA, De Smet I. Look Closely, the Beautiful May Be Small: Precursor-Derived Peptides in Plants. *Annu Rev Plant Biol.* 2019;70:153–186. doi: 10.1146/annurev-arplant-042817-040413
26. Abramson J, Adler J, Dunger J, et al. Accurate structure prediction of biomolecular interactions with AlphaFold 3. *Nature.* 2024;630(8016):493–500. doi: 10.1038/s41586-024-07487-w
27. Wang H, Ngwenyama N, Liu Y, Walker JC, Zhang S. Stomatal Development and Patterning Are Regulated by Environmentally Responsive Mitogen-Activated Protein Kinases in Arabidopsis. *Plant Cell.* 2007;19(1):63–73. doi: 10.1105/tpc.106.048298
28. Takata N, Yokota K, Ohki S, Mori M, Taniguchi T, Kurita M. Evolutionary relationship and structural characterization of the EPF/EPFL gene family. *PLoS One.* 2013;8(6):e65183. doi: 10.1371/journal.pone.0065183
29. Bowman JL, Kohchi T, Yamato KT, et al. Insights into Land Plant Evolution Garnered from the Marchantia polymorpha Genome. *Cell.* 2017;171(2):287–304.e15. doi: 10.1016/j.cell.2017.09.030
30. Rychel AL, Peterson KM, Torii KU. Plant twitter: ligands under 140 amino acids enforcing stomatal patterning. *J Plant Res.* 2010;123(3):275–280. doi: 10.1007/s10265-010-0330-9
31. Caine RS, Chater CC, Kamisugi Y, et al. An ancestral stomatal patterning module revealed in the non-vascular land plant Physcomitrella patens. *Development.* 2016;143(18):3306–3314. doi: 10.1242/dev.135038
32. Caine RS, Chater CCC, Fleming AJ, Gray JE. Stomata and Sporophytes of the Model Moss Physcomitrium patens. *Front Plant Sci.* 2020;11:643. doi: 10.3389/fpls.2020.00643
33. Jia M, Wang Y, Jin H, et al. Comparative Genomics Analysis of the Populus Epidermal Pattern Factor (EPF) Family Revealed Their Regulatory Effects in Populus euphratica Stomatal Development. *Int J Mol Sci.* 2024;25(18):10052. doi: 10.3390/ijms251810052
34. Li P, Zhao Z, Wang W, et al. Genome-wide analyses of member identification, expression pattern, and protein–protein interaction of EPF/EPFL gene family in Gossypium. *BMC Plant Biol.* 2024;24(1):554. doi: 10.1186/s12870-024-05262-7
35. McElwain JC, Chaloner WG. Stomatal Density and Index of Fossil Plants Track Atmospheric Carbon Dioxide in the Palaeozoic. *Annals Bot.* 1995;76(4):389–395. doi: 10.1006/anbo.1995.1112
36. Qiao R, Yang J, Deng Y, et al. Genome-Wide Identification of Epidermal Pattern Factor (EPF) Gene Family in Potato and Functional Characterization of StEPF4 in Regulating Drought Stress. *Agronomy.* 2024;14(12):2948. doi: 10.3390/agronomy14122948
37. Wang S, Wang W, Chen J, et al. Comprehensive Identification and Expression Profiling of Epidermal Pattern Factor (EPF) Gene Family in Oilseed Rape (Brassica napus L.) under Salt Stress. *Genes.* 2024;15(7):912. doi: 10.3390/genes15070912
38. Liu S, Chen T, Li X, Cui J, Tian Y. Genome-wide identification and expression analysis of EPF/EPFL gene family in Populus trichocarpa. *Front Genet.* 2024;15:1432376. doi: 10.3389/fgene.2024.1432376
39. Xiong L, Huang Y, Liu Z, et al. Small EPIDERMAL PATTERNING FACTOR-LIKE2 peptides regulate awn development in rice. *Plant Physiol.* 2022;190(1):516–531. doi: 10.1093/plphys/kiac278
40. Zhiling L, Wenhua D, Fangyuan Z. Genome-wide identification and phylogenetic and expression pattern analyses of EPF/EPFL family genes in the Rye (Secale cereale L.). *BMC Genomics.* 2024;25(1):532. doi: 10.1186/s12864-024-10425-9
41. Jiao Z, Wang J, Shi Y, et al. Genome-Wide Identification and Analysis of the EPF Gene Family in Sorghum bicolor (L.) Moench. *Plants (Basel).* 2023;12(22):3912. doi: 10.3390/plants12223912
42. Liu R, Xu K, Li Y, et al. Investigation on the Potential Functions of ZmEPF/EPFL Family Members in Response to Abiotic Stress in Maize. *Int J Mol Sci.* 2024;25(13):7196. doi: 10.3390/ijms25137196
43. Wei D, Chang P, Liu JY, et al. Genome-wide identification of EPF/EPFL gene family in wheat (Triticum

aestivum) and analysis of TaEPF1-2B associated with stomatal traits. *J Triticeae Crop.* 2021;41(11):1317–1329. doi: 10.7606/j.issn.1009-1041.2021.11.01
44. Lee JS, Hnilova M, Maes M, et al. Competitive binding of antagonistic peptides fine-tunes stomatal patterning. *Nature.* 2015;522(7557):439–443. doi: 10.1038/nature14561
45. Hunt L, Bailey KJ, Gray JE. The signalling peptide EPFL9 is a positive regulator of stomatal development. *New Phytol.* 2010;186(3):609–614. doi: 10.1111/j.1469-8137.2010.03200.x
46. Kawamoto N, Carpio DPD, Hofmann A, et al. A Peptide Pair Coordinates Regular Ovule Initiation Patterns with Seed Number and Fruit Size. *Curr Biol.* 2020;30(22):4352–4361.e4. doi: 10.1016/j.cub.2020.08.050
47. Tameshige T, Ikematsu S, Torii KU, Uchida N. Stem development through vascular tissues: EPFL–ERECTA family signaling that bounces in and out of phloem. *J Exp Bot.* 2017;68(1):45–53. doi: 10.1093/jxb/erw447
48. Kosentka PZ, Overholt A, Maradiaga R, Mitoubsi O, Shpak ED. EPFL Signals in the Boundary Region of the SAM Restrict Its Size and Promote Leaf Initiation. *Plant Physiol.* 2019;179(1):265–279. doi: 10.1104/pp.18.00714
49. Fujihara R, Uchida N, Tameshige T, et al. The boundary-expressed EPIDERMAL PATTERNING FACTOR-LIKE2 gene encoding a signaling peptide promotes cotyledon growth during Arabidopsis thaliana embryogenesis. *Plant Biotechnol (Tokyo).* 2021;38(3):317–322. doi: 10.5511/plantbiotechnology.21.0508a
50. Kimura Y, Tasaka M, Torii KU, Uchida N. ERECTA-family genes coordinate stem cell functions between the epidermal and internal layers of the shoot apical meristem. *Development.* 2018;145(1):dev156380. doi: 10.1242/dev.156380
51. Zhang L, DeGennaro D, Lin G, Chai J, Shpak ED. ERECTA family signaling constrains CLAVATA3 and WUSCHEL to the center of the shoot apical meristem. *Development.* 2021;148(5):dev189753. doi: 10.1242/dev.189753
52. Huang Y, Chai M, Xi X, et al. Functional analysis of EPF/EPFL genes in Arabidopsis resistance to Sclerotinia sclerotiorum. *J Fujian Agric For Univ (Nat Sci Ed).* 2022;51(4):486–492.
53. Uchida N, Lee JS, Horst RJ, et al. Regulation of inflorescence architecture by intertissue layer ligand–receptor communication between endodermis and phloem. *Proc Natl Acad Sci U S A.* 2012;109(16):6337–6342. doi: 10.1073/pnas.1117537109
54. Cai H, Huang Y, Liu L, et al. Signaling by the EPFL-ERECTA family coordinates female germline specification through the BZR1 family in Arabidopsis. *Plant Cell.* 2023;35(5):1455–1473. doi: 10.1093/plcell/koad032
55. Li M, Lv M, Wang X, et al. The EPFL–ERf–SERK signaling controls integument development in Arabidopsis. *New Phytol.* 2023;238(1):186–201. doi: 10.1111/nph.18701
56. Negoro S, Hirabayashi T, Iwasaki R, Torii KU, Uchida N. EPFL peptide signalling ensures robust self-pollination success under cool temperature stress by aligning the length of the stamen and pistil. *Plant Cell Environ.* 2023;46(2):451–463. doi: 10.1111/pce.14498
57. He Y, He X, Wang X, et al. An EPFL peptide signaling pathway promotes stamen elongation via enhancing filament cell proliferation to ensure successful self-pollination in Arabidopsis thaliana. *New Phytol.* 2023;238(3):1045–1058. doi: 10.1111/nph.18806
58. Jangra R, Brunetti SC, Wang X, et al. Duplicated antagonistic EPF peptides optimize grass stomatal initiation. *Development.* 2021;148(16):dev199780. doi: 10.1242/dev.199780
59. Caine RS, Chater CC, Kamisugi Y, et al. An ancestral stomatal patterning module revealed in the non-vascular land plant Physcomitrella patens. *Development.* 2016;143(18):3306–3314. doi: 10.1242/dev.135038
60. Uzair M, Urquidi Camacho RA, Liu Z, et al. An updated model of shoot apical meristem regulation by ERECTA family and CLAVATA3 signaling pathways in Arabidopsis. *Development.* 2024;151(12):dev202870. doi: 10.1242/dev.202870
61. Ikematsu S, Tasaka M, Torii KU, Uchida N. ERECTA-family receptor kinase genes redundantly prevent premature progression of secondary growth in the Arabidopsis hypocotyl. *New Phytol.* 2017;213(4):1697–1709. doi: 10.1111/nph.14335
62. Uchida N, Tasaka M. Regulation of plant vascular stem cells by endodermis-derived EPFL-family peptide hormones and phloem-expressed ERECTA-family receptor kinases. *J Exp Bot.* 2013;64(17):5335–5343. doi: 10.1093/jxb/ert196
63. Yuan B, Wang H. Peptide Signaling Pathways Regulate Plant Vascular Development. *Front Plant Sci.* 2021;12:719606. doi: 10.3389/fpls.2021.719606
64. Hu Y, Xie Q, Chua NH. The Arabidopsis Auxin-Inducible Gene ARGOS Controls Lateral Organ Size. *Plant Cell.* 2003;15(9):1951–1961. doi: 10.1105/tpc.013557
65. Guo T, Lu ZQ, Xiong Y, et al. Optimization of rice panicle architecture by specifically suppressing ligand–receptor pairs. *Nat Commun.* 2023;14(1):1640. doi: 10.1038/s41467-023-37326-x
66. Guo T, Lu ZQ, Shan JX, Ye WW, Dong NQ, Lin HX. ERECTA1 Acts Upstream of the OsMKKK10-OsMKK4-OsMPK6 Cascade to Control Spikelet Number by Regulating Cytokinin Metabolism in Rice. *Plant Cell.* 2020;32(9):2763–2779. doi: 10.1105/tpc.20.00351
67. Sun Q, Qu J, Yu Y, et al. TaEPFL1, an EPIDERMAL PATTERNING FACTOR-LIKE (EPFL) secreted peptide gene, is required for stamen development in wheat. *Genetica.* 2019;147(2):121–130. doi: 10.1007/s10709-019-00061-7
68. Huang Y, Tao Z, Liu Q, et al. BnEPFL6, an EPIDERMAL PATTERNING FACTOR-LIKE (EPFL) secreted peptide gene, is required for filament elongation in Brassica napus. *Plant Mol Biol.* 2014;85(4–5):505–517. doi: 10.1007/s11103-014-0200-2
69. Jin J, Hua L, Zhu Z, et al. GAD1 Encodes a Secreted Peptide That Regulates Grain Number, Grain Length, and Awn Development in Rice Domestication. *Plant Cell.* 2016;28(10):2453–2463. doi: 10.1105/tpc.16.00379
70. Xia H, Wang Q, Chen Z, et al. Identification and Functional Analysis of the EPF/EPFL Gene Family in Maize (Zea mays L.): Implications for Drought Stress Response. *Agronomy.* 2024;14(8):1734. doi: 10.3390/agronomy14081734
71. Jiang Q, Yang J, Wang Q, Zhou K, Mao K, Ma F. Overexpression of MdEPF2 improves water use efficiency and reduces oxidative stress in tomato. *Environ Exp Bot.* 2019;162:321–332. doi: 10.1016/j.envexpbot.2019.03.009
72. Liu S, Wang C, Jia F, et al. Secretory peptide PdEPF2 enhances drought tolerance by modulating stomatal density and regulates ABA response in transgenic Arabidopsis thaliana. *Plant Cell Tissue Organ Cult.* 2016;125(3):419–431. doi: 10.1007/s11240-016-0957-x
73. Lyapina I, Ganaeva D, Rogozhin EA, et al. Comparative analysis of small secreted peptide signaling during defense response: insights from vascular and non-vas-

cular plants. *Physiol Plant*. 2025;177(2):e70147. doi: 10.1111/ppl.70147
74. Slezina MP, Istomina EA, Korostyleva TV, et al. Molecular Insights into the Role of Cysteine-Rich Peptides in Induced Resistance to Fusarium oxysporum Infection in Tomato Based on Transcriptome Profiling. *Int J Mol Sci*. 2021;22(11):5741. doi: 10.3390/ijms22115741
75. Jordá L, Sopeña-Torres S, Escudero V, et al. ERECTA and BAK1 Receptor Like Kinases Interact to Regulate Immune Responses in Arabidopsis. *Front Plant Sci*. 2016;7:897. doi: 10.3389/fpls.2016.00897
76. Tateda C, Obara K, Abe Y, et al. The Host Stomatal Density Determines Resistance to Septoria gentianae in Japanese Gentian. *Mol Plant Microbe Interact*. 2019;32(4):428–436. doi: 10.1094/MPMI-05-18-0114-R
77. Godiard L, Sauviac L, Torii KU, et al. ERECTA, an LRR receptor-like kinase protein controlling development pleiotropically affects resistance to bacterial wilt. *Plant J*. 2003;36(3):353–365. doi: 10.1046/j.1365-313X.2003.01877.x
78. Adie BAT, Pérez-Pérez J, Pérez-Pérez MM, et al. ABA Is an Essential Signal for Plant Resistance to Pathogens Affecting JA Biosynthesis and the Activation of Defenses in Arabidopsis. *Plant Cell*. 2007;19(5):1665–1681. doi: 10.1105/tpc.106.048041
79. Häffner E, Karlovsky P, Splivallo R, Traczewska A, Diederichsen E. ERECTA, salicylic acid, abscisic acid, and jasmonic acid modulate quantitative disease resistance of Arabidopsis thaliana to Verticillium longisporum. *BMC Plant Biol*. 2014;14:85. doi: 10.1186/1471-2229-14-85
80. Cai H, Huang Y, Chen F, et al. ERECTA signaling regulates plant immune responses via chromatin-mediated promotion of WRKY33 binding to target genes. *New Phytol*. 2021;230(2):737–756. doi: 10.1111/nph.17200
81. Llorente F, Alonso-Blanco C, Sánchez-Rodriguez C, Jorda L, Molina A. ERECTA receptor-like kinase and heterotrimeric G protein from Arabidopsis are required for resistance to the necrotrophic fungus Plectosphaerella cucumerina. *Plant J*. 2005;43(2):165–180. doi: 10.1111/j.1365-313X.2005.02440.x
82. Sánchez-Rodríguez C, Estévez JM, Llorente F, et al. The ERECTA Receptor-Like Kinase Regulates Cell Wall–Mediated Resistance to Pathogens in Arabidopsis thaliana. *Mol Plant Microbe Interact*. 2009;22(8):953–963. doi: 10.1094/MPMI-22-8-0953
83. Sopeña-Torres S, Jordá L, Sánchez-Rodríguez C, et al. YODA MAP3K kinase regulates plant immune responses conferring broad-spectrum disease resistance. *New Phytol*. 2018;218(2):661–680. doi: 10.1111/nph.15007

Mitophagy in Age-Dependent Neurodegeneration

V. S. Sukhorukov[1,2], A. V. Egorova[1,2*], A. S. Romanenko[1,2], M. S. Ryabova[1,2], A. P. Krasilnikova[3]
[1]Russian Center of Neurology and Neurosciences, Moscow, 125367 Russia
[2]Pirogov Russian National Research Medical University, Moscow, 117513 Russia
[3]M.V. Lomonosov Moscow State University, Moscow, 119234 Russia
*E-mail: AV_Egorova@bk.ru
Received April 18, 2025; in final form, July 02, 2025
DOI: 10.32607/actanaturae.27674

ABSTRACT **Mitochondrial dysfunction is one of the pathogenetic mechanisms of neuronal damage during aging. The high energy dependence of neurons makes them particularly vulnerable to age-related changes accompanied by oxidative stress and impaired energy metabolism. The maintenance of a pool of functional mitochondria is regulated by mitophagy, which ensures the utilization of damaged organelles, thereby preventing the progression of mitochondrial dysfunction. Brain aging is accompanied by a reduced level of activity of metabolic processes, aggravated mitochondrial dysfunction, and an increased risk of developing neurodegenerative diseases such as Alzheimer's disease and Parkinson's disease. This review highlights the molecular and signaling pathways of mitophagy and its dysregulation during physiological and pathological aging, which is of particular interest for identifying pharmaceutical targets and developing potential therapies for neurodegenerative conditions.**
KEYWORDS **mitophagy, mitochondria, aging, Alzheimer's disease, Parkinson's disease.**
ABBREVIATIONS **AD – Alzheimer's disease; PD – Parkinson's disease.**

INTRODUCTION

The age-related alterations inevitably developing in the brain during aging pose a significant societal challenge, as they are frequently accompanied by the onset of cognitive impairment and underlie the pathogenesis of a number of neurodegenerative diseases [1, 2].

Mitochondria, organelles with a broad range of functions aimed at coordinating the intracellular homeostasis, play a particularly crucial role in maintaining adequate neuronal function upon the age-related and pathological involution of the brain [3]. Mitochondrial dysfunction significantly increases the risk of one developing age-related neurodegenerative diseases because of the energy deficit that develops in nervous tissue, as well as the overproduction of reactive oxygen species, initiation of apoptosis and inflammatory responses, and the disruption to synaptic transmission [4].

The structural and functional characteristics of mitochondria are consistently under rapid transformation, their key stages being collectively known as "the mitochondrial dynamics." Mitochondrial dynamics involve key processes such as biogenesis, fission, and fusion of these organelles, even as they also require an adequate system for their elimination known as mitophagy [5].

Mitophagy is a process that aims to dispose of damaged organelles and regulate the cellular content of mitochondria within the boundaries required for maintaining a metabolic balance [6]. It involves the swallowing of defective mitochondria by specialized vesicles, followed by their fusion with the lysosomes responsible for the degradation of defective organelles [7–9].

Mitophagy is critically important in maintaining a functional pool of neurons because of the unique structure and function of the nervous tissue, its voracious appetite for energy, and the need for a continuous renewal of the components of the cytoplasm.

Brain aging is accompanied by a decline in mitophagic activity, which aggravates mitochondrial dysfunction, and increases the risk of developing neurodegenerative diseases [10, 11]. According to current understanding, the accumulation of neurotoxic protein aggregates, which play a pivotal role in the patho-

genesis of this pathology, is attributed to mutations in the genes coding for mitophagy-initiating proteins (PINK1, Parkin, and DJ-1) [12].

Despite the relevance and high societal significance of this issue, many aspects of brain aging remain insufficiently studied. Elucidating the role played by mitochondrial dysfunction and identifying the key markers of mitophagy in age-related involution are topical problems in modern gerontology and a much-needed step in identifying novel pharmaceutical neurodegeneration targets.

THE GENERAL DATA ON THE MECHANISMS OF MACROAUTOPHAGY. MITOPHAGY

Large intracellular substrates (aged and damaged organelles in particular) are removed through macroautophagy – the type of autophagy in which the identification and further degradation of defective structures take place within the autophagosome, which is formed via fusion of a lysosome and a phagophore, a double-membraned organelle. Autophagic processes within the cell are triggered by various factors such as the accumulation of pathological protein aggregates, exposure to hypoxia, nutrient deficiency, and oxidative stress. Numerous proteins encoded by autophagy-related genes (*Atg*) are involved in the perception of autophagy initiation signals and autophagosome formation [13]. The LC3 (ATG8) protein, which resides on the phagophore membrane and binds to a pre-ubiquitinated target via adaptor proteins, plays a special role in autophagosome degradation [14]. The best-studied autophagy adaptors include p62 (the key adaptor protein in nearly all mitophagy pathways), NBR1 (involved in peroxisome degradation), NDP52 (involved in ubiquitin-dependent mitophagy), as well as TAX1BP1 and optineurin (OPTN), which are required for ubiquitin-dependent mitophagy and the autophagy of protein aggregates [15].

The plasma membrane and cellular organelles (the Golgi complex, the endoplasmic reticulum, and mitochondria) are the potential sources of phagophore formation.

De novo assembly of the phagophore is initiated by two cytoplasmic protein complexes: PI3K (class III PI3K complex I) and the Atg1/ULK1 complex, which are comprised of catalytic and regulatory subunits [6, 16, 17]. Phosphorylation of the PI3K class III complex induces the local production of the membrane phospholipid PI3P (phosphatidylinositol 3-phosphate) in specialized endoplasmic reticulum subdomains known as omegasomes [18]. PI3P is needed in order to recruit the phospholipid molecules involved in phagophore growth via binding of the effector proteins WIPI and DFCP. These proteins mediate the interplay between PI3P and the two conjugation systems, LC3/ATG7/ATG3 and ATG5/12/ATG16L1 [19]. At the next stage, autophagy-related (Atg) proteins are incorporated into the isolation membrane, resulting in phagophore formation [20, 21]. The conjugation systems are required not only for phagophore expansion, but also for the completion of autophagosome formation and cargo sequestration. Selective uptake of various targets is ensured by receptor proteins residing on the surface of an autophagy target through specialized autophagic adaptor proteins [22]. Despite their versatility, adaptors seem to utilize a common autophagy mechanism: recruitment of the ULK1/2 complex and binding to the FIP200 subunit (an adhesion protein) to initiate autophagosome formation [15, 23].

After substrate degradation in the autophagosome, macromolecules are released into the cytosol and they re-enter the metabolic processes in the cell [16, 24]. Autophagy is regulated by the two key signaling pathways:

(1) The PI3K/AKT/mTOR pathway inhibiting the autophagy and preventing autophagosome formation. The activity of mTORC1 (the mammalian target of rapamycin complex 1) is affected by the intracellular levels of amino acids, insulin, and growth factors.

(2) The AMPK signaling pathway that responds to the ATP level and is activated under hypoxic conditions [16, 25].

The roles played by other signaling molecules such as sirtuins, TFEB (transcription factor EB), etc., in the autophagy mechanisms are less studied and require detailed investigation.

Phagophore assembly is also regulated by mitochondrial proteins. Thus, the well-known protein Beclin 1, a component of the pro-autophagic class III PI3K complex involved in phagophore assembly, initiates Beclin 1-dependent autophagy at the levels of both the endoplasmic reticulum and mitochondria [26, 27].

Another autophagy initiator, the protein endophilin B1, can be recruited to the outer mitochondrial membrane under stress conditions, where it activates the aforementioned class III PI3K initiation complex by binding to the adaptor protein Beclin 1 [26].

Mitophagy is the selective degradation of mitochondria via autophagosome processing. The mitophagy is preceded by changes in the mitochondrial morphology. Thus, mitochondrial fission mediated by the DRP1 and Fis1 proteins ensures the peripheral fragmentation of mitochondria, isolating the damaged segments of the organelle to be subsequently eliminated [28].

The mechanism of classical mitophagy is based on the induction of mitochondrial membrane PTEN-induced putative kinase 1 (PINK1) and the Parkin

protein (PARK2), a cytosolic E3 ubiquitin ligase. Hence, the *PINK1* (*PARK6*) and *PARK2* genes encoding the proteins associated with the familial Parkinson's disease play a crucial role in mitochondrial quality control. In this case, the loss of the inner mitochondrial membrane potential accompanying damage to mitochondria is a signal for mitophagy activation. Known PINK1 substrates include ubiquitin and the ubiquitin-like domain of Parkin. Phosphorylation of these targets at a conserved serine residue (S65) induces Parkin activation, followed by absorbtion of damaged mitochondria and autophagosome formation [29] (*Fig. 1*).

Parkin translocation from the cytosol to the outer mitochondrial membrane is dependent on the PINK1 activity. In turn, Parkin catalyzes the ubiquitination and proteasomal degradation of various outer mitochondrial membrane proteins, including Drp1, Miro, and mitofusins 1 and 2 (MFN1/2). This mechanism blocks mitochondrial fusion, making it possible to isolate damaged organelles and initiate autophagy via a system of adaptor proteins.

Under hypoxic conditions and exposure to various toxic agents, mitophagy can proceed via a PINK1–Parkin-independent pathway through the following mitochondrial membrane receptors containing LIR motifs:

- The proteins AMBRA1, BNIP3, FUNDC1, and NIX on the outer mitochondrial membrane;
- Cardiolipin and PHB2 on the inner mitochondrial membrane.

Ubiquitination of these receptors is a signal for the cargo receptors p62/SQSTM1, NDP52, optineurin, etc., which bind to ubiquitin and the autophagosomal membrane protein LC3B, thereby mediating the mitophagy [30].

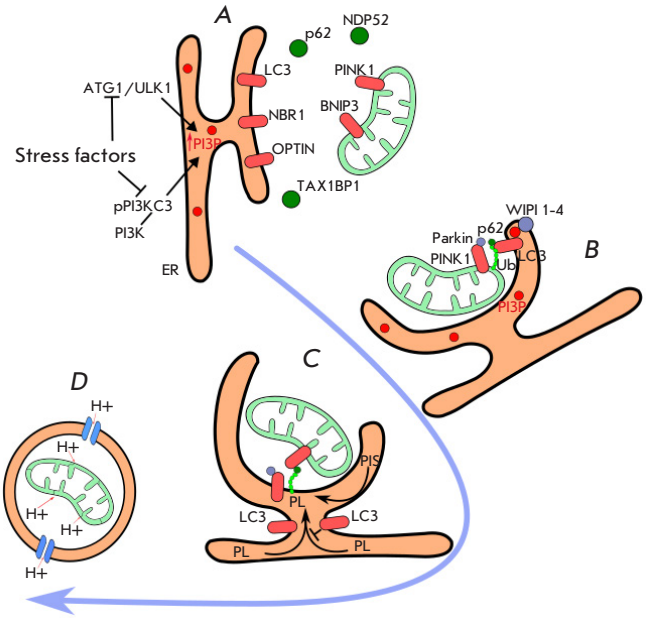

Fig. 1. The mechanism of mitophagy. Stages: (*A*) mitophagy initiation; (*B*) receptor interactions; (*C*) phagophore growth; (*D*) vesicle–lysosome fusion. Mitophagy initiation occurs under the influence of stress factors and is accompanied by the activation of ATG1/ULK1 and phosphorylation of PI3K, which induces PI3P production in the ER. PI3P is required for the binding of the effector WIPI proteins that interact with the LC3 conjugation system. The selective mitochondrial uptake is implemented with the participation of specialized adaptor proteins (TAX1BP1, NBP52, p62, OPTIN, and NBR1) (*A*). Next, Parkin and ubiquitin-mediated LC3 binding to PINK1 on the mitochondrial membrane occurs. By joining to PI3P WIPI 1–4 ensures interplay with LC3 and proper functioning of the complex (*B*). Phagophore growth takes place through the transfer of PLs from the ER lumen, with the participation of PI3P. Simultaneously, PIS is activated in the phagophore walls, initiating *de novo* phospholipid synthesis (*C*). LC3 ensures vesicle cleavage from the ER. It merges with the lysosome, followed by the destruction of its contents (*D*). PI3K – phosphoinoside-3-kinase; PI3P – phosphatidylinositol-3-phosphate; TAX1BP1 – Tax1-binding protein 1; NBP52 – calcium-binding protein 2; OPTIN – optineurin; PINK1 – PTEN-induced kinase 1; BNIP3 – protein 3 interacting with protein BCL2; PL – phospholipids; PIS – phosphatidylinositol synthase; ER – endoplasmic reticulum

MITOPHAGY DURING PHYSIOLOGICAL AGING

As confirmed by electron microscopy studies, mitochondrial disorganization that progresses with aging is accompanied by mitochondrial dysfunction [31].

Research into the mitochondrial ultrastructure during physiological aging revealed a reduction in the length and surface area of mitochondria, along with changes in cristae and membranes. These morphological changes were shown to correlate with an upregulated expression of phosphorylated Drp1, a marker of mitochondrial fission, as well as reduced levels of the mitochondrial fusion protein Mfn2 and the autophagy marker LC3B. The increased fragmentation of mitochondria observed during aging alters their function, including a reduction in ATP/ADP transport due to reduced levels of the VDAC1 protein (involved in the regulation of mitochondrial membrane permeability), as well as a greater severity of oxidative damage. Defective mitochondria are characterized by rupture of the outer membrane and release of apoptogenic factors into the cytoplasm, followed by cell death. The aforementioned age-related morphofunctional modifications of organelles reduce neuronal density and exacerbate neurodegeneration [3].

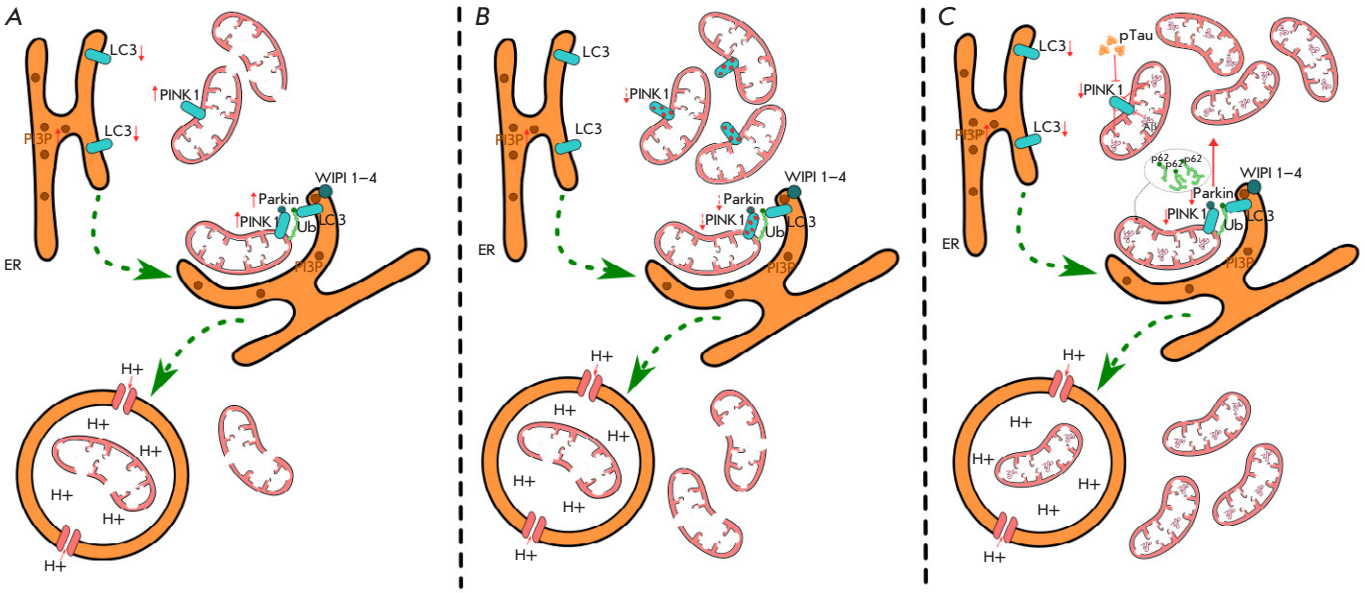

Fig. 2. Changes in the mitophagy process at the initiation stage and receptor interactions upon physiological aging and neurodegenerative diseases. (*A*) Aging. Characterized by the accumulation of defective mitochondria and mitophagy dysfunction. Progressive mitochondrial disorganization is accompanied by a compensatory increase in the PINK1 and Parkin levels. Reduced LC3 expression disrupts the interaction between phagophore receptors and mitochondria, leading to the inhibition of mitophagy. (*B*) Parkinson's disease. Accompanied by decreased utilization of mitochondria. In genetic forms of PD, mutations are detected in the genes encoding the PINK1 and Parkin synthesis, leading to inactivation of the respective proteins. (*C*) Alzheimer's disease. Characterized by a significant increase in the pool of defective mitochondria and reduced intensity of mitophagy. The accumulation of abnormal protein aggregates contributes to mitochondrial damage, reduces the PINK1 and Parkin levels, and increases the LC3 and p62 levels. PI3P – phosphatidylinositol-3-phosphate; p62 – ubiquitin-binding protein p62. ⊥ – mediated effect

Numerous studies prove that autophagy intensity progressively decreases during age-related involution and in age-related diseases [32–37].

The use of the mt-Keima probe (a monomeric acid-stable fluorescent protein with an affinity to the mitochondrial matrix) for quantifying mitophagy in a transgenic mouse line revealed age-related reduction of the mitophagy levels in neurons in the hippocampal dentate gyrus [33]. Overexpression of the key markers of PINK1–Parkin-dependent mitophagy in aging models was found to be accompanied by longer lifespans in the model organisms (*Drosophila melanogaster* and *Caenorhabditis elegans*) [34]. An elevated Parkin level, both in the brain tissue and cerebral vessels, was revealed in a group of old mice aged 24 months in [35, 36]. Upregulated Parkin expression was found to reduce the number of point mutations in mitochondrial DNA that cause mitochondrial dysfunction in [37].

It has been demonstrated using cellular models that neuroapoptosis decreases in the absence of PINK1, confirming the role played by this protein in neuronal survival during aging [38].

Memory loss during aging has been found to correlate with the downregulated expression of the *Mfn1*, *Mfn2*, *Opa1*, *LAMP2*, and *LC3* genes, while *PINK1* and *Parkin* expression is upregulated, which affects the mitochondrial membrane potential. These changes in the dynamics of *LAMP2*, *LC3*, *PINK1*, and *Parkin* expressions are indicative of mitophagy dysfunction [3] (*Fig. 2*).

There is a growing body of evidence showing that physical activity effectively induces autophagy, alters mitochondrial dynamics to keep them functioning, and has a neuroprotective effect. Different types of physical exercises can induce autophagy in the cerebral cortex of young and adult animals and mitigate autophagic dysfunction in the aged brain. Recent studies have revealed that physical training elevates the levels of the autophagy-related proteins LC3-II/LC3-I, LC3-II, p62, Atg7, Bnip3L, and Parkin, as well as the Mfn2 and Drp1 levels [39]. Furthermore, Liu et al.

in [33] demonstrated how strenuous physical exercise induced PINK1-dependent mitophagy in mt-Keima mice.

Hence, the balance between the mitochondrial dynamics and mitophagy is a specific compensatory mechanism playing a pivotal role in maintaining the stability of the functioning of these organelles in the aging brain.

MITOPHAGY IN NEURODEGENERATIVE DISEASES

Mitophagy plays a critical role in the pathogenesis of neurodegenerative diseases such as Alzheimer's disease (AD) and Parkinson's disease (PD), whose risk increase significantly with age [2].

Mitochondrial dysfunction and oxidative stress were found to be central pathogenic factors in genetically determined forms of Parkinson's disease [40]. The early-onset forms of PD can be caused by mutations in the *PARK2* (Parkin), *PINK1*, and *DJ-1* genes, which code for proteins residing in mitochondria (*Fig. 2*). The loss of these proteins increases the susceptibility to oxidative stress and disrupts the energy metabolism [41]. INK1 overexpression was shown to inhibit the translation of DRP1 mRNA and reduce its translocation from the cytosol to the mitochondrial surface, thus causing the formation of elongated chain-linked mitochondria and impeding the elimination of damaged organelles. PINK1-mediated ubiquitination of DRP1 results in its proteasomal degradation followed by inactivation, thus also reducing the intensity of mitochondrial fission [42]. Meanwhile, *PINK1* knockdown increases mitochondrial fragmentation [43].

Since PINK1 is the only known kinase that catalyzes ubiquitin phosphorylation, the detection of ubiquitin phosphorylated at S65 can be used to assess PINK1 activity and is viewed as a biomarker of mitochondrial stress and autophagy [44]. Mitochondrial damage leads to PINK1 accumulation because of its impaired degradation by the PARL (presenilin-associated rhomboid-like protein) protease residing on the mitochondrial inner membrane [45]. Unlike for idiopathic Parkinson's disease, Lewy bodies sometimes are not detected in substantia nigra neurons in postmortem specimens collected from patients carrying *PINK1* or *Parkin* mutations [46]. This is presumably caused by the involvement of *PINK1* and *Parkin* in the long-term survival of dopaminergic neurons, and disruption of this process results in their rapid death, without the accumulation of pathological proteins, which is supported by *PINK1* knockdown experiments.

Research has demonstrated that the PINK1–Parkin-independent pathway involving cardiolipin also has defects [47]. Neurons carrying the *SNCA* mutation typical of Parkinson's disease are characterized by a more intense cardiolipin translocation to the outer mitochondrial membrane. In turn, this phospholipid, capable of refolding α-synuclein fibrils, enhances mitophagic flux by interacting with LC3 on mitochondria, thus leading to mitochondrial dysfunction, which is further complicated by defects in mitophagy. At early stages of PD, synaptic mitochondria lose their cardiolipin cluster, thus reducing the intensity of mitophagy [47, 48].

A number of studies have demonstrated that mitochondrial deubiquitinase (USP30) can be a promising target for maintaining mitophagy in patients with Parkinson's disease. Reduction of the USP30 levels in various models of this disease has been shown to optimize mitochondrial function [5, 49, 50].

The mitochondrial dynamics and mitophagy are also impaired during the development of Alzheimer's disease (*Fig. 2*). This is evidenced by alterations in the expression of the *ATG5*, *Beclin1*, *LC3A*, *LC3B*, *PINK1*, *TERT*, *BCL2*, and *BNIP3L* genes detected in a mouse model of AD [51].

A 30–50% reduction in the basal mitophagy level was observed in the hippocampus of AD patients, accompanied by the accumulation of damaged mitochondria characterized by reduced size, disorganized cristae, and decreased ATP production [52]. Elevated PINK1 levels were detected in the hippocampus of patients with early-stage AD, while Parkin levels were increased at its late stages, which is indicative of impaired mitophagy because of defective initiation of the PINK1/Parkin-dependent pathway [45]. Impaired recruitment of activated LC3 to phagophore membranes, dysfunction of the AMPK signaling cascade, and disrupted fusion of mitophagosomes with lysosomes have also been observed [52].

An increased p62 level, an elevated LC3II/LC3I ratio, and a reduced PINK1 level were observed in mitochondrial fractions isolated from the brains of patients with late-stage AD, which is also indicative of mitophagy failure [53]. The accumulation of pathological protein aggregates in Alzheimer's disease significantly affects the mitochondrial dynamics and mitophagy. Thus, intraventricular administration of β-amyloid in rats reduced the PINK1, Parkin, and BCL-1 levels, while increasing the hippocampal level of p62 in [54]. The accumulation of total and phosphorylated tau protein is accompanied by an increase in the mitochondrial membrane potential, preventing PINK1 stabilization on the outer mitochondrial membrane and impeding Parkin recruitment. The reduced PINK1 content on the outer mitochondrial membrane suppresses the activation of Parkin and E3 ubiquitin

ligase, thus disrupting the further stages of autophagy and mitophagy [55]. Parkin overexpression restores mitophagy and the mitochondrial membrane potential [56]. Alterations in the mitochondrial dynamics accompanying the development of AD involve enhanced organelle fission. The accumulation of toxic tau protein and β-amyloid increases DRP1 phosphorylation and promotes its translocation into mitochondria [57]. Mitochondrial hyperfragmentation ultimately triggers cell death and neurodegeneration.

Sukhorukov et al. [11] suggested that alterations in ATP and NAD+ homeostasis can be among the reasons behind impaired mitophagy in AD, which was supported by the fact that a reduced intracellular NAD+ level initiates the aggregation of misfolded proteins, promoting defective autophagy, followed by neuronal death.

The activity of two neuroprotective genes, *Sirtuin1* (*SIRT1*) and *Sirtuin3* (*SIRT3*), which encode the synthesis of eponymous proteins, is also reduced in AD. Sirtuin-1 functions to induce autophagy/mitophagy via deacetylating the ATG5, ATG7, and ATG8/LC3 proteins. Moreover, sirtuin-1 stabilizes PINK1 and increases the levels of LC3 and Nix/BNIP3, which are involved in mitophagy [58]. In turn, sirtuin-3 activates the *FOXO3* gene regulating apoptosis and autophagy [59].

The altered dynamics of lysosomal activity, which is typical of the pathogenesis of AD, stems from a deficiency of the lysosomes in brain tissue. In turn, this disrupts the clearance of autophagic aggregates and is also believed to cause defective mitophagy. Thus, in the hereditary form of AD, mutations in the *PSEN1* gene encoding presenilin 1 cause hyper-alkalinization of the lysosomal environment, pathological reduction in lysosomal hydrolase activities, and a rise in p62 levels [56].

Many diseases, including neurodegenerative disorders, are characterized by excessive accumulation of advanced glycation end-products which induce oxidative stress and inflammation by generating reactive oxygen species. In turn, reactive oxygen species are considered a primary factor in the triggering of stress-induced mitophagy. Upregulated expression of the receptor for advanced glycation end-products was detected in post-mortem brain specimens from AD patients [60, 61].

Hence, although the involvement of the PINK1–Parkin-dependent pathway in mitophagy mechanisms and its role in the pathogenesis of neurodegenerative diseases have been studied relatively well, a number of questions remain open. Much focus has recently been directed at investigating alternative mitophagy pathways such as the degradation of mitochondrial components via mitochondrial-derived vesicles containing oxidized proteins, lipids, mutant mitochondrial DNA, and reactive oxygen species [43]. A link between mitochondrial-derived vesicles, mitophagy defects, and autoimmune responses that cause neuronal death in Parkinson's disease has recently been discovered [62].

CONCLUSIONS

Mitophagy plays a pivotal role in maintaining physiological homeostasis, the aging mechanisms, and the pathogenesis of neurodegenerative disorders. Various molecules that modulate mitophagic activity in nervous tissues are currently under study as potential candidates for developing therapeutics against neurodegenerative diseases. Meanwhile, given the diversity of the regulatory pathways of mitophagy, there is no question that this list of candidates will expand due to the multiple factors that are indicative of the state of mitophagy in specific types of nervous tissue cells in response to various stressors.

Overall, regardless of the existing interest in the role of mitophagy in age-related involution and the pathogenesis of age-related diseases, the mechanisms through which it affects the organismal aging remain insufficiently studied. The range of questions that need to be resolved includes the involvement of various regulatory signaling molecules in coordination with inter-organelle interactions, the specific features of the mitochondrial dynamics preceding the mitophagy, and the mechanisms of autophagosome degradation under mitochondrial stress. Particular focus should be placed on the mechanisms of initiation (activation) of both classical and receptor-mediated autophagy.

Hence, further research into the interplay between potential key markers of mitophagy and their relative contribution to neurodegeneration is of extreme importance for identifying novel promising pharmaceutical targets. ●

This work was supported by a grant from the Ministry of Science and Higher Education of the Russian Federation for major scientific projects in priority areas of scientific and technological development (project No. 075-15-2024-638).

REFERENCES

1. Loeffler DA. Influence of Normal Aging on Brain Autophagy: A Complex Scenario. *Front Aging Neurosci.* 2019;11:49. doi: 10.3389/fnagi.2019.00049
2. Hou Y, Dan X, Babbar M, et al. Ageing as a risk factor for neurodegenerative disease. *Nat Rev Neurol.* 2019;15(10):565–581. doi: 10.1038/s41582-019-0244-7
3. Mishra E, Thakur MK. Alterations in hippocampal mitochondrial dynamics are associated with neurodegeneration and recognition memory decline in old male mice. *Biogerontology.* 2022;23(2):251–271. doi: 10.1007/s10522-022-09960-3
4. Gleixner AM, Pulugulla SH, Pant DB, Posimo JM, Crum TS, Leak RK. Impact of aging on heat shock protein expression in the substantia nigra and striatum of the female rat. *Cell Tissue Res.* 2014;357(1):43–54. doi: 10.1007/s00441-014-1852-6
5. Cai Q, Jeong YY. Mitophagy in Alzheimer's Disease and Other Age-Related Neurodegenerative Diseases. *Cells.* 2020;9(1):150. doi: 10.3390/cells9010150
6. Garza-Lombó C, Pappa A, Panayiotidis MI, Franco R. Redox homeostasis, oxidative stress and mitophagy. *Mitochondrion.* 2020;51:105–117. doi: 10.1016/j.mito.2020.01.002
7. Lukyanova LD. Signaling mechanisms of hypoxia. Moscow: Russian Academy of Sciences; 2019. (in Russian).
8. Oliver DMA, Reddy PH. Molecular Basis of Alzheimer's Disease: Focus on Mitochondria. *J Alzheimers Dis.* 2019;72(s1):S95–116. doi: 10.3233/jad-190048
9. Lou G, Palikaras K, Lautrup S, Scheibye-Knudsen M, Tavernarakis N, Fang EF. Mitophagy and Neuroprotection. *Trends Mol Med.* 2020;26(1):8–20. doi: 10.1016/j.molmed.2019.07.002
10. Jang JY, Blum A, Liu J, Finkel T. The role of mitochondria in aging. *J Clin Invest.* 2018;128(9):3662–3670. doi: 10.1172/jci120842
11. Sukhorukov V, Voronkov D, Baranich T, Mudzhiri N, Magnaeva A, Illarioshkin S. Impaired Mitophagy in Neurons and Glial Cells during Aging and Age-Related Disorders. *Int J Mol Sci.* 2021;22(19):10251. doi: 10.3390/ijms221910251
12. Fivenson EM, Lautrup S, Sun N, et al. Mitophagy in neurodegeneration and aging. *Neurochem Int.* 2017;109:202–209. doi: 10.1016/j.neuint.2017.02.007
13. Freidlin IS, Mammedova JT, Strikova EA. The Role of Autophagy in Infections. *Russ J Physiol.* 2019;105(12):1486–1501. doi: 10.1134/s0869813919120057
14. Kwon YT, Ciechanover A. The Ubiquitin Code in the Ubiquitin-Proteasome System and Autophagy. *Trends Biochem Sci.* 2017;42(11):873–886. doi: 10.1016/j.tibs.2017.09.002
15. Turco E, Savova A, Gere F, et al. Reconstitution defines the roles of p62, NBR1 and TAX1BP1 in ubiquitin condensate formation and autophagy initiation. *Nat Commun.* 2021;12(1):5212. doi: 10.1038/s41467-021-25572-w
16. Walker SA, Ktistakis NT. Autophagosome Biogenesis Machinery. *J Mol Biol.* 2020;432(8):2449–2461. doi: 10.1016/j.jmb.2019.10.027
17. Nakatogawa H, Ichimura Y, Ohsumi Y. Atg8, a Ubiquitin-like Protein Required for Autophagosome Formation, Mediates Membrane Tethering and Hemifusion. *Cell.* 2007;130(1):165–178. doi: 10.1016/j.cell.2007.05.021
18. Uemura T, Yamamoto M, Kametaka A, et al. A Cluster of Thin Tubular Structures Mediates Transformation of the Endoplasmic Reticulum to Autophagic Isolation Membrane. *Mol Cell Biol.* 2014;34(9):1695–1706. doi: 10.1128/mcb.01327-13
19. Müller AJ, Proikas-Cezanne T. Function of human WIPI proteins in autophagosomal rejuvenation of endomembranes? *FEBS Lett.* 2015;589(14):1546–1551. doi: 10.1016/j.febslet.2015.05.008
20. Dikic I, Elazar Z. Mechanism and medical implications of mammalian autophagy. *Nat Rev Mol Cell Biol.* 2018;19(6):349–364. doi: 10.1038/s41580-018-0003-4
21. Melia TJ, Lystad AH, Simonsen A. Autophagosome biogenesis: From membrane growth to closure. *J Cell Biol.* 2020;219(6): e202002085. doi: 10.1083/jcb.202002085
22. Lamark T, Johansen T. Mechanisms of Selective Autophagy. *Annu Rev Cell Dev Biol.* 2021;37:143–169. doi: 10.1146/annurev-cellbio-120219-035530
23. Vargas JNS, Wang C, Bunker E, et al. Spatiotemporal Control of ULK1 Activation by NDP52 and TBK1 during Selective Autophagy. *Mol Cell.* 2019;74(2):347–362.e6. doi: 10.1016/j.molcel.2019.02.010
24. Yim WWY, Mizushima N. Lysosome biology in autophagy. *Cell Discov.* 2020;6:6 doi: 10.1038/s41421-020-0141-7
25. Wang JL, Xu CJ. Astrocytes autophagy in aging and neurodegenerative disorders. *Biomed Pharmacother.* 2020;122:109691. doi: 10.1016/j.biopha.2019.109691
26. Rambold AS, Lippincott-Schwartz J. Mechanisms of mitochondria and autophagy crosstalk. *Cell Cycle.* 2011;10(23):4032–4038. doi: 10.4161/cc.10.23.18384
27. Wei Y, Liu M, Li X, Liu J, Li H. Origin of the Autophagosome Membrane in Mammals. *Biomed Res Int.* 2018;2018:1012789. doi: 10.1155/2018/1012789
28. Kleele T, Rey T, Winter J, et al. Distinct fission signatures predict mitochondrial degradation or biogenesis. *Nature.* 2021;593(7859):435–439. doi: 10.1038/s41586-021-03510-6
29. Guan R, Zou W, Dai X, et al. Mitophagy, a potential therapeutic target for stroke. *J Biomed Sci.* 2018;25(1):87. doi: 10.1186/s12929-018-0487-4
30. Swerdlow NS, Wilkins HM. Mitophagy and the Brain *Int J Mol Sci.* 2020;21(24):9661. doi: 10.3390/ijms21249661
31. Skulachev VP, Vyssokikh MY, Chernyak BV, et al. Six Functions of Respiration: Isn't It Time to Take Control over ROS Production in Mitochondria, and Aging Along with It? *Int J Mol Sci.* 2023;24(16):12540. doi: 10.3390/ijms241612540
32. Bondy SC. Mitochondrial Dysfunction as the Major Basis of Brain Aging. *Biomolecules.* 2024;14(4):402. doi: 10.3390/biom14040402
33. Liu YT, Sliter DA, Shammas MK, et al. Mt-Keima detects PINK1-PRKN mitophagy in vivo with greater sensitivity than mito-QC. *Autophagy.* 2021;17(11):3753–3762. doi: 10.1080/15548627.2021.1896924
34. Rana A, Oliveira MP, Khamoui AV, et al. Promoting Drp1-mediated mitochondrial fission in midlife prolongs healthy lifespan of Drosophila melanogaster. *Nat Commun.* 2017;8(1):448. doi: 10.1038/s41467-017-00525-4
35. Liang W, Moyzis AG, Lampert MA, Diao RY, Najor RH, Gustafsson ÅB. Aging is associated with a decline in Atg9b-mediated autophagosome formation and appearance of enlarged mitochondria in the heart. *Aging Cell.* 2020;19(8):e13187. doi: 10.1111/acel.13187
36. Tyrrell DJ, Blin MG, Song J, Wood SC, Goldstein DR. Aging Impairs Mitochondrial Function and Mitophagy and Elevates Interleukin 6 Within the Cerebral Vasculature. *J Am Heart Assoc.* 2020;9(23):e017820. doi: 10.1161/jaha.120.017820

37. Gaziev AI, Abdullaev S, Podlutsky A. Mitochondrial function and mitochondrial DNA maintenance with advancing age. *Biogerontology.* 2014;15(5):417–438. doi: 10.1007/s10522-014-9515-2
38. Wood-Kaczmar A, Gandhi S, Yao Z, et al. PINK1 is necessary for long term survival and mitochondrial function in human dopaminergic neurons. *PLoS One.* 2008;3(6):e2455. doi: 10.1371/journal.pone.0002455
39. Qin YY, Pan SY, Dai JR, et al. Alleviation of ischemic brain injury by exercise preconditioning is associated with modulation of autophagy and mitochondrial dynamics in cerebral cortex of female aged mice. *Exp Gerontol.* 2023;178:112226. doi: 10.1016/j.exger.2023.112226
40. Dagda RK. Role of Mitochondrial Dysfunction in Degenerative Brain Diseases, an Overview. *Brain Sci.* 2018;8(10):178. doi: 10.3390/brainsci8100178
41. Ma K, Zhang Z, Chang R, et al. Dynamic PGAM5 multimers dephosphorylate BCL-xL or FUNDC1 to regulate mitochondrial and cellular fate. *Cell Death Differ.* 2020;27(3):1036–1051. doi: 10.1038/s41418-019-0396-4
42. Sulkshane P, Ram J, Thakur A, Reis N, Kleifeld O, Glickman MH. Ubiquitination and receptor-mediated mitophagy converge to eliminate oxidation-damaged mitochondria during hypoxia. *Redox Biol.* 2021;45:102047. doi: 10.1016/j.redox.2021.102047
43. Macdonald R, Barnes K, Hastings C, Mortiboys H. Mitochondrial abnormalities in Parkinson's disease and Alzheimer's disease: can mitochondria be targeted therapeutically? *Biochem Soc Trans.* 2018;46(4):891–909. doi: 10.1042/bst20170501
44. Fiesel FC, Springer W. Disease relevance of phosphorylated ubiquitin (p-S65-Ub). *Autophagy.* 2015;11(11):2125–2126. doi: 10.1080/15548627.2015.1091912
45. Wong YC, Holzbaur ELF. Autophagosome dynamics in neurodegeneration at a glance. *J Cell Sci.* 2015;128(7):1259–1267. doi: 10.1242/jcs.161216
46. Takanashi M, Li Y, Hattori N. Absence of Lewy pathology associated with PINK1 homozygous mutation. *Neurology.* 2016;86(23):2212–2213. doi: 10.1212/wnl.0000000000002744
47. Ryan T, Bamm VV, Stykel MG, et al. Cardiolipin exposure on the outer mitochondrial membrane modulates α-synuclein. *Nat Commun.* 2018;9(1):817. doi: 10.1038/s41467-018-03241-9
48. Chung SY, Kishinevsky S, Mazzulli JR, et al. Parkin and PINK1 Patient iPSC-Derived Midbrain Dopamine Neurons Exhibit Mitochondrial Dysfunction and α-Synuclein Accumulation. *Stem Cell Reports.* 2016;7(4):664–677. doi: 10.1016/j.stemcr.2016.08.012
49. Bingol B, Tea JS, Phu L, et al. The mitochondrial deubiquitinase USP30 opposes parkin-mediated mitophagy. *Nature.* 2014;510(7505):370–375. doi: 10.1038/nature13418
50. Bakula D, Scheibye-Knudsen M. MitophAging: Mitophagy in Aging and Disease. *Front Cell Dev Biol.* 2020;8:239. doi: 10.3389/fcell.2020.00239
51. Reddy PH, Yin X, Manczak M, et al. Mutant APP and amyloid beta-induced defective autophagy, mitophagy, mitochondrial structural and functional changes and synaptic damage in hippocampal neurons from Alzheimer's disease. *Hum Mol Genet.* 2018;27(14):2502–2516. doi: 10.1093/hmg/ddy154
52. Fang EF, Hou Y, Palikaras K, et al. Mitophagy inhibits amyloid-β and tau pathology and reverses cognitive deficits in models of Alzheimer's disease. *Nat Neurosci.* 2019;22(3):401–412. doi: 10.1038/s41593-018-0332-9
53. Vaillant-Beuchot L, Mary A, Pardossi-Piquard R, et al. Accumulation of amyloid precursor protein C-terminal fragments triggers mitochondrial structure, function, and mitophagy defects in Alzheimer's disease models and human brains. *Acta Neuropathol.* 2021;141(1):39–65. doi: 10.1007/s00401-020-02234-7
54. Han Y, Wang N, Kang J, Fang Y. β-Asarone improves learning and memory in Aβ1-42-induced Alzheimer's disease rats by regulating PINK1-Parkin-mediated mitophagy. *Metab Brain Dis.* 2020;35(7):1109–1117. doi: 10.1007/s11011-020-00587-2
55. Chen RH, Chen YH, Huang TY. Ubiquitin-mediated regulation of autophagy. *J Biomed Sci.* 2019;26(1):80. doi: 10.1186/s12929-019-0569-y
56. Martín-Maestro P, Sproul A., Martinez H., et al. Autophagy Induction by Bexarotene Promotes Mitophagy in Presenilin 1 Familial Alzheimer's Disease iPSC-Derived Neural Stem Cells. *Mol Neurobiol.* 2019;56(12):8220–8236. doi: 10.1007/s12035-019-01665-y
57. Yan J, Liu XH, Han MZ, et al. Blockage of GSK3β-mediated Drp1 phosphorylation provides neuroprotection in neuronal and mouse models of Alzheimer's disease. *Neurobiol Aging.* 2015;36(1):211–227. doi: 10.1016/j.neurobiolaging.2014.08.005
58. Lee IH. Mechanisms and disease implications of sirtuin-mediated autophagic regulation. *Exp Mol Med.* 2019;51(9):1–11. doi: 10.1038/s12276-019-0302-7
59. Meng H, Yan WY, Lei YH, et al. SIRT3 Regulation of Mitochondrial Quality Control in Neurodegenerative Diseases. *Front Aging Neurosci.* 2019;11:313. doi: 10.3389/fnagi.2019.00313
60. Srikanth V, Maczurek A, Phan T, et al. Advanced glycation endproducts and their receptor RAGE in Alzheimer's disease. *Neurobiol Aging.* 2011;32(5):763–777. doi: 10.1016/j.neurobiolaging.2009.04.016
61. Sukhorukov VS, Mudzhiri NM, Voronkova AS, Baranich TI, Glinkina VV, Illarioshkin SN. Mitochondrial Disorders in Alzheimer's Disease. *Biochemistry (Mosc).* 2021;86(6):667–679. doi: 10.1134/s0006297921060055
62. Matheoud D, Sugiura A, Bellemare-Pelletier A, et al. Parkinson's Disease-Related Proteins PINK1 and Parkin Repress Mitochondrial Antigen Presentation. *Cell.* 2016;166(2):314–327. doi: 10.1016/j.cell.2016.05.039

Whole-Genome Sequencing Uncovers Metabolic and Immune System Variations in *Propionibacterium freudenreichii* Isolates

I. D. Antipenko[1*], S. A. Venedyukhina[1], N. P. Sorokina[2], I. V. Kucherenko[2], T. S. Smirnova[2], G. N. Rogov[2], M. Yu. Shkurnikov[1]

[1]Laboratory for Research on Molecular Mechanisms of Longevity, Department of Biology and Biotechnology, HSE University, Moscow, 101000 Russia

[2]All-Russian Research Institute of Butter and Cheese Making, Branch of the Gorbatov Federal Research Center for Food Systems, Uglich, 109316 Russia

[*]E-mail: iantipenko@hse.ru

Received July 31, 2025; in final form, September 29, 2025

DOI: 10.32607/actanaturae.27764

ABSTRACT ***Propionibacterium freudenreichii*** **plays a crucial role in the production of Swiss-type cheeses; however, genomic variability among strains, which affects their technological traits, remains insufficiently explored. In this study, whole-genome sequencing and comparative analysis were performed on five industrial** *P. freudenreichii* **strains. Despite their overall high genomic similarity, the strains proved different in gas production and substrate metabolism. Phylogenetic analysis revealed a close relationship between strain FNCPS 828 and** *P. freudenreichii* **subsp.** *shermanii* **(z-score = 0.99948), with the latter being unable to reduce nitrates but being able to metabolize lactose. The** *narG* **gene encoding the nitrate reductase alpha subunit was detected in only one of the five analyzed strains – FNCPS 828 – and in 39% of previously described** *P. freudenreichii* **genomes, suggesting its potential as a marker of nitrate-reducing capability. Analysis of 112 genomes showed that the I–G CRISPR–Cas system was present in more than 90% of the strains, whereas the type I–E system was found in approximately 25%. All the five study strains harbored the type I–G system; strain FNCPS 3 additionally contained a complete type I–E system with the highest number of CRISPR spacers, some of which matched previously published bacteriophage sequences. The most prevalent anti-phage defense systems included RM I, RM IV, AbiE, PD-T4-6, HEC-06, and ietAS. These findings highlight the genetic diversity of** *P. freudenreichii* **strains, which is of great importance in their industrial applications. The identification of** *narG* **as a potential marker of nitrate-reducing activity, along with detailed mapping of CRISPR–Cas systems, boosts opportunities for the rational selection and engineering of starter cultures with tailored metabolic properties and increased resistance to bacteriophages.**

KEYWORDS ***Propionibacterium*****, whole-genome sequencing, metabolism, CRISPR–Cas, bacteriophages.**

INTRODUCTION

Members of the genus *Propionibacterium* play an important role in the food industry. In particular, *Propionibacterium freudenreichii* strains are widely used in the ripening of Swiss-type cheeses [1]. The key metabolic pathway in *P. freudenreichii* is the Wood–Werkmann cycle, where lactate is first converted to pyruvate and then metabolized: one portion is converted to propionate that gives the cheese its characteristic flavor, and the other portion is converted to acetate and carbon dioxide that form the characteristic "eyes" [2].

Each *P. freudenreichii* strain is characterized by a unique set of enzymes that underlies the specific features of its metabolic activity [3], which affects fermented carbohydrates and provides the taste of the final product [4]. Furthermore, these bacteria synthesize vitamins B9 and B12, conjugated linoleic acid, trehalose, bacteriocins, and organic acids and exhibit probiotic properties [5].

Bacteriophage contamination is a serious problem for the dairy industry, because it can result in fermentation failure and product defects. Bacteriophages are detected in approximately half of Swiss-type cheeses at a concentration of at least 10^5 PFU/g; they multiply as propionic acid bacteria grow in a warm chamber during cheese ripening [6]. Given the key role of *P. freudenreichii* in shaping the organoleptic characteristics of cheeses, investigation of their immune defense systems is of great practical importance for identifying phage-resistant strains and minimizing the risk of process failures during the ripening stage [7].

Despite the industrial significance of *P. freudenreichii*, genomic characterization of industrial strains of this species is very limited. Whole-genome sequencing identifies interstrain variations and reveals links between genotype and technological properties, including metabolism, stress resistance, and defense systems [4].

In this study, we present the results of whole-genome sequencing of five *P. freudenreichii* strains used in the dairy industry and comprehensive genomic characterization of these strains, focusing on their metabolic characteristics, defense mechanisms, and functional gene variability.

EXPERIMENTAL

Strains and culture conditions

In this study, we used five *P. freudenreichii* strains: FNCPS 2 (GCA_044990475.1), FNCPS 3 (GCA_044990455.1), FNCPS 4 (GCA_044990515.1), FNCPS 6 (GCA_044990495.1), and FNCPS 828 (GCA_044990435.1) received from the collection of the All-Russian Research Institute of Butter and Cheese Making of the Dairy Industry (VNIIMS, a branch of the Gorbatov Federal Research Center for Food Systems of the Russian Academy of Sciences). Strains FNCPS 2 and FNCPS 3 were isolated from raw milk samples, and the others were isolated from cheese samples. All strains were isolated from dairy products manufactured in Altai Krai, Russia.

Propionibacterium bacteria were cultivated in a liquid culture medium containing peptone (10 g), yeast extract (10 g), cobalt chloride (0.01 g), potassium monobasic phosphate (1 g), and 20 cm^3 of 40% lactic acid. These components were dissolved in 1 L of distilled water, the pH was adjusted to 7.1 ± 0.1, and the mixture was then poured into test tubes and sterilized at 121 ± 2°C for 15 min. The same medium was used to study the gas-producing activity of *P. freudenreichii* strains.

The effect of milk protein proteolysis products on gas production by propionibacterium was studied using the same culture medium. However, the components were added to pancreatin-hydrolyzed skim milk diluted with distilled water at a ratio of 1 : 2.

To produce propionibacterium cultures, the culture medium was inoculated with 1% of the inoculum and incubated in a thermostat at 30 ± 1°C for 72 h.

Phenotypic characterization of the strains

The rate of gas production and the volume of released gas were measured during culturing in graduated Dunbar tubes with a 1% inoculum dose at 30 ± 1°C. The volume of released gas was measured daily for 15 days. The rate of gas production was calculated as the maximum gas volume divided by the number of culture days.

The effect of temperature on the gas-producing activity of the cultures was assessed by culturing cells in graduated Dunbar tubes with a 1% inoculum dose at 18 ± 1°C, 22 ± 1°C, and 30 ± 1°C. The gas volume was measured daily for 15 days.

Anaerobic bacteria were identified by measurements of the biochemical activity of the cultures using the API 20A test system (bioMérieux, France) according to the manufacturer's instructions. Test strip results were analyzed using the APIWEB online database (bioMérieux).

Bacterial genome sequencing and assembly

DNA for genome sequencing was isolated using an ExtractDNA Blood and Cells kit (Eurogen, Russia) according to the manufacturer's instructions. DNA libraries were prepared using the MGIEasy Fast FS DNA Library Prep Set V2.0 (Cat. No. 940-001196-00, MGI, China) according to the manufacturer's protocol. Library quality was assessed using a Qubit 1X dsDNA High Sensitivity DNA Assay kit (Cat. No. Q33230, Thermo Fisher Scientific, USA) and a Qubit Fluorometer (Thermo Fisher Scientific). The length of DNA library fragments was estimated using QIAxcel Advanced capillary gel electrophoresis with a QX DNA Fast Analysis kit (Cat. No. 929008, Qiagen, Germany). Sequencing was performed using an FCS flow cell on an MGI DNBSEQ-G50 platform (BGI, China) in the PE150 mode.

Bacterial genomes were assembled using SPAdes [8] in the "isolate" mode. To improve final assembly quality, raw reads were aligned to contigs using Bowtie2 [9], after which the alignment files were sorted and indexed using SAMtools [10] and transferred to Pilon [11] to correct assembly inaccuracies. Assembly quality was assessed using QUAST [12], and the completeness of the assembled genomes was evaluated using BUSCO [13]. The assembled genomic sequences were deposited in the NCBI database (BioProject: PRJNA1184111).

Table 1. Genomic characteristics of the study *P. freudenreichii* strains, based on whole-genome sequencing data

P. freudenreichii	FNCPS 2	FNCPS 3	FNCPS 4	FNCPS 6	FNCPS 828
Contigs	599	205	159	446	83
GC content	65.95	67.04	66.68	66.38	67.24
Contig L50	9	11	5	11	9
Genome length, bp	2806765	2894278	2649124	2734816	2579802
Contig N50	101.834	63836	169499	79634	93772
CDS	2.684	2.768	2.497	2.603	2.349
tRNA	48	173	44	58	45
Repeat regions	44	48	13	46	38
rRNA	3	3	4	3	4
Hypothetical proteins	935	933	790	845	670
Proteins with functional annotation	1.749	1.835	1.707	1.758	1.679

Genome analysis

Genome annotation and functional analysis were performed using the NCBI Prokaryotic Genome Annotation Pipeline [14] and the BV-BRC platform [15] that employs the RASTtk algorithm [16]. Comparative analysis of gene presence in propionibacterium was performed using the BV-BRC platform based on high-quality, open-access complete *P. freudenreichii* genome assemblies (n = 112).

Identification of bacterial immune systems

Bacterial immune systems were identified using the PADLOC software (v2.0.0) [17]. CRISPR repeats and spacers were identified using the CRISPR–Cas Finder tool (v4.3.2) [18], and Cas proteins were annotated using PADLOC. To identify potential targets, spacers were aligned to bacterial phage genomes using Bowtie2 v2.5.4 [19]. Nucleotide sequences of 575 phage genomes were obtained from the NCBI database (accessed July 4, 2025).

Phylogenetic analysis

Phylogenetic identification and determination of closely related strains were performed using tetranucleotide correlation analysis via the JSpeciesWS web service [20]. Average nucleotide identity (ANI) was compared using the OrthoANI algorithm [21].

RESULTS

General genomic characterization

Whole-genome sequencing is considered the gold standard for genetic characterization of microorganisms. General characteristics of the genomic sequences of the five strains are presented in *Table 1*.

Tetracorrelation analysis revealed that the type strain *P. freudenreichii* subsp. *shermanii* CCUG 36819 had the closest similarity to the study strains *P. freudenreichii* FNCPS 828, 2, 6, and 4 (z-score: 0.99948, 0.96457, 0.97622, and 0.98812, respectively). *P. freudenreichii* subsp. *freudenreichii* DSM 20271 was closest to strain FNCPS 3 (z-score = 0.98812). Calculation of OrthoANI values among all the study strains and the reference genomes showed a high phylogenetic closeness (ANI > 98%), which indicates that they probably belong to the same clonal group. The results are presented as a pairwise similarity matrix (*Fig. 1*).

Strain phenotyping

Gas production. Gas production (CO_2 production) is one of the key technological characteristics of propionic acid bacteria, which enables the formation of "eyes" in Emmental-type cheeses [22]. The main CO_2 producer during ripening is *P. freudenreichii* that metabolizes lactic acid to form propionate, acetate, and CO_2.

To assess gas-producing activity, we conducted experiments using two types of culture media: with and without milk hydrolyzate. The results are presented in *Fig. 2A,B*.

Strain *P. freudenreichii* FNCPS 2 growing on the medium without milk hydrolyzate was characterized by the highest rate and volume of gas production, whereas these indicators in strains FNCPS 3 and FNCPS 4 were low. On the medium with hydrolyzed milk, the differences among the strains decreased: activity of *P. freudenreichii* FNCPS 2 remained high, indicators of FNCPS 6 and FNCPS 828 significantly increased, while the volume of released gas in FNCPS 3 was low. Thus, strain FNCPS 2 is characterized by stable and high gas production, whereas FNCPS 3 exhibits low activity, regardless of culture conditions.

The dependence of gas production by *P. freudenreichii* strains on temperature is shown in *Fig. 3*. At

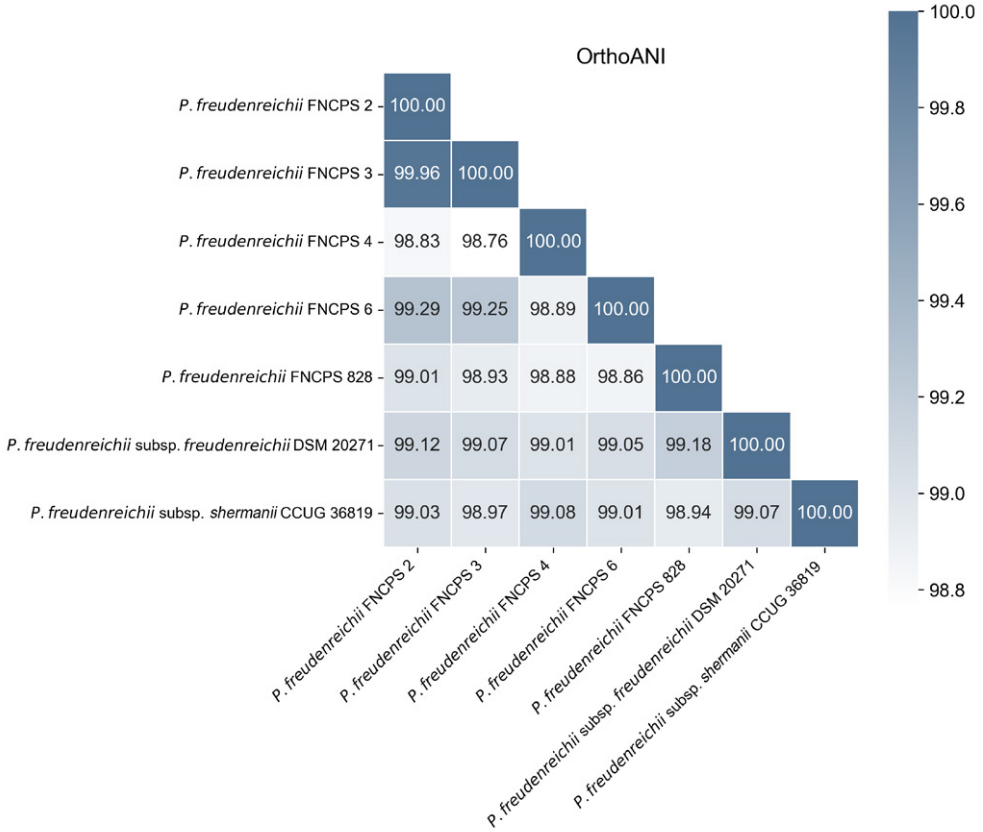

Fig. 1. Heatmap of orthoANI alignment of *Propionibacterium freudenreichii* strains. Numbers represent the percentage of average nucleotide identity (ANI) among orthologous genes of different strains. Diagonal numbers (100%) indicate self-identity of each strain

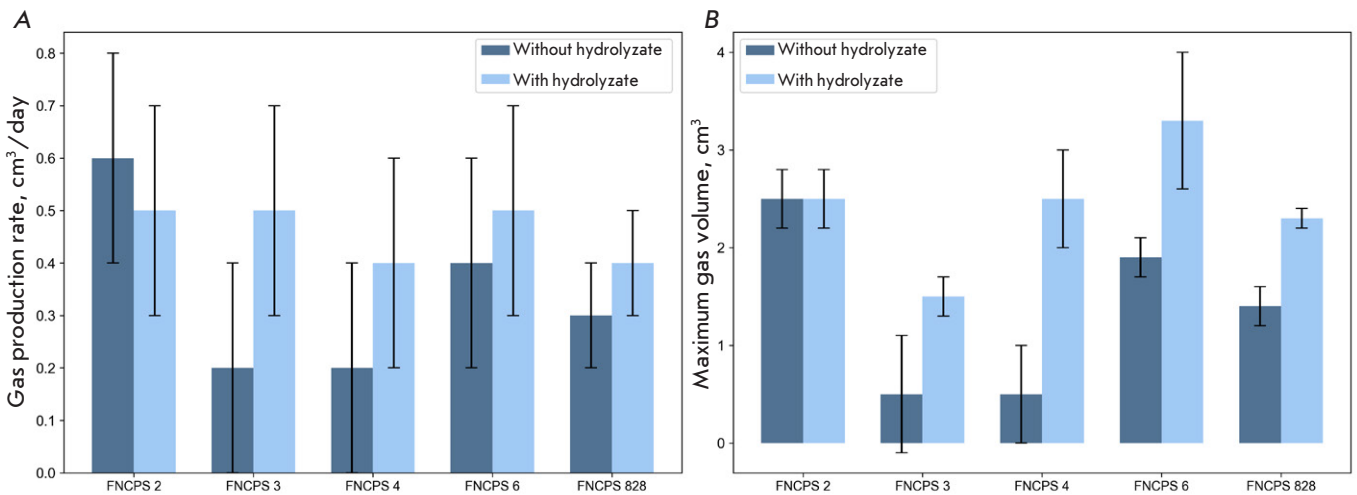

Fig. 2. (*A*) Maximum gas production rate by *Propionibacterium* strains grown on different culture media. (*B*) Maximum volume of gas released. Values are presented as mean ± standard deviation

18°C, FNCPS 4 exhibited the highest volume of CO_2 release, whereas FNCPS 3 produced no gas. Elevating the temperature to 22 and 25°C increased the volume of CO_2 production in all strains, especially in FNCPS 6 and FNCPS 828, which showed the highest values among all the strains by day 14.

Metabolic profiling of bacteria

Metabolic profiling of the strains was performed using the BioMérieux system. The results are presented in *Fig. 4*.

According to the data, the only substrates metabolized by all the strains were *D*-mannose, *D*-glucose,

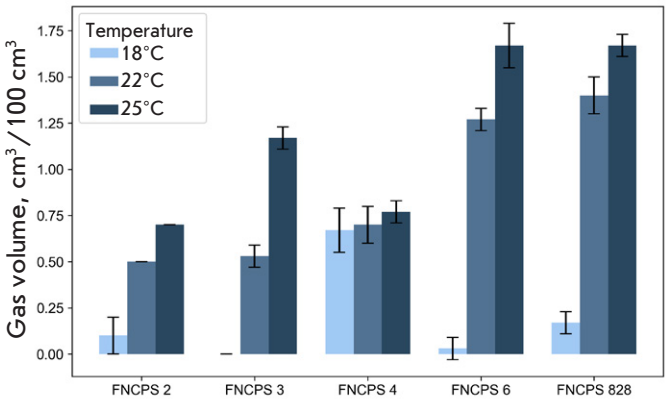

Fig. 3. Effect of temperature on gas production volume. Values are presented as mean ± standard deviation

and *D*-lactose. Strain FNCPS 3, unlike the other strains, was not able to utilize glycerol and lacked catalase activity. *P. freudenreichii* FNCPS 2 had the broadest metabolic profile (12 of 20 substrates tested). In addition, strains FNCPS 828 and FNCPS 4 were able to degrade gelatin, which was not typical of the other strains.

Genome analysis

Analysis of the coding sequences at the role level of annotated biological gene functions revealed that all strains possessed a comparable number of unique functional groups (from 738 to 750), of which 724 were common to all (*Fig. 5*). The most related strains were FNCPS 4 and 828, which shared 16 unique functional gene groups.

Polymorphic variants of a number of genes in the study strains may play a key role in the cheese ripening process, influencing the organoleptic properties of products, the efficiency of metabolic pathways, and the overall nutritional value. For example, only strains *P. freudenreichii* FNCPS 4 and FNCPS 828 were found to contain a complete set of genes encoding the enzymes involved in 1,2-propanediol metabolism and components of the propanediol dehydratase complex (*PduA*, *PduB*, *PduJ*, *PduK*, *PduN*, *PduU*, and *PduV* genes), which indicates the ability of these strains to anaerobically convert propanediol into propanol and propionate [23].

Strains FNCPS 2, 3, and 6 contain aspartate racemase [EC 5.1.1.13] involved in the synthesis of *D*-aspartate, as well as the *OppB* gene encoding a component of an oligopeptide transporter that ensures the uptake of peptides from the environment – an important source of nitrogen in the fermentation matrix.

The only difference at the functional class level was the absence of genes belonging to the *Nitrogen Metabolism* class in strain FNCPS 828.

Subspecies identification

The *P. freudenreichii* species is traditionally divided into two subspecies: *freudenreichii* and *shermanii*. The main traits differentiating these subspecies are

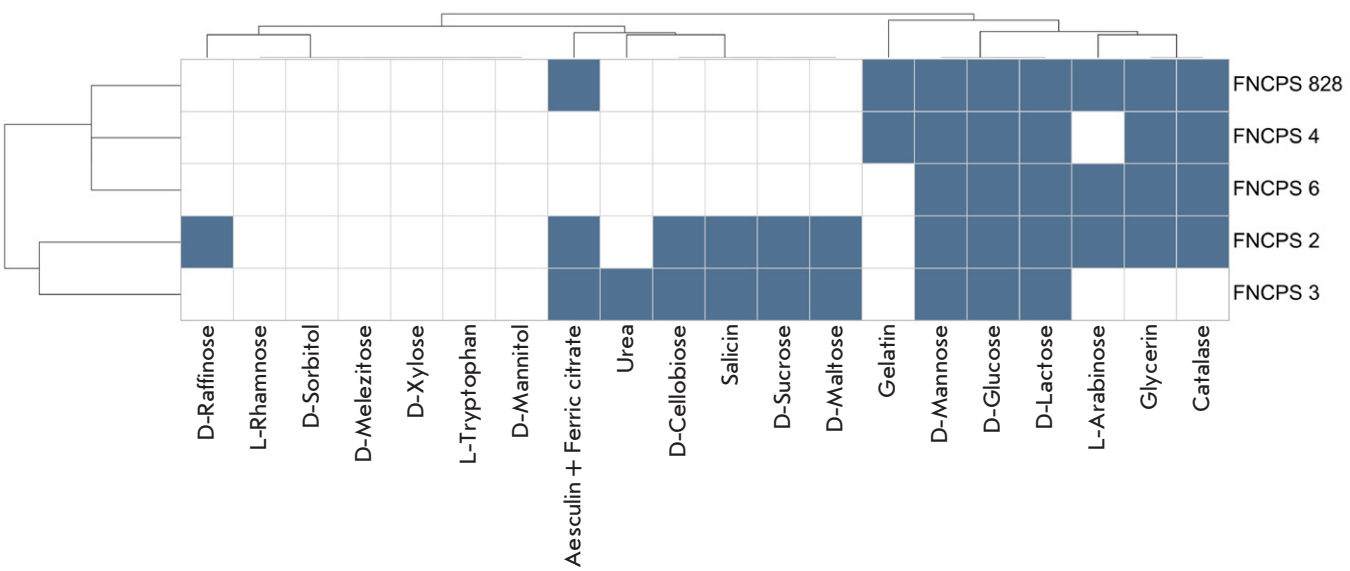

Fig. 4. Heatmap of the enzymatic and biochemical profiles of *P. freudenreichii* strains. The color scale indicates the presence (blue) or absence (white) of a positive response to the corresponding substrate. Strains are grouped based on similarity in biochemical activity; clustering results are shown as a dendrogram

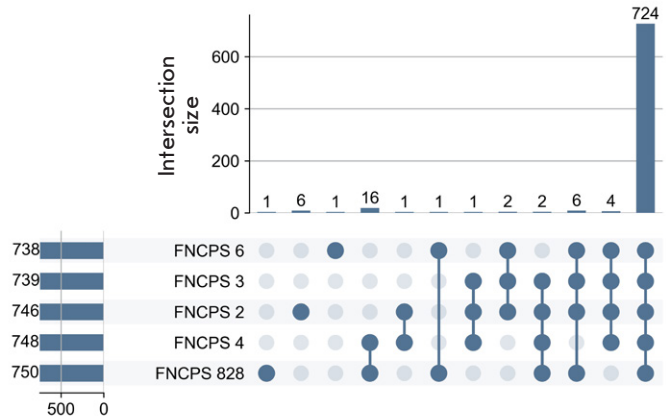

Fig. 5. Intersections of functional groups among *P. freudenreichii* strains. The bar height represents the number of identified functional groups found in one or more strain groups. The dots below indicate which specific strains contain these functions

the ability to reduce nitrates and ferment lactose [4]. Usually, ssp. *freudenreichii* strains reduce nitrates but do not metabolize lactose, whereas ssp. *shermanii* are able to ferment lactose but not able to reduce nitrates [24].

The key enzyme involved in nitrate reduction is the respiratory nitrate reductase complex [EC 1.7.99.4]. This enzyme functions as a final electron acceptor under anaerobic conditions, participating in energy generation. Genomic analysis revealed that strain FNCPS 828 lacked the *narG* gene encoding the respiratory nitrate reductase alpha chain that directly reduces nitrate to nitrite [25]. The lack of this gene was detected in 44 of 112 (39%) analyzed *P. freudenreichii* genomes (*Fig. 6A*). In this case, none of the *narG* gene-containing strains had been previously classified as a *shermanii* subspecies.

The only difference in the genetic profile of strain FNCPS 828 from the other study strains was the lack

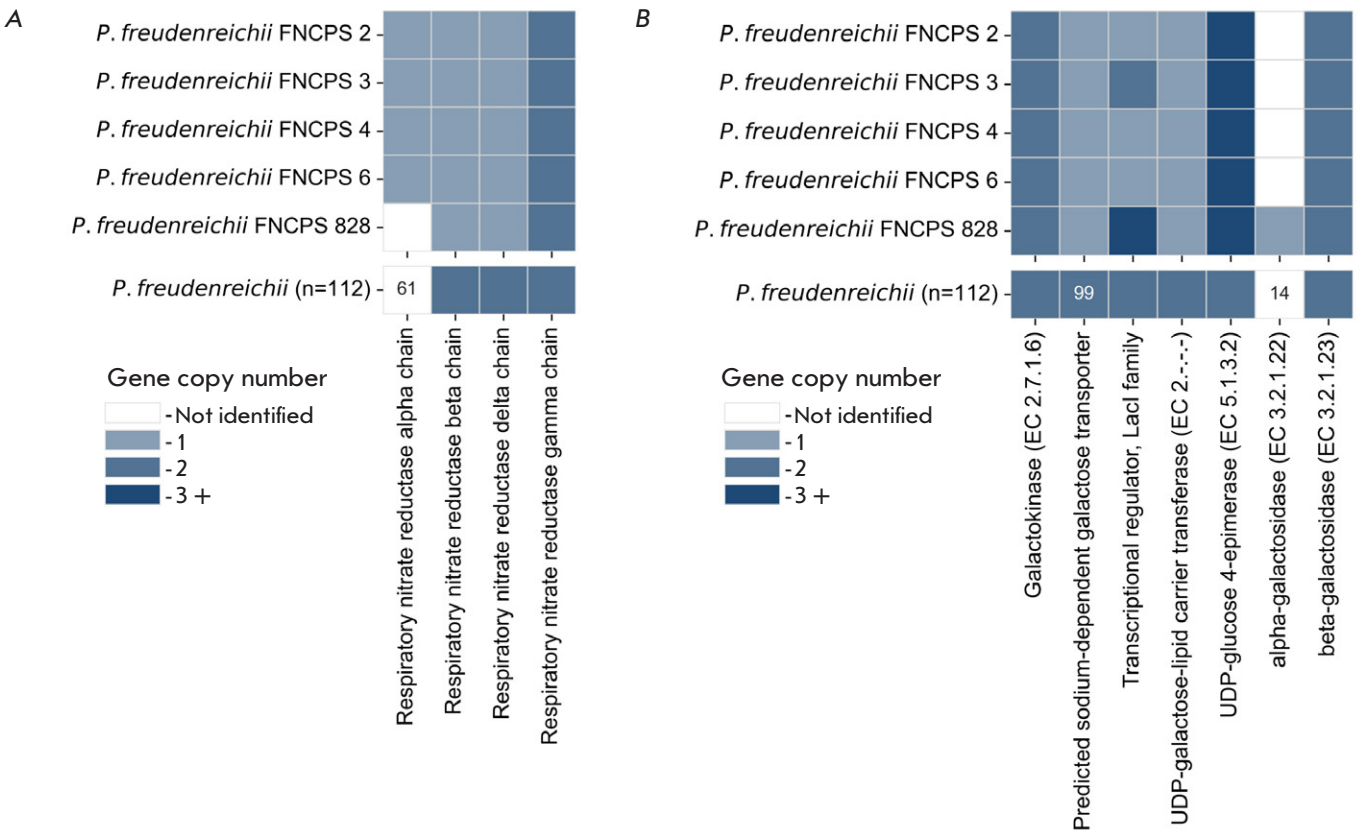

Fig. 6. Distribution of nitrate and lactose metabolism genes in *P. freudenreichii* strains ($n = 112$) and the study isolates. (*A*) Respiratory nitrate reductase genes (EC 1.7.99.4); (*B*) Genes associated with lactose metabolism. Top panel: a gene presence/absence matrix (blue – present; white – absent; numbers indicate copy count); Bottom panel: the percentage distribution of each gene in the population

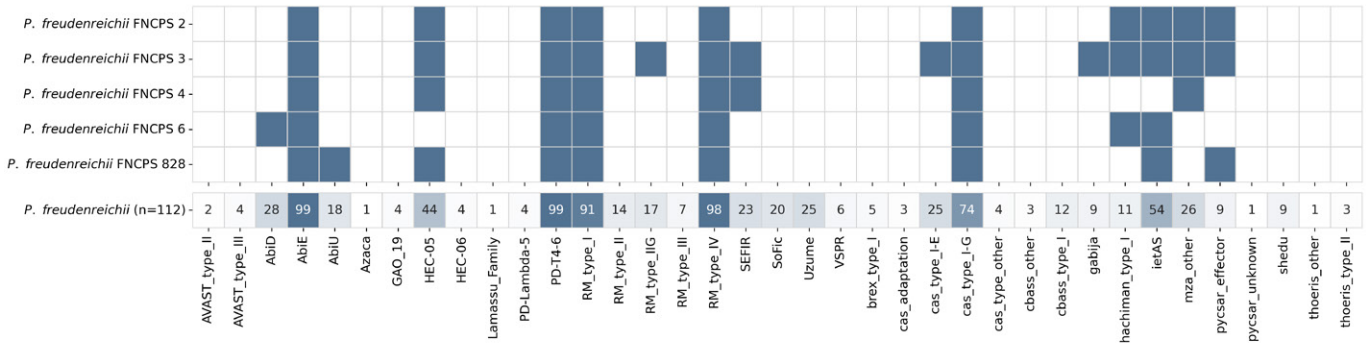

Fig. 7. Bacterial immune systems in *P. freudenreichii* ($n = 112$) and the five study strains. The upper panel shows a binary matrix: blue indicates the presence of a system, and white indicates its absence. The lower panel shows the percentage representation of each gene in the population

Table 2. Characterization of CRISPR-Cas systems in the *P. freudenreichii* strains studied

P. freudenreichii strain	CRISPR–Cas system, type	Cas proteins, number	Unique spacers, number	Unique CRISPRs, number
FNCPS 2	I–G	6	44	2
FNCPS 3	I–G, I–E	14	170	5
FNCPS 4	I–G	6	13	3
FNCPS 6	I–G	6	62	4
FNCPS 828	I–G	5	37	2

of the gene encoding α-galactosidase, an enzyme that breaks down α-*D*-galactooligosaccharides and polysaccharides, including melibiose, raffinose, stachyose, and verbascose. The α-galactosidase gene was detected in only 14% of *P. freudenreichii* genomes and was not identified in any of the typical representatives of ssp. *freudenreichii* (*Fig. 6B*).

Characterization of bacterial defense systems

General characterization. Bacteriophages represent a serious threat to propionic acid bacteria, because their infection decreases cellular metabolic activity, which is very important under production conditions [26]. During evolution, bacteria have developed a variety of defense systems against a bacteriophage infection.

Analysis of 112 previously published *P. freudenreichii* genomes revealed that abortive infection (AbiE, PD-T4-6) and type I and IV restriction–modification (RM) systems were the most common bacterial immune systems, present in over 90% of the genomes. The type I–G CRISPR–Cas system was also quite common, being identified in 74% of the strains (83 of 112) (*Fig* 7). All of these defense mechanisms were also identified in the five study strains.

In addition to the widespread systems, less well-studied anti-phage mechanisms were also found in the five analyzed genomes. For example, the HEC-06 system, which uses nucleases to recognize and degrade modified phage DNA [27], was identified in all strains, except FNCPS 6. In the *P. freudenreichii* population, it is present in 44% of the genomes. The IetAS system, which is characteristic of 54% of strains in this species, is present in all study genomes, except FNCPS 3. Although its mechanism of action has not yet been fully elucidated, it is believed to function synergistically with other defense systems [28].

Interestingly, despite the relatively high detection frequency of systems such as SoFic (20%) and Uzume (25%) in *P. freudenreichii* strains, they were absent in all five study genomes. However, systems less common in the population, Hachiman I (11%) and Pycsar (9%), were identified in three of the five strains.

CRISPR–Cas

CRISPR–Cas is one of the best-known adaptive defense systems, which provides immunity to previously encountered phages by integrating fragments of their DNA into the bacterial genome [29]. The presence and

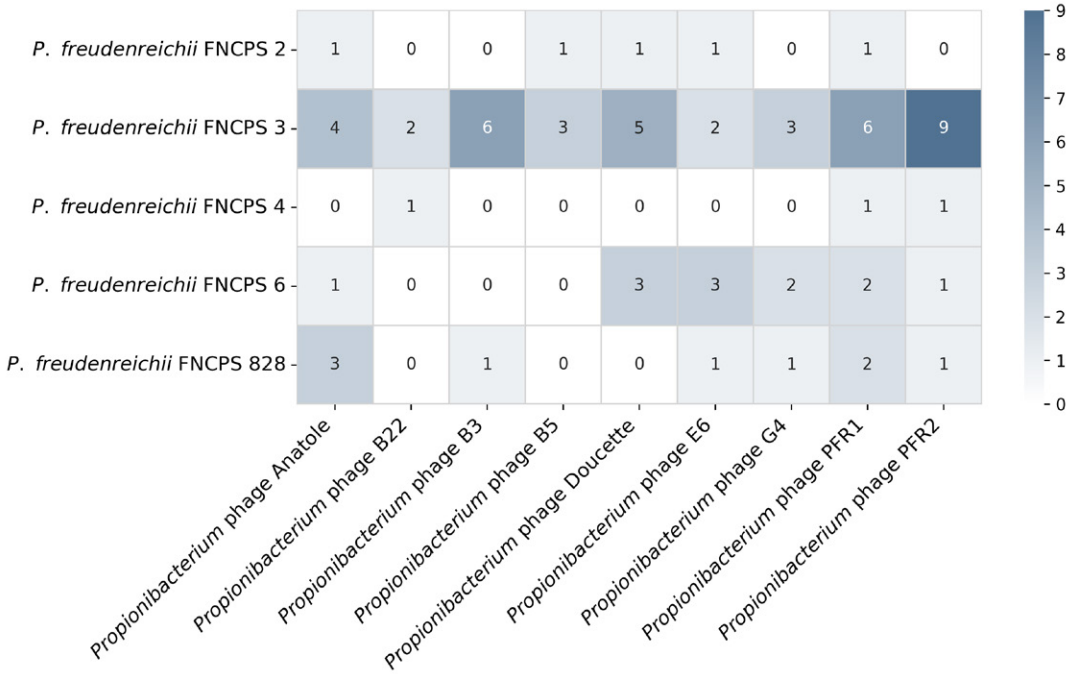

Fig. 8. Heatmap of spacer matches to the genomes of the tested phages. The numbers in cells indicate the number of spacers from each bacterial strain, which are aligned to the corresponding phage genome

composition of CRISPR–Cas systems in the five study *P. freudenreichii* strains were analyzed (*Table 2*).

Strains FNCPS 2, FNCPS 4, and FNCPS 6 were found to possess a complete type I–G system including all the necessary proteins: Cas1, Cas2, Cas3, Cas56, Cas7, and Cas8, which indicates its potential functionality. Strain FNCPS 3 contains two CRISPR–Cas systems: complete I–G and I–E clusters (Cas1, Cas2, Cas3, Cas5, Cas6, Cas7, Cas8, and Cas11), which may provide increased resistance to foreign DNA.

Strain FNCPS 828 was found to possess an incomplete I–G CRISPR–Cas system: it lacked the Cas2 protein involved in inserting new spacers into the CRISPR array. However, other key components were present.

A total of 326 unique spacers were identified in the five *P. freudenreichii* strains. To search for potential targets of CRISPR–Cas systems, we aligned the identified spacers with the previously published genomes of 575 bacteriophages infecting bacteria used in the dairy industry. The analysis revealed matches of 69 spacers (21%) with the genomes of nine different phages, all of which infect propionibacterium (*Fig. 8*).

DISCUSSION

This paper presents the results of an analysis of five phylogenetically related *P. freudenreichii* strains with significant phenotypic differences. Despite a high degree of genomic identity (orthoANI > 99.9), strains *P. freudenreichii* FNCPS 2 and FNCPS 3 differed significantly in a number of phenotypic traits. *P. freudenreichii* FNCPS 2 exhibited stable and high gas-producing activity, both in standard medium and in medium with milk hydrolyzate, whereas FNCPS 3 produced gas only in the presence of hydrolyzate. Both strains were grouped into a single cluster based on their metabolic profiles, indicating adaptation to the environment of their common origin. However, FNCPS 3 did not utilize *L*-arabinose, *D*-raffinose, and glycerol, compounds potentially present in the dairy medium, whereas FNCPS 2 metabolized the largest number of substrates, which is consistent with its pronounced gas-forming activity. Previously, the intensity of gas production in *P. freudenreichii* was shown to be directly related to the availability of metabolites, primarily lactate: upon nutrient depletion, the fermentation level and CO_2 release decreased [30]. Also, the use of carbon substrates, such as whey lactose and glycerol, affects fermentation and gas production in *P. freudenreichii* ssp. *shermanii*, confirming the dependence of this process on the type and diversity of nutrient sources [31, 32]. Thus, differences in the metabolism of easily digestible carbon sources likely explain the observed differences in gas production among strains [33].

Recent studies have demonstrated that the traditional division of *P. freudenreichii* into the subspecies *freudenreichii* and *shermanii*, based on the ability to ferment lactose and reduce nitrates, does not reflect the actual genetic and phenotypic diversity of this

species. Strains with various combinations of these traits have been reported [24, 34], and phylogenetic analysis using MLST has not revealed a clear clustering consistent with the existing subspecies classification [34]. A recent phenotype-based reclassification showed that more than 45% of the strains examined could not be assigned to any of the subspecies [24]. In addition, some strains were probably misclassified as non-nitrate-reducing due to insufficient incubation time [24]. In this regard, the development of genetic markers to correctly distinguish subspecies and predict phenotypes is becoming topical.

Strain FNCPS 828 demonstrated high phylogenetic closeness to type strain *P. freudenreichii* subsp. *shermanii* CCUG 36819 (ESK = 0.99948) and was capable of lactose metabolism, but lacked the full set of genes required for nitrate reduction. The only variable gene associated with this ability in *P. freudenreichii* strains was *narG* encoding the respiratory nitrate reductase alpha subunit, which makes it a potential marker for subspecies identification.

To date, a limited number of studies have been devoted to the defense systems of *P. freudenreichii*. The most common defense mechanism in bacteria is the restriction–modification system [35] also identified in *P. freudenreichii* [36]. As previously reported, the most common CRISPR–Cas system in these bacteria is type I–G, although type I–E is also present [37]. Our analysis of 112 *P. freudenreichii* strains confirmed the predominance of the I–G system, whereas the I–E system was present in approximately 25% of the strains. In addition, AbiE, PD-T4-6, and type I and IV restriction–modification systems were found in more than 90% of the strains analyzed.

All the five study strains contained the type I–G CRISPR–Cas system. In strain FNCPS 828, this system was incomplete and lacked the gene encoding the Cas2 protein. Strain FNCPS 3, in addition to the type I–G system, also possessed an additional type I–E CRISPR–Cas system. This strain was also characterized by the highest number of spacer sequences, including the highest number of spacers whose targets matched previously reported propionibacterium phages. Previously, *P. freudenreichii* strains were reported to contain spacers to phages B22, Anatole, E1, Doucette, E6, G4, and B3 [38]. In our study, only strain FNCPS 3 had spacers to all previously described phages, except E1, and also contained additional spacers to phages B5, PFR1, and PFR2, which reflects significant viral pressure during the co-evolution of the strain with bacteriophages. In addition to CRISPR–Cas systems, all strains were found to possess the most common defense mechanisms in *P. freudenreichii,* as well as the less studied HEC-06 and ietAS complexes, which indicates a layered antiviral defense system in members of this species.

CONCLUSION

In this study, we analyzed both the common traits and intraspecific diversity of *P. freudenreichii* strains, which has direct implications for the dairy industry. Differences in gas-producing activity, the range of metabolized substrates, and bacterial defense systems reflect the adaptation of strains to various technological conditions and underscore the need for their targeted selection to optimize starter cultures. The identification of the *narG* gene as a potential marker for nitrate reduction and the description of defense system diversity, including CRISPR–Cas, open up prospects for more accurate strain typing and prediction of their technological properties. These findings provide the basis for the development of starter cultures with increased stability, predictable characteristics, and resistance to bacteriophages, which ultimately facilitates the generation of more reliable and functional industrial cultures adapted to the profile of specific fermentation processes. ●

This work was supported by a grant from the Ministry of Science and Higher Education of the Russian Federation for major research projects in priority areas of scientific and technological development (No. 075-15-2024-483).

REFERENCES

1. de Rezende Rodovalho V, Rodrigues DLN, Jan G, Le Loir Y, de Azevedo VA, Guédon E. Propionibacterium freudenreichii: General characteristics and probiotic traits. *Prebiotics and Probiotics-From Food to Health.* IntechOpen; 2021. doi: 10.5772/intechopen.97560
2. Turgay M, Falentin H, Irmler S, et al. Genomic rearrangements in the aspA-dcuA locus of Propionibacterium freudenreichii are associated with aspartase activity. *Food Microbiol.* 2022;106:104030. doi: 10.1016/j.fm.2022.104030
3. Loux V, Mariadassou M, Almeida S, et al. Mutations and genomic islands can explain the strain dependency of sugar utilization in 21 strains of Propionibacterium freudenreichii. *BMC Genomics.* 2015;16(1):296. doi: 10.1186/s12864-015-1467-7
4. Piwowarek K, Lipińska E, Hać-Szymańczuk E, Kieliszek M, Kot AM. Sequencing and analysis of the genome of Propionibacterium freudenreichii T82 strain: Importance for industry. *Biomolecules.* 2020;10(2):348. doi: 10.3390/biom10020348

5. Coronas R, Zara G, Gallo A, et al. Propionibacteria as promising tools for the production of pro-bioactive scotta: A proof-of-concept study. *Front Microbiol.* 2023;14:1223741. doi: 10.3389/fmicb.2023.1223741
6. Gautier M, Rouault A, Sommer P, Briandet R. Occurrence of Propionibacterium freudenreichii bacteriophages in Swiss cheese. *Appl Environ Microbiol.* 1995;61(7):2572-2576. doi: 10.1128/aem.61.7.2572-2576.1995
7. Cheng L, Marinelli LJ, Grosset N, et al. Complete genomic sequences of Propionibacterium freudenreichii phages from Swiss cheese reveal greater diversity than Cutibacterium (formerly Propionibacterium) acnes phages. *BMC Microbiol.* 2018;18(1):19. doi: 10.1186/s12866-018-1159-y
8. Prjibelski A, Antipov D, Meleshko D, Lapidus A, Korobeynikov A. Using SPAdes de novo assembler. *Curr Protoc Bioinformatics.* 2020;70(1):e102. doi: 10.1002/cpbi.102
9. Langdon WB. Performance of genetic programming optimised Bowtie2 on genome comparison and analytic testing (GCAT) benchmarks. *BioData Min.* 2015;8(1):1. doi: 10.1186/s13040-014-0034-0
10. Li H, Handsaker B, Wysoker A, et al. The sequence alignment/map format and SAMtools. *Bioinformatics.* 2009;25(16):2078-2079. doi: 10.1093/bioinformatics/btp352
11. Walker BJ, Abeel T, Shea T, et al. Pilon: an integrated tool for comprehensive microbial variant detection and genome assembly improvement. *PLoS One.* 2014;9(11):e112963. doi: 10.1371/journal.pone.0112963
12. Gurevich A, Saveliev V, Vyahhi N, Tesler G. QUAST: quality assessment tool for genome assemblies. *Bioinformatics.* 2013;29(8):1072-1075. doi: 10.1093/bioinformatics/btt086
13. Seppey M, Manni M, Zdobnov EM. BUSCO: assessing genome assembly and annotation completeness. *Methods Mol Biol.* 2019;1962:227-245. doi: 10.1007/978-1-4939-9173-0_14
14. Tatusova T, DiCuccio M, Badretdin A, et al. NCBI prokaryotic genome annotation pipeline. *Nucleic Acids Res.* 2016;44(14):6614-6624. doi: 10.1093/nar/gkw569
15. Olson RD, Assaf R, Brettin T, et al. Introducing the Bacterial and Viral Bioinformatics Resource Center (BV-BRC): a resource combining PATRIC, IRD and ViPR. *Nucleic Acids Res.* 2023;51(D1):D678-D689. doi: 10.1093/nar/gkac1003
16. Brettin T, Davis JJ, Disz T, et al. RASTtk: A modular and extensible implementation of the RAST algorithm for building custom annotation pipelines and annotating batches of genomes. *Sci Rep.* 2015;5:8365. doi: 10.1038/srep08365
17. Payne LJ, Meaden S, Mestre MR, et al. PADLOC: a web server for the identification of antiviral defence systems in microbial genomes. *Nucleic Acids Res.* 2022;50(W1):W541-W550. doi: 10.1093/nar/gkac400
18. Couvin D, Bernheim A, Toffano-Nioche C, et al. CRISPRCasFinder, an update of CRISRFinder, includes a portable version, enhanced performance and integrates search for Cas proteins. *Nucleic Acids Res.* 2018;46(W1):W246-W251. doi: 10.1093/nar/gky425
19. Langmead B, Salzberg SL. Fast gapped-read alignment with Bowtie 2. *Nat Methods.* 2012;9(4):357-359. doi: 10.1038/nmeth.1923
20. Richter M, Rosselló-Móra R, Oliver Glöckner F, Peplies J. JSpeciesWS: a web server for prokaryotic species circumscription based on pairwise genome comparison. *Bioinformatics.* 2016;32(6):929-931. doi: 10.1093/bioinformatics/btv681
21. Lee I, Ouk Kim Y, Park SC, Chun J. OrthoANI: An improved algorithm and software for calculating average nucleotide identity. *Int J Syst Evol Microbiol.* 2016;66(2):1100-1103. doi: 10.1099/ijsem.0.000760
22. Atasever M, Mazlum H. Biochemical Processes During Cheese Ripening. *Vet Sci Pract.* 2024;19(3):174-182. doi: 10.17094/vetsci.1609184
23. Shu L, Wang Q, Jiang W, et al. The roles of diol dehydratase from pdu operon on glycerol catabolism in Klebsiella pneumoniae. *Enzyme Microb Technol.* 2022;157:110021. doi: 10.1016/j.enzmictec.2022.110021
24. de Freitas R, Madec MN, Chuat V, et al. New insights about phenotypic heterogeneity within Propionibacterium freudenreichii argue against its division into subspecies. *Dairy Sci Technol.* 2015;95(4):465-477. doi: 10.1007/s13594-015-0229-2
25. Lledó B, Martínez-Espinosa RM, Marhuenda-Egea FC, Bonete MJ. Respiratory nitrate reductase from haloarchaeon Haloferax mediterranei: biochemical and genetic analysis. *Biochim Biophys Acta.* 2004;1674(1):50-59. doi: 10.1016/j.bbagen.2004.05.007
26. Maske BL, de Melo Pereira GV, da Silva Vale A, Marques Souza DS, De Dea Lindner J, Soccol CR. Viruses in fermented foods: Are they good or bad? Two sides of the same coin. *Food Microbiol.* 2021;98:103794. doi: 10.1016/j.fm.2021.103794
27. Payne LJ, Hughes TCD, Fineran PC, Jackson SA. New antiviral defences are genetically embedded within prokaryotic immune systems. *bioRxiv.* Published online January 30, 2024. doi: 10.1101/2024.01.29.577857
28. Gao L, Altae-Tran H, Böhning F, et al. Diverse enzymatic activities mediate antiviral immunity in prokaryotes. *Science.* 2020;369(6507):1077-1084. doi: 10.1126/science.aba0372
29. Makarova KS, Wolf YI, Iranzo J, et al. Evolutionary classification of CRISPR–Cas systems: a burst of class 2 and derived variants. *Nat Rev Microbiol.* 2020;18(2):67-83. doi: 10.1038/s41579-019-0299-x
30. Aburjaile FF, Rohmer M, Parrinello H, et al. Adaptation of Propionibacterium freudenreichii to long-term survival under gradual nutritional shortage. *BMC Genomics.* 2016;17(1):1007. doi: 10.1186/s12864-016-3367-x
31. Kośmider A, Drożdżyńska A, Blaszka K, Leja K, Czaczyk K. Propionic acid production by Propionibacterium freudenreichii ssp. shermanii using crude glycerol and whey lactose industrial wastes. *Pol J Environ Stud.* 2010;19(6):1249-1253
32. de Assis DA, Machado C, Matte C, Ayub MAZ. High cell density culture of dairy propionibacterium sp. and acidipropionibacterium sp.: A review for food industry applications. *Food Bioproc Tech.* 2022;15(4):734-749. doi: 10.1007/s11947-021-02748-2
33. Dank A, Abee T, Smid EJ. Expanded metabolic diversity of Propionibacterium freudenreichii potentiates novel applications in food biotechnology. *Curr Opin Food Sci.* 2023;52:101048. doi: 10.1016/j.cofs.2023.101048
34. Dalmasso M, Nicolas P, Falentin H, et al. Multilocus sequence typing of Propionibacterium freudenreichii. *Int J Food Microbiol.* 2011;145(1):113-120. doi: 10.1016/j.ijfoodmicro.2010.11.037
35. Georjon H, Bernheim A. The highly diverse antiphage defence systems of bacteria. *Nat Rev Microbiol.* 2023;21(10):686-700. doi: 10.1038/s41579-023-00934-x
36. Deptula P, Laine PK, Roberts RJ, et al. De novo as-

sembly of genomes from long sequence reads reveals uncharted territories of Propionibacterium freudenreichii. *BMC Genomics*. 2017;18(1):790. doi: 10.1186/s12864-017-4165-9
37. Fatkulin AA, Chuksina TA, Sorokina NP, et al. Comparative Analysis of Spacer Targets in CRISPR-Cas Systems of Starter Cultures. *Acta Naturae*. 2024;16(4):81-85. doi: 10.32607/actanaturae.27533
38. Bücher C, Burtscher J, Domig KJ. Propionic acid bacteria in the food industry: An update on essential traits and detection methods. *Compr Rev Food Sci Food Saf*. 2021;20(5):4299-4323. doi: 10.1111/1541-4337.12804

Comprehensive Characterization of Five *Lactococcus* Strains: From Phenotypic Traits to Genomic Features

I. D. Antipenko[1*], N. P. Sorokina[2], I. V. Kucherenko[2], E. V. Kuraeva[2], E. S. Masezhnaya[2], M. Yu. Shkurnikov[1]

[1]Laboratory for Research on Molecular Mechanisms of Longevity, Department of Biology and Biotechnology, HSE University, Moscow, 101000 Russia

[2]All-Russian Research Institute of Butter and Cheese Making, Branch of the Gorbatov Federal Research Center for Food Systems, Uglich, 109316 Russia

[*]E-mail: iantipenko@hse.ru

Received July 16, 2025; in final form, August 21, 2025

DOI: 10.32607/actanaturae.27747

ABSTRACT **The efficiency of dairy product fermentation directly depends on the properties of the lactic acid bacteria used, particularly on their metabolic activity and resistance to bacteriophages. Therefore, an understanding of the relationships between the genetic and phenotypic traits of industrial strains is of elevated importance. In this study, we comprehensively analyzed five *Lactococcus* strains widely used in the Russian dairy industry, combining whole-genome sequencing with phenotypic profiling. Despite the fact of genetic similarity among four of the *L. lactis* strains, we still identified significant differences in their metabolic activity. Comparative structural analysis of previously published genomes of 337 *L. lactis* and 147 *L. cremoris* strains revealed species-specific features of the lactose metabolism; in particular, the absence of the *lacZ* gene in *L. cremoris*. Notably, prophages were found in three of the studied strains, which was in correlation with their reduced acidification activity. *L. lactis* FNCPS 51n and 73n strains displayed resistance to all 50 tested bacteriophages, which may be associated with the presence of the AbiB abortive infection system. These findings underscore the importance of integrating genomic and phenotypic analyses when selecting efficient and phage-resistant *Lactococcus* starters in the dairy industry.**

KEYWORDS *Lactococcus*, **fermentation, genomic profiling, prophages, starter cultures, bacteriophages.**

INTRODUCTION

Members of the genus *Lactococcus*, which are able to efficiently convert lactose into lactic acid, are among the key microorganisms used in the production of fermented dairy products [1].

In the dairy industry, the most widely used cultures are *L. lactis* and *L. cremoris*, with the latter having been recently elevated to the species level [2]. These species differ in the genes associated with carbohydrate and amino acid metabolism [3], as well as in their stress response mechanisms [4].

I addition, there are industrially significant differences at the intraspecific level. For example, the subspecies *L. lactis subsp. lactis* comprises the *diacetylactis* biovar that is capable of metabolizing citrate into diacetyl, a compound that imparts a characteristic buttery, creamy flavor to the product [5], which is an important component of the aroma of cheeses like Camembert, Emmental, and Cheddar [6]. Fermentation strain combinations are selected based on the product type: *diacetylactis* and *L. cremoris* are frequently used in fermented milk production, whereas *L. lactis subsp. lactis* is used in cheesemaking [7]. In the case of lactococcal starters, the fermentation rate has been shown to depend more on the individual characteristics of the strain than on its species classification [8].

The diversity of technologically significant traits in *Lactococcus* has expanded through evolutionary processes and horizontal gene transfer, including plasmids carrying genes associated with sugar metabolism, flavor compound synthesis, and bacteriophage resistance [9]. Different countries and regions use both commercial and local lactic acid bacteria (LAB)

strains selected based on either a long tradition of their use or their unique technological properties [10].

In this study, we comparatively analyzed five *Lactococcus* strains widely used in Russia in the production of fermented dairy products. We also identified the metabolic and genetic characteristics of these strains, including resistance to bacteriophages, and identified the traits underlying their technological value.

EXPERIMENTAL

Strains and culturing conditions

In this study, we used five strains: *L. cremoris* FNCPS 23 (GCA_044990555.1) and *L. lactis* FNCPS 51_n, 43_n, 81_n, and 73_n (GCA_044990575.1, GCA_044990535.1, GCA_044990605.1, and GCA_044990625.1, respectively) from the collection of the All-Russian Research Institute of Butter and Cheese Making (VNIIMS, a branch of the Gorbatov Federal Research Center for Food Systems of the Russian Academy of Sciences). Strains 81_n and 43_n were isolated from indigenous sour cream, and the others were isolated from milk. All the strains were isolated from products from the Yaroslavl region of Russia, except the *L. cremoris* FNCPS 23 strain, which was isolated from a sample from Lithuania.

Phenotypic characterization

Growth was assessed spectrophotometrically using a KFK-3-ZOMZ photoelectric photometer (Zagorsk Optical and Mechanical Plant, Russia). Strains were cultured in 10% sterile reconstituted skim milk added with a 1% inoculum from 16-h culture at 30°C. The optical density (OD) was measured at 560 nm at 60-min intervals for 10 h.

To determine the maximum titratable acidity, 10% sterile reconstituted skim milk was combined with 0.1% of a 16-h lactococcal culture and incubated at 30 ± 1°C for 7 days. Acidity was evaluated by titration with a NaOH solution using a Titrette bottletop burette, 50 mL, (Brand, Germany) according to a previously described method [11] and expressed as Therner degrees (°T).

The pH was measured in 10% sterile reconstituted skim milk before fermentation (control pH, 6.53) and at control points during fermentation using a STARTER 2100 digital pH meter (Ohaus, Switzerland).

Coagulation activity was assessed by the ability of the strain to form a clot in 10% reconstituted skim milk containing 0.015% litmus. For this purpose, sterile litmus milk was combined with an inoculum of each strain in three replicates. Clot formation and litmus color changes (reduction) were assessed hourly during incubation at 30 and 40°C [12].

Acetoin and diacetyl formation was determined using the Voges–Proskauer test: a 48-h culture was mixed with 30% KOH, and color intensity was assessed on a 5-point scale.

Analysis of bacteriophage lytic profiles

The lytic spectrum of bacteriophages was determined by culturing them on double-layer agar in Petri dishes [13]. Sensitivity to bacteriophages was assessed by the presence or absence of zones of clearing at the point of phage spotting.

Genome sequencing

DNA for genome sequencing was isolated using an ExtractDNA Blood and Cells kit (Eurogen, Russia), according to the manufacturer's instructions. DNA libraries were prepared using the MGIEasy Fast FS DNA Library Prep Set V2.0 (Cat. No. 940-001196-00, MGI) according to the manufacturer's protocol. Library quality was assessed using a Qubit 1X dsDNA High Sensitivity DNA Assay kit (Cat. No. Q33230, Thermo Fisher Scientific, USA) and a Qubit Fluorometer (Thermo Fisher Scientific, USA). The length of the DNA library fragments was estimated by QIAxcel Advanced capillary gel electrophoresis using a QX DNA Fast Analysis kit (Cat. No. 929008, Qiagen). Sequencing was performed using an FCS flow cell on an MGI DNBSEQ-G50 platform (BGI, China) in PE150 mode.

Bacterial genomes were assembled using SPAdes [14] in isolate mode. To improve the quality of the final assembly, raw reads were aligned to contigs using Bowtie2 [15], after which the alignment files were sorted and indexed using SAMtools [16] then transferred to Pilon [17] to correct assembly inaccuracies. Assembly quality was assessed using QUAST [18], and the completeness of the assembled genomes was evaluated using BUSCO [19].

Genome analysis

Genome annotation and functional analysis were performed using the NCBI Prokaryotic Genome Annotation Pipeline [20], BlastKOALA [21], and the BV-BRC platform [22]. The presence of metabolic genes in the genomes of the *Lactococcus* strains was analyzed using the BV-BRC platform, based on high-quality, open-access complete genome assemblies: *L. lactis* (n = 337) and *L. cremoris* (n = 147).

Prophages in bacterial genomes were identified using the PHASTEST tool, with deep search settings [23]. Bacterial defense systems were identified using the DefenseFinder web tool (v2.0.0, model database

Table 1. General genome characteristics of the study *Lactococcus* strains

Parameter	*L. lactis* FNCPS 73n	*L. lactis* FNCPS 51n	*L. lactis* FNCPS 43n	*L. lactis* FNCPS 81n	*L. cremoris* FNCPS 23
Genome size, bp	3110896	2258993	3084214	2963565	2528857
GC-composition, %	34.91	35.52	34.97	35.35	35.78
tRNA	75	44	57	60	53
rRNA	8	5	7	8	5
Hypothetical proteins	965	720	907	1121	765
Proteins with established function	3349	2575	3292	3649	2224
CRISPR locus	–	1	1	–	9
Cas protein	–	–	–	–	–
Prophages	–	+	+	–	+
Plasmids	repUS33	repUS4, rep32	repUS33, repUS4	repUS33	repUS33

Table 2. Phenotypic characteristics of the study strains

Strain	Coagulation activity				Limiting acidity, °T	Diacetyl formation, points
	at 30°C, h		at 40°C, h			
	Litmus reduction	Coagulation	Litmus reduction	Coagulation		
L. lactis 73n	8	8	8	8	98	–
L. lactis 81n	6	9	6	11	96	–
L. lactis 51n	10	16	9	11	98	4/5
L. lactis 43n	12 incomplete	12	13	13	90	5/5
L. cremoris 23	13	14	–	–	88	–

v2.0.2) [24]. HMMER-based results were filtered using the following criteria: i-evalue $\leqslant 1e^{-5}$, profile coverage $\geqslant$ 70%, and sequence coverage $\geqslant$ 70%.

Additionally, spacers and CRISPR-Cas system components were identified using CRISPRCasFinder [25]. Plasmids were identified using PlasmidFinder v2.0.1 (database: 2020-07-13) with $\geqslant$ 95% identity and $\geqslant$ 60% coverage thresholds [26].

Phylogenetic analysis

Phylogenetic identification and determination of closely related strains was performed using tetranucleotide correlation analysis via the JSpeciesWS web service [27]. Average nucleotide identity (ANI) comparison was performed using the OrthoANI algorithm [28].

RESULTS

General genomic characteristics

Genomic sequence characteristics of the five analyzed strains are presented in *Table 1*. They proved similar to the reported characteristics of the strains of the corresponding LAB species. Four strains were classified as *L. lactis*, and one strain was classified as *L. cremoris*. The closest type-specific genomes were *L. lactis subsp. lactis* NCDO176 (Z-score > 0.996) for *L. lactis* and *L. cremoris* ATCC 19257 (Z-score = 0.998) for *L. cremoris*. OrthoANI analysis revealed high genome similarity among *L. lactis* strains (> 99.5%), indicating their close relation (*Fig. 1*). The *L. cremoris* strain was characterized by low ANI values (88 to 89%) compared with those of *L. lactis*, confirming its separate species status.

Strain phenotyping

The results of the phenotypic tests of the study strains are presented in *Table 2*.

Growth of the study strains was assessed by changes in optical density (*OD*) during culturing. The *L. lactis* 73n, 81n, and 51n strains demonstrated similar growth rates, whereas *L. lactis* 43n and *L. cremoris* 23 grew more slowly. Seven hours after the start of the experiment, *OD* reached a plateau, which may indicate the end of the active growth phase (*Fig. 2A*).

Differences among the strains were also evident in their limiting acidity: *L. lactis* 43n and *L. cremoris* 23 had the lowest values (*Table 2*). A similar pattern was observed in pH measurements: the steepest decrease

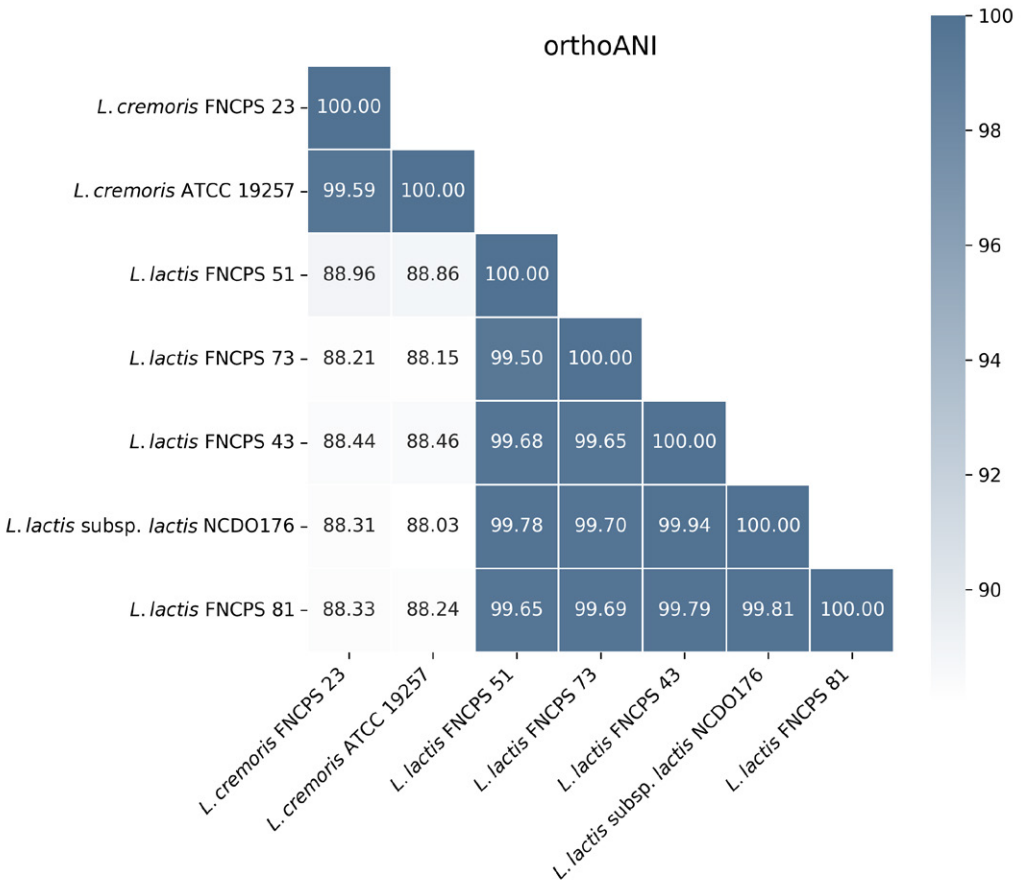

Fig. 1. Heatmap of average nucleotide identity of orthologous genes (orthoANI). Numbers depict the percentage of average nucleotide identity among orthologous genes in different strains. Diagonal numbers (100%) indicate strain self-identity

in the pH of the culture medium was observed for *L. lactis* 73n and 81n, whereas minimal medium acidification by the final stage of culturing was observed for *L. lactis* 43n (*Fig. 2B*).

Assessment of coagulation activity at 30 and 40°C (*Table 2*) confirmed a high metabolic activity for *L. lactis* 73n and 81n: litmus reduction occurred within 6–8 h, and milk coagulation occurred within 8–11 h at both temperatures. *L. lactis* 51n demonstrated a temperature dependence: coagulation occurred 5 h earlier at 40°C than at 30°C. *L. lactis* 43n and *L. cremoris* 23 exhibited the least activity: coagulation occurred after 12–14 h, with 43n exhibiting incomplete litmus reduction. *L. cremoris* 23 did not exhibit coagulation or litmus reduction at 40°C.

Metabolic gene analysis

Proteolytic system and amino acid catabolism. Efficient growth of LAB in milk requires the breakdown of proteins, particularly casein that accounts for approximately 80% of all milk proteins [29]. The casein molecule is enriched in proline residues, which makes it accessible to caseinolytic proteases. Two types of extracellular proteinases, PI and PIII, have been described in *Lactococcus*. They differ in their specificity to casein fractions [29]. Lactosepin I (PI) preferentially hydrolyzes β-casein, forming over 100 oligopeptides of 4 to 30 amino acid residues in length. PIII exhibits a broader specificity, cleaving αs1-, β-, and κ-casein. However, half of industrial *L. lactis* strains lack the *prtP* gene encoding these enzymes [30].

The *prtP* gene was found in three of the five strains studied: *L. cremoris* 23 and *L. lactis* 51n and 81n. The proteins of *L. cremoris* 23 and *L. lactis* 51n showed high identity (97%), whereas a 427 amino acid deletion was found in *L. lactis* 81n, which reduced identity to 76.6–77.2%. All proteins are classified as PI-type proteinases. Comparison with the reference PI-type proteinase (PrtP, P16271) revealed a degree of identity of 97.8% in *L. cremoris* 23, 95.9% in *L. lactis* 51n, and 74.9% in *L. lactis* 81n.

Peptides formed during casein digestion are transported into the cell by the Opp, DtpT, and Dpp systems [31], whose genes are present in all five strains. In the cytoplasm, the peptides are cleaved by exo- and endoproteases [29]. Comparative analysis of the genomes revealed a similar protease gene profile in

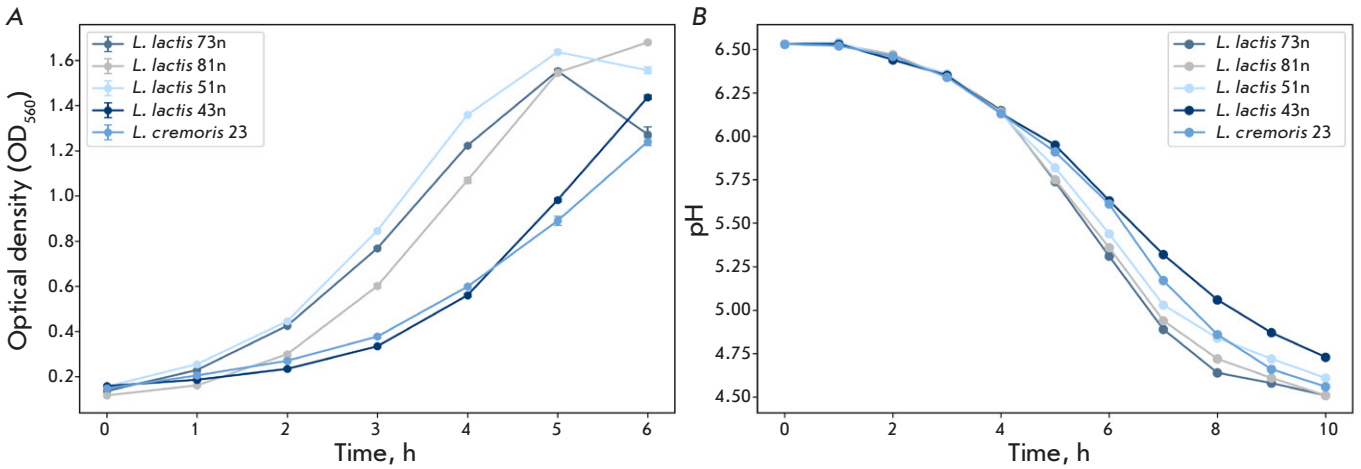

Fig. 2. (*A*) Optical density changes in the culture medium during growth of the study strains. (*B*) pH changes in the culture medium during growth of the same strains

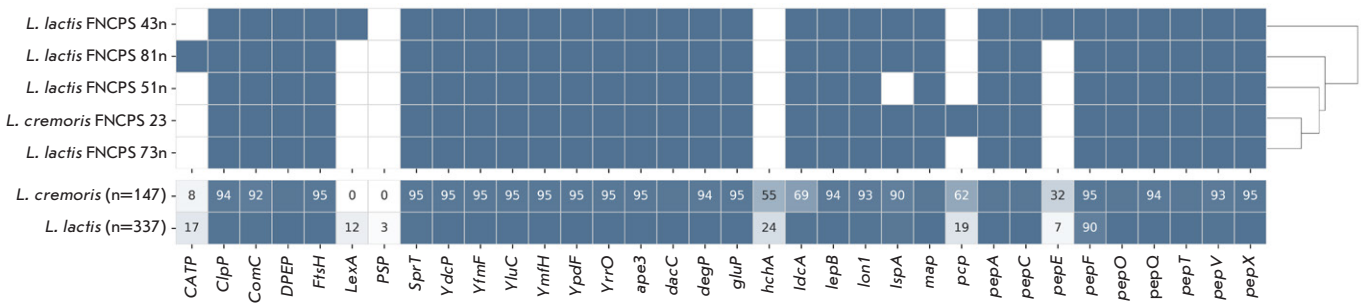

Fig. 3. Presence of proteolytic enzyme genes in *L. lactis* (*n* = 337), *L. cremoris* (*n* = 147), and the five study strains. The upper panel shows a binary matrix: blue indicates the presence of a gene, and white denotes absence. The lower panel displays the percentage of each gene in the population; numerical values are shown only for genes present in less than 95% of the strains. Strains are grouped according to the similarity of their proteolytic genomic profiles; clustering results are presented as a dendrogram

all five strains, which was typical of the general pattern for the genus *Lactococcus* (*Fig. 3*).

The main differences between *L. cremoris* and *L. lactis* resided in the frequency of occurrence of the pyrrolidone carboxylate peptidase (*pcp*, [EC 3.4.19.3]) and peptidase E (*pepE*) genes that, according to the UniProt database, are localized in plasmids. The *pcp* gene was found in 62% of *L. cremoris* strains and only 19% of *L. lactis* strains, whereas *pepE* was found in 32% of *L. cremoris* strains and 7% of *L. lactis* strains. In contrast, the *CATP* (a protein of the CAAX amino-terminal protease family) and *LexA* genes were more common in *L. lactis* (17 and 12%, respectively) than in *L. cremoris* (8 and 0%, respectively).

The analyzed strains differed in the presence of five proteolytic enzyme genes. Namely, the *L. cremoris* 23 strain contained the *pcp* gene, the *L. lactis* 81n strain contained *CATP*, the *L. lactis* 43n strain contained *LexA* and *pepE*, and the 51n strain lacked the *lspA* gene encoding signal lipoprotein peptidase.

Lactose metabolism. Lactose is the main carbon source for LAB in milk. Lactose and galactose are metabolized via the Leloir and tagatose-6-phosphate pathways [32]. Analysis of *L. lactis* strains revealed that 31% (104 of 337) of them contained all the genes of the tagatose-6-phosphate pathway, in contrast to 78% (115 of 147) for the *L. cremoris* strains. All the five studied strains also contained a complete set of the corresponding genes (*Fig. 4*).

The key enzyme of the Leloir pathway is β-galactosidase LacZ, which catalyzes the breakdown of lactose into glucose and galactose. The *lacZ* gene was not found in any of the *L. cremoris* genomes, in-

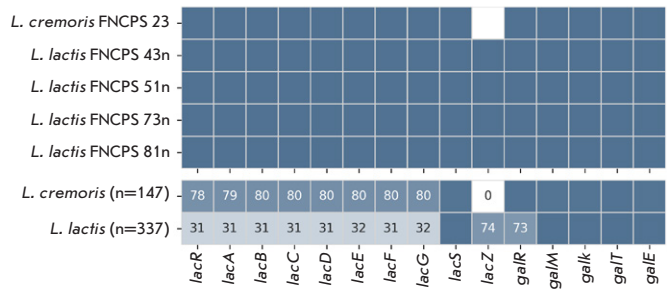

Fig. 4. Presence of lactose metabolism genes in *L. lactis* ($n = 337$), *L. cremoris* ($n = 147$), and the five study strains. The upper panel shows a binary matrix: blue indicates the presence of a gene, and white indicates absence. The lower panel displays the percentage of each gene in the population; numerical values are shown only for genes present in less than 95% of the strains

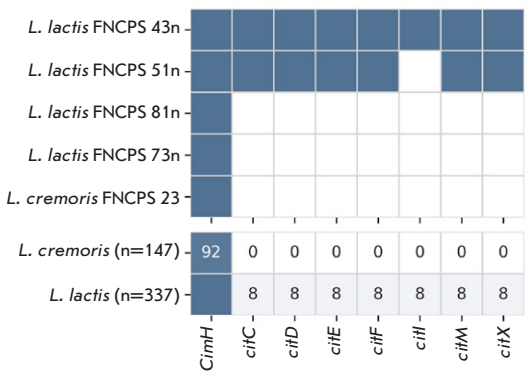

Fig. 5. Presence of citrate metabolism genes in *L. lactis* ($n = 337$), *L. cremoris* ($n = 147$), and the five study strains. The upper panel shows a binary matrix: blue indicates the presence of a gene, and white indicates absence. The lower panel displays the percentage of each gene in the population; numerical values are shown only for genes present in less than 95% of the strains

cluding the strain FNCPS 23, but was identified in 74% of the *L. lactis* strains, including all four studied strains of this species (*Fig. 4*).

Citrate metabolism. Among the study strains, only *L. lactis* 43n and 51n produced diacetyl, with 43n exhibiting higher activity (*Table 2*). Genetic analysis identified the genes responsible for citrate metabolism exclusively in these two strains (*Fig. 5*). All *L. cremoris* representatives lacked the corresponding genes: overall, they were found in only 8% (28 of 337) of the *L. lactis* strains, indicating a limited distribution of the *diacetylactis* biovar.

Bacteriophage resistance

Bacteriophages are a common cause of mishaps in dairy product fermentation, leading to economic losses [33]. DNA of phages specific to *Lactococcus* and *Streptococcus* was found in 37% of samples of milk for fermentation in [34], which makes assessment of phage resistance an important step in the selection of industrial strains.

Figure 6 shows the results of a test of 50 bacteriophages (only those that caused lysis of at least one strain are shown). The *L. lactis* 73n and 51n strains demonstrated resistance to all phages. Strains 81n and 43n and *L. cremoris* 23 were sensitive to some bacteriophages, but they retained resistance to others.

Since differences in phage resistance may be associated with variability in the phage-specific defense systems encoded by bacterial genomes, we conducted our analysis using DefenseFinder (*Fig. 7*). The only system common to all strains was Dnd, an innate immunity mechanism based on DNA phosphorothioate modifications [35].

The AbiB system was detected only in the resistant strains. In addition, AbiC, DS-15, and Dodola were found in *L. lactis* 73n. A unique type II restriction-modification (RM) system was identified in *L. lactis* 51n and was lacking in the other strains. The *L. lactis* 81n strain was the most sensitive to phage infection (4/50 phages caused lysis). This strain lacked a type I RM system restriction enzyme and S subunit genes, as well as PrrC system genes, which may explain its sensitivity to phages. *L. cremoris* 23 demonstrated the highest sensitivity, being lysed by 12 phages that were inactive against other strains. In this case, no defense system present in all *L. lactis* strains but absent in *L. cremoris* 23 was detected, which may indicate the involvement of the cell wall structure in susceptibility to phage infection [36].

Cas (types I–IV) genes were not detected, but CRISPR spacers were present in the genomes of all strains, except *L. lactis* 81n and 73n.

Prophage detection

Genome analysis revealed phage nucleotide sequences, indicating the presence of prophages in most of the study strains. No phage sequence insertions were detected in the *L. lactis* 73n and 81n strains, which indicates the absence of integrated prophages.

Two contigs with phage genes were found in the *L. cremoris* 23 genome: one (33.5 kb) is similar to PHAGE_Lactoc_62503, and the other (8.1 kb) is similar to PHAGE_Lactoc_bIL309. These contigs contain 40 and 11 coding sequences with a GC content of 35.04–35.29%. The first fragment is likely a functional

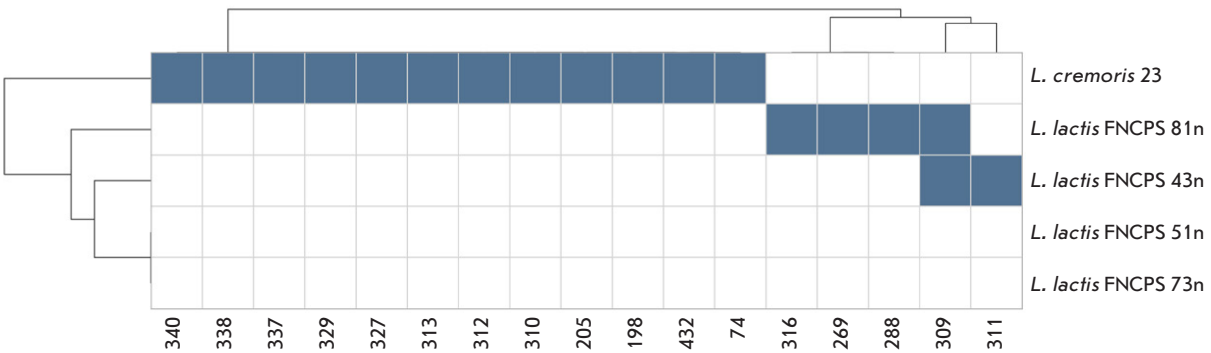

Fig. 6. Lytic spectrum of bacteriophage interactions with the study strains. Bacteriophage names are shown on the X-axis. Blue cells indicate strain sensitivity to the corresponding phage, and white cells indicate lack of the lytic effect. Strains and bacteriophages are grouped according to the similarity of their lytic profiles; clustering results are presented as a dendrogram

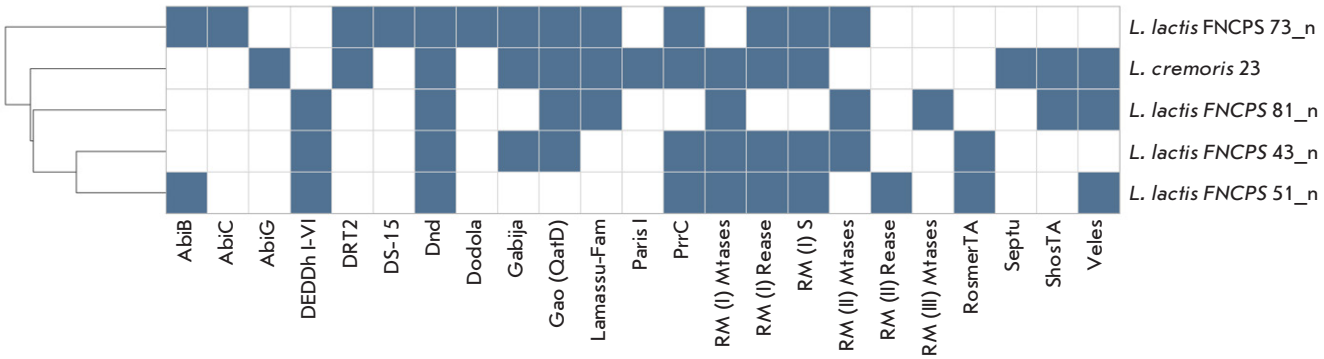

Fig. 7. Profile of the bacterial immune systems in the study strains. Defense system names are shown on the X-axis. The study strains are depicted on the Y-axis. Blue cells indicate the presence of corresponding genes, and white cells indicate absence. Strains are grouped according to similarity in the abundance of defense system genes; clustering results are displayed as a dendrogram

prophage, whereas the second is a residual inactive insertion.

The *L. lactis* 51n genome includes four contigs with phage sequences (2.8–7.3 kb, a total of about 22 kb) which are similar to the phages bIL312, bIL309, D4410, and bIL286. These regions may be either vestigial remnants or parts of a single prophage separated during genome assembly.

In *L. lactis* 43n, we found six phage-containing contigs, with the largest ones reaching 13.5 kb (a total length of approximately 44 kb). We identified sequences similar to the phages bIL312, bIL285, and bIL309, as well as 98201, bIL311, and BK5_T. Phage proteins are synthesized from both DNA strands, which indicates the double-stranded nature of the phage genome.

Since none of the phage DNA fragments in the *L. lactis* 43n and *L. lactis* 51n strains were integrated into the contig containing bacterial genes, we suggest that the identified sequences are DNA of phages that entered the sample during the culture stage, rather than prophages integrated into the genome.

DISCUSSION

In this study, we characterized five industrial strains of the genus *Lactococcus*. Genomic analysis revealed high similarity among the *L. lactis* strains, indicating their clonal origin, whereas *L. cremoris* 23 proved taxonomically distinct. Despite their close relation, the strains differed in their metabolic activities: *L. lactis* 73n and 81n were characterized by high growth and acid production rates, whereas *L. lactis* 43n and *L. cremoris* 23 were characterized by low growth and acid production rates. Strain 51n, which exhibited moderate activity, increased the rate of milk coagulation at 40°C, a temperature unusual for *Lactococcus* [37], which may be important for the production of cooked cheeses (Parmesan, Emmental, etc.). In addi-

tion, the *L. lactis* strains 43n and 51n happened to belong to the *diacetylactis* biovar, which was confirmed by the presence of citrate metabolism genes and the ability to produce diacetyl. In this case, the level of diacetyl production was lower in strain 51n than in 43n, which is probably due to the lack of the citrate lyase transcriptional regulator gene (*citI*) that is involved in the activation of the transcription of the corresponding operon in the presence of citrate [38]. The correlation between diacetyl production activity and the presence of the *citI* gene may be of industrial interest; however, experiments on genome editing and assessment of the mRNA expression of the corresponding genes are necessary to confirm its role.

Genomic analysis revealed genes encoding the Opp, DtpT, and Dpp peptide transport systems, as well as a characteristic set of LAB proteolytic enzymes [29]. The presence of the *prtP* gene encoding type I extracellular protease in the *L. lactis* 51n and *L. cremoris* 23 strains did not correlate with their metabolic activity. Recently, the abundance of individual peptidase genes (*Pcp*, *PepE/G*, *PepI*, *PepR*, *PepL*, and *PepQ*) in lactic acid bacteria genomes has been shown to vary significantly, affecting fermentation activity [39]. The study strains also differed in the composition of the genes encoding individual intracellular peptidases, including *pcp*, *pepE*, *CATP*, *lspA*, and *lexA*. Although the identified variations did not explain the phenotypic differences, they may have functional significance. To confirm their role in phenotype formation, functional testing of the corresponding genes and assessment of proteolytic activity are necessary. Furthermore, the lack of an obvious correlation may be due to differences in the copy numbers of these genes and their possible plasmid localization, which has not been assessed in this study and constitutes a limitation.

We confirmed significant differences in lactose metabolism between *L. lactis* and *L. cremoris*, as previously noted in the literature [1, 40]. The absence of *lacZ* in *L. cremoris* is a species-specific feature, whereas this gene is present in most *L. lactis*. In this case, 80% of *L. cremoris* and one-third of *L. lactis* express genes for the tagatose-6-phosphate pathway. All the *L. lactis* strains studied possess genes for both pathways, which reflects their adaptation to industrial conditions.

The *L. lactis* 73n and 51n strains demonstrated resistance to all the phages tested. These strains are characterized by the presence of the AbiB abortive infection system, but total resistance is likely due to a number of factors. In addition, as shown previously, the AbiB system is effective primarily against *Lactococcus* 936-type phages [41]. Therefore, to confirm its contribution to the resistance of these strains, it is necessary to identify the types of phages used in testing. Our results are consistent with the findings of longitudinal monitoring of phage dynamics in cheese-making factories where lactococcal resistance to bacteriophages was also associated with abortive infection systems (Abi) [42]. It was discovered that starter culture rotation affected the composition and abundance of phages, and that the use of resistant strains may allow one to control the formation of a phage ecosystem at the production site [42]. CRISPR loci were identified in three strains. In this case, the absence of Cas proteins is consistent with data on incomplete or degraded CRISPR systems in *Lactococcus* [43].

Phage DNA sequences were found in the genomes of *L. lactis* 51n and 43n and *L. cremoris* 23. In 51n and 43n, these sequences likely correspond to extragenomic satellite phages or viruses that entered the samples during culturing. The prophage detected in *L. cremoris* 23 is likely integrated, but activation experiments are required to confirm its ability to be induced.

According to previously published data, *L. cremoris* generally exhibits a lower fermentation rate than *L. lactis* [44], although individual *cremoris* strains may exhibit higher activity than some *lactis* strains [8]. The decreased enzymatic activity observed in the *L. lactis* 51n and 43n and *L. cremoris* 23 strains compared with that in *L. lactis* 73n and 81n may also be due to intraspecific differences, the cause of which remains to be determined. Despite the lack of complete cell lysis, the presence of prophages in the genome likely creates additional physiological stress. This may be due to the activation of abortive defense systems (AbiC, AbiG, etc.) that prevent phage dissemination but simultaneously disrupt normal cellular metabolism, which may reduce the overall functional activity of the bacterial colony due to concomitant metabolic stress.

CONCLUSION

This study demonstrated that the metabolic features of *Lactococcus* used in lactic acid fermentation are largely determined by strain-specific characteristics rather than phylogenetic affiliation. This is supported by the pronounced phenotypic variability of closely related *L. lactis* strains. The possible association between the presence of prophages and reduced metabolic activity in the *L. lactis* 51n and 43n and *L. cremoris* 23 strains stresses the importance of phage profiling upon selection of strains for industrial use. Furthermore, the presence of the AbiB system in 51n and 73n strains resistant to a wide range of bacteriophages makes this system a promising marker of

phage resistance. Taken together, these findings emphasize the need for an integrated approach combining genomic and phenotypic methods to effectively select strains with high productivity and resistance for use in the dairy industry. ●

This work was supported by a grant from the Ministry of Science and Higher Education of the Russian Federation for major research projects in priority areas of scientific and technological development (No. 075-15-2024-483).

REFERENCES

1. Kondrotiene K, Zavistanaviciute P, Aksomaitiene J, Novoslavskij A, Malakauskas M. Lactococcus lactis in dairy fermentation—Health-promoting and probiotic properties. *Fermentation*. 2023;10(1):16. doi: 10.3390/fermentation10010016
2. Li TT, Tian WL, Gu CT. Elevation of Lactococcus lactis subsp. cremoris to the species level as Lactococcus cremoris sp. nov. and transfer of Lactococcus lactis subsp. tructae to Lactococcus cremoris as Lactococcus cremoris subsp. tructae comb. nov. *Int J Syst Evol Microbiol*. 2021;71(3):004727. doi: 10.1099/ijsem.0.004727
3. Torres Manno M, Zuljan F, Alarcón S, et al. Genetic and phenotypic features defining industrial relevant Lactococcus lactis, L. cremoris and L. lactis biovar. diacetylactis strains. *J Biotechnol*. 2018;282:25-31. doi: 10.1016/j.jbiotec.2018.06.345
4. Kim WS, Ren J, Dunn NW. Differentiation of Lactococcus lactis subspecies lactis and subspecies cremoris strains by their adaptive response to stresses. *FEMS Microbiol Lett*. 1999;171(1):57-65. doi: 10.1111/j.1574-6968.1999.tb13412.x
5. van Mastrigt O, Mager EE, Jamin C, Abee T, Smid EJ. Citrate, low pH and amino acid limitation induce citrate utilization in Lactococcus lactis biovar diacetylactis. *Microb Biotechnol*. 2018;11(2):369-380. doi: 10.1111/1751-7915.13031
6. Curioni PMG, Bosset JO. Key odorants in various cheese types as determined by gas chromatography-olfactometry. *Int Dairy J*. 2002;12(12):959-984. doi: 10.1016/s0958-6946(02)00124-3
7. Castellone V, Bancalari E, Rubert J, Gatti M, Neviani E, Bottari B. Eating fermented: Health benefits of LAB-fermented foods. *Foods*. 2021;10(11):2639. doi: 10.3390/foods10112639
8. Poudel R, Thunell RK, Oberg CJ, et al. Comparison of growth and survival of single strains of Lactococcus lactis and Lactococcus cremoris during Cheddar cheese manufacture. *J Dairy Sci*. 2022;105(3):2069-2081. doi: 10.3168/jds.2021-20958
9. Kelleher P, Mahony J, Bottacini F, Lugli GA, Ventura M, van Sinderen D. The Lactococcus lactis Pan-Plasmidome. *Front Microbiol*. 2019;10:707. doi: 10.3389/fmicb.2019.00707
10. Panebianco F, Giarratana F, Caridi A, Sidari R, De Bruno A, Giuffrida A. Lactic acid bacteria isolated from traditional Italian dairy products: Activity against Listeria monocytogenes and modelling of microbial competition in soft cheese. *Lwt*. 2021;137:110446. doi: 10.1016/j.lwt.2020.110446
11. Tomovska J, Gjorgievski N, Makarijoski B. Examination of pH, titratable acidity and antioxidant activity in fermented Milk. *J Mater Sci Eng A*. 2016;6(11-12):326-333. doi: 10.17265/2161-6213/2016.11-12.006
12. Gutierrez-Mendez N, Rodríguez-Figueroa JC, Gonzalez-Cordova AF, Nevarez-Moorillon GV, Rivera-Chavira B, Vallejo-Cordoba B. Phenotypic and genotypic characteristics of Lactococcus lactis strains isolated from different ecosystems. *Can J Microbiol*. 2010;56(5):432-439. doi: 10.1139/w10-026
13. Kutter E. Phage host range and efficiency of plating. *Methods Mol Biol*. 2009;501:141-149. doi: 10.1007/978-1-60327-164-6_14
14. Prjibelski A, Antipov D, Meleshko D, Lapidus A, Korobeynikov A. Using SPAdes de novo assembler. *Curr Protoc Bioinformatics*. 2020;70(1):e102. doi: 10.1002/cpbi.102
15. Langdon WB. Performance of genetic programming optimised Bowtie2 on genome comparison and analytic testing (GCAT) benchmarks. *BioData Min*. 2015;8(1):1. doi: 10.1186/s13040-014-0034-0
16. Li H, Handsaker B, Wysoker A, et al. The sequence alignment/map format and SAMtools. *Bioinformatics*. 2009;25(16):2078-2079. doi: 10.1093/bioinformatics/btp352
17. Walker BJ, Abeel T, Shea T, et al. Pilon: an integrated tool for comprehensive microbial variant detection and genome assembly improvement. *PLoS One*. 2014;9(11):e112963. doi: 10.1371/journal.pone.0112963
18. Gurevich A, Saveliev V, Vyahhi N, Tesler G. QUAST: quality assessment tool for genome assemblies. *Bioinformatics*. 2013;29(8):1072-1075. doi: 10.1093/bioinformatics/btt086
19. Seppey M, Manni M, Zdobnov EM. BUSCO: assessing genome assembly and annotation completeness. *Methods Mol Biol*. 2019;1962:227-245. doi: 10.1007/978-1-4939-9173-0_14
20. Tatusova T, DiCuccio M, Badretdin A, et al. NCBI prokaryotic genome annotation pipeline. *Nucleic Acids Res*. 2016;44(14):6614-6624. doi: 10.1093/nar/gkw569
21. Kanehisa M, Sato Y, Morishima K. BlastKOALA and GhostKOALA: KEGG Tools for Functional Characterization of Genome and Metagenome Sequences. *J Mol Biol*. 2016;428(4):726-731. doi: 10.1016/j.jmb.2015.11.006
22. Olson RD, Assaf R, Brettin T, et al. Introducing the Bacterial and Viral Bioinformatics Resource Center (BV-BRC): a resource combining PATRIC, IRD and ViPR. *Nucleic Acids Res*. 2023;51(D1):D678-D689. doi: 10.1093/nar/gkac1003
23. Wishart DS, Han S, Saha S, et al. PHASTEST: faster than PHASTER, better than PHAST. *Nucleic Acids Res*. 2023;51(W1):W443-W450. doi: 10.1093/nar/gkad382
24. Tesson F, Planel R, Egorov AA, et al. A Comprehensive Resource for Exploring Antiphage Defense: DefenseFinder Webservice,Wiki and Databases. *Peer Community J*. 2024;4:e91. doi: 10.24072/pcjournal.470
25. Couvin D, Bernheim A, Toffano-Nioche C, et al. CRISPRCasFinder, an update of CRISRFinder, includes a portable version, enhanced performance and integrates search for Cas proteins. *Nucleic Acids Res*. 2018;46(W1):W246-W251. doi: 10.1093/nar/gky425
26. Carattoli A, Zankari E, García-Fernández A, et al. In Silico Detection and Typing of Plasmids using PlasmidFinder and Plasmid Multilocus Sequence Typing. *Antimicrob Agents Chemother*. 2014;58(7):3895-3903. doi: 10.1128/aac.02412-14

27. Richter M, Rosselló-Móra R, Oliver Glöckner F, Peplies J. JSpeciesWS: a web server for prokaryotic species circumscription based on pairwise genome comparison. *Bioinformatics*. 2016;32(6):929-931. doi: 10.1093/bioinformatics/btv681
28. Lee I, Ouk Kim Y, Park SC, Chun J. OrthoANI: An improved algorithm and software for calculating average nucleotide identity. *Int J Syst Evol Microbiol*. 2016;66(2):1100-1103. doi: 10.1099/ijsem.0.000760
29. Kieliszek M, Pobiega K, Piwowarek K, Kot AM. Characteristics of the proteolytic enzymes produced by lactic acid bacteria. *Molecules*. 2021;26(7):1858. doi: 10.3390/molecules26071858
30. Passerini D, Beltramo C, Coddeville M, et al. Genes but Not Genomes Reveal Bacterial Domestication of Lactococcus Lactis. *PLoS One*. 2010;5(12):e15306. doi: 10.1371/journal.pone.0015306
31. Venegas-Ortega MG, Flores-Gallegos AC, Martínez-Hernández JL, Aguilar CN, Nevárez-Moorillón GV. Production of Bioactive Peptides from Lactic Acid Bacteria: A Sustainable Approach for Healthier Foods. *Compr Rev Food Sci Food Saf*. 2019;18(4):1039-1051. doi: 10.1111/1541-4337.12455
32. Iskandar CF, Cailliez-Grimal C, Borges F, Revol-Junelles AM. Review of lactose and galactose metabolism in Lactic Acid Bacteria dedicated to expert genomic annotation. *Trends Food Sci Technol*. 2019;88:121-132. doi: 10.1016/j.tifs.2019.03.020
33. Garneau JE, Moineau S. Bacteriophages of lactic acid bacteria and their impact on milk fermentations. *Microb Cell Fact*. 2011;10(S1):S20. doi: 10.1186/1475-2859-10-S1-S20
34. del Rio B, Binetti AG, Martín MC, Fernández M, Magadán AH, Alvarez MA. Multiplex PCR for the detection and identification of dairy bacteriophages in milk. *Food Microbiol*. 2007;24(1):75-81. doi: 10.1016/j.fm.2006.03.001
35. Gan R, Wu X, He W, et al. DNA phosphorothioate modifications influence the global transcriptional response and protect DNA from double-stranded breaks. *Sci Rep*. 2014;4:6642. doi: 10.1038/srep06642
36. Ainsworth S, Sadovskaya I, Vinogradov E, et al. Differences in Lactococcal Cell Wall Polysaccharide Structure Are Major Determining Factors in Bacteriophage Sensitivity. *mBio*. 2014;5(3):e00880-14. doi: 10.1128/mbio.00880-14
37. Chen J, Shen J, Ingvar Hellgren L, Ruhdal Jensen P, Solem C. Adaptation of Lactococcus lactis to high growth temperature leads to a dramatic increase in acidification rate. *Sci Rep*. 2015;5:14199. doi: 10.1038/srep14199
38. Martin MG, Magni C, de Mendoza D, López P. CitI, a Transcription Factor Involved in Regulation of Citrate Metabolism in Lactic Acid Bacteria. *J Bacteriol*. 2005;187(15):5146-5155. doi: 10.1128/jb.187.15.5146-5155.2005
39. Shi Z, Fan X, Tu M, Wu Z, Pan D. Comparison of changes in fermented milk quality due to differences in the proteolytic system between Lactobacillus helveticus R0052 and Lactococcus lactis subsp. lactis JCM5805. *Food Biosci*. 2023;51:102271. doi: 10.1016/j.fbio.2022.102271
40. Rodríguez J, Vázquez L, Flórez AB, Mayo B. Phenotype testing, genome analysis, and metabolic interactions of three lactic acid bacteria strains existing as a consortium in a naturally fermented milk. *Front Microbiol*. 2022;13:1000683. doi: 10.3389/fmicb.2022.1000683
41. Chopin MC, Chopin A, Bidnenko E. Phage abortive infection in lactococci: variations on a theme. *Curr Opin Microbiol*. 2005;8(4):473-479. doi: 10.1016/j.mib.2005.06.006
42. Jolicoeur AP, Lemay ML, Beaubien E, et al. Longitudinal Study of Lactococcus Phages in a Canadian Cheese Factory. *Appl Environ Microbiol*. 2023;89(5):e0042123. doi: 10.1128/aem.00421-23
43. Mileriene J, Aksomaitiene J, Kondrotiene K, et al. Whole-Genome Sequence of Lactococcus lactis Subsp. lactis LL16 Confirms Safety, Probiotic Potential, and Reveals Functional Traits. *Microorganisms*. 2023;11(4):1034. doi: 10.3390/microorganisms11041034
44. Garvie EI, Farrow JAE. NOTES: Streptococcus lactis subsp. cremoris (Orla-Jensen) comb. nov. and Streptococcus lactis subsp. diacetilactis (Matuszewski et al.) nom. rev., comb. nov. *Int J Syst Bacteriol*. 1982;32(4):453-455. doi: 10.1099/00207713-32-4-453

Dimephosphon Radioprotective Properties on the Model of Radiation Injury *In Vivo*

D. A. Kiseleva[1*], M. A. Melchenko[1,2], O. I. Yarovaya[1,2], N. V. Basov[1,2], A. D. Rogachev[1,2], A. G. Pokrovsky[2], N. F. Salakhutdinov[1], T. G. Tolstikova[1]

[1]N.N. Vorozhtsov Novosibirsk Institute of Organic Chemistry, Siberian Branch of Russian Academy of Sciences, Novosibirsk, 630090 Russia

[2]Novosibirsk State University, Novosibirsk, 630090 Russia

[*]E-mail: dasha.halikova@mail.ru

Received March 26, 2025; in final form, July 02, 2025

DOI: 10.32607/actanaturae.27662

ABSTRACT **Radiation therapy is a commonly used cancer treatment modality. However, its application is limited because of its toxicity to healthy tissue. The search for effective radioprotective agents remains one of the key goals of radiation oncology and radiobiology. This study focuses on experimental modeling of radiation injury in animals and the investigation of Dimephosphon radioprotective properties, a drug exhibiting anti-acidotic, antitumor, and antioxidant activities. It was shown that 14-day administration of the drug at a dose of 750 mg/kg after single-dose (5 Gy) irradiation of CD-1 mice resulted in a local radioprotective effect, reducing the severity of the radiation-induced injury to the intestinal epithelium and splenic capsule. The results of metabolomic screening revealed that the levels of the key metabolites responsible for antioxidant properties such as alpha-tocopherol, nicotinamide riboside, N-carbamoyl-L-aspartate, and adenylosuccinate were significantly increased, indicating that the Dimephosphon drug provides enhanced antioxidant protection.**

KEYWORDS **radioprotective properties, radiation injury, Dimephosphon, metabolomic screening.**

INTRODUCTION

Cancer remains one of the leading causes of mortality worldwide. As of 2023, the incidence rate of malignant neoplasms in Russia was more than 670,000 new cases; and this parameter was on the increase by 8.0% compared to 2022 [1]. Radiation therapy (RT) is an effective method for combatting malignancies. It is estimated that ~ 50% of cancer patients receive radiation therapy, whereas ~ 70% require this treatment, and in some cases radiation therapy is the sole cancer treatment option available [2]. The lack of selectivity toward cancer cells, which disrupts metabolic processes in healthy tissues and organs and results in severe complications, including radiation-induced injury, is the primary factor limiting broader application of RT [3]. The emergence of more selective RT modalities does not eliminate the toxicity to healthy tissues. Therefore, approaches that would combine radiation therapy and systemic administration of radioprotective agents are currently being investigated. Importantly, the radioprotective drugs approved for use in Russia are associated with serious adverse effects such as splenic rupture, acute respiratory distress syndrome, alveolar hemorrhage, and atrioventricular block, which limit the widespread application of these agents [4–6]. For this reason, the radioprotective potential of natural compounds is currently being extensively investigated; however, all the developments remain at the preclinical phase [7, 8]. Therefore, searching for effective low-toxicity agents protecting healthy tissues against radiation-induced damage during radiation therapy remains a critical challenge in radiation oncology and radiobiology.

To perform preclinical studies of novel radioprotective agents and optimize treatment strategies for different types of cancer, it is essential to be in possession of adequate animal models of radiation injury that would reliably and accurately replicate the key clinical manifestations and pathogenetic mechanisms of the disease in humans. The suitability of X-ray radiation with a peak voltage of 320 kV for inducing radiation injury on *in vivo* models has previously been demonstrated [9].

We have developed a procedure for inducing radiation injury in laboratory animals (mice) that allows one to assess the efficacy and safety of radioprotective agents. The original drug Dimephosphon, manufactured in Russia, was selected as a radioprotective

Fig. 1. The structural formula of the active substance of Dimephosphon

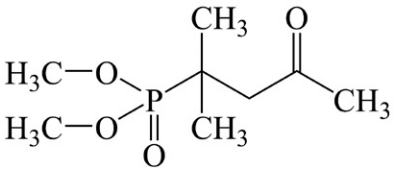

agent for validating this procedure. Dimephosphon is an aqueous solution of (1,1-dimethyl-3-oxobutyl)phosphonic acid dimethyl ester (*Fig. 1*); it is characterized by low toxicity and high bioavailability and can easily cross the blood–tissue barriers [10, 11].

In 1983, the drug (a 15% solution for oral and topical administration) was approved for clinical use as an anti-acidotic and vasoactive agent [12–14]. Later, the efficacies of three radioprotective compounds (sea buckthorn oil, Evdoshchenko oil solution, and drug Dimephosphon) were evaluated in the context of radiation therapy for laryngeal cancer. Administration of Dimephosphon resulted in the smallest quantitative differences in the laryngeal air column thickness, a key indicator of acute radiation syndrome, measured before the initiation of radiation therapy and after a 40-Gy dose had been administered [15].

EXPERIMENTAL

Animals

All the manipulations with animals were conducted in strict compliance with the legislation of the Russian Federation, Decision No. 81 "On the Approval of the Rules of Good Laboratory Practice of the Eurasian Economic Union in the Field of Drug Circulation" dated November 3, 2016, and the provisions of Directive 2010/63/EU of the European Parliament and the Council of the European Union dated September 22, 2010 on the protection of animals used for scientific purposes. The study protocol was approved by the Bioethics Commission of the Laboratory of Pharmacological Research, N.N. Vorozhtsov Novosibirsk Institute of Organic Chemistry, SB RAS (Protocol No. R-14-2025-01-01 dated January 10, 2025).

Female outbred CD-1 mice (weight, 25–30 g) were procured from the SPF vivarium of the Institute of Cytology and Genetics, SB RAS, Russia. The animals were housed under optimal conditions (temperature, 21 ± 1.5°C; humidity, 40–60%; 12-h day/night cycle; ad libitum access to water and pelleted forage). Prior to the experiments, the mice were acclimatized to the housing conditions for 1 week.

Compound under study

Dimephosphon® (OJSC "Tatchempharmpreparaty", Kazan, Russia) used in this study was administered intragastrically at a dose of 750 mg/kg (0.1 mL per 10 g of body weight). The animals received the first dose 3 h prior to irradiation; the drug was then administered as a single dose every 24 h during 14 days.

Experimental design and setup

An X-RAD 320 irradiation system (Precision X-Ray Inc., Branford, CT, USA) with a fixed distance from a radiation source (SSD 50 cm), equipped with a medium-hardness filter (0.75 mm tin, 0.25 mm copper, 1.5 mm aluminum), was used to experimentally induce radiation injury in mice. Total-body single-dose (5 and 7.5 Gy) irradiation of mice (n = 6) was performed at a dose rate of ~ 0.98 Gy/min. The survival rate of the animals was assessed on days 4, 7, 11, and 14 post-irradiation, and a radiation dose for studying the radioprotective effect of the drug was selected.

The radioprotective properties of Dimephosphon were assessed at the next stage in mice that had received a single selected radiation dose. The animals were randomly allocated into three groups (n = 8): mice in group 1 were administered 750 mg/kg Dimephosphon (DMPN); mice in group 2 were administered 750 mg/kg Dimephosphon + total-body irradiation (DMPN + IR); and mice in group 3 were subjected to total-body irradiation only (IR).

Animals' body weight was measured prior to irradiation (point 0) and then on days 4, 7, 11, and 14. Blood samples were collected from the retro-orbital sinus to conduct metabolomic screening and hematology testing. All the mice were euthanized on day 14; their organs (the thymus, heart, lungs, liver, and spleen) were weighed to calculate the organ mass indices and further used for histological examination.

Hematology testing

Complete blood count was performed using a MINDRAY BC-2800 Vet automatic hematology analyzer (Shenzhen Mindray Animal Medical Technology Co. Ltd., China). Peripheral blood samples (20 μL) collected into vials containing a standard volume of isotonic diluent were used for testing. The total counts of leukocytes, erythrocytes, platelets, hemoglobin concentration, and hematocrit, were determined.

Histological examination

The collected organs (the thymus, heart, lungs, liver, and spleen) were weighed to calculate the organ mass indices. The spleen and small intestine were fixed in 10% neutral buffered formalin, dehydrated in ethanol and xylene of different concentrations using a MICROM automated system (Carl Zeiss, Germany). The tissue samples were then embedded in paraffin blocks. Sections (4 μm thick) were prepared using

a rotary microtome and stained with Hematoxylin and Eosin (H&E). The prepared samples were examined by optical microscopy (×100 magnification), with Köhler illumination alignment. The AxioVision software was used to perform a morphometric analysis of the histopathological images and calculate the intervillous space, length of intestinal villi, and thickness of the splenic capsule for assessing the severity of organ damage.

Metabolomic screening

Sample preparation. Dried whole-blood spot samples were prepared for metabolomic analysis. A 10 μL aliquot of blood was applied to Whatman 903™ protein saver cards (GE Healthcare, #10534612, USA) and air-dried at room temperature for 3 h. The samples were stored at –70°C until sample preparation, which was conducted in accordance with the protocol described in ref. [16]. The dried blood spots were resected from the cards, placed into 0.5 mL polypropylene vials, and 150 μL of a pre-cooled MeOH–ACN–H_2O mixture (40:40:20, v/v/v) was added. The samples were incubated at +4...+5°C for 20 min and centrifuged at 16,000 rpm (~ 24,000 *g*) on an Eppendorf 5417R centrifuge for 10 min at +4°C. The supernatant was transferred to plastic inserts for chromatographic vials and analyzed.

Analysis of the samples

The samples were analyzed by high-performance liquid chromatography–tandem mass spectrometric assay (HPLC-MS/MS) according to ref. [17]. Chromatographic separation was conducted on an LC-20AD Prominence chromatography system (Shimadzu, Japan) and an CTO-10ASvp column oven. The mobile phase consisted of eluent A (a 20 mM aqueous solution of ammonium carbonate adjusted to pH 9.8 with a 25% aqueous solution of ammonia, and 5 vol.% acetonitrile) and eluent B (100% acetonitrile). Each sample was analyzed twice: in the hydrophilic interaction liquid chromatography (HILIC) and reverse-phase chromatography (RPC) modes. The following conditions were used. HILIC gradient: 0 min – 98% B, 2 min – 98% B, 6 min – 0% B, 10 min – 0% B. The column was equilibrated for 4 min. RPC gradient: 0 min – 0% B, 1 min – 0% B, 6 min – 98% B, 16 min – 98% B. The column was equilibrated for 3 min. The flow rate in each analysis was 300 μL/min. Sample volume was 2 μL. In both chromatography modes, the analysis was conducted using a monolithic column (2 × 60 mm) based on 1-vinyl-1,2,4-triazole. The monolithic material of the column was synthesized according to ref. [18]: copolymerization of a mixture consisting of styrene/divinylbenzene/1-vinyl-1,2,4-triazole monomers at a 10 : 50 : 40 volume ratio was performed in a glass tube.

Mass-spectrometric detection was conducted using an API 6500 QTRAP mass spectrometer (AB SCIEX, USA) equipped with an electrospray ionization source. A total of 489 metabolites were detected in the multiple reaction monitoring (MRM) mode in the regions of positive and negative ionization with polarity switching. The key mass spectrometric parameters were as follows: voltage of the ion source (IS), 5,500 and −4,500 V for the positive and negative ionization, respectively; drying gas temperature, 475°C; gas in the collision-activated dissociation cell was set at "high"; pressure of the nebulizing gas (GS1), drying gas (GS2), and the curtain gas (CUR) was 33, 33 and 30 psi, respectively. The declustering potential (DP) was ±91 V, the entrance potential (EP) was ±10 V, and the collision cell exit potential (CXP) was ±9 V. The dwell time for each MRM transition was 3 ms. Instrument control and data acquisition were performed using the Analyst 1.6.3 software (AB SCIEX). The precursor-to-product ion transitions, metabolite names, fragmentation times, and the respective collision energies were adapted from refs [19, 20].

Statistical analysis

Statistical analysis was performed with the Statistica 10.0 software (StatSoft, USA). The data were tested for normality using the Kolmogorov–Smirnov test. The Student's t-test was used for the normally distributed samples; the Mann–Whitney U test was employed for the nonnormally distributed samples. The results are presented as the mean ± standard error of the mean (M ± SEM) or the mean ± confidence interval for nonparametric samples. The differences were considered statistically significant at $p < 0.05$. The diagrams were plotted using the Seaborn library (Python) and the Origin software.

RESULTS AND DISCUSSION

Assessment of animals' survival rate exposed to irradiation with 5 and 7.5 Gy doses

The optimal radiation dose for modeling radiation injury in experimental animals was determined at the first stage of the study. Total-body irradiation at a dose of 7.5 Gy caused 100% lethality on experiment day 11 (*Fig. 2*). Hence, the absolute lethal dose (causing death in 100% of mice) was identified; its further use was unreasonable. After single-dose (5 Gy) irradiation, 50% of mice remained alive by the end of the experiment (day 14), corresponding to the sublethal radiation dose (death in 50% of mice, LD_{50}).

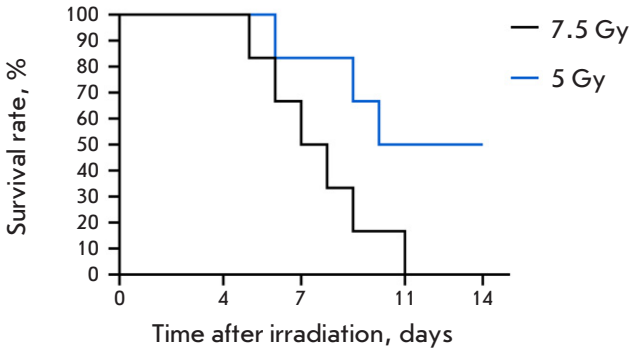

Fig. 2. The survival rate of CD-1 mice after single-dose irradiation (5 and 7.5 Gy) ($n = 6$)

The survival rate, mean body weight, and hematological parameters of mice exposed at a dose of 5 Gy radiation and administered Dimephosphon

The effect of Dimephosphon oral administration on the organism of experimental animals subjected to single-dose (5 Gy) total-body irradiation was evaluated at the second stage of the study.

The use of Dimephosphon did not increase the survival rate of the animals after exposure to X-ray radiation (*Fig. 3A*). On experiment day 14, the survival rate in the IR group was 50%, being ~ 40% in the DMPN + IR group. This was probably caused by the varying animal sensitivity to radiation [21], since the LD_{50} of the drug orally administered to mice was 3 g/kg [10]. Furthermore, the mean body weight of the irradiated animals was significantly reduced compared to the baseline, without statistical differences between the groups of irradiated (DMPN + IR, IR) and non-irradiated mice (DMPN) (*Fig. 3B*).

According to published scholarship, the development of radiation injury involves three syndromes: the hematopoietic (occurring at doses > 1 Gy), gastrointestinal (at doses of 6–15 Gy), and cerebrovascular (at doses > 20 Gy) ones. In other words, the hematopoietic system, spleen, thymus, and intestinal epithelium are first to sustain damage in response to exposure to ionizing radiation [22].

The dynamics of hematological parameters were identical across the groups of irradiated animals. On day 4 post-irradiation, mice in both the DMPN + IR and IR groups had acute leukopenia; leukocyte counts started to recover on day 14 in both groups (*Fig. 4A*). The decline in erythrocyte count was related to a concurrent reduction in the hematocrit and hemoglobin levels on days 4 through 14 (*Fig. 4C–E*). Platelet count dropped abruptly by day 7 but started to recover on day 14 post-irradiation. Administration of Dimephosphon statistically significantly accelerated only the platelet count recovery in irradiated animals on day 14 (*Fig. 4B*).

Histological examination of the internal organs of mice exposed at a dose of 5 Gy radiation and administered Dimephosphon

Exposure to X-ray radiation statistically significantly altered the mass index of the thymus (*Table 1*). The observed acute involution of the thymus (reduction in its mass index more than twofold) in the DMPN + IR and IR groups was probably associated with an abrupt decline in the counts of T-lymphocytes and thymic epithelial cells [23]. The mass ratio of the spleen was also increased in the groups of mice exposed to radiation. However, this effect was statistically non-significant.

The histological data showed that mice in the DMPN group had a typical structure of the small intestine, with normal length of the intestinal villi and normal crypt depth (*Fig. 5B*). Contrariwise, mice in the IR group suffered radiation-induced injury to the

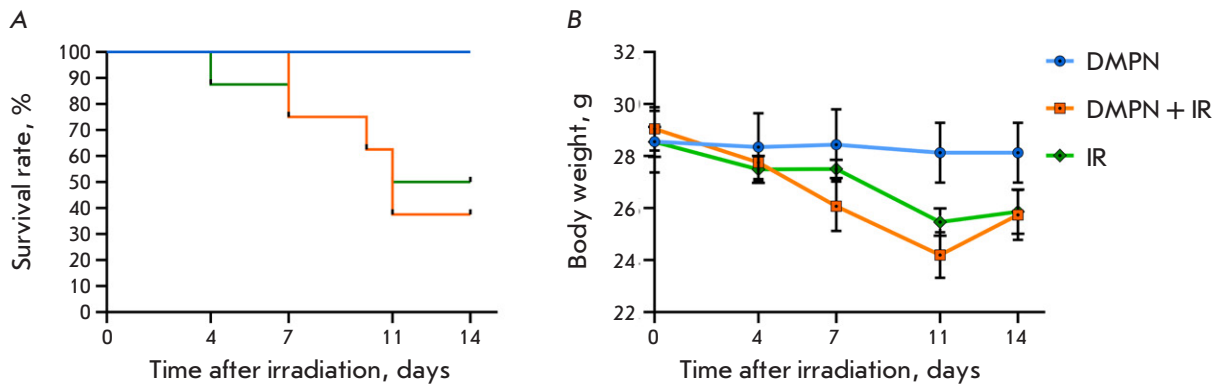

Fig. 3. The effect of oral administration of 750 mg/kg Dimephosphon 3 h before 5 Gy total-body irradiation and daily after in CD-1 mice ($n = 8$, M ± SEM). (*A*) animal survival; (*B*) the mean body weight dynamics of the animals

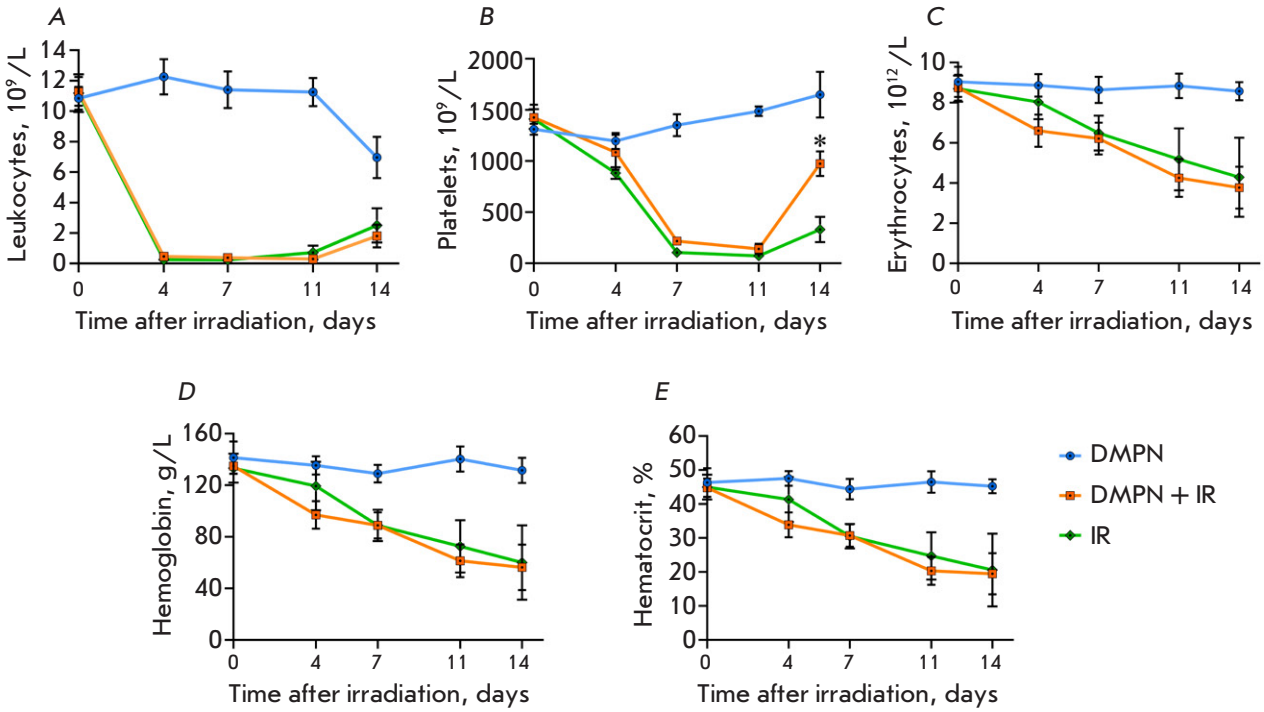

Fig. 4. The dynamics of the hematological parameters of the blood of CD-1 mice ($n = 8$, M ± SEM) that received Dimephosphon after total-body irradiation at a dose of 5 Gy. (*A*) leukocytes; (*B*) platelets; (C) erythrocytes; (*D*) hemoglobin; and (*E*) hematocrit on days 4, 7, 11, and 14 post-irradiation. The statistical analysis was performed using the Mann–Whitney U test, *$p < 0.05$ compared to IR

small intestine such as atrophy and shortening of the intestinal villi, along with an increased distance between them (*Fig. 5A,E*). Furthermore, thickness of the small intestinal mucosa was smaller compared to the DMPN and DMPN + IR groups (*Fig. 5B*). Administration of Dimephosphon to irradiated mice mitigated the severity of the radiation-induced injury: increased length of the intestinal villi, reduced intervillous space, and greater crypt depth were observed (*Fig. 5A,D*). Mucosa thickness in the DMPN + IR group was greater than that in the DMPN group, being probably related to enhanced regeneration of the intestinal epithelium (*Fig. 5B*).

The splenic architecture morphology in the animals in the DMPN group was normal (white and red pulp separated by a marginal zone and covered by a connective tissue capsule) (*Fig. 6B*). The splenic architecture was altered by day 14 post-irradiation: white pulp had expanded because of cell proliferation, and the distinct boundary between the red and white pulp had disappeared (*Fig. 6D*). Massive lymphocytic infiltration of the red pulp was observed, with lymphocytes initially residing in splenic sinusoids and ligaments. The sinusoidal spaces were enlarged and had increased blood filling. Furthermore, thickness of the splenic capsule in the IR group was reduced compared to the control group (*Fig. 6A*), which is consistent with the observed trend toward an elevated mass ratio for this organ (*Table 1*) and is an indicator of splenomegaly [24]. Administration of Dimephosphon to mice exposed to radiation did not change the architecture of the splenic parenchyma but contributed to a restoration of normal thickness for the splenic capsule (*Fig. 6A,C*).

Hence, the histological findings give grounds for suggesting that Dimephosphon exerts a local radioprotective effect by mitigating the severity of radiation-induced injury to the small intestine and splenic inflammation.

Table 1. Organ mass index (%) of CD-1 mice after total-body irradiation at a dose of 5 Gy (M ± SEM)

Organ	DMPN	DMPN+IR	IR
Thymus	0.38 ± 0.01	0.15 ± 0.02*	0.11 ± 0.03*
Heart	0.52 ± 0.02	0.53 ± 0.01	0.46 ± 0.02
Lungs	0.98 ± 0.07	1.05 ± 0.07	0.96 ± 0.05
Liver	5.85 ± 0.27	4.78 ± 0.60	5.34 ± 0.44
Spleen	0.74 ± 0.11	1.18 ± 0.40	1.29 ± 0.23

Note: Statistical analysis was carried out using the Mann–Whitney U test, *$p < 0.05$ compared to DMPN.

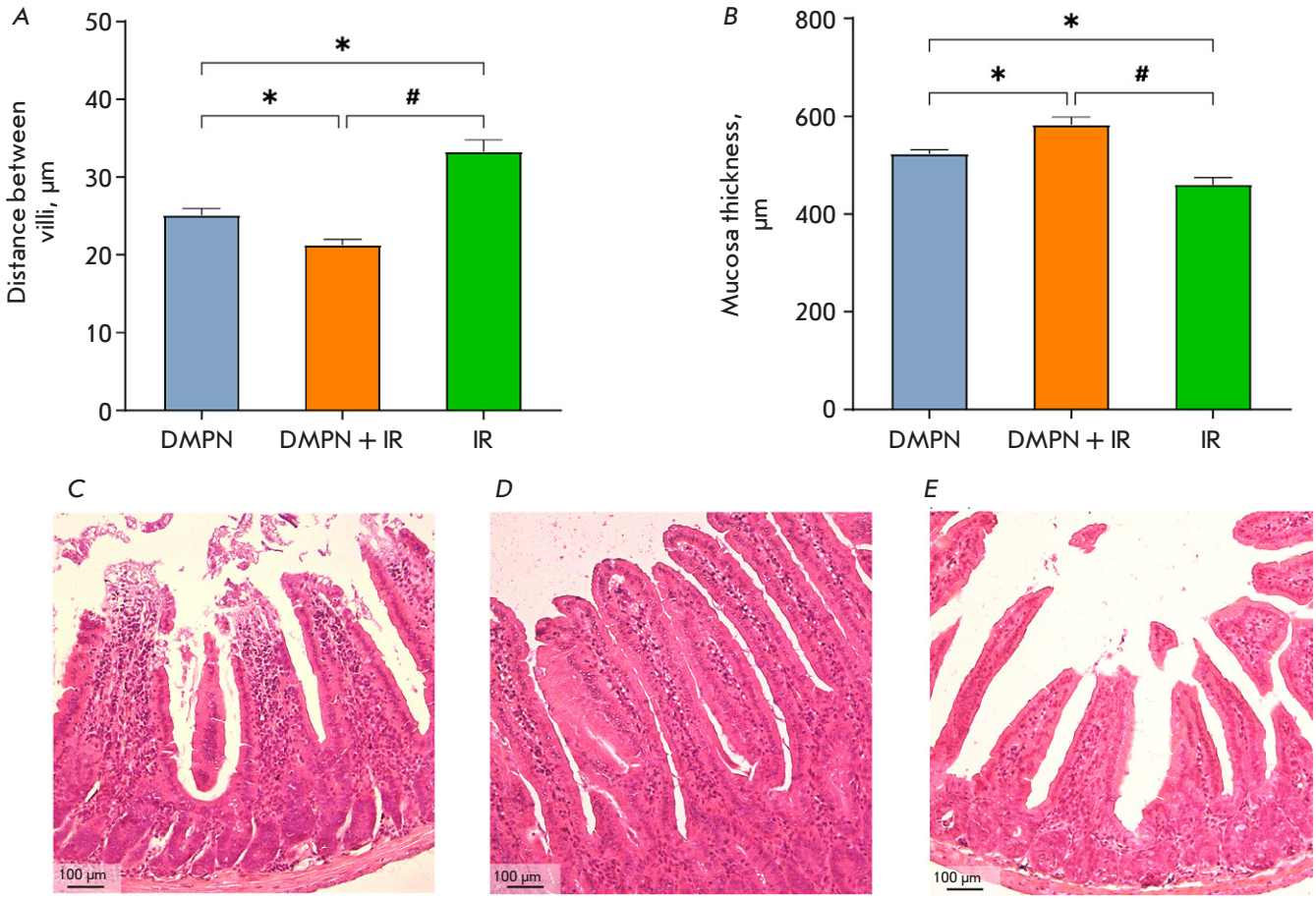

Fig. 5. The effect of Dimephosphon on radiation-induced damage to the small intestine of CD-1 mice. (*A*) The distance between villi and (*B*) thickness of the small intestine mucosa (M ± SEM). The histological presentation of the small intestine in the groups: (*C*) DMPN; (*D*) DMPN + IR; and (*E*) IR. Hematoxylin and Eosin staining, ×100 magnification. The statistical analysis was performed using the Student's t test, $^{*}p < 0.05$ compared to DMPN, $^{\#}p < 0.05$ compared to DMPN + IR

Metabolomic screening of the blood samples from mice exposed at a dose of 5 Gy radiation and administered Dimephosphon

Metabolomic screening of 489 metabolites was conducted for mice in the DMPN + IR and IR groups at key experimental time points. The statistical analysis algorithm involved metabolite examination between days 0 and 11; among those, metabolites having statistically significant differences were selected. Set intersections were analyzed to identify metabolites unique to each group. A total of 208 metabolites were found to show negative dynamics (153 metabolites exhibited negative dynamics in both groups, 13 metabolites were unique to the IR group, and 42 metabolites were unique to the DMPN + IR group); 26 metabolites showed positive dynamics (15 metabolites exhibited positive dynamics in both groups, 5 metabolites were unique to the IR group, and 6 metabolites were unique to the DMPN + IR group) (*Fig.* 7).

After the irradiation, mice in the IR group had abnormal tocopherol metabolism, characterized by a gradual decline in its level throughout the experiment, increasing the organism's susceptibility to free radical damage. *Figure 8A* shows that the blood level of tocopherol in the DMPN + IR group was not reduced, as opposed to that in the IR group. Alpha-tocopherol is a potent fat-soluble antioxidant exhibiting antioxidant and radioprotective effects due to free radical scavenging [25] and the indirect impact on the secretion of specific growth factors and cytokines [26]. Therefore, the observed dynamics of the alpha-tocopherol level can indirectly attest to the radioprotective mechanism of the drug.

The adenylosuccinate level (*Fig. 8B*) was decreasing abruptly in both groups until day 7 post-irradiation, followed by a significant rise in the metabolite level in the DMPN + IR group, which was not observed in the IR group. Adenylosuccinate is involved in purine

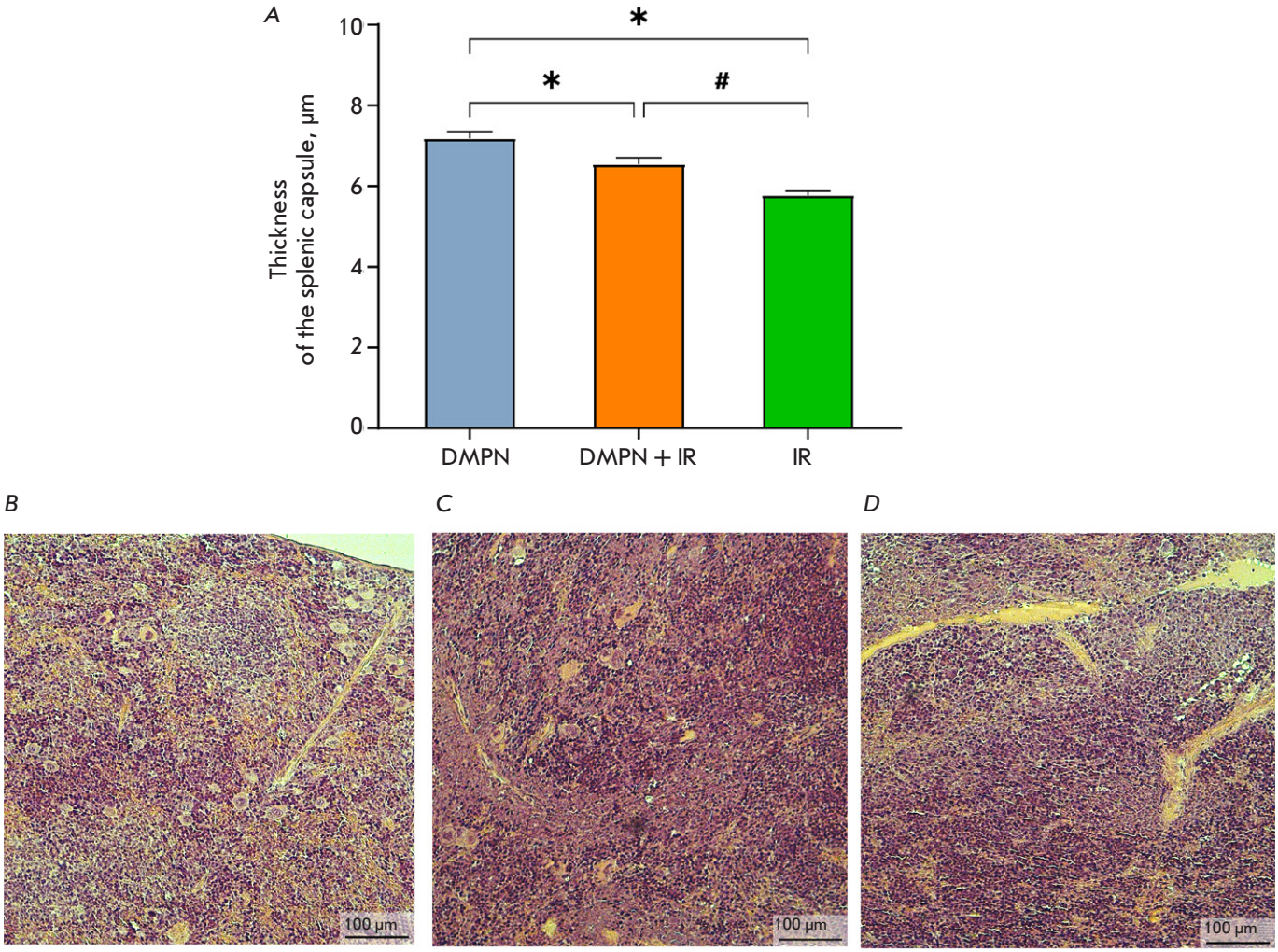

Fig. 6. The effect of Dimephosphon on radiation-induced splenic damage in CD-1 mice. (*A*) Thickness of the splenic capsule (M ± SEM). The histological presentation of the spleen in the groups: (*B*) DMPN; (*C*) DMPN + IR; and (*D*) IR. Hematoxylin and Eosin staining, ×100 magnification. The statistical analysis was performed using the Student's t test, $^{*}p < 0.05$ compared to DMPN, $^{\#}p < 0.05$ compared to DMPN + IR

recycling, energy homeostasis, as well as mitigation of inflammation and other types of cellular stress [27]. Importantly, the blood levels of purine metabolites correlate with cellular resistance to radiation; their exogenous administration contributes to the repair of double-strand DNA breaks after exposure to radiation [28]. Hence, the administered drug Dimephosphon compensated for the effects of irradiation by increasing the blood level of adenylosuccinate, which may be indication that the drug can enhance the organism's resistance to radiation.

The level of nicotinamide riboside remained virtually unchanged after irradiation; a slight rise was observed by day 7. However, administration of the drug abruptly increased the blood level of this metabolite in mice by day 4, which persisted until the end of the experiment (*Fig. 8C*). Nicotinamide riboside is a precursor of NAD+, which acts as a coenzyme for many cellular reactions involved in the physiological homeostasis of various organs and systems. This metabolite was shown to affect the progression of acute radiation syndrome; its oral administration exerts a radioprotective effect by inhibiting cellular senescence in the spleen and normalizing the serum metabolite profile in mice [29]. Furthermore, recent studies have demonstrated that NAD+ precursors, and nicotinamide riboside in particular, play a pivotal role in maintaining the integrity of the intestinal barrier [30]. The positive dynamics of the nicotinamide riboside level observed in our study are consistent with the histological data and can explain the radioprotective effect in the small intestine exerted by the drug.

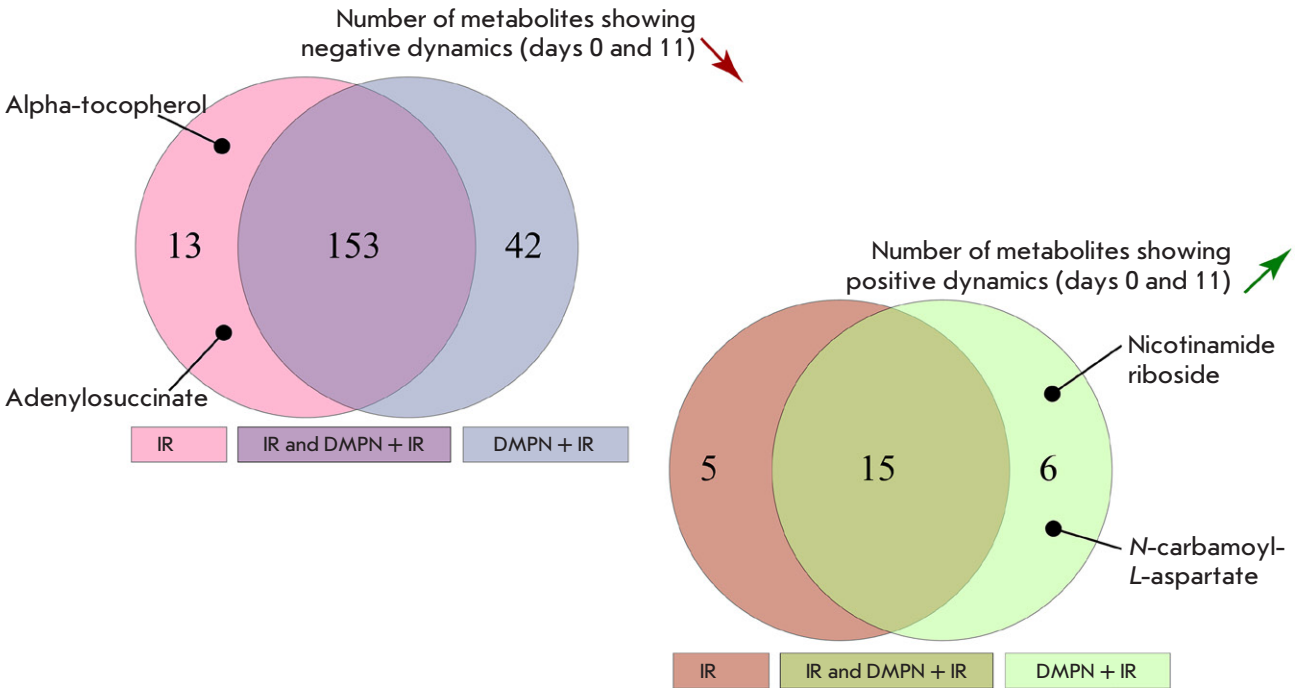

Fig. 7. Euler diagrams for metabolites showing the positive and negative dynamics

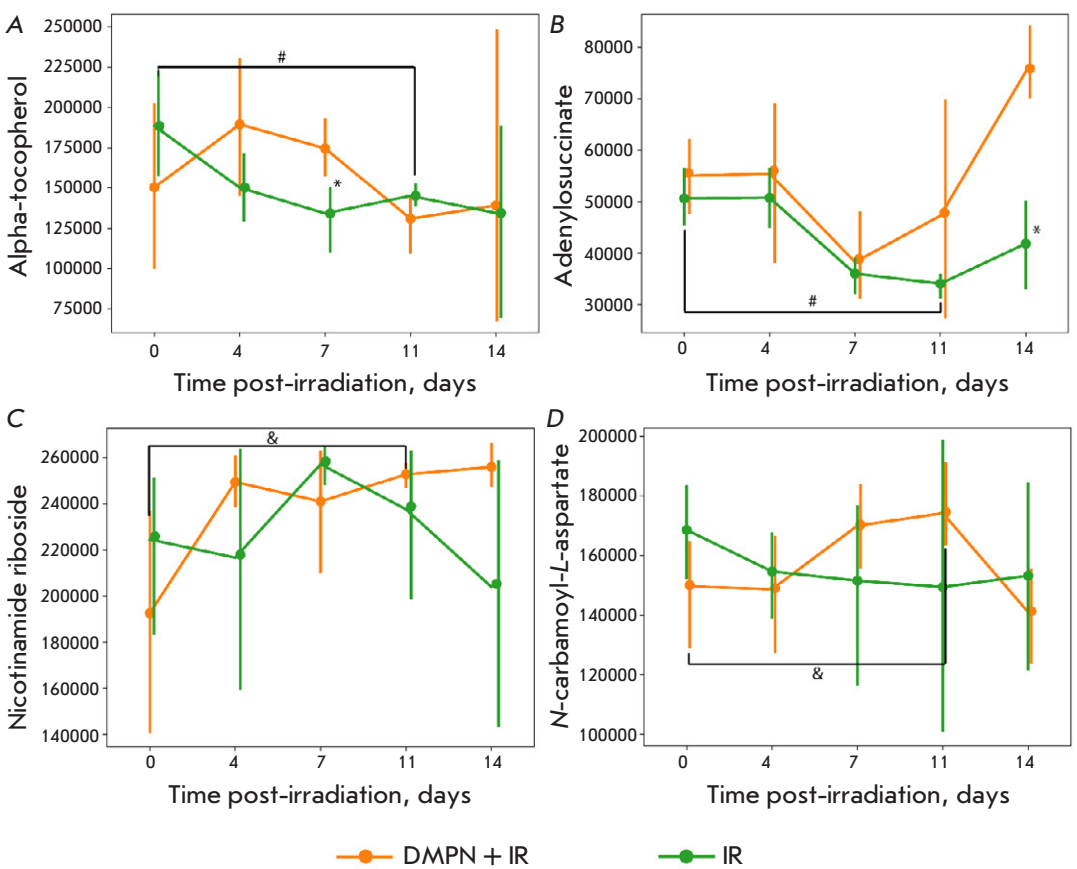

Fig. 8. Metabolites characterized by the most statistically significant changes in the blood levels of CD-1 mice in the DMPN+IR and IR groups: (*A*) alpha-tocopherol, (*B*) adenylosuccinate; (*C*) nicotinamide riboside; and (*D*) N-carbamoyl-L-aspartate. Data are presented as mean ± confidence interval for a nonparametric sample. The statistical analysis was performed using the Mann–Whitney U test, $^{*}p < 0.05$ between the DMPN + IR and IR groups, $^{\#}p < 0.05$ between days 0 and 11 in the IR group, $^{\&}p < 0.05$ between days 0 and 11 in the DMPN + IR group

In the IR group, the N-carbamoyl-*L*-aspartate level remained constant, whereas increased levels were observed on days 7 and 11 after administration of Dimephosphon (*Fig. 8D*). Cheema et al. [31] reported the level of this metabolite decreasing in mouse intestinal tissues after single-dose total-body gamma irradiation. N-carbamoyl-*L*-aspartate is an early intermediate in the *de novo* synthesis of pyrimidines, which is essential for cell proliferation and damaged tissue repair. N-carbamoyl-*L*-aspartate is formed via the condensation of carbamoyl phosphate and aspartate, catalyzed by aspartate carbamoyltransferase. The elevated N-carbamoyl-*L*-aspartate level in the DMPN + IR group may attest to an activation of pyrimidine synthesis aimed at epithelial repair and involvement of this compound in the radiation-induced adaptive response. That would be consistent with the fact revealed in our study that the intestinal mucosa was restored after administration of the drug.

In this study, we have revealed alterations in the levels of alpha-tocopherol, adenylosuccinate, nicotinamide riboside, and N-carbamoyl-*L*-aspartate. The observed differences in their levels between the IR and DMPN + IR groups can be the biochemical markers of the radioprotective efficacy of the drug. These metabolites are involved in the antioxidant processes taking place in the cells; the detected metabolomic changes are indicative of the processes manifesting themselves at the tissue level as reduced severity of injury to the small intestinal mucosa and reduction in the thickness of the splenic capsule.

CONCLUSIONS

Our findings allowed us to choose the radiation dose and characterize the key indicators of systemic injury to further study potentially promising radioprotective agents. Dimephosphon was also found to mitigate the severity of radiation-induced injury to the small intestinal mucosa and the splenic capsule, as well as contribute to the restoration of platelet counts in CD-1 mice after single-dose irradiation. Meanwhile, the analysis of other key hematological parameters and animal survival rates yielded no evidence of the radioprotective effect of Dimephosphon. The metabolomic data, namely, the significant increase in the blood levels of alpha-tocopherol, nicotinamide riboside, N-carbamoyl-*L*-aspartate, and adenylosuccinate in mice administered Dimephosphon, are in line with the histological findings for the intestinal mucosa and spleen and demonstrate that Dimephosphon exhibits an antioxidant activity. ●

This work was supported by the Russian Science Foundation (project No. 25-25-00119).

REFERENCES

1. Kaprin AD, Starinsky VV, Shakhzadova AO. *State of oncologic care for the Russian population in 2023*. P.A. Hertsen MORI – branch of FSBI «NMMRC» of the Ministry of Health of the Russian Federation; 2024.
2. Martin OA, Martin RF. Cancer Radiotherapy: Understanding the Price of Tumor Eradication. *Front Cell Dev Biol*. 2020;8:261. doi: 10.3389/fcell.2020.00261
3. Velsher LZ, Kosmynin AA, Byakhov MYu, Duditskaya TK, Reshetov DN. Targeted Therapy: A New Approach for the Treatment of Locally Advanced Oropharyngeal Cancer. *Acta Naturae*. 2012;4(1):82–85. doi: 10.32607/20758251-2012-4-1-82-85
4. Dale DC, Crawford J, Klippel Z, et al. A Systematic Literature Review of The Efficacy, Effectiveness, and Safety of Filgrastim. *Support Care Cancer*. 2018;26(1):7–20. doi: 10.1007/s00520-017-3854-x
5. Lee M, Yee J, Kim JY, et al. Risk Factors for Neutropenia and Febrile Neutropenia Following Prophylactic Pegfilgrastim. *Asia Pac J Clin Oncol*. 2019;15(4):231–237. doi: 10.1111/ajco.13152
6. Andreassen CN, Grau C, Lindegaard JC. Chemical Radioprotection: A Critical Review of Amifostine as a Cytoprotector in Radiotherapy. *Semin Radiat Oncol*. 2003;13(1):62–72. doi: 10.1053/srao.2003.50006
7. Mun GI, Kim S, Choi E, Kim CS, Lee YS. Pharmacology of Natural Radioprotectors. *Arch Pharm Res*. 2018;41(11):1033–1050. doi: 10.1007/s12272-018-1083-6
8. Raj S, Manchanda R, Bhandari M, Alam MS. Review on Natural Bioactive Products as Radioprotective Therapeutics: Present and Past Perspective. *Curr Pharm Biotechnol*. 2022;23(14):1721–1738. doi: 10.2174/1389201023666220110104645
9. Scott BR, Lin Y, Saxton B, Chen W, Potter CA, Belinsky SA. Modeling Cell Survival Fraction and Other Dose-Response Relationships for Immunodeficient C.B-17 SCID Mice Exposed to 320-kV X Rays. *Dose Response*. 2021;19(2):15593258211019887. doi: 10.1177/15593258211019887
10. Vizel AA, Vizel AO, Shchukina LI. Dimethyl oxobutylphosphonyl dimethylate (Dimephosphone): use in pulmonology and phthisiology. *Pulmonologiya*. 2013;3(3):40–44.
11. Maksimov ML, Malykhina AI, Shikaleva AA. Time-tested pharmacotherapy: from mechanisms to clinical efficacy. *RMJ*. 2020;9:71–76.
12. Studentsova IA, Danilov VI, Khafizyanova RH, et al. Results of Clinical Testing of Dimephosphon as a Vasoactive Agent That Normalizes the Functions of the Nervous System. *Kazanskiy Meditsinskiy Zhurnal*. 1995;76(5):214–218.
13. Mironov VF, Buzykin BI, Garaev RS, et al. Dimephosphone analogs: a pharmacological aspect. *Russ Chem Bull*. 2014;63:2114–2125. doi: 10.1007/s11172-014-0708-2
14. Poluektov MG, Podymova IG, Golubev VL. Possibilities of using the drug dimephosphone in neurology and neurosurgery. *Doctor.Ru*. 2015; 5–6(106–107):5–10.
15. Gileva TG, Lukin AV, Nyushkin AA, Agachev AR, Studentsova IA, Vizel AO. Metrology of acute radiation reaction in patients with laryngeal cancer. *Kazanskiy Meditsinskiy Zhurnal*. 1994;75(5):389. doi: 10.17816/kazmj90685

16. Li K, Naviaux JC, Monk JM, Wang L, Naviaux RK. Improved Dried Blood Spot-Based Metabolomics: A Targeted, Broad-Spectrum, Single-Injection Method. *Metabolites*. 2020;10(3):82. doi: 10.3390/metabo10030082
17. Basov NV, Rogachev AD, Aleshkova MA, et al. Global LC-MS/MS Targeted Metabolomics Using a Combination Of HILIC and RP LC Separation Modes on an Organic Monolithic Column Based on 1-vinyl-1,2,4-triazole. *Talanta*. 2024;267:125168. doi: 10.1016/j.talanta.2023.125168
18. Patrushev YuV, Sotnikova YuS, Sidel'nikov VN. A Monolithic Column with a Sorbent Based on 1-Vinyl-1,2,4-Triazole for Hydrophilic HPLC. *Prot Met Phys Chem Surf*. 2020;56:49–53. doi: 10.1134/S2070205119060248
19. Yuan M, Breitkopf SB, Yang X, Asara JM. A Positive/Negative Ion-Switching, Targeted Mass Spectrometry-Based Metabolomics Platform for Bodily Fluids, Cells, and Fresh and Fixed Tissue. *Nat Protoc*. 2012;7(5):872–881. doi: 10.1038/nprot.2012.024
20. Li K, Naviaux JC, Bright AT, Wang L, Naviaux RK. A robust, single-injection method for targeted, broad-spectrum plasma metabolomics. *Metabolomics*. 2017;13(10):122. doi: 10.1007/s11306-017-1264-1
21. Tairbekov MG, Petrov VM. Medical-biological effects of ionizing radiation. Moscow: MEPhI. 2005.
22. Macià I Garau M, Lucas Calduch A, López EC. Radiobiology of the Acute Radiation Syndrome. *Rep Pract Oncol Radiother*. 2011;16(4):123–130. doi: 10.1016/j.rpor.2011.06.001
23. Horie K, Namiki K, Kinoshita K, et al. Acute Irradiation Causes a Long-Term Disturbance in the Heterogeneity and Gene Expression Profile of Medullary Thymic Epithelial Cells. *Front Immunol*. 2023;14:1186154. doi: 10.3389/fimmu.2023.1186154
24. Tripathi AM, Khan S, Chaudhury NK. Radiomitigation by Melatonin in C57BL/6 Mice: Possible Implications as Adjuvant in Radiotherapy and Chemotherapy. *In Vivo*. 2022;36(3):1203–1221. doi: 10.21873/invivo.12820
25. Tucker JM, Townsend DM. Alpha-tocopherol: Roles in Prevention and Therapy of Human Disease. *Biomed Pharmacother*. 2005;59(7):380–387. doi: 10.1016/j.biopha.2005.06.005
26. Singh VK, Beattie LA, Seed TM. Vitamin E: Tocopherols and Tocotrienols as Potential Radiation Countermeasures. *J Radiat Res*. 2013;54(6):973–988. doi: 10.1093/jrr/rrt048
27. Rybalka E, Kourakis S, Bonsett CA, Moghadaszadeh B, Beggs AH, Timpani CA. Adenylosuccinic Acid: An Orphan Drug with Untapped Potential. *Pharmaceuticals (Basel)*. 2023;16(6):822. doi: 10.3390/ph16060822
28. Zhou W, Yao Y, Scott AJ, et al. Purine Metabolism Regulates DNA Repair and Therapy Resistance in Glioblastoma. *Nat Commun*. 2020;11(1):3811. doi: 10.1038/s41467-020-17512-x
29. Li W, Wang X, Dong Y, et al. Nicotinamide Riboside Intervention Alleviates Hematopoietic System Injury of Ionizing Radiation-Induced Premature Aging Mice. *Aging Cell*. 2023;22(11):e13976. doi: 10.1111/acel.13976
30. Niño-Narvión J, Rojo-López MI, Martinez-Santos P, et al. NAD^+ Precursors and Intestinal Inflammation: Therapeutic Insights Involving Gut Microbiota. *Nutrients*. 2023;15(13):2992. doi: 10.3390/nu15132992
31. Cheema AK, Suman S, Kaur P, Singh R, Fornace AJ Jr, Datta K. Long-Term Differential Changes in Mouse Intestinal Metabolomics after γ and Heavy Ion Radiation Exposure. *PLoS One*. 2014;9(1):e87079. doi: 10.1371/journal.pone.0087079

Chiral Chromatographic Analysis of Amino Acids with Pre-column Derivatization by *o*-Phthalaldehyde: Improving the Determination of Enantiomers Using Ion-Pair Reagents

N. V. Panin[1], I. V. Pirogov[2], D. T. Guranda[1], V. K. Švedas[1,3*]
[1]Lomonosov Moscow State University, Belozersky Institute of Physicochemical Biology, Moscow, 119234 Russia
[2]Lomonosov Moscow State University, Faculty of Chemistry, Moscow, 119234 Russia
[3]Lomonosov Moscow State University, Faculty of Bioengineering and Bioinformatics, Moscow, 119234 Russia
*E-mail: vytas@belozersky.msu.ru
Received May 20, 2025; in final form, August 05, 2025
DOI: 10.32607/actanaturae.27703

ABSTRACT **The development of effective and accessible methods for the chiral analysis of amino acids is an important scientific and practical necessity. One of the most common and convenient techniques is the chromatographic determination of individual enantiomers of amino acids with preliminary conversion of enantiomers into diastereomers, which can then be separated on conventional achiral columns. We have shown that by adding ion-pair reagents to the eluent and varying their structure, one can regulate the efficiency of a chiral amino acid analysis based on the chromatographic determination and resolution of the diastereomeric isoindoles obtained upon pre-column derivatization of amino acids by *o*-phthalaldehyde in the presence of N-acetyl-*L*-cysteine. The use of ion-pair reagents allows one to achieve a better resolution of diastereomeric isoindole peaks, while the analysis time can be reduced by increasing the ionic strength. Hence, adding ion-pair reagents and optimizing the mobile phase composition are useful approaches in the engineering of an amino acid chiral analysis, along with the synthesis of new chiral SH compounds and the choice of stationary phases.**

KEYWORDS **Chiral analysis of amino acids, *o*-phthalaldehyde, N-acetyl-*L*-cysteine, pre-column modification, HPLC conditions, ion-pair reagents, separation of diastereomeric isoindoles.**

ABBREVIATIONS **OPA – *o*-phthalaldehyde; NAC – N-acetyl-*L*-cysteine; HPLC – high-performance liquid chromatography; IPR – ion-pair reagent; TBA – tetrabutylammonium bromide; OTMA – N,N,N-trimethyloctylammonium bromide; CDR – chiral derivatizing SH reagent; BTCC – N-*tert*-butylthiocarbamoyl-*L*-cysteine ethyl ester; NAP – N-acetyl-*D*-penicillamine; NMC – N-(R)-mandelyl-*L*-cysteine; DiC – N,N-dimethyl-*L*-cysteine; IBLC – N-isobutyryl-*L*-cysteine; NPPC – N-phenylacetyl-(R)-phenylglycyl-*L*-cysteine; MP – 1-mercapto-2-propanol; BC – Boc-*L*-cysteine; a.u. – arbitrary units.**

INTRODUCTION

The need to determine individual enantiomers in the total content of amino acids and other amino compounds is an important undertaking both in fundamental research and medical diagnostics, as well as in the characterization of raw materials and manufactured products in the pharmaceutical and food industries [1–12]. Significant attention is also paid to the stereoisomerism of amino acids in the environment under prebiotic conditions when studying the origin of life [13, 14]. The scale and complexity of the problems related to determining the individual enantiomers of amino acids in complex mixtures has increased significantly in recent years, as highly effective methods of chiral metabolomics are pursued [15–17]. Methods for an efficient, rapid, and widely accessible chiral analysis of amino acids as building blocks of physiologically active compounds and mark-

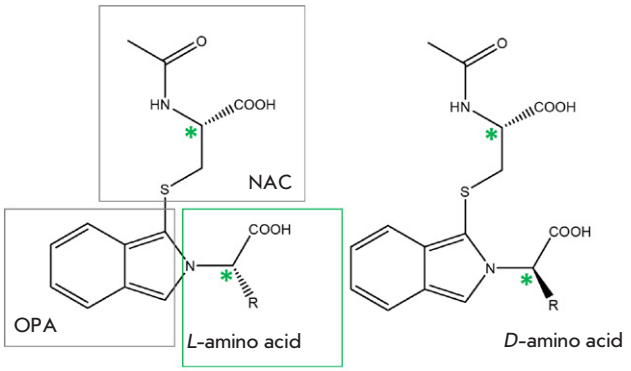

Fig. 1. Diastereomeric isoindole adducts formed upon derivatization of amino acids by OPA and a chiral thiol (N-acetyl-*L*-cysteine). R is the side chain of the amino acid

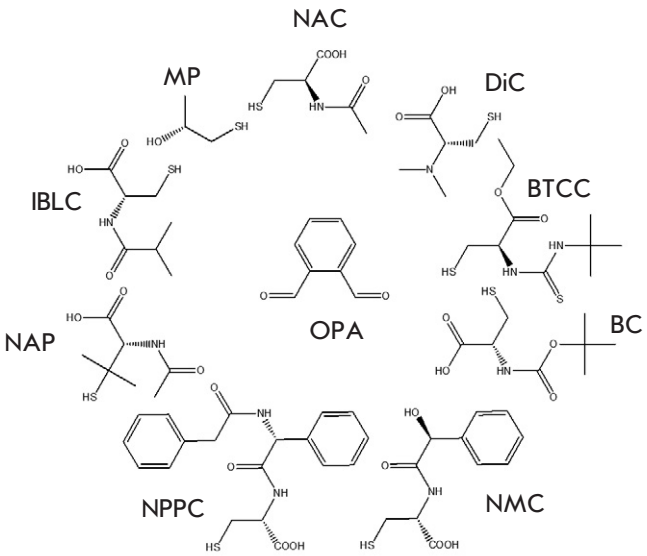

Fig. 2. Chiral thiols used for pre-column derivatization by OPA

ers of various pathological processes are sorely needed in systematic research into living systems in the postgenomic era. Chromatographic methods – primarily high-performance liquid chromatography (HPLC) with pre-column derivatization of enantiomers into diastereomers which can then be separated on conventional achiral columns – are the most widely used means for the chiral analysis of amino compounds. One of the most accessible, convenient, and effective methods is pre-column modification of amino groups by *o*-phthalaldehyde (OPA) and a chiral derivatizing SH reagent (CDR) [18, 19]. This modification of amino compounds occurs quite quickly: unlike the method utilizing ninhydrin, there is no need to increase the temperature; the resulting diastereomeric isoindoles are usually stable under the conditions of the analysis and are characterized by different retention times on standard HPLC columns. Isoindoles have a characteristic absorption maximum at 340 nm and a molar absorption coefficient of 6,000 $M^{-1}cm^{-1}$ and are good fluorophores, which allows one to determine the femtomoles of the amino compounds using fluorescent detectors if the sensitivity of spectrophotometric measurements is insufficient [20, 21].

In the best-known version of this method, a very cheap and accessible CDR, N-acetyl-*L*-cysteine (NAC) (*Fig. 1*) [18], is used to determine the enantiomers of α-amino acids. However, it remains impossible to achieve the required resolution for all the compounds belonging to this class, as well as for other amino compounds. NAC analogs have been proposed to improve the efficiency of this procedure (*Fig. 2*): N-isobutyryl-*L*-cysteine [22], ethyl ester of N-*tert*-butylthiocarbamoyl-*L*-cysteine (BTCC) [23], Boc-*L*-cysteine, N-acetyl-(R)-penicillamine (NAP) [24], N-phenylacetyl-(R)-phenylglycyl-*L*-cysteine (NPPC) [25], N-(R)-mandelyl-*L*-cysteine (NMC) [26, 27], N,N-dimethyl-*L*-cysteine (DiC) [28], 1-mercapto-2-propanol (MP) [29] and other SH reagents.

The use of SH reagents that have various structures allows one to significantly broaden the application range of the method used to determine the enantiomers of a wide range of amino compounds: amino acids, primary amines, and amino alcohols. Thus, whereas it is possible to achieve an acceptable resolution only for a small number of aliphatic amines for the conventional NAC, when using R-NMC, which contains two chiral centers and a large number of intramolecular contacts, it is possible to pinpoint a number of amine and amino alcohol enantiomers, including those that are not resolved even on chiral columns [26]. However, most of the proposed SH compounds are not readily available, since they are not commercial reagents and are mainly used by the research groups that have proposed them to solve a limited range of analytical problems. This fact makes any assessment of the prospects for a wider application of novel SH reagents rather challenging. Along with creating new CDRs, engineering the analytical process *per se* (the stationary and mobile phases, as well as the analytical conditions) can be an alternative approach to improving the efficiency of chromatographic determination of the diastereomers of amino compounds. Adding ion-pair reagents (IPRs) is one of the unexplored possibilities of mobile phase engineering in reversed-phase HPLC for a more efficient resolution of diastereomers. The experience of using ion-

pair reagents to improve the chromatographic resolution of structurally similar compounds demonstrates that this approach is rather promising [30–32]. The introduction of an IPR carrying a charged functional group and nonpolar fragments (alkyl radicals) can increase analyte retention on a chromatographic column through reagent sorption on the surface of the reversed-phase adsorbent and changes in the interaction with the analyte. The resolution of organic acids was thus improved by adding quaternary ammonium salts in the mobile phase (tetrabutylammonium bromide (TBA) being one used most commonly) [30].

The feasibility of using ion-pair reagents for a more efficient chromatographic resolution of diastereomers obtained upon pre-column derivatization of α-amino acids by OPA and the chiral thiol NAC was investigated for the first time in this study.

EXPERIMENTAL

Reagents

o-Phthalaldehyde (OPA; 99%, Koch Light, England), N-acetyl-*L*-cysteine (NAC; 99%, AppliChem, Germany), phenylalanine (Reakhim, Russia), glutamate (Aurat, Russia), leucine, asparagine and arginine (Reanal, Hungary), tetrabutylammonium bromide (TBA), N,N,N-trimethyloctylammonium bromide (OTMA) (ABCR GmbH, Germany) were used in this study. Buffer components, acids, and alkalis were the domestic products of highest purity available; methanol (PanReac, Spain) was of pure, for the analysis, grade; acetonitrile (Kriokhrom, Russia) was of HPLC grade.

HPLC analysis

The HPLC analysis was performed in a Perkin Elmer 200 Series chromatographic system: Kromasil Eternity 5-C18 4.6 × 250 mm reversed-phase chromatography column; injection volume, 10 μL; flow rate, 1 mL/min. The two-channel system operation mode was used to prepare the mobile phase with a given acetonitrile concentration: channel A – 5 mM phosphate buffer pH 6.8, 10% acetonitrile; channel B – 5 mM phosphate buffer pH 6.8, 80% acetonitrile.

When studying the effect of IPR, elution was performed in the isocratic mode using only channel A. TBA or OTMA at a final concentration of 5 mM and, in different experiments 15%, 20%, or 30% acetonitrile were added to the mobile phase based on 5 mM phosphate-buffered saline pH 6.8. HPLC analysis with the addition of an IPR was performed after preliminary column equilibration for 1 h to ensure maximal reproducibility of the results. When studying the effect of the ionic strength, NaCl was additionally added in channel A at a final concentration of 50 mM. Isoindole diastereomers were detected spectrophotometrically at 340 nm. The absorption intensity was measured in μV (arbitrary units, a.u.). TotalChrom Navigator 6.3.2 was used for HPLC system control and data processing.

Pre-column derivatization

Derivatization of primary amino groups was performed automatically using the Derivatization software function of the autosampler as follows: 20 μL of a 5 mM amino acid solution, 20 μL of a 10 mM methanolic OPA solution, and 20 μL of a 40 mM NAC solution were successively added to a cell containing 500 μL of 0.1 M borate buffer, pH 9.6, using an autosampler needle, followed by stirring of the reaction mixture with an autosampler needle in the automatic mode. The mixture prepared in this way was left to rest for 15 min; 50 μL of a 50 mM IPR solution was then added (if necessary) for preliminary equilibration of the system and analyzed by HPLC.

RESULTS AND DISCUSSION

Resolution of amino acid enantiomers after pre-column derivatization

The series of enantiomers to be resolved included α-amino acids with different physicochemical side chain characteristics: glutamic acid, arginine, phenylalanine, leucine, and asparagine. At the first step, chromatographic analysis after pre-column derivatization by OPA and NAC was carried out on a conventional achiral C18 column at a neutral pH 6.8 in the gradient elution mode (0–10 min: 10% CH_3CN, 10–60 min: 10–40% CH_3CN). Under these conditions, resolution of diastereomeric isoindole derivatives was observed only for arginine and phenylalanine (*Fig. 3*); therefore, ion-pair reagents were added to the mobile phase at the next step to improve the resolution of other analytes.

The effect of adding ion-pair reagents

Quaternary ammonium salts with different alkyl substituents were chosen as IPRs, since the isoindole adducts to be resolved upon chromatographic analysis at pH 6.8 carry two negatively charged carboxyl groups. Addition of tetrabutylammonium bromide (TBA) as an IPR to the eluent leads to chromatographic resolution of the isoindole derivatives of leucine and glutamic acid enantiomers, as well as to a significant improvement in the case of phenylalanine (*Fig. 4*). Efficient chiral analysis of glutamate enantiomers is achieved at a lower concentration of the organic solvent in the eluent.

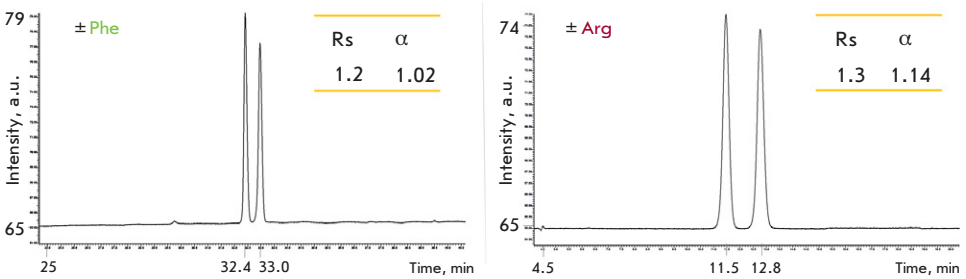

Fig. 3. Chromatograms of isoindole derivatives of phenylalanine and arginine enantiomers obtained upon pre-column derivatization by OPA in the presence of NAC. Gradient elution mode: 5 mM phosphate-buffered saline, pH 6.8, 0—10 min 10% CH_3CN, 10—60 min 10—40% CH_3CN

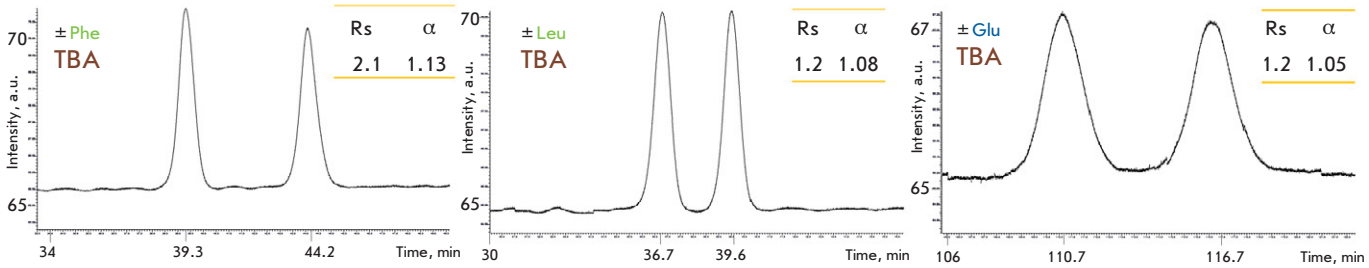

Fig. 4. The effect of adding an IPR to the mobile phase during a chromatographic analysis of isoindole derivatives obtained upon precolumn derivatization of phenylalanine, leucine, and glutamate enantiomers by OPA in the presence of NAC. Isocratic mode: 5 mM phosphate-buffered saline, pH 6.8, 5 mM TBA, 20% CH_3CN (in the case of Glu), 30% CH_3CN (in the case of Leu and Phe)

Interestingly, addition of this IPR does not improve the chromatographic resolution of arginine, since the formation of an ion-pair associate with TBA is apparently hindered by the presence of a positively charged guanidine group in the amino acid side chain, and effective chiral analysis of arginine can be done in the "normal" mode (see *Fig. 3*).

The effect of the structure of the ion-pair reagent

An asymmetric IPR, N,N,N-trimethyloctylammonium bromide OTMA (*Fig. 5*), was used along with symmetric TBA when studying the effect of the IPR structure on the resolution of isoindole derivatives of amino acid enantiomers.

Compared to TBA, addition of OTMA reduces the elution time of isoindole derivatives of glutamic acid, phenylalanine, and leucine. For the negatively charged glutamic acid, in contrast to neutral phenylalanine and leucine, the analysis time is reduced and the resolution is improved (*Fig. 5*). This impact can be explained by the fact that when asymmetric OTMA is added to the mobile phase, the long aliphatic radical becomes deeply and firmly bound by the C18 stationary phase and a classical strong anion exchanger is formed [33]: the resolution of anions occurs on it via a competing mechanism. The ion-exchange mechanism of an-

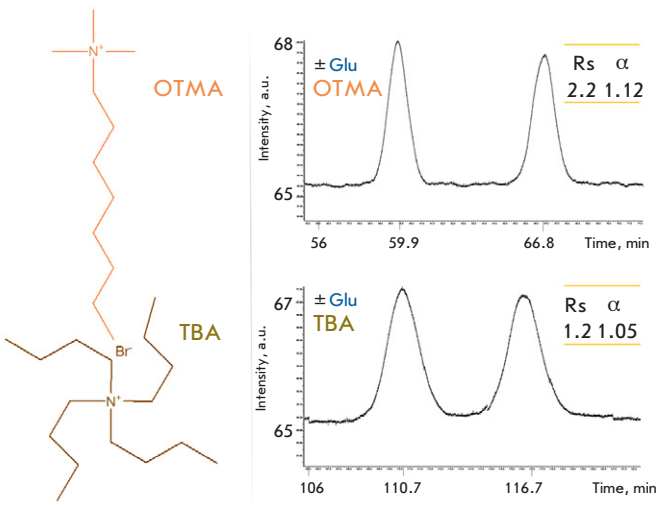

Fig. 5. The effect of symmetric (TBA) and asymmetric (OTMA) IPR on the chromatographic resolution of isoindole derivatives obtained upon precolumn derivatization of glutamic acid enantiomers by OPA in the presence of NAC. Isocratic mode: 5 mM phosphate-buffered saline, pH 6.8, 20% CH_3CN, 5 mM IPR

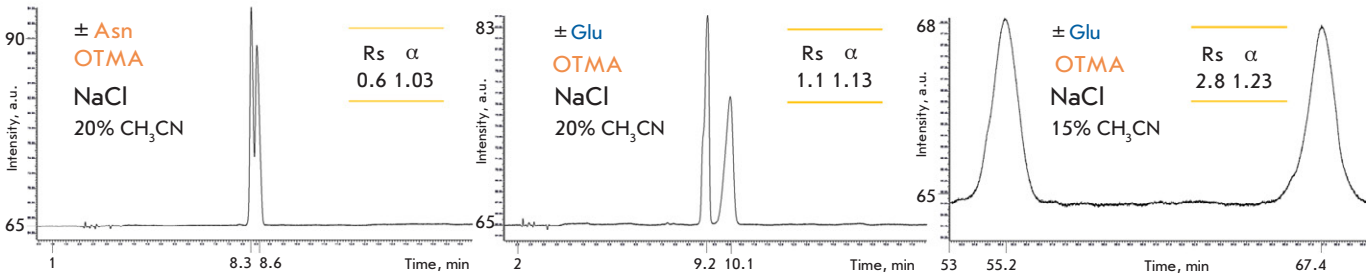

Fig. 6. Chromatograms of isoindole derivatives of asparagine and glutamic acid enantiomers obtained upon pre-column derivatization by OPA in the presence of NAC. Isocratic mode: 5 mM phosphate-buffered saline, pH 6.8, 5 mM OTMA, 50 mM NaCl, 20% CH_3CN (left and center) and 15% CH_3CN (right)

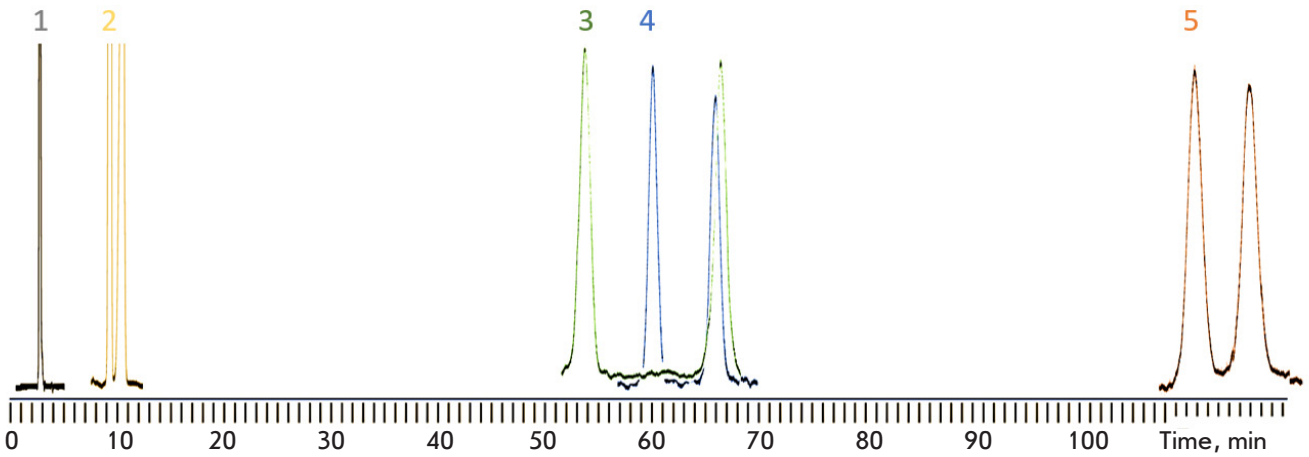

Chromatogram	1	2	3	4	5
Factor	reduction of organic solvent concentration	addition of asymmetric IPR, increase in ionic strength	addition of asymmetric IPR, increase in ionic strength, reduction of organic solvent concentration	addition of asymmetric IPR	addition of symmetric IPR
Conditions	10% CH_3CN	5 mM OTMA, 50 mM NaCl, 20% CH_3CN	5 mM OTMA, 50 mM NaCl, 15% CH_3CN	5 mM OTMA, 20% CH_3CN	5 mM TBA, 20% CH_3CN
Result	fast analysis, no separation	fast analysis, acceptable separation	very efficient separation, slow analysis	efficient separation, slow analysis	acceptable separation, very slow analysis

Fig. 7. The influence of various factors on the efficiency of chromatographic resolution and the time of analysis of isoindole derivatives of glutamic acid enantiomers obtained upon pre-column derivatization by OPA in the presence of NAC. Isocratic mode: 5 mM phosphate-buffered saline, pH 6.8

ion sorption is proven to be involved by the fact that retention strongly depends on the ionic strength of the eluent, which is the main mean of regulating the strength of anion retention.

The effect of the ionic strength

In order to understand how the ionic strength influences the impacts of the addition of IPRs to the mobile phase, 50 mM of NaCl was added to the eluent containing OTMA. The study showed that an increase in ionic strength significantly reduces the retention time of diastereomeric isoindoles and shortens the analysis time (*Fig. 6*, left and center). Under these conditions, the isoindole derivatives of polar-uncharged asparagine also start to separate (*Fig. 6*, left). Improved resolution can be achieved at lower concen-

trations of the organic solvent in the eluent (compare *Fig. 6*, right and center).

Our experiments showed that by adding IPRs to the eluent and varying their structure, one can regulate the efficiency of a chiral amino acid analysis based on the chromatographic determination and resolution of diastereomeric isoindoles obtained upon pre-column derivatization of amino acids by OPA in the presence of NAC. Better resolution of the peaks of the identified isoindoles of phenylalanine, leucine, glutamic acid and asparagine can be achieved by using IPRs. Although it is accompanied by longer analyte retention on the column, the analysis time can be reduced by using an asymmetric IPR (OTMA) and increasing the ionic strength of the eluent. *Figure 7* shows the characteristic effect of various factors on the efficiency of the chromatographic resolution of the isoindole derivatives of amino acid enantiomers using glutamic acid.

CONCLUSIONS

The development of effective and accessible methods for the chiral analysis of amino acids is an important issue in scientific research, medical diagnostics, and the characterization of a wide range of products manufactured by the pharmaceutical and food industries. Chromatographic determination of the individual enantiomers of natural and synthetic amino acids using achiral columns after pre-column derivatization of samples by OPA in the presence of chiral SH compounds is one of the most common and convenient techniques used today. This study showed that we can achieve better resolution of the peaks of the determined diastereomeric isoindoles using ion-pair reagents. By varying the structure of the ion-pair reagent and increasing the ionic strength of the mobile phase, one can achieve a more efficient resolution of diastereomers and shorten the analysis time. Hence, addition of ion-pair reagents to the mobile phase is a useful approach in engineering a chiral amino acid analysis, along with the synthesis of chiral SH compounds and the choice of stationary phases. ●

This study was conducted under the state assignment of Lomonosov Moscow State University, topic 119042590056-2 of Belozersky Institute of Physicochemical Biology.

REFERENCES

1. Knol MGE, Wulfmeyer VC, Müller RU, Rinschen MM. Amino acid metabolism in kidney health and disease. *Nat Rev Nephrol.* 2024;20(12):771–788. doi: 10.1038/s41581-024-00872-8
2. Chen J, Cui L, Lu S, Xu S. Amino acid metabolism in tumor biology and therapy. *Cell Death Dis.* 2024;15(1):42. doi: 10.1038/s41419-024-06435-w
3. Gałęzowska G, Ratajczyk J, Wolska L. Determination of amino acids in human biological fluids by high-performance liquid chromatography: critical review. *Amino Acids.* 2021;53(7):993–1009. doi: 10.1007/s00726-021-03002-x
4. Ksenofontov AL, Boyko AI, Mkrtchyan GV, et al. Analysis of free amino acids in mammalian brain extracts. *Biochemistry (Mosc).* 2017;82(10):1183–1192. doi: 10.1134/S000629791710011X
5. Pereira V, Pontes M, Câmara JS, Marques JC. Simultaneous analysis of free amino acids and biogenic amines in honey and wine samples using in loop orthophthaldehyde derivatization procedure. *J Chromatogr A.* 2008;1189(1–2):435–443. doi: 10.1016/j.chroma.2007.12.014
6. Cuchiaro H, Laurens LML. Total Protein Analysis in Algae via Bulk Amino Acid Detection: Optimization of Amino Acid Derivatization after Hydrolysis with O-Phthalaldehyde 3-Mercaptopropionic Acid (OPA-3MPA). *J Agric Food Chem.* 2019;67(19):5672–5679. doi: 10.1021/acs.jafc.9b00884
7. Hall AE, Moraru CI. Comparative effects of high pressure processing and heat treatment on in vitro digestibility of pea protein and starch. *NPJ Sci Food.* 2022;6(1):2. doi: 10.1038/s41538-021-00116-0
8. Tanwar S, Bhushan R. Enantioresolution of Amino Acids: A Decade's Perspective, Prospects and Challenges. *Chromatographia.* 2015;78:1113–1134. doi: 10.1007/s10337-015-2933-8
9. Ilisz I, Péter A, Lindner W. State-of-the-art enantioseparations of natural and unnatural amino acids by high-performance liquid chromatography. *Trends Anal Chem.* 2016;81:11–22. doi: 10.1016/j.trac.2016.01.016
10. Grishin DV, Zhdanov DD, Pokrovskaya MV, Sokolov NN. D-amino acids in nature, agriculture and biomedicine. *All Life.* 2020;13(1):11–22. doi: 10.1080/21553769.2019.1622596
11. Uifălean A, Iacobescu M, Salantă LC, Heghes SC, Moldovan RC, Iuga C-A. Biological and Analytical Perspectives on D-Amino Acids in Cancer Diagnosis and Therapy. *Pharmaceuticals(Basel).* 2025;18(5):705. doi: 10.3390/ph18050705
12. Pollegioni L, Kustrimovic N, Piubelli L, Rosini E, Rabattoni V, Sacchi S. d-amino acids: new functional insights. *FEBS J.* 2025;292(17):4395–4417. doi: 10.1111/febs.70083
13. Nemoto A, Horie M, Imai EI, Honda H, Hatori K, Matsuno K. Enantiomeric Excess of Amino Acids in Hydrothermal Environments. *Orig Life Evol Biosph.* 2005;35(2):167–174. doi: 10.1007/s11084-005-0638-y
14. Jiang L, Dziedzic P, Spacil Z, et al. Abiotic synthesis of amino acids and self-crystallization under prebiotic conditions. *Sci Rep.* 2014;4:6769. doi: 10.1038/srep06769
15. Kimura T, Hamase K, Miyoshi Y, et al. Chiral amino acid metabolomics for novel biomarker screening in the prognosis of chronic kidney disease. *Sci Rep.* 2016;6:26137. doi: 10.1038/srep26137
16. Chang X, Zhang Y, Chen X, et al. Gut microbiome and serum amino acid metabolome alterations in autism spectrum disorder. *Sci Rep.* 2024;14:4037. doi: 10.1038/s41598-024-54717-2

17. Lella C, Nestor L, De Bundel D, Vander Heyden Y, Van Eeckhaut A. Targeted Chiral Metabolomics of D-Amino Acids: Their Emerging Role as Potential Biomarkers in Neurological Diseases with a Focus on Their Liquid Chromatography–Mass Spectrometry Analysis upon Chiral Derivatization. *Int J Mol Sci.* 2024;25(22):12410. doi: 10.3390/ijms252212410
18. Nimura N, Kinoshita T. *o*-Phthalaldehyde-N-acetyl-L-cysteine as a chiral derivatization reagent for liquid chromatographic optical resolution of amino acid enantiomers and its application to conventional amino acid analysis. *J Chromatogr A.* 1986;352:169–177. doi: 10.1016/S0021-9673(01)83377-X
19. García Alvarez-Coque MC, Medina Hernández MJ, Villanueva Camañas RM, Mongay Fernández C. Studies on the formation and stability of isoindoles derived from amino acids, o-phthalaldehyde and N-acetyl-L-cysteine. *Anal Biochem.* 1989;180(1):172–176. doi: 10.1016/0003-2697(89)90107-3
20. Švedas VJ, Galaev IJ, Borisov IL, Berezin IV. The interaction of amino acids with o-phthaldialdehyde: a kinetic study and spectrophotometric assay of the reaction product. *Anal Biochem.* 1980;101(1):188–195. doi: 10.1016/0003-2697(80)90059-7
21. Meyer MW, Meyer VR, Ramseyer S. The kinetics of diastereomeric amino acids with o-phthaldialdehyde. *Chirality.* 1991;3(6):471–475. doi: 10.1002/chir.530030611
22. Brückner H, Westhauser T, Godel H. Liquid chromatographic determination of d- and l-amino acids by derivatization with o-phthaldialdehyde and N-isobutyryl-l-cysteine applications with reference to the analysis of peptidic antibiotics, toxins, drugs and pharmaceutically used amino acids. *J Chromatogr A.* 1995;711(1):201–215. doi: 10.1016/0021-9673(95)00158-j
23. Nimura N, Fujiwara T, Watanabe A, et al. A novel chiral thiol reagent for automated precolumn derivatization and high-performance liquid chromatographic enantioseparation of amino acids and its application to the aspartate racemase assay. *Anal Biochem.* 2003;315(2):262–269. doi: 10.1016/S0003-2697(02)00705-4
24. Buck RH, Krummen K. High-performance liquid chromatographic determination of enantiomeric amino acids and amino alcohols after derivatization with o-phthaldialdehyde and various chiral mercaptans. *J Chromatogr.* 1987;387:255–265. doi: 10.1016/S0021-9673(01)94529-7
25. Guranda DT, Shapovalova IV, Švedas VK. A new N-acyl derivative of (S)-cysteine for quantitative determination of enantiomers of amino compounds by HPLC with a precolumn modification with *o*-phthalaldehyde. *Bioorg Khim.* 2004;30(5):451–457. doi: 10.1023/b:rubi.0000043781.72807.f5
26. Guranda DT, Kudryavtsev PA, Khimiuk AY, Švedas VK. Efficient enantiomeric analysis of primary amines and amino alcohols by high-performance liquid chromatography with precolumn derivatization using novel chiral SH-reagent N-(R)-mandelyl-(S)-cysteine. *J Chromatogr A.* 2005;1095(1–2):89–93. doi: 10.1016/j.chroma.2005.07.125
27. Chernobrovkin MG, Shapovalova EN, Guranda DT, Kudryavtsev PA, Švedas VK, Shpigun OA. Chiral high-performance liquid chromatography analysis of α-amino acid mixtures using a novel SH reagent-N-R-mandelyl-l-cysteine and traditional enantiomeric thiols for precolumn derivatization. *J Chromatogr A.* 2007;1175(1):89–95. doi: 10.1016/j.chroma.2007.10.034
28. Lkhagva A, Tai HC. Dimethylcysteine (DiCys)/o-Phthalaldehyde Derivatization for Chiral Metabolite Analyses: Cross-Comparison of Six Chiral Thiols. *Molecules.* 2021;26(24):7416. doi: 10.3390/molecules26247416
29. Naghashian-Haghig A, Hemmateenejad B, Shamsipur M. Determination of enantiomeric excess of some amino acids by second-order calibration of kinetic-fluorescence data. *Anal Biochem.* 2018;550:15–26. doi: 10.1016/j.ab.2018.04.004
30. Sychev KS. Practical Guide to Liquid Chromatography. Moscow: Tekhnosfera. 2010:192–197.
31. Cecchi T. Ion Pairing Chromatography. *Crit Rev Anal Chem.* 2008;38(3):161–213. doi: 10.1080/10408340802038882
32. Sagi-Kiss V, Li Y, Carey MR, et al. Ion-Pairing Chromatography and Amine Derivatization Provide Complementary Approaches for the Targeted LC-MS Analysis of the Polar Metabolome. *J Proteome Res.* 2022;21(6):1428–1437. doi: 10.1021/acs.jproteome.2c00030
33. Saprykin LV, Saprykina LV. Some aspects of the practical application of dynamic modification in HPLC on silica gel sorbents. *Sorption and Chromatographic Processes.* 2006;6(2):284–301.

The Potential of the Peptide Drug Semax and Its Derivative for Correcting Pathological Impairments in the Animal Model of Alzheimer's Disease

A. I. Radchenko[1], E. V. Kuzubova[1], A. A. Apostol[1], V. A. Mitkevich[2*], L. A. Andreeva[3], S. A. Limborska[3], Yu. V. Stepenko[1], V. S. Shmigerova[1], A. V. Solin[1], M. V. Korokin[1], M. V. Pokrovskii[1], N. F. Myasoedov[3], A. A. Makarov[2]

[1]Belgorod State National Research University, Belgorod, 308015 Russia
[2]Engelhardt Institute of Molecular Biology, Russian Academy of Sciences, Moscow, 119991 Russia
[3]National Research Center "Kurchatov Institute", Moscow, 123182 Russia
[*]E-mail: mitkevich@gmail.com

Received September 03, 2025; in final form, September 29, 2025
DOI: 10.32607/actanaturae.27808

ABSTRACT **Alzheimer's disease, first described over a century ago, is currently among the most common neurodegenerative diseases whose significance is increasingly growing with the aging of populations. Throughout the entire period of its study, no remedies have been found that would be effective in treating – or at least significantly slowing – the pathological process, while being sufficiently safe. In this regard, significant attention is paid to the development and application of natural peptide drugs lacking side effects. The present study assessed the effect of the known neuroprotective peptide Semax and its derivative on the behavioral characteristics and development of amyloidosis in transgenic APPswe/PS1dE9/Blg mice acting as a model of Alzheimer's disease. The open field, novel object recognition, and Barnes maze tests demonstrated that both Semax and its derivative improved cognitive functions in mice. Histological examination showed that these peptides reduced the number of amyloid inclusions in the cortex and hippocampus of the animals' brains. These findings demonstrate the high potential of Semax and its derivatives when used to develop therapeutic and corrective strategies for Alzheimer's disease.**

KEYWORDS **Alzheimer's disease, peptide drug, behavioral testing, histological analysis, amyloidosis.**

ABBREVIATIONS **AD – Alzheimer's disease; Aβ – beta-amyloid peptide; APP/PS1 – APPswe/PS1dE9 transgenic mice; ACTH(4–7) – adrenocorticotropic hormone fragment (4–7); Heptapeptide – Met-Glu-Asp-Arg-Pro-Gly-Pro peptide; WT – Wild type, C57BL/6 mice.**

INTRODUCTION

Alzheimer's disease (AD) is currently among the most prevalent neurodegenerative disorders in the elderly and senile populations [1–4]. The progressive form of AD can be caused by cerebral disorders, intoxication, infection, and defects in the pulmonary and circulatory systems, leading to reduced oxygen supply to the brain, by nutrient and vitamin B12 deficiency, as well as by tumors [5–8]. AD is the most common type of dementia and can be defined as a slowly progressive neurodegenerative disease characterized by the formation of senile plaques and neurofibrillary tangles via the accumulation of beta-amyloid peptide (Aβ) and tau protein within the most affected brain regions: the medial temporal lobe and neocortical structures [9–11].

The number of pharmaceuticals used to treat Alzheimer's disease remains limited [12, 13]. Therefore, there is an ongoing need for novel compounds that would mitigate the cognitive impairment caused by disease progression [14, 15].

Animal models of AD play a crucial role in this research, as they make possible a detailed investigation of drug effects on key characteristics of the disease. The APPswe/PS1dE9/Blg (APP/PS1) transgenic mouse line, commonly used to study the mechanisms of AD and methods to correct them, is such a model [16].

Significant attention is currently directed toward developing drugs based on natural regulatory peptides, which are characterized by mild action and a lack of significant adverse effects [17]. Special at-

tention has been focused on Semax, one of the well-known and long-used peptide-based drugs containing the Met-Glu-His-Phe-Pro-Gly-Pro sequence. Semax is a hybrid molecule carrying an adrenocorticotropic hormone fragment, ACTH(4–7), and the Pro-Gly-Pro tripeptide, which affords increased resistance to peptidase activity. Semax does not exhibit any hormonal activity and is included in the Russian List of "Vital and Essential Drugs for Medical Application" (Appendix No. 1 to Decree No. 2406-r of the Government of the Russian Federation, dated October 12, 2019). It is used to treat neurological pathologies and stress conditions. Semax exhibits nootropic effects, stimulating learning, attention, and memory formation in animals and humans [18–22]. This very feature makes it a promising candidate for AD therapy. A preliminary trial of Semax in a limited cohort of AD patients showed that it can potentially be used to prevent and treat Alzheimer's disease [23]. However, a further, more detailed investigation of the effects of the drug on various characteristics of AD is needed before its broader application [24, 25]. Furthermore, it is reasonable to study other derivatives of this peptide drug, whose architecture would incorporate structural features capable of improving the physiological properties of the potential therapeutic agent. This study employed a peptide derivative of Semax, with two amino acid substitutions. These substitutions (His-Phe to Asp-Arg) resulted in the Glu-Asp-Arg sequence within its structure. Previous studies using cellular models of AD had indicated that the Glu-Asp-Arg tripeptide plays a positive role in improving the functional state of neurons [26].

The effects of Semax and its derivative, the Heptapeptide Met-Glu-Asp-Arg-Pro-Gly-Pro, on the behavior of APP/PS1 mice and the amyloid load in brain tissues were investigated in this study to assess the therapeutic potential of these peptides during the development of Alzheimer's-type pathologic changes.

EXPERIMENTAL

Animals

The experiments were conducted using 60 male APPswe/PS1dE9/Blg (APP/PS1) mice with a mixed C57Bl6/Chg genetic background and 20 male C57Bl6/Chg (wild-type, WT) mice. The housing conditions complied with the current sanitary regulations for the design, equipment, and maintenance of experimental biological clinics: ten animals per cage; temperature, 22°C; *ad libitum* access to water and forage; and a 12-h light cycle (from 8 a.m. to 8 p.m.). The laboratory animals with the Specific Pathogen-Free (SPF) status were procured from the Research Institute of Pharmacology of Living Systems at the Belgorod State University (Belgorod, Russian Federation). All the procedures were conducted in compliance with the Law of the Russian Federation "On the Protection of Animals from Cruel Treatment" dated June 24, 1998, the Good Laboratory Practice (GLP) regulations for preclinical studies in the Russian Federation (State Standards GOST 3 51000.3-96 and GOST R 53434-2009), and the EU Directive (86/609/EEC). All the stages of the study adhered to the Russell and Burch's 3R principles.

Synthesis of peptides and their characteristics

The Met-Glu-Asp-Arg-Pro-Gly-Pro peptide (Heptapeptide) based on the adrenocorticotropic hormone fragment was synthesized by the conventional liquid-phase peptide chemistry approach using protected and free L-amino acids. The purity and identity of the synthesized compound were confirmed by high-performance liquid chromatography and mass spectrometry.

Semax, a synthetic peptide drug, an analog of $ACTH_{4-10}$, which is entirely devoid of hormonal activity, was obtained according to the procedure described previously [4, 18, 25]. All the amino acids were L-stereoisomers.

The formation of experimental groups

The mice were allocated into four study groups. The first group (the APP/PS1 group) was used as the positive control and comprised APP/PS1 mice with confirmed manifestations of Alzheimer's-type pathology. The second group (the WT group) was the negative control and comprised wild-type animals. The third and fourth groups consisted of APP/PS1 mice intranasally administered either Semax (the Semax group) or its derivative (the Heptapeptide group) at a dose of 50 μg per kg, starting from the age of 6 months. The animals received the drug every other day during one month (a total of 15 doses). Next, the animals in the groups were divided into two subgroups. The first subgroup of animals in each group (10 animals) was allocated for histological analysis at the age of 7.5 months. The animals in the second subgroup underwent a one-month washout period during which they did not receive the drug. At an age of 8 months, the animals underwent behavioral testing during a 14-day period. The following tests were conducted: the open field test, the novel object recognition test, and the Barnes maze test. Once testing had been completed, histological examination of the animal's brain sections was conducted (*Fig. 1*).

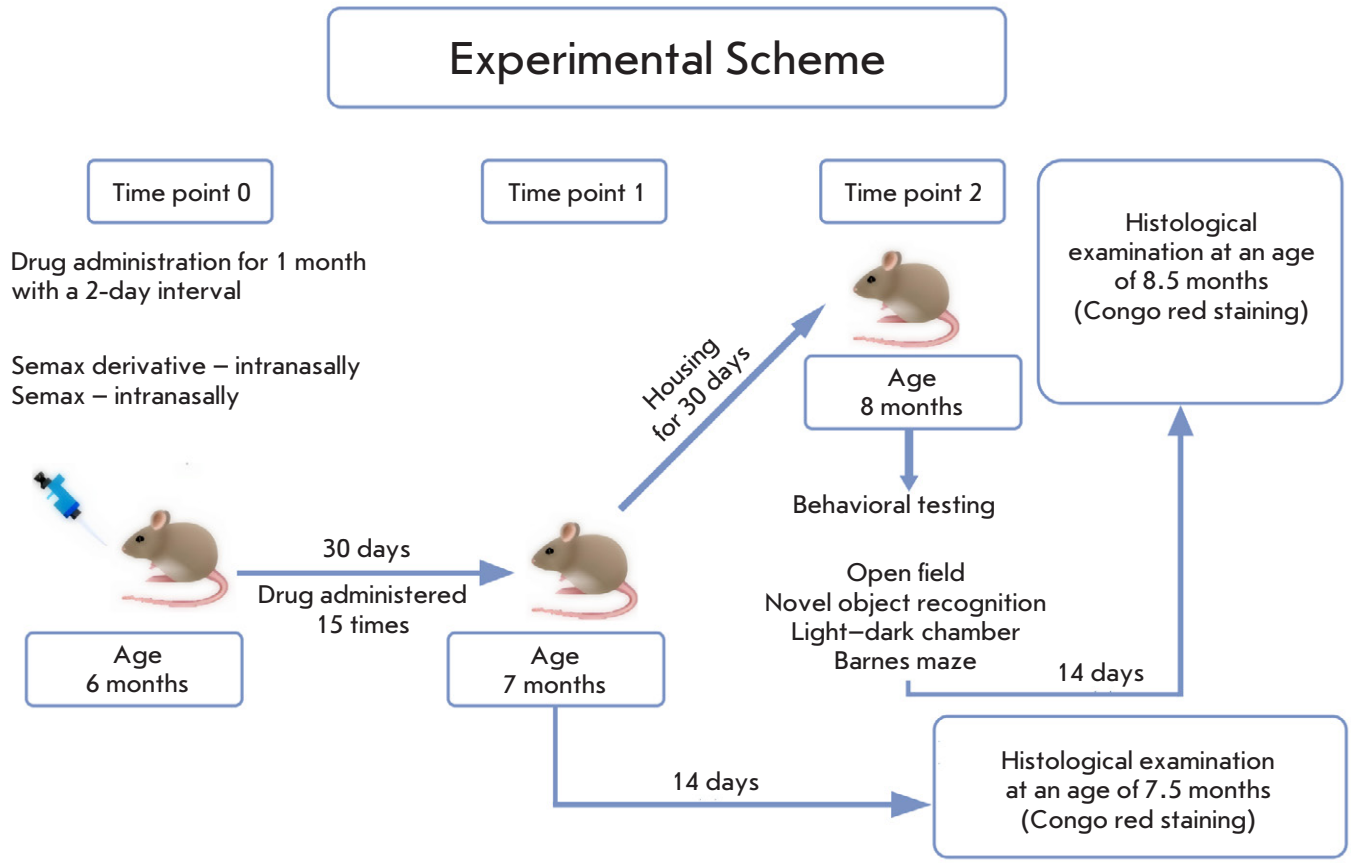

Fig. 1. The experiment design in the study investigating the effects of Semax and the Heptapeptide on APP/PS1 mice

Behavioral testing

The open field test. This test allows one to assess the locomotor activity of, exploratory behavior, and anxiety in the animals. The animals were placed in an arena made of opaque plexiglass (50 × 50 cm base; wall height, 50 cm) (OpenScience, Russia). A single mouse was tested for 5 min under ambient lighting conditions of 35–40 lx. The following parameters were documented in the online test: the total number of movements; the total movement time (s); the total distance traveled (cm); the average speed of all the movements (cm/s); the resting time (s); the distance traveled in the peripheral zone (cm); the total time spent moving in the periphery zone (s); the distance traveled in the central zone (cm); the time spent in the central zone (s); and the number of center crossings. The EthoVision software (Version 16, Netherlands) was used for data recording and processing.

The novel object recognition test. This test was used to assess the animals' cognitive functions, and memory in particular, by exploring the animals' preference for exploring a novel object compared to a familiar one. The test is subdivided into three phases: the habituation, training, and testing phases. The open field test was conducted on day 1 of the novel object recognition test. On day 2 of the test, the animal was also placed in the arena for 5 min; two objects (toys) of the same color were placed in certain zones. On day 3, the animal was placed in the arena for 5 min again, one of the objects being replaced with a new one of a different color. The following parameters were recorded using the EthoVision software: the locomotor activity, the number of approaches made toward the novel and familiar objects, and the time spent near them. After data analysis, the preference index for the novel object was calculated using the formula:

$$\mathrm{PI} = \frac{b}{b+a} \cdot 100\%,$$

where a is the number of approaches to the old object and b is the number of approaches to the novel object.

The Barnes maze test. This test was used to study spatial learning and memory of the animals. The objective of the Barnes maze test was to let a mouse explore the space and memorize the location of the

escape box using the configuration of distal visual cues placed around the testing area. The setup consisted of an arena 122 cm in diameter, with 40 holes 5 cm in diameter, one of them being the exit (the escape box). The distal visual cues were four black-and-white images with different figures and patterns, positioned in the cardinal directions (north, south, west, and east).

The Barnes maze test was carried out during five days: four days were intended for training and learning, and day 5 was the test day. During the first four days, the animals were placed in the arena for 3 min. After that, if the rodent had managed to find the escape box on its own, the box with the mouse inside was carefully transferred to its home cage. If the animal had failed to find the escape box independently, the experimenter gently guided it towards the box. Each rodent made four trials per training day with a 15-min interval. On day 5, the escape box was removed, and the hole was covered with a partition. The animal was placed in the arena for 5 min. The EthoVision software was used to measure the distance traveled, animal velocity, latency to find the target zone, and time spent near the former location of the escape box.

Histological examination

The animals were euthanized by cervical dislocation, and tissue specimens were prepared for analysis. The brain was dissected and fixed with Carnoy's solution (six parts 96% ethanol, three parts chloroform, and one part glacial acetic acid) overnight. Tissue was dehydrated using a sequential series of ethanol solutions of increasing concentration: 75% solution, 1 h; 96% solution (I), 5 min; 96% solution (II), 45 min; 100% solution (I), 5 min; 100% (II). After incubation in a 100% ethanol–chloroform (1:1) mixture for 30 min and in chloroform (I) for 1 h, the specimens were left overnight in chloroform (II) and the tissues were then impregnated with paraffin (3 changes, 1 h each) at 60°C. Paraffin blocks were prepared using a Leica EG1160 tissue embedding center (Leica Biosystems). Paraffin sections (8 μm thick) were mounted onto polylysine-coated glass slides.

Five glass slides, each containing ten brain sections, were prepared from a 400 μm thick brain region; every fifth brain section was placed on a single glass slide. The sections were then deparaffinized in xylene for 20 min, rehydrated by sequential incubation in ethanol solutions (100% solution, 10 min; 95% solution, 5 min; and 50% solution, 5 min), followed by three washes with deionized water for 5 min. The sections were stained with a Congo red dye solution (0.5% Congo red in 50% ethanol) for 5 min, differentiated in a 0.2% KOH solution in 80% ethanol for 1 min, washed thrice with deionized water for 5 min, and embedded into the Immu-Mount™ aqueous-based mountant (Thermo Scientific).

After brain fixation, dehydration, incubation, and paraffin embedding, tissue was sectioned and stained with Congo red dye. The total number of plaques across all the brain sections in the cortical and hippocampal regions was counted for each group throughout the study, and the arithmetic mean was calculated. Amyloid plaques were counted using the QuPath v0.5.1 software.

Statistical analysis

The descriptive statistics were employed for the statistical analysis of the data. All the behavioral testing data were characterized by parametric distribution by the Kruskal–Wallis H test. Two-way analysis of variance (two-way ANOVA) using generalized linear models (GLMs) was applied for intergroup comparisons in the Barnes maze test. Intergroup comparisons of changes in the histological variables were performed using the Kolmogorov–Smirnov test. Furthermore, the Šidák correction was used to control for the type I error rate during multiple hypothesis testing, which adjusts the significance threshold based on the number of planned comparisons. Differences were considered statistically significant at $p < 0.05$. The statistical analysis was conducted using the Statistica 10.0 software.

RESULTS

The effects of Semax and Heptapeptide on animal behavior

Mouse behavior in the open field test was evaluated at the first stage of the study (*Fig. 2*). A comparative analysis of the behavior of the animals in the WT and APP/PS1 groups revealed that the developing pathology in APP/PS1 mice statistically significantly reduced the number of entries into the center of the arena and entries into the periphery zone, as well as the time spent in the center of the arena. Administration of Semax prevented all these behavioral impairments in APP/PS1 animals. Furthermore, administration of Semax made the animals generally more active; their velocity and total distance traveled increased. Administration of the Heptapeptide statistically significantly increased the time spent in the periphery zone compared to the APP/PS1 animal group. However, the Heptapeptide exerted no significant effect on animal velocity, distance traveled, the number of entries into the periphery zone or center of the arena, or time spent in the center.

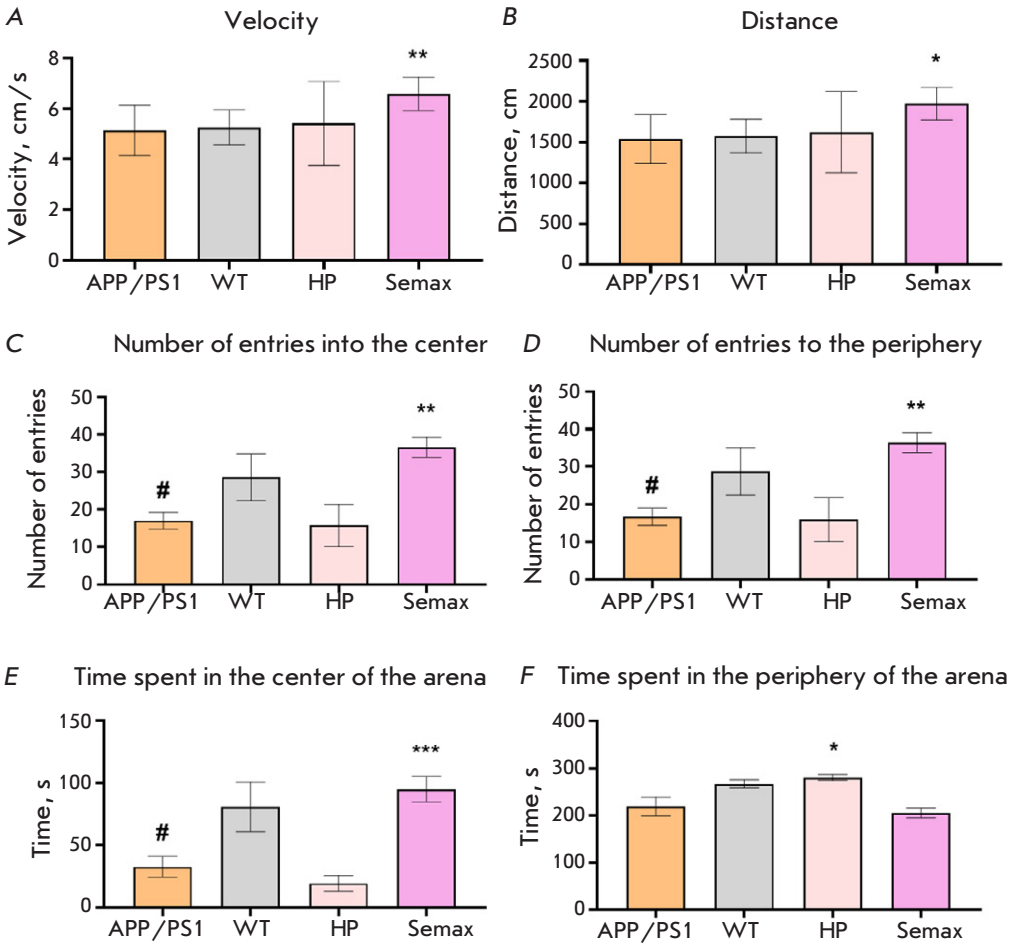

Fig. 2. Results of the open field test. Velocity (*A*); total distance traveled (*B*); number of entries into the center zone (*C*); number of entries into the periphery zone (*D*); time spent in the center zone (*E*); and time spent in the peripheral zone (*F*). Here and thereafter: APP/PS1 (APPswe/PS1dE9/Blg transgenic mice), WT (wild-type animals), HP (APP/PS1 mice treated with Heptapeptide), Semax (APP/PS1 mice treated with Semax); * – $p < 0.05$, ** – $p < 0.01$, *** – $p < 0.001$, respectively (compared to the untreated APP/PS1 group); # – $p > 0.05$ (APP/PS1 mice compared to wild-type animals) (Kruskal–Wallis H test). Number of animals per group, $n = 10$

The novel object recognition test was subsequently conducted (*Fig. 3*). On test day 3, the animals from the APP/PS1 group traveled a greater distance at a higher velocity compared to the animals in the WT group. Meanwhile, interest in exploring the novel object in APP/PS1 mice was significantly lower compared to that in wild-type mice. No differences in the preference index were observed for these two groups.

Administration of the Heptapeptide had no effect on the animals' velocity, distance traveled, or exploration of the novel object. However, the preference index in these animals increased by almost 30% compared to that in the APP/PS1 mice. Administration of Semax significantly increased interest in the novel object and the preference index for the novel object in the animals.

The Barnes maze test was then conducted. At the first stage of testing, the animals were trained during four days (*Fig. 4*). No significant differences in velocity and distance traveled were uncovered among all the studied groups, except for the animals receiving Semax. This drug significantly increased the velocity and reduced the distance traveled by the animals. On test days 2 and 3, the latency to find the target zone was significantly reduced in these animals; however, their performance deteriorated on test day 4.

On day 5 of the Barnes maze test, the experimental trial was performed, where the animals were let go in the arena; the results are shown in *Fig. 5*. The APP/PS1 animals traveled a greater distance at a higher velocity and were slower to find the zone where the escape box had previously been located compared to the wild-type animals.

The administration of the Heptapeptide significantly reduced the distance traveled by the animals and their velocity, increased the time spent in the area where the escape box had previously been located, and reduced the latency to find the target zone compared to the APP/PS1 animal group. However, the Heptapeptide did not significantly affect the number of entries into the target zone. The drug Semax significantly reduced the velocity, distance traveled, time spent in the target zone, the number of entries into the target zone, and the latency to find the area

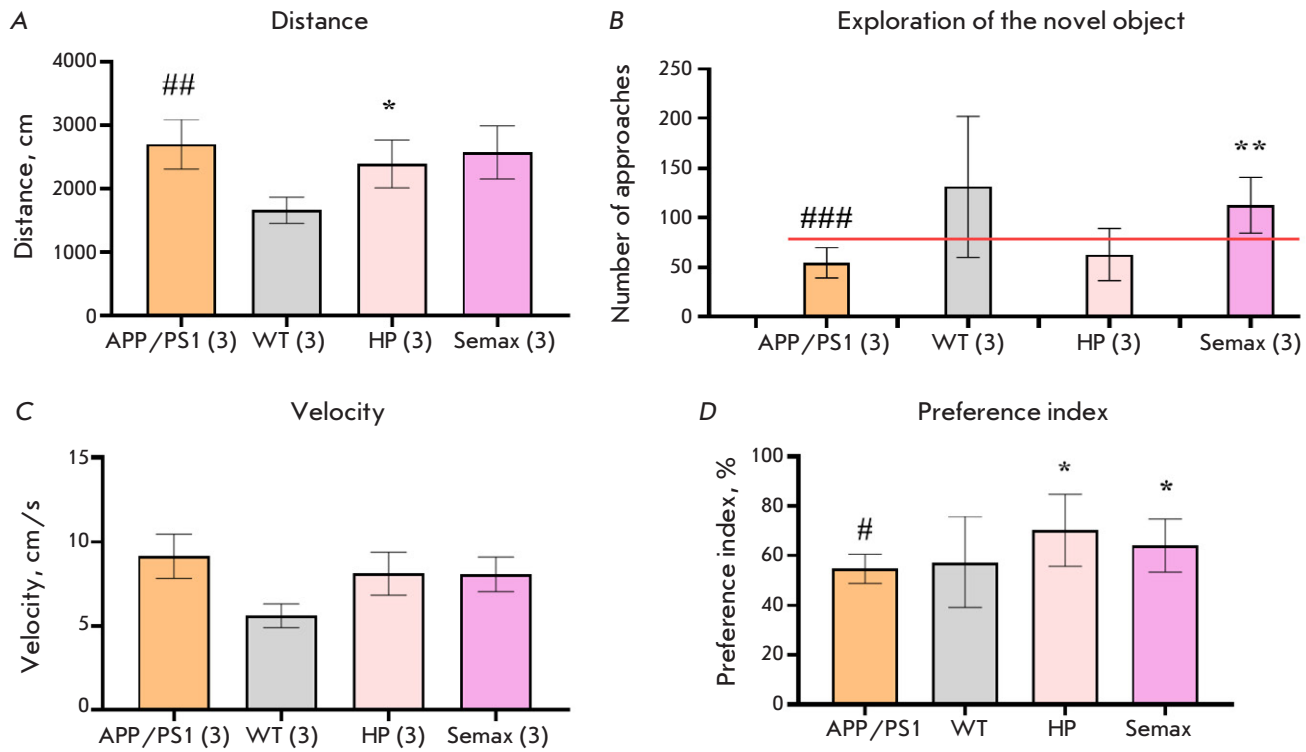

Fig. 3. Results of the novel object recognition test on day 3. Total distance traveled (*A*); the number of approaches to the novel object on day 3 (*B*); velocity (*C*); discrimination index (*D*); * – $p < 0.05$, ** – $p < 0.01$, respectively (compared to the untreated APP/PS1 group); # – $p > 0.05$, ## – $p < 0.01$, ### – $p < 0.001$, respectively (APP/PS1 mice compared to wild-type animals) (Kruskal–Wallis H test). $n = 10$

where the escape box had previously been located. Therefore, both the Heptapeptide and Semax led to a notable correction in the behavioral parameters of the APP/PS1 animals to a level comparable to that in the wild-type animals.

The results of histological studies

The histological examination was performed to assess the effect of Semax and Heptapeptide on the development of amyloidosis in APP/PS1 mice. Experiments were carried out at two time points: the number of amyloid plaques in the animal brain was determined two weeks (in mice aged 7.5 months) and 1.5 months (in mice aged 8.5 months) after drug administration.

In the animals aged 7.5 months, therapy with Heptapeptide and Semax reduced the number of amyloid plaques in the cortical area by a factor of 1.6 and 2.8, respectively, compared to the untreated animals (*Fig. 6*). An analysis of the size distribution of amyloid plaques revealed that most of them were sized < 100 μm^2: those were the recently formed inclusions whose size would further increase with age. Heptapeptide and Semax significantly decreased the prevalence of this plaque population.

The same trend was observed when analyzing amyloid plaques in the hippocampal area (*Fig. 6*). The number of amyloid plaques in the Heptapeptide and Semax groups was 1.7-fold and 2.6-fold smaller than that in the APP/PS1 group, respectively. The drug-induced reduction in the plaque count was most significant for the population of amyloid inclusions with an area of ⩽ 100 μm^2.

In the APP/PS1 animals aged 8.5 months, the number of amyloid plaques was significantly increased both in the cortex and hippocampus (*Fig. 7*). Meanwhile, the protective effects of Heptapeptide and Semax were nearly identical to that observed for the 7.5-month-old animals. The numbers of amyloid plaques in the cortex of the mice in the Heptapeptide and Semax groups were 1.8-fold and 2.2-fold smaller than that in the APP/PS1 group. The number of plaques in the hippocampus of the mice in the Heptapeptide group was 1.6-fold smaller compared to mice in the APP/PS1 group, while the animals in the Semax group had 1.7 times fewer plaques. A size distribution analysis of amyloid plaques revealed that the largest reduction in number was observed for plaques sized up to 100 μm^2 in

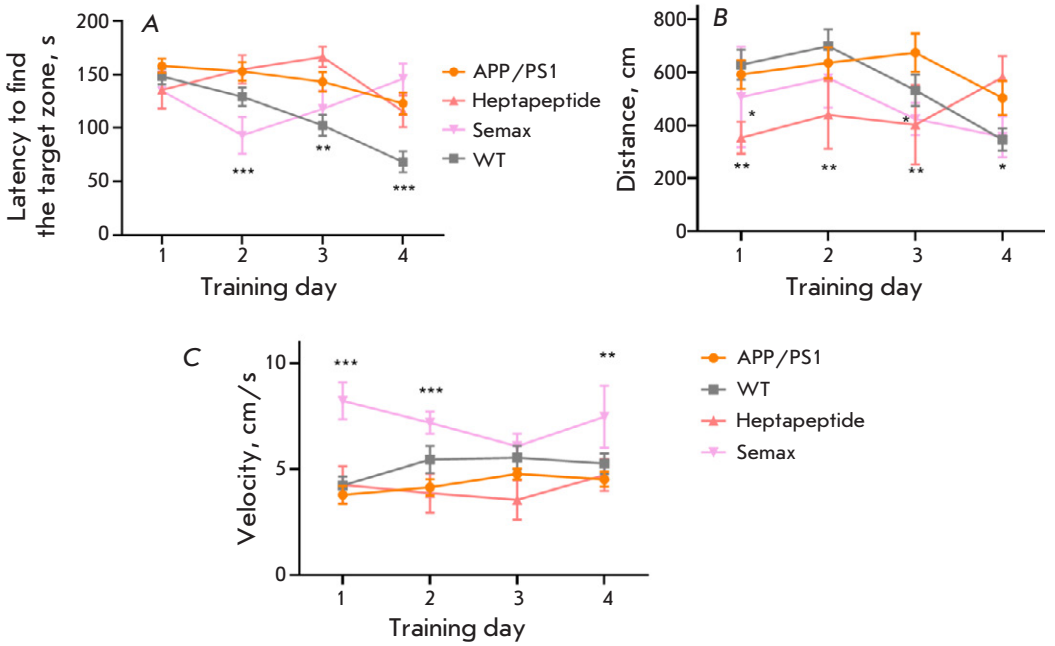

Fig. 4. Results of the Barnes maze test (days 1–4). Latency to find the target zone (*A*); total distance traveled (*B*); velocity (*C*); * – $p < 0.05$, ** – $p < 0.01$, *** – $p < 0.001$, respectively (compared to the untreated APP/PS1 group), two-way ANOVA. $n = 10$

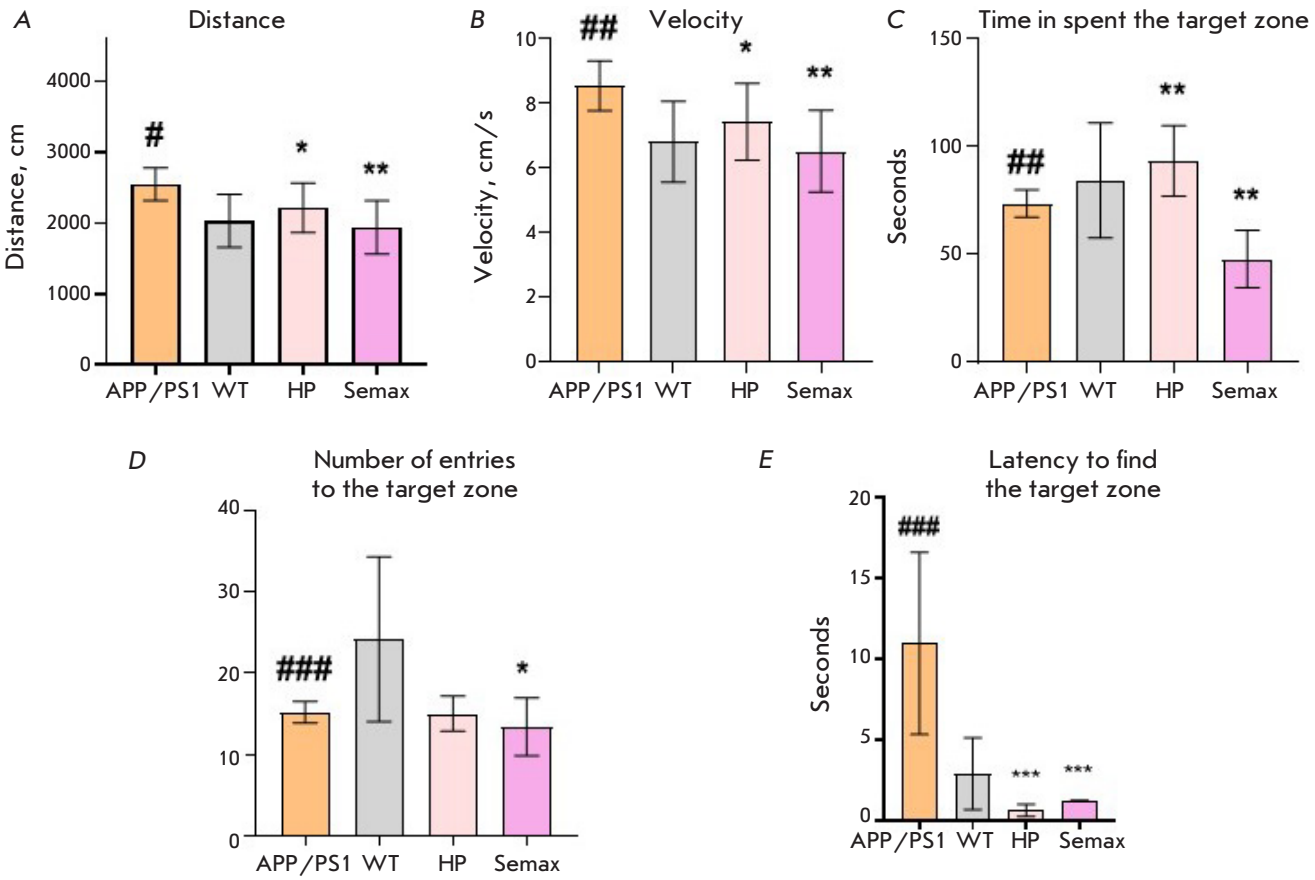

Fig. 5. The results of the Barnes maze test (day 5). Total distance traveled (*A*); velocity (*B*); time spent in the target zone (*C*); number of entries into the target zone (*D*); latency to find the target zone (*E*); * – $p < 0.05$, ** – $p < 0.01$, *** – $p < 0.001$, respectively (compared to the untreated APP/PS1 group); # – $p > 0.05$, ## – $p < 0.01$, ### – $p < 0.001$, respectively (APP/PS1 mice compared to wild-type animals) (Kruskal–Wallis H test). $n = 10$

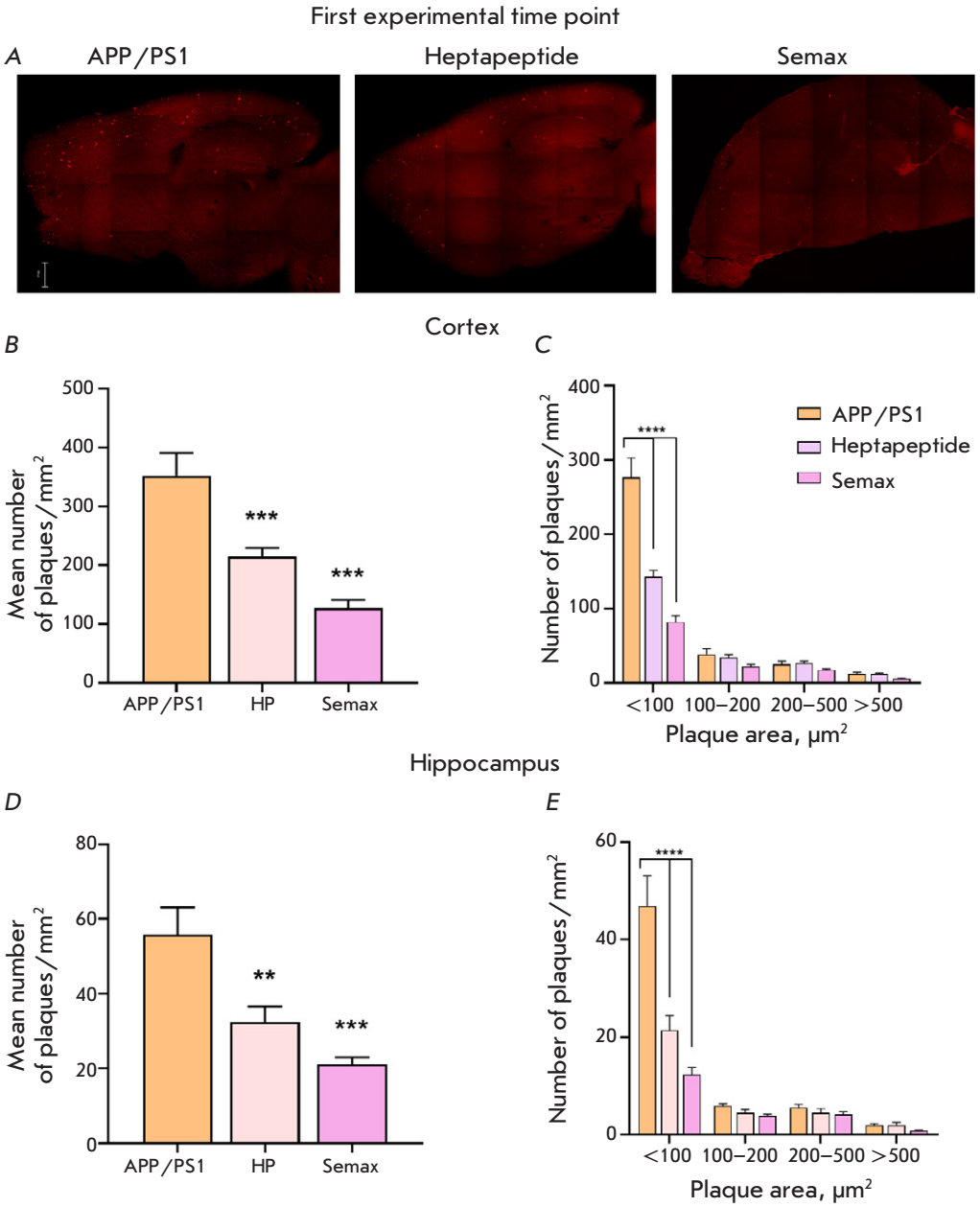

Fig. 6. The results of the histological analysis of APP/PS1 mice at the age of 7.5 months. (*A*) Representative micrographs of the brain sections from the control animals and mice administered Heptapeptide and Semax. Amyloid plaques are stained bright red. Scale bar: 500 μm. The mean number of amyloid plaques (*B*, *D*) and plaque size distribution (*C*, *E*) in the brains of APP/PS1 mice in the cortex (*B*, *C*) and hippocampus (*D*, *E*) at the first experimental time point. ** – $p < 0.05$, ***–$p<0.01$, Kolmogorov–Smirnov test; **** – $p < 0.0001$, Šidák correction for multiple comparisons. $n = 10$

mice of both ages (7.5 and 8.5 months) that had received the drugs.

DISCUSSION

The peptide Semax, which exhibits neuroprotective and nootropic properties, is a long-acting memory enhancer [17]. The proposed modifications to Semax, yielding the Heptapeptide, are expected to enhance the effect of the peptide on the key pathological features of AD.

Testing of animal behavior revealed that APP/PS1 mice had significantly impaired behavioral and cognitive characteristics compared to those of wild-type mice. After a course of peptide drugs, many of these functions were restored, either completely or partially. Semax exhibited a significant favorable effect in the open field and novel object recognition tests. In the Barnes maze test, the Heptapeptide improved certain behavioral parameters of APP/PS1 mice to a level comparable to that of wild-type animals. Semax had a positive effect on an even greater number of parameters in this test.

Hence, a number of behavioral and cognitive characteristics in animals with a Alzheimer's-type pathology showed improvement one month after the course of peptide drugs.

The most significant data were collected through the histological examination of animals' brains.

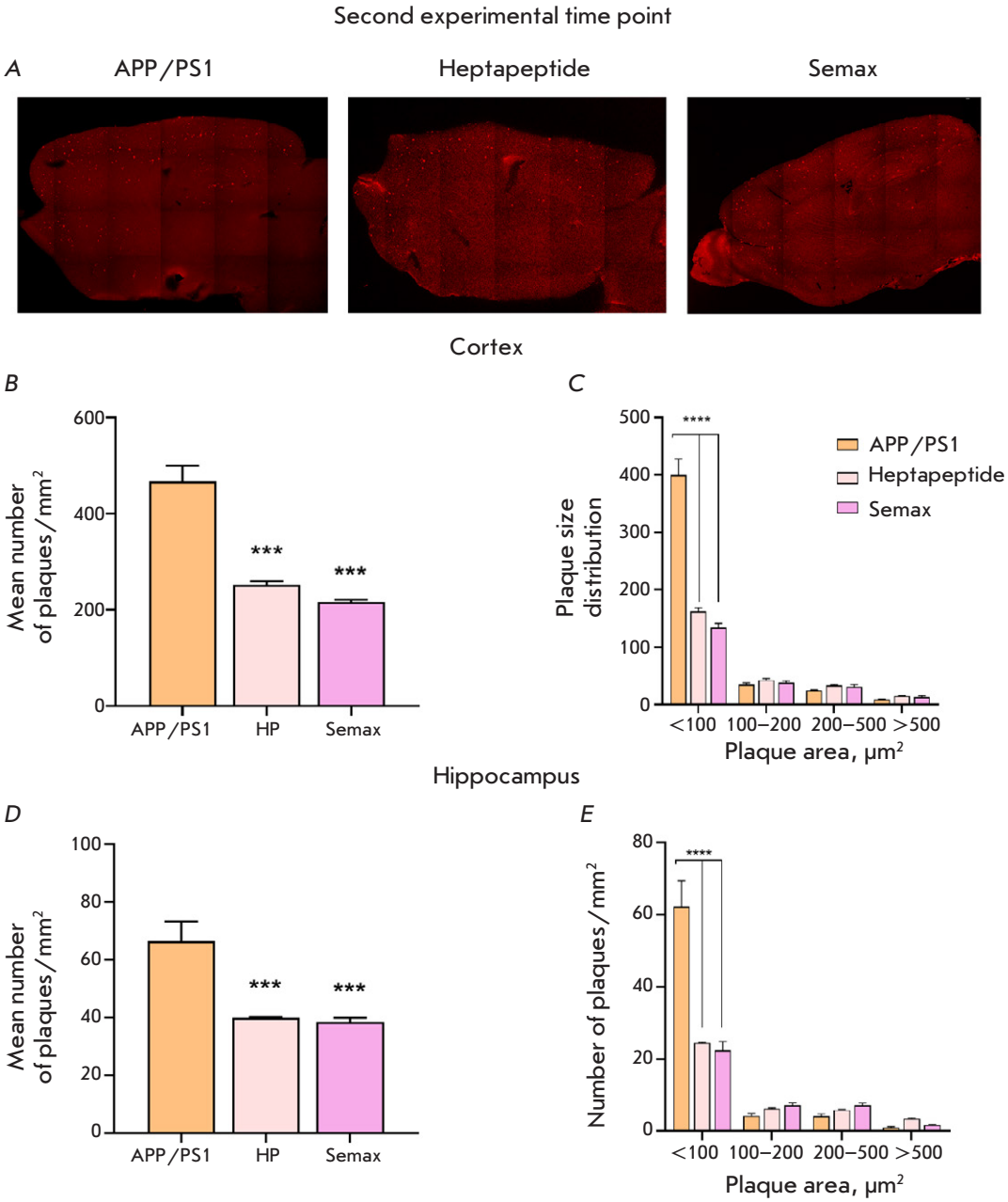

Fig. 7. Results of the histological analysis of APP/PS1 mice at the age of 8.5 months. (*A*) Representative microphotographs of the brain sections from the control animals and mice administered with Heptapeptide and Semax. Amyloid plaques are stained bright red. The mean number of amyloid plaques (*B*, *D*) and plaque size distribution (*C*, *E*) in the brains of APP/PS1 mice in the cortex (*B*, *C*) and hippocampus (*D*, *E*) at the second experimental time point. ** – $p < 0.05$, *** – $p < 0.01$, Kolmogorov–Smirnov test; **** – $p < 0.0001$, Šidák correction for multiple comparisons. $n = 10$

Amyloid plaques were detected in the cerebral cortex and hippocampus two weeks after the administration of the peptide during one month. At this stage, the mean number of amyloid plaques in the APP/PS1 group was > 350 per mm^2, while this number decreased 1.6-fold and 2.8-fold in the Heptapeptide and Semax groups, respectively. The peptides primarily reduced the number of small plaques (sized < 100 μm^2), which is indication that they inhibit the formation of new plaques. As expected, the mean plaque number in the hippocampal region was smaller (< 50 per mm^2). In APP/PS1 mice, the peptides also reduced the number of plaques (1.7-fold for the Heptapeptide group and 2.6-fold for the Semax group). Therefore, at this stage, course therapy with either peptide significantly reduced the formation of amyloid plaques in both brain regions, Semax being the more efficient of these two peptides.

The next histological examination stage was conducted 1.5 months after drug administration using animal brain specimens. During this period, the mean number of plaques (per mm^2) in the cerebral cortex of APP/PS1 animals had exceeded 400. In the Heptapeptide and Semax groups, this value increased

only slightly, remaining significantly lower (1.8- and 2.2-fold, respectively). Similar findings were obtained for the hippocampal specimens. Hence, both peptides decreased the number of amyloid inclusions within tissues, and this effect persisted for 1.5 months post-administration. The effect of these peptides may potentially be based on an important feature of many peptides: their ability to allosterically interact with various receptors, thus altering their impact on controlled signaling pathways [27].

The previously proposed concept of amyloid matrices relies on a long-term interplay between modified beta-amyloid variants and partner proteins, including the alpha-4 nicotinic acetylcholine receptor. The resulting complexes can act as seeds for pathological aggregation of intact beta-amyloid molecules to induce the formation of amyloid plaques [28, 29]. Hence, it is fair to hypothesize that both of the studied peptides bind allosterically to receptors, including acetylcholine ones, and alter their configuration, thus either fully preventing or substantially reducing the degree to which they bind to the modified form of beta-amyloid. In this case, this particular amyloid plaque formation pathway can be inhibited by the peptides under study; this inhibitory effect persists for more than a month following the treatment course.

Our findings demonstrate that intranasal administration of Semax or Heptapeptide improves the cognitive function in the mouse model of Alzheimer's disease. Both Semax and Heptapeptide significantly reduce the amyloid load in the animal brain. These data prove that Semax and its derivatives are promising for developing therapeutic and corrective strategies for Alzheimer's disease. ●

This work was supported by the Russian Science Foundation (grant No. 19-74-30007, behavioral tests and histological examination) and the State Assignment to the National Research Center "Kurchatov Institute" (peptide design and synthesis).

REFERENCES

1. Scheltens P, Blennow K, Breteler MMB, et al. Alzheimer's Disease. *Lancet.* 2016;388(10043):505-517. doi: 10.1016/S0140-6736(15)01124-1
2. Kuhla A, Rühlmann C, Lindner T, et al. APPswe/PS1dE9 mice with cortical amyloid pathology show a reduced NAA/Cr ratio without apparent brain atrophy: A MRS and MRI study. *NeuroImage Clin.* 2017;15:581-586. doi: 10.1016/j.nicl.2017.06.009
3. Konttinen H, Cabral-da-Silva MEC, Ohtonen S, et al. PSEN1ΔE9, APPswe, and APOE4 Confer Disparate Phenotypes in Human iPSC-Derived Microglia. *Stem Cell Reports.* 2019;13(4):669-683. doi: 10.1016/j.stemcr.2019.08.004
4. Koroleva SV, Myasoedov NF. Semax As a Universal Drug for Therapy and Research. *Biology Bulletin.* 2018;45(6):589-600. doi: 10.1134/S1062359018060055
5. Cummings J, Lee G, Ritter A, Sabbagh M, Zhong K. Alzheimer's disease drug development pipeline: 2019. *Alzheimers Dement (N Y).* 2019;5:272-293. doi: 10.1016/j.trci.2019.05.008
6. Bairamova SP, Petelin DS, Akhapkin RV, et al. The endogenic neurosteroid system and its role in the pathogenesis and therapy of mental disorders. *Res Results Pharmacol.* 2023; 9(1):61-69. doi: 10.18413/rrpharmacology.9.10015
7. Khan S, Barve KH, Kumar MS. Recent Advancements in Pathogenesis, Diagnostics and Treatment of Alzheimer's Disease. *Curr Neuropharmacol.* 2020;18(11):1106-1125. doi: 10.2174/1570159X18666200528142429
8. Stepenko YV, Shmigerova VS, Kostina DA, et al. Study of the neuroprotective properties of the heteroreceptor EPOR/CD131 agonist of peptide structure in tau-proteinopathy modeling. *Res Results Pharmacol.* 2024;10(2) 41-47. doi: 10.18413/rrpharmacology.10.492
9. Platt B, Drever B, Koss D, et al. Abnormal cognition, sleep, EEG and brain metabolism in a novel knock-in Alzheimer mouse, PLB1. *PLoS One.* 2011;6(11):e27068. doi: 10.1371/journal.pone.0027068
10. Lysikova EA, Kukharsky MS, Chaprov KD, et al. Behavioural impairments in mice of a novel FUS transgenic line recapitulate features of frontotemporal lobar degeneration. *Genes Brain Behav.* 2019;18(8):e12607. doi: 10.1111/gbb.12607
11. Forest KH, Alfulaij N, Arora K, et al. Protection against β-amyloid neurotoxicity by a non-toxic endogenous N-terminal β-amyloid fragment and its active hexapeptide core sequence. *J Neurochem.* 2018;144(2):201-217. doi: 10.1111/jnc.14257
12. Kozin SA, Barykin EP, Mitkevich VA, Makarov AA. Anti-amyloid therapy of Alzheimer's disease: Current state and prospects. *Biochemistry (Mosc).* 2018;83(9):1057-1067. doi: 10.1134/S0006297918090079
13. Istrate AN, Tsvetkov PO, Mantsyzov AB, et al. NMR solution structure of rat aβ(1-16): toward understanding the mechanism of rats' resistance to Alzheimer's disease. *Biophys J.* 2012;102(1):136-143. doi: 10.1016/j.bpj.2011.11.4006
14. Cummings J, Fox N. Defining Disease Modifying Therapy for Alzheimer's Disease. *J Prev Alzheimers Dis.* 2017;4(2):109-115. doi: 10.14283/jpad.2017.12
15. Sengupta U, Nilson AN, Kayed R. The Role of Amyloid-β Oligomers in Toxicity, Propagation, and Immunotherapy. *EBioMedicine.* 2016;6:42-49. doi: 10.1016/j.ebiom.2016.03.035
16. Lysikova EA, Kuzubova EV, Radchenko AI, et al. APPswe/PS1dE9/Blg Transgenic Mouse Line for Modeling Cerebral Amyloid Angiopathy in Alzheimer's Disease. *Mol Biol (Mosc).* 2023;57(1):85-94. doi: 10.31857/S0026898423010081
17. Ashmarin IP, Nezaviba'tko VN, Myasoedov NF, et al. A nootropic adrenocorticotropin analog 4-10-semax (15 years experience in its design and study). *Zh Vyssh Nerv Deiat Im I P Pavlova.* 1997;47(2):420-430
18. Myasoedov NF, Grivennikov IA. Neuropeptides and their analogues in the regulation of the functions of the mammalian nervous system, including humans. From the synthesis and study of their mechanisms of action to the

creation of new generation medicines. In: *Problemy i perspektivy molekulyarnoi genetiki* [Problems and prospects of molecular genetics]. Moscow: Nauka; 2004.2:195–236.
19. Potaman VN, Antonova LV, Dubynin VA, et al. Entry of the synthetic ACTH(4–10) analogue into the rat brain following intravenous injection. *Neurosci Lett*. 1991;127(1):133-136. doi: 10.1016/0304-3940(91)90912-d
20. Ponomareva-Stepnaia MA, Bakharev VD, Nezavibatko VN, Andreeva LA, Alfeeva LYu, Potaman VN. Sravnitelnye issledovaniia analogov AKTG(4–10) stimulatorov obucheniia i pamiati. *Khimiko-farmatsevticheskii zhurnal*. 1986;20(6):667–670.
21. Levitskaya NG, Glazova NYu, Sebentsova EA, et al. Investigation of the Spectrum of Physiological Activities of the Heptapeptide Semax, an ACTH 4–10 Analogue. *Neurochemical J.* 2008;2(1–2):95-101. doi: 10.1134/S1819712408010182
22. Levitskaya NG, Sebentsova EA, Glazova NYu, et al. Study on the neurotropic activity of the products of Semax enzymatic degradation. *Dokl Biol Sci* 2000;372:243-246
23. Mjasoedov NF, Gavrilova SI, Kalyn JaB, et al, inventors; Federal Service for Intellectual Property, assignee. Agent and method for prevention and treatment of the patients with Alzheimer's disease. Russian Federation patent RUS 2384343. March 20, 2010.
24. Ilina AR, Popovich IG, Ryzhak GA, Khavinson VKh. Prospects for use of short peptides in pharmacotherapeutic correction of Alzheimer's disease. *Adv Geront.* 2024:37(1-2):10-20. doi: 10.34922/AE.2024.37.1-2.001
25. Ponomareva-Stepnaia MA, Nezavibatko VN, Antonova LV, et al. Analog ACTG(4–10) stimulator obucheniia prolongirovannogo deistviia. *Khimiko-farmatsevticheskii zhurnal.* 1984;18(7):790-795.
26. Ryzhak GA, Ilina AR. Prospects of using peptide drugs for the prevention and treatment of Alzheimer's disease. *Problems of Geroscience.* 2024;4:223-226. doi: 10.37586/2949-4745-4-2024-223-226
27. Vyunova TV, Andreeva LA, Shevchenko KV, Myasoedov NF. An integrated approach to study the molecular aspects of regulatory peptides biological mechanism. *J Labelled Comp Radiopharm.* 2019;62(12):812-822. doi: 10.1002/jlcr.3785
28. Kozin SA, Makarov AA. The convergence of Alzheimer's disease pathogenesis concepts. *Mol Biol (Mosk).* 2019;53(6):1020-1028. doi: 10.1134/S0026898419060107
29. Barykin EP, Garifulina AI, Kruykova EV, et al. Isomerization of Asp7 in Beta-Amyloid Enhances Inhibition of the alpha7 Nicotinic Receptor and Promotes Neurotoxicity. *Cells.* 2019;8(8):771-787. doi: 10.3390/cells8080771

Recombinant Production, Species-Specific Activity at the TRPA1 Channel, and Significance of the *N*-Terminal Residue of ProTx-I Toxin from *Thrixopelma Pruriens* Tarantula Venom

M. A. Shulepko[1], M. Zhang[1], E. A. Zhivov[2,3], D. S. Kulbatskii[2], A. S. Paramonov[2], Yu. Che[1], A. V. Kuznetsov[1], A. V. Popov[2,4], M. P. Kirpichnikov[2,5], Z. O. Shenkarev[2,3*], E. N. Lyukmanova[1,2,3,5*]

[1]Faculty of Biology, Shenzhen MSU-BIT University, Shenzhen, Guangdong Province, 518172 China
[2]Shemyakin–Ovchinnikov Institute of Bioorganic Chemistry, Moscow, 117997 Russia
[3]Moscow Center for Advanced Studies, Moscow, 123592 Russia
[4]Kurchatov Medical Primatology Center of National Research Center "Kurchatov Institute", Krasnodarskiy kray, Sochi, 354376 Russia
[5]Interdisciplinary Scientific and Educational School "Molecular Technologies of the Living Systems and Synthetic Biology", Faculty of Biology, Lomonosov Moscow State University, Moscow, 119234 Russia
*E-mail: zakhar-shenkarev@yandex.ru; lyukmanova_ekaterina@smbu.edu.cn
Received December 11, 2024; in final form, August 03, 2025
DOI: 10.32607/actanaturae.27590

ABSTRACT **The ProTx-I toxin from *Thrixopelma pruriens* tarantula venom inhibits voltage-gated sodium (Na_V), potassium, and calcium channels, as well as the chemosensitive TRPA1 ion channel, affecting the activating processes of these channels. Due to its action at the $Na_V1.7$, $Na_V1.8$, and TRPA1 channels involved in pain perception and propagation, ProTx-I may be used as a model for the development of next-generation analgesics. ProTx-I consists of 35 amino acid residues, with three disulfide bonds forming an inhibitor cystine knot (ICK) motif, which challenges its heterologous production. An efficient ProTx-I production system is necessary to study, at the molecular level, the mechanism by which the toxin acts. In this study, we tested several approaches for bacterial production of disulfide-containing toxins. Cytoplasmic expression of ProTx-I fused with either thioredoxin or glutathione-S-transferase failed to yield a correctly folded toxin. However, the natively folded ProTx-I was successfully obtained by "direct" expression in the form of cytoplasmic inclusion bodies, followed by renaturation, as well as by secretion into the periplasmic space via fusion with maltose-binding protein. The activity of the recombinant ProTx-I was studied by electrophysiology in *X. laevis* oocytes expressing rat and human TRPA1 channels. The toxin proved to be more active on the rat channel than on the human channel (IC_{50} = 250 ± 85 and 840 ± 190 nM, respectively). The presence of an additional *N*-terminal methionine residue in the toxin obtained through "direct" expression significantly attenuated its activity.**

KEYWORDS **cystine knot, TRPA1 channel, gating modifier toxin, bacterial production, disulfide-rich proteins.**

ABBREVIATIONS **AITC – allyl isothiocyanate; GST – glutathione S-transferase; ICK – inhibitory cystine knot; MBP – maltose-binding protein; Na_V – voltage-gated sodium channel; TRX – thioredoxin; IPTG – isopropyl β-*D*-1-thiogalactopyranoside.**

INTRODUCTION

Spider venoms are a rich source of polypeptide toxins that act on various membrane receptors and ion channels [1–3]. Many spider toxins belong to the knottin family that includes small (20–50 aa) β-structural peptides containing a conserved inhibitory cystine knot (ICK) motif [4] formed by three disulfides: C1–C4, C2–C5, and C3–C6. This spatial structure is responsible for the high physicochemical and proteolytic stability of knottins, making the ICK motif a promising basis for the design of new peptide drugs [5].

Spider knottins include membrane-active toxins that affect the activation or inactivation of sodium (Na_V), potassium, and calcium voltage-gated channels (so-called gating modifier toxins) [6]. The ProTx-I toxin (Protoxin-I or β/ω-theraphotoxin-Tp1a, 35 aa) is a membrane-active knottin of the Peruvian green velvet tarantula *Thrixopelma pruriens*. ProTx-I effectively inhibits a number of voltage-gated channels [7], as well as the chemosensitive TRPA1 channel [8]. Among the ProTx-I targets, $Na_V1.7$, $Na_V1.8$, and TRPA1 channels are promising therapeutic targets for the treatment of pain and neurological inflammatory syndromes [9–11]. Studying the mechanism of ProTx-I action on these channels may yield valuable insight that could help in the development of new analgesics and other biomedical drugs.

The first step that is required in order to study the mechanism of ProTx-I action and, eventually, design new variants of this knottin is to develop an efficient production system. Traditionally, small polypeptide toxins, including spider knottins, are produced using methods of peptide synthesis followed by refolding to form the correct system of disulfide bonds [12]. In addition, recombinant knottins are produced in *Pichia pastoris* cells [12–14] and *Escherichia coli* cells [15, 16]. However, during cytoplasmic production, these proteins accumulate as insoluble inclusion bodies [17, 18]. In *E. coli* cells, disulfide-rich toxins are produced through (1) "direct" expression followed by isolation of the peptide from inclusion bodies and its refolding; (2) fusion with proteins that promote the formation of disulfide bonds and increase the level of production, e.g., thioredoxin A (TRX) or glutathione S-transferase (GST); and (3) secretion of recombinant peptides into the *E. coli* periplasmic space where formation of disulfide bonds occurs [17, 19].

We compared these approaches in bacterial ProTx-I production and, for the first time, produced a correctly folded recombinant toxin and characterized its activity at human and rat TRPA1 channels. The obtained data demonstrate a significant species-specificity of the inhibitory action of ProTx-I, as well as the influence of the *N*-terminal sequence of the toxin on its activity. The developed bacterial production system opens new opportunities for the production of mutant and isotope-labeled ProTx-I variants for further structural and functional studies.

EXPERIMENTAL

Design of expression vectors

The *ProTx-I* gene was constructed based on the amino acid sequence P83480 from the UniProt database. The nucleotide sequence of the gene was optimized in accordance with the codon usage frequency in *E. coli*. Vectors for the cytoplasmic expression of the TRX–ProTx-I and GST–ProTx-I fusion proteins were prepared by cloning the *ProTx-I* gene into the *pET-32a*(+) (Novagene, USA) and *pET-32a*(+)*/GST* vectors at the KpnI/BamHI and BamHI/HindIII sites, respectively. The *pET-32a*(+)*/GST* plasmid was produced prior by replacing the *TRX* gene sequence in the *pET-32a*(+) plasmid with the *GST* gene sequence. The vector for bacterial secretion of the MBP–ProTx-I fusion protein was generated by cloning the *ProTx-I* gene into the *pLicC-MBP-APETx2* plasmid (Addgene, #72668) at the KpnI and SacI sites [20]. The vector for direct expression of *Met-ProTx-I* was prepared by cloning the *ProTx-I* gene into the *pET-22b*(+) vector (Novagene) at the NdeI and BamHI sites. In this case, the *N*-terminus of the ProTx-I molecule contained an additional methionine residue encoded by the *ATG* start codon. To produce 6His-Met-ProTx-I, an additional sequence encoding the 6His-tag and a linker sequence containing a methionine residue were inserted at the 5'-end of the *ProTx-I* gene. This gene was then cloned into the *pET-22b*(+) vector at the NdeI and BamHI sites. Schematic representations of the constructs used in the study are shown in *Fig. 1*.

Bacterial production of the TRX–ProTx-I, GST–ProTx-I, and MBP–ProTx-I fusion proteins

To produce the TRX–ProTx-I and GST–ProTx-I fusion proteins, *E. coli* BL21(DE3) and SHuffle T7 Express (NEB) strains were transformed with the *pET-32a*(+)*/TRX–ProTx-I* and *pET-32a*(+)*/GST–ProTx-I* vectors, respectively. MBP–ProTx-I was produced in the *E. coli* Rosetta-gami (DE3) strain. Cells were grown in a TB medium (12 g of bactotryptone, 24 g of yeast extract, 4 mL of glycerol, 2.3 g of KH_2PO_4, 12.5 g of K_2HPO_4 per 1 L of medium, pH 7.4) containing 100 μg/mL ampicillin (Sigma, USA) to OD_{600} ~ 0.6. Expression was induced by adding 0.1 mM isopropyl-β-*D*-1-thiogalactopyranoside (IPTG, Sigma). The cells were cultivated at 20°C for 16 h for

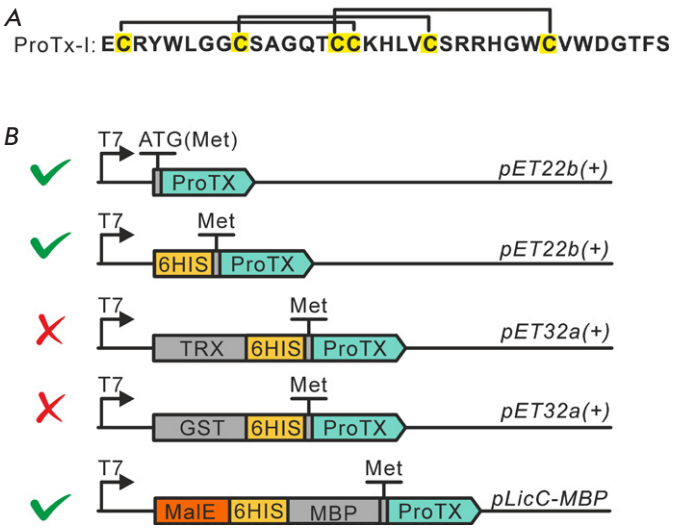

Fig. 1. Design of expression vectors for ProTx-I production in *E. coli* cells. (*A*) The amino acid sequence of the ProTx-I toxin. Cysteine residues are shown in yellow; disulfide bonds are indicated with solid lines. (*B*) Schematic representation of expression vectors. From top to bottom: vectors for "direct" expression of Met-ProTx-I and 6His-Met-ProTx-I; vectors for the cytoplasmic production of ProTx-I with the partners TRX and GST; the vector for ProTx-I secretion as a fusion protein with MBP. Check marks indicate the vectors successfully used for the production of correctly folded ProTx-I

GST–ProTx-I or at 13°C for 72 h for MBP–ProTx-I and TRX–ProTx-I.

Bacterial production of Met-ProTx-I and 6His-Met-ProTx-I

Met-ProTx-I and 6His-Met-ProTx-I were produced in the *E. coli* BL21(DE3) strain transformed with the *pET-22b(+)/Met-ProTx-I* or *pET-22b(+)/6His-Met-ProTx-I* vector. To produce Met-ProTx-I, cells were grown in a TB medium at 37°C to OD_{600} of ~0.6 and expression was induced by adding 0.2 mM IPTG. To produce 6His-Met-ProTx-I, cells were grown in a SB medium (32 g of bactotryptone, 20 g of yeast extract, 5 g of NaCl, pH 7.4) at 37°C to OD_{600} of ~6.0 and expression was induced with 1 mM IPTG. After induction, cell cultivation was continued at 37°C for 18 h.

Isolation and purification of the TRX–ProTx-I, GST–ProTx-I, and MBP–ProTx-I fusion proteins

Cells were collected by centrifugation at 10,000 g and 4°C for 20 min. The cell pellet was resuspended in buffer A (20 mM Tris-HCl, 300 mM NaCl, pH 8.0) in the presence of 1 mM phenylmethylsulfonyl fluoride (PMSF, Sigma). The cells were disrupted by ultrasound (Branson Digital Sonifier, USA) at an output power of 500 W and 4°C for 6 min. The suspension was centrifuged at 30,000 g at 4°C for 30 min. Fusion proteins were purified by metal-chelate affinity chromatography on a Ni-Sepharose FastFlow resin (Cytiva, USA) pre-equilibrated in buffer A. Recombinant proteins were eluted by imidazole (Macklin, China) gradient (20–500 mM).

Isolation and purification of reduced Met-ProTx-I and 6His-Met-ProTx-I

Isolation of Met-ProTx-I from cytoplasmic inclusion bodies and its purification under denaturing conditions were performed according to the protocols reported elsewhere [19]. After chromatography, Met-ProTx-I was reduced with a 500-fold molar excess of dithiothreitol (DTT, Sigma). Cytoplasmic inclusion bodies containing 6His-Met-ProTx-I were solubilized in denaturing buffer (20 mM Tris-HCl, 300 mM NaCl, 10 mM β-mercaptoethanol, 8 M urea, pH 8.0) for 3 h, centrifuged, and the supernatant was applied on a Ni-Sepharose FastFlow chromatography resin equilibrated with denaturing buffer. 6His-Met-ProTx-I was eluted by imidazole gradient (20–500 mM). Before BrCN hydrolysis (Sigma), chromatographic fractions of 6His-Met-ProTx-I were supplemented with a 500-fold molar excess of DTT.

Hydrolysis of recombinant proteins with BrCN

The recombinant proteins 6His-Met-ProTx-I, TRX–ProTx-I, GST–ProTx-I, and MBP–ProTx-I at a concentration of 4 mg/mL were hydrolyzed by adding 0.3 M HCl and a 50-fold molar excess (relative to methionine residues) of BrCN. The reaction proceeded in the dark at room temperature overnight. BrCN was then removed by evaporation using a Centrivap (Labconco, USA) equipped with a cryogenic trap.

Renaturation of Met-ProTx-I and ProTx-I

Renaturation of Met-ProTx-I and ProTx-I (produced by BrCN hydrolysis of 6His-Met-ProTx-I) was initiated by transferring the recombinant proteins to the refolding buffer (0.1 M Tris-HCl, 2 M urea, 1.5 mM GSH, and 0.15 mM GSSG, pH 7.5) using gel filtration on NAP-25 chromatography columns (Cytiva). The final concentration of recombinant toxins in the refolding buffer was 0.02 mg/mL.

Purification and analysis of recombinant ProTx-I variants by HPLC

HPLC analysis of recombinant ProTx-I variants was performed on a Jupiter C4 column

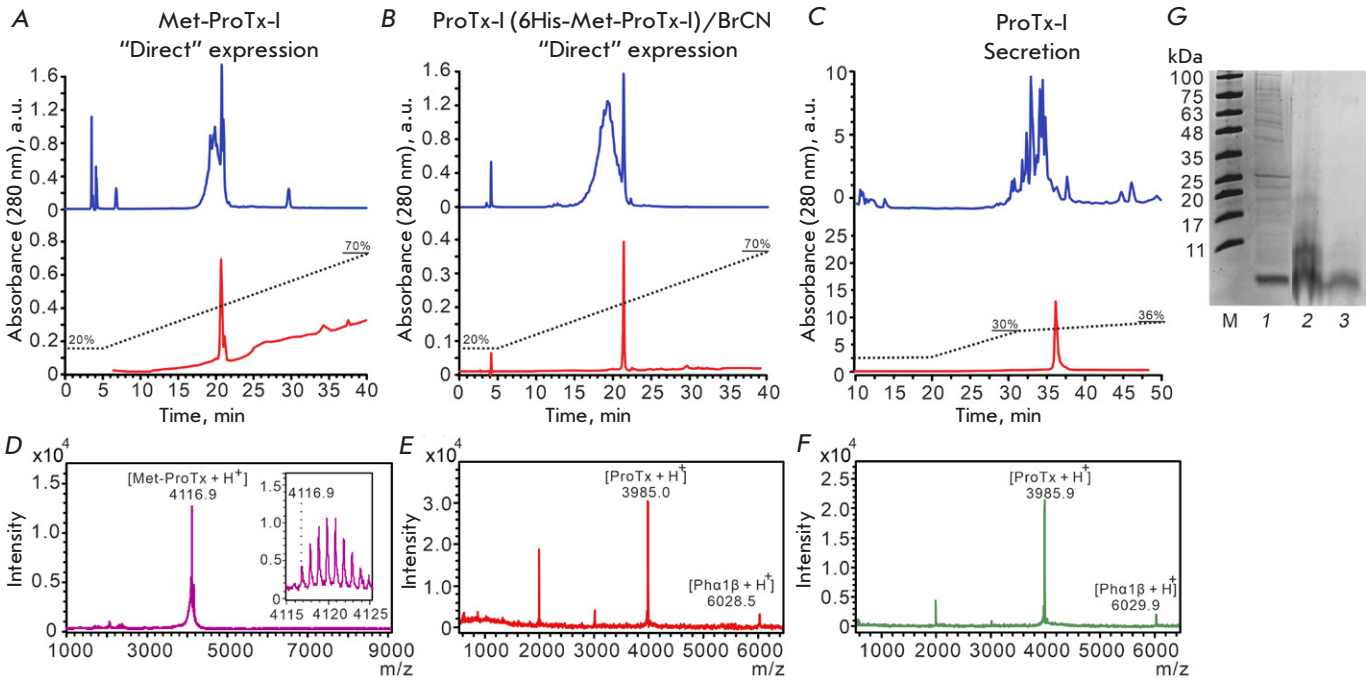

Fig. 2. Purification and characterization of recombinant ProTx-I variants. (*A–C*) Representative HPLC chromatograms of the purification (upper panel) and analysis (lower panel) of recombinant ProTx-I variants. (*A*) Refolded Met-ProTx-I. (*B*) ProTx-I produced by "direct" expression of 6His-Met-ProTx-I, followed by BrCN hydrolysis and refolding. (*C*) ProTx-I produced by bacterial secretion of MBP-ProTx-I, followed by BrCN hydrolysis. (*D–F*) MALDI-MS spectra of recombinant ProTx-I variants shown in (*A–C*), respectively. The Phα1β toxin was added to the samples shown in (*E* and *F*). [ProTx-I+2H$^+$] and [Phα1β+2H$^+$] doubly charged ions are also observed in (*E* and *F*). (*G*) Electrophoretic analysis of the ProTx-I samples produced by "direct" expression: M, marker (BioSharp BL712A); 1, Met-ProTx-I before refolding; 2, ProTx-I after hydrolysis of 6His-Met-ProTx-I with BrCN; 3, ProTx-I as in lane 2 after refolding

(A300, 4.6 × 250 mm, Phenomenex) using the Vanquish Core and Ultimate 3000 chromatographs (ThermoFisher, USA). Toxins were eluted by an acetonitrile gradient containing 0.1% trifluoroacetic acid (TFA) at a flow rate of 1 mL/min. The resulting toxin samples were lyophilized.

Mass spectrometry

The Met-ProTx-I sample was analyzed using a Rapiflex MALDI-TOF/TOF spectrometer (Bruker, Germany) in the reflection positive ion mode. The resulting m/z value (4116.9 Da, *Fig. 2D*) was close to an expected monoisotopic [Met-ProTx-I + H$^+$] mass of 4116.7 Da for a toxin molecule with closed disulfide bonds.

Analysis of the ProTx-I variants produced by the hydrolysis of 6His-Met-ProTx-I (*Fig. 2E*) or bacterial secretion (*Fig. 2F*) was performed using the Ultraflex MALDI-TOF/TOF spectrometer (Bruker, Germany). Trypsin autolysis products were used for spectrometer calibration. The molecular masses of ProTx-I (3985.0 and 3985.9 Da) achieved in both cases corresponded to the calculated monoisotopic ProTx-I mass (3985.7 Da, [ProTx-I + H$^+$]) within the measurement error. In both cases, the samples additionally contained the Phα1β toxin (calculated mass 6029.5 Da [Phα1β + H$^+$]) to verify calibration and its measured mass was 6028.5 and 6029.9 Da, respectively.

NMR spectroscopy

NMR spectra were measured in an aqueous solution (5% D_2O, pH 4.5, 30°C) using an AVANCE-800 NMR spectrometer (Bruker) with an operating proton frequency of 800 MHz. A commercial toxin sample obtained by chemical synthesis (Smartox Biotechnology Inc., France) was used as a positive control for the correct spatial structure.

Electrophysiological experiments

Currents through human and rat TRPA1 [21] were recorded in *X. laevis* oocytes expressing these channels. Oocyte isolation, mRNA injection, and exper-

imental recordings have been described previously [22]. All solutions were prepared on the day of the experiment using calcium-free ND-96 containing 96 mM NaCl, 2 mM KCl, 1 mM $MgCl_2$, and 10 mM HEPES at pH 7.4. Currents were stimulated by the application 100 μM AITC (Sigma-Aldrich). The solution was manually added to the perfusion chamber, and the currents were recorded using voltage ramps as reported in [22]. For each oocyte, we sequentially recorded three responses to AITC application, as well as the subsequent leakage current in the presence of a specific TRPA1 inhibitor: HC030031 (Sigma-Aldrich). The first response amplitude was used to normalize the data obtained on different oocytes. To induce the second response, AITC was applied together with ProTx-I or HC030031. The amplitude of this response was measured, normalized, averaged across different oocytes, and used to plot dose–response curves. Dose–response curves were approximated by the Hill equation:

$$Y = \frac{100\%}{1 + \left(\frac{[ProTx\text{-}I]}{EC_{50}}\right)^{nH}},$$

where nH is the Hill coefficient.

Statistical data processing was performed using GraphPad Prism 9.0. To compare current amplitudes at specific toxin concentrations, either a two-tailed Student's *t*-test or one-way ANOVA and Dunnett's multiple comparison test was used. Dose–response curve parameters were compared using the F-test.

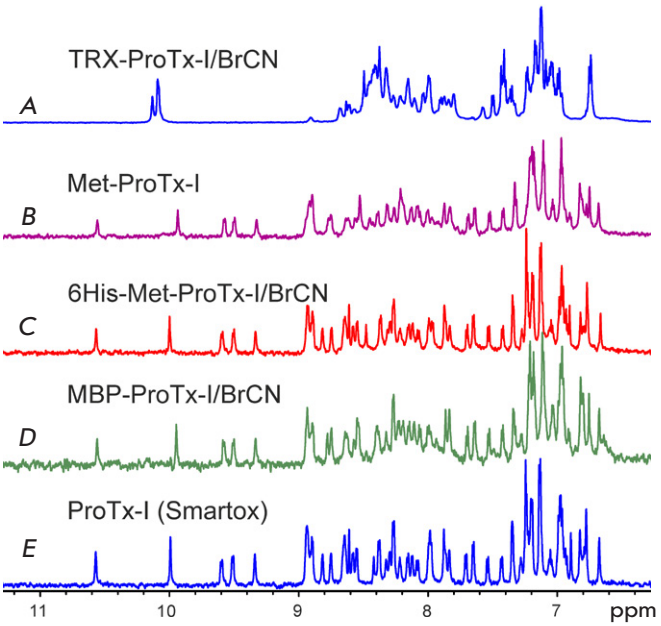

Fig. 3. 1D ^{1}H NMR spectra of recombinant ProTx-I variants (pH 4.5, 30°C). (*A*) The spectrum of an incorrectly folded ProTx-I produced as a TRX-ProTx-I fusion protein, followed by BrCN hydrolysis. (*B*) The spectrum of a refolded Met-ProTx-I. (*C*) The spectrum of ProTx-I obtained by "direct" expression of the 6His-Met-ProTx-I, followed by BrCN hydrolysis and refolding. (*D*) The spectrum of ProTx-I produced by secretion of an MBP-ProTx-I fusion protein followed by BrCN hydrolysis. (*E*) The spectrum of commercial, synthetic ProTx-I

RESULTS AND DISCUSSION

Production of ProTx-I as a fusion protein with TRX and GST

Five different approaches were tested to produce recombinant ProTx-I. Toxin was produced as a soluble fusion protein with TRX, GST, and maltose-binding protein (MBP), and in the form of cytoplasmic inclusion bodies with and without six *N*-terminal histidine residues – 6His-tag (*Fig. 1*). The efficiency of recombinant production of spider toxins fused with TRX and GST was demonstrated previously [23–26], and the efficiency of production as cytoplasmic inclusion bodies, followed by refolding, has been demonstrated by us for a number of disulfide-rich proteins, including snake venom toxins and human proteins from the Ly6/uPAR family [27].

Cultivation of BL21(DE3) cells transformed with the *pET-32a/ProTx-I* plasmid at 37°C resulted in the production of an insoluble TRX–ProTx-I fusion protein, whereas reducing the cell culture temperature to 13°C resulted in the production of a soluble protein with a yield of 20 mg/L of bacterial culture. Since the ProTx-I molecule lacks methionine residues, we used BrCN to hydrolyze the fusion protein [28] at an additional methionine residue introduced upstream of the first ProTx-I residue. MALDI analysis of the purified ProTx-I sample confirmed the expected molecular mass of the toxin with closed disulfide bonds. However, comparison of the ^{1}H NMR spectra of the recombinant toxin and commercial ProTx-I revealed absence of the correct spatial structure for recombinant ProTx-I (*Fig. 3A,E*). Employing GST as a protein partner also failed to yield a correctly folded ProTx-I. These results underscore the need for an analysis of the spatial structure of recombinant toxins before any further analysis. Production of a soluble fusion protein and verification of its molecular mass do not guarantee proper protein folding and the formation of correct disulfide bonds.

Production of Met-ProTx-I in inclusion bodies

By "direct" expression, the *ProTx-I* gene contains the *ATG* start codon at the 5'-end, which is necessary for translation initiation. Therefore, a final recombinant protein produced as cytoplasmic inclusion bodies contains an additional *N*-terminal methionine residue (*Fig. 1B*). To purify Met-ProTx-I, we used a previously developed protocol that involved cytoplasmic inclusion body solubilization to obtain a denatured toxin with cysteine residues chemically modified to S-sulfonate, followed by ion-exchange chromatography on a DEAP-spheronite-OH resin [27]. The yield of denatured Met-ProTx-I at this stage was 6 mg/L of bacterial culture. The purified Met-ProTx-I was treated with DTT to remove S-sulfonate groups from cysteine residues, then DTT was removed by gel filtration, and the toxin was transferred to the renaturation buffer. The toxin refolding protocol was based on a protocol previously reported for chemically synthesized ProTx-I [29] and was similar to the protocols we used for the refolding of other disulfide-rich proteins [27]. Refolded Met-ProTx-I, purified by HPLC (*Fig. 2A*), had the native spatial structure (*Fig. 3B*), but the efficiency of toxin refolding using this approach was extremely low. The final yield of the refolded toxin was only ~0.05 mg/L of bacterial culture.

Production of ProTx-I with the native *N*-terminal sequence

The low efficiency of Met-ProTx-I refolding may be due to insufficient purity of the sample before the refolding procedure. To overcome this problem, a 6His-tag was introduced into the *N*-terminal sequence of ProTx-I. A similar approach was previously used for recombinant production of other spider toxins [30]. Additional residues in the *N*-terminal sequence of toxins can affect their structure and activity [31]. Therefore, to produce a toxin with the native *N*-terminal sequence, we introduced an additional methionine residue after the 6His-tag for subsequent BrCN hydrolysis (*Fig. 1B*). The yield of 6His-Met-ProTx-I after purification by metal-chelate chromatography was ~13 mg/L of bacterial culture. Thus, the introduction of the 6His-tag into the *N*-terminal sequence not only increased the purity of the toxin preparation before renaturation (*Fig. 2G*) but also elevated the level of toxin production, which is consistent with our earlier observation that the *N*-terminal sequence can affect the yield of recombinant proteins [32]. The denatured 6His-Met-ProTx-I was hydrolyzed with BrCN, and the refolding was performed similarly to that for the Met-ProTx-I. The final yield of the refolded ProTx-I with the native *N*-terminal sequence after HPLC (*Fig. 2B*) was 0.3 mg/L of bacterial culture. Thus, the introduction of the 6His-tag into the ProTx-I molecule not only increased the production level of the toxin but also yielded a folded peptide with the native sequence, which was confirmed by NMR spectroscopy (*Fig. 3C*).

Secretion of ProTx-I

An alternative approach for the production of proteins with correctly formed disulfide bonds in *E. coli* cells is secretion into the periplasmic space [20]. To enhance toxin production, we used the peptide fused with MBP. To secrete the fusion protein into the periplasmic space, we introduced the MalE signal peptide into the *N*-terminal sequence of MBP [33] (*Fig. 1B*). Also, a methionine residue was inserted before the toxin sequence to cleave ProTx-I from MBP. For this step, we used *E. coli* Rosetta-gami™ (Origami™ derivative), which had proven itself to be effective in the production of disulfide-rich proteins, including animal toxins [34, 35]. To increase the yield of soluble protein, we lowered the cell culture temperature after induction to 13°C, which slowed the rate of protein synthesis and promoted the correct formation of disulfide bonds [36]. The yield of the MBP–ProTx-I protein after purification from a total cell lysate using metal chelate affinity chromatography was 75 mg/L of bacterial culture. The MBP–ProTx-I protein was then hydrolyzed with BrCN, and ProTx-I with the native *N*-terminal sequence was purified by HPLC (*Fig. 2C*). The final yield of the secreted, correctly folded ProTx-I (*Fig. 3D*) was ~0.15 mg/L of bacterial culture. Minor differences in the positions of individual signals in the NMR spectra of recombinant and commercial toxins (*Fig. 3D,E*) are explained by pH variations (within 0.1 units) in the samples.

The *N*-terminal sequence of ProTx-I influences toxin–TRPA1 interaction

Activity of the chemically synthesized ProTx-I was previously demonstrated in HEK293 cells expressing human and mouse TRPA1 receptors [8]. In the present study, we compared the functional activity of Met-ProTx-I and ProTx-I, with the latter being produced by hydrolysis of 6His-Met-ProTx-I, at the human TRPA1 channel expressed in *X. laevis* oocytes. Consistent with [8], we found that 10 μM of recombinant ProTx-I almost completely inhibited the current through the TRPA1 channel induced by 100 μM of the covalent agonist allyl isothiocyanate (AITC) (*Fig. 4A*). This effect was similar to that of 50 μM HC0300301, a selective TRPA1 antagonist (*Fig. 4A*).

Comparison of the dose–response curves of recombinant and commercial ProTx-I confirmed their simi-

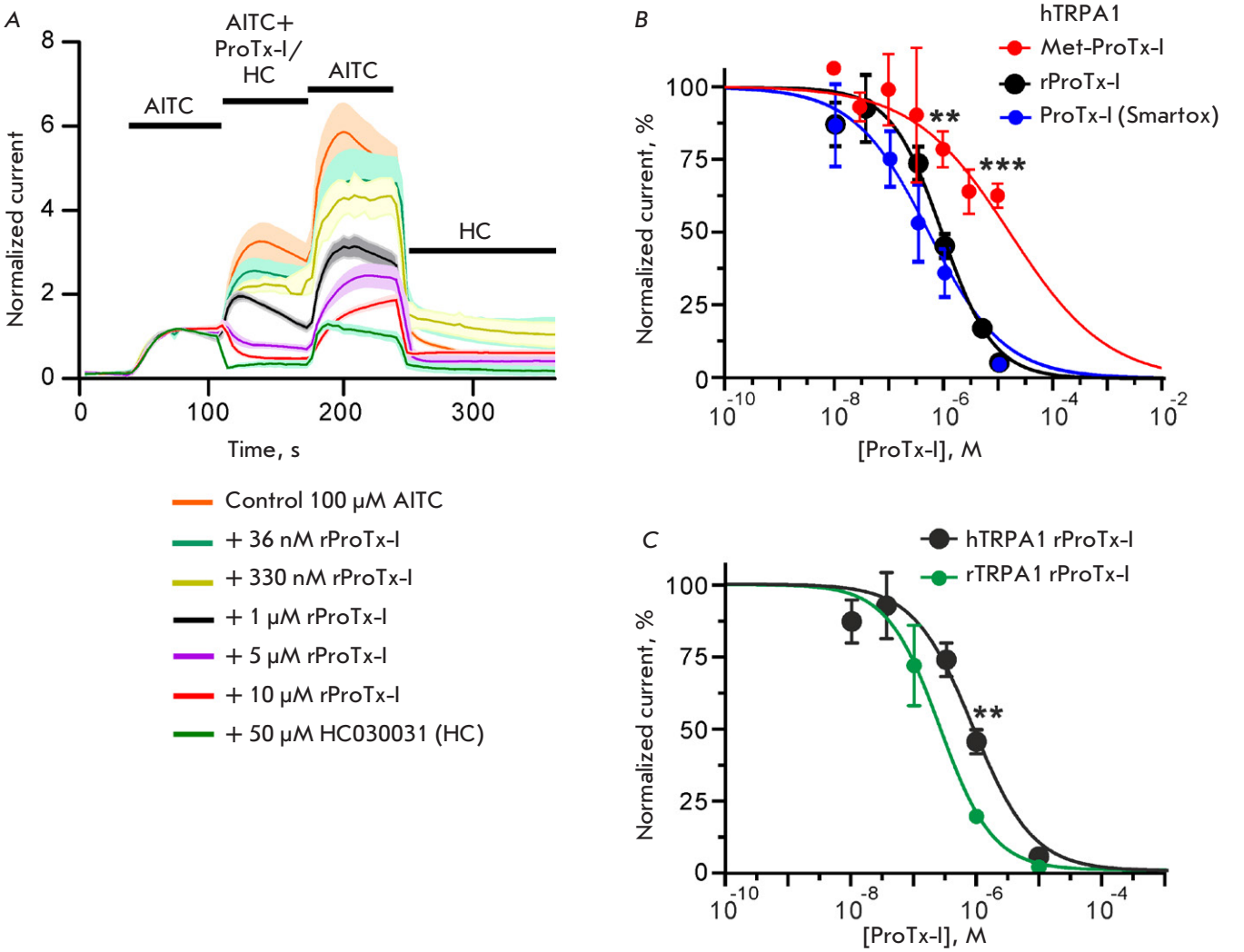

Fig. 4. Effect of ProTx-I variants on AITC-induced outward currents through TRPA1 in *X. laevis* oocytes. (*A*) Average normalized current traces for the human TRPA1 channel in the absence and presence of the selective antagonist HC030031 or ProTx-I. Data are presented as mean ± SEM (lines and shaded areas, respectively, $n = 3–6$ oocytes). Compound application periods are shown by solid black bars above the traces. (*B*) Dose-response curves for the inhibition of human TRPA1 by recombinant rProTx-I, Met-ProTx-I, and commercial synthetic ProTx-I (Smartox). **($p < 0.01$) and ***($p < 0.001$) indicate a significant difference in the current amplitudes between Met-ProTx-I and other variants according to the ANOVA/Dunnett criterion. The difference in IC_{50} values for the corresponding curves approximated by the Hill equation (*Table 1*) is statistically significant with $p < 0.0001$ (F-test). (*C*) Dose-response curves for recombinant rProTx-I at human (hTRPA1) and rat (rTRPA1) ion channels. The difference in IC_{50} values for these curves is statistically significant with $p = 0.006$ (F-test). **($p < 0.01$) indicates a significant difference in the amplitude of currents at rat and human channels according to the two-sided *t*-test. Data in *B* and *C* (mean ± SEM, $n = 3–6$ oocytes) are normalized to the response recorded without ProTx-I (100%)

Table 1. The Hill equation parameters for the inhibition curve analysis

Receptor/toxin	IC_{50}, μM	Hill coefficient
hTRPA1/Met-ProTx-I	8.9 ± 7.0	= 1.0*
hTRPA1/ProTx-I (Smartox)	0.41 ± 0.16	0.68 ± 0.24
hTRPA1/rProTx-I	0.84 ± 0.19	0.91 ± 0.18
rTRPA1/rProTx-I	0.25 ± 0.07	1.03 ± 0.26

*The Hill coefficient was set equal to 1.0 to analyze the dose-response curve for this toxin variant.

larity (*Fig. 4B*, *Table 1*). The curve parameters (IC_{50} and Hill coefficient) were not statistically different. However, analysis of Met-ProTx-I revealed a dramatic, statistically significant decline in the activity of this toxin variant. For example, recombinant and synthetic ProTx-I at a concentration of 10 μM inhibited currents to ~5%, whereas Met-ProTx-I inhibited currents only to ~60%, with the IC_{50} value increased by an order of magnitude (*Fig. 4B*, *Table 1*). Thus, the *N*-terminal amino acid sequence of the toxin is critically important for its interaction with the receptor. It is noteworthy that previous data on the ProTx-I active site had not included the *N*-terminal residues [8].

ProTx-I inhibits rat TRPA1 more efficiently than the human channel

Comparison of recombinant ProTx-I activity at rat and human TRPA1 channels revealed higher activity of the toxin at the rat receptor (IC_{50} ~ 250 and 840 nM, respectively; the difference in IC_{50} was statistically significant, *Fig. 4B*, *Table 1*). It is noteworthy that a previous comparative study of ProTx-I at human and mouse TRPA1, conversely, revealed higher activity at the human channel [8]. The difference in the toxin's action on human, rat, and mouse receptors may be explained by significant differences in the amino acid sequences of the extracellular S1–S2 and S3–S4 loops of these TRPA1 channels, the primary site of toxin interaction [8]. For example, the conserved residue Glu754 (numbering is given for the human channel) is replaced by Gly in the mouse channel, and Glu825 in the human channel is replaced by Asp and Asn in the rat and mouse channels, respectively. There are also other point differences. As a result, two negatively charged residues in the toxin-binding site of the mouse channel are replaced by neutral residues, which probably attenuates the binding of the positively charged toxin molecule (charge +2).

CONCLUSION

A system for the recombinant production of the ProTx-I toxin in the folded state was developed for the first time. We showed that ProTx-I exhibits different activities relative to human and rat TRPA1 channels, and that modification of the *N*-terminal sequence of ProTx-I may lead to toxin inactivation. ●

This study was supported by the Russian Science Foundation (Project No. 22-14-00326). The work of Yu. Che was supported by the project of the Ministry of Education of Guangdong Province of China (No. 2022KCXTD034).

The work of M.A. Shulepko, A.V. Kuznetsov, and E.N. Lyukmanova was supported by the key special project of the Ministry of Education of Guangdong Province of China (No. 2023ZDZX2072).

Design of expression vectors performed by A. Popov was carried out within the state assignment of NRC "Kurchatov Institute". The research was carried out at the «Primat» Shared Research Facilities using its equipment.

The authors express their gratitude to the Centre for Collective Use "Human Proteome" of the Orekhovich Institute of Biomedical Chemistry (Moscow, Russia) for mass spectrometric measurements.

REFERENCES

1. Kuhn-Nentwig L, Stöcklin R, Nentwig W. Venom Composition and Strategies in Spiders. Is Everything Possible? *Adv Insect Physiol.* 2011;40:1–86. doi: 10.1016/B978-0-12-387668-3.00001-5
2. Peigneur S, de Lima ME, Tytgat J. Phoneutria nigriventer venom: A pharmacological treasure. *Toxicon.* 2018;151:96–110. doi: 10.1016/j.toxicon.2018.07.008
3. Lyukmanova EN, Shenkarev ZO. Toxins from Animal Venom – A Rich Source of Active Compounds with High Pharmacological Potential. *Toxins (Basel).* 2024;16(12):512. doi: 10.3390/toxins16120512
4. Cardoso FC, Lewis RJ. Structure-Function and Therapeutic Potential of Spider Venom-Derived Cysteine Knot Peptides Targeting Sodium Channels. *Front Pharmacol.* 2019;10:366. doi: 10.3389/fphar.2019.00366
5. Kintzing JR, Cochran JR. Engineered knottin peptides as diagnostics, therapeutics, and drug delivery vehicles. *Curr Opin Chem Biol.* 2016;34:143–150. doi: 10.1016/j.cbpa.2016.08.022
6. Milescu M, Bosmans F, Lee S, Alabi AA, Kim JI, Swartz KJ. Interactions between lipids and voltage sensor paddles detected with tarantula toxins. *Nat Struct Mol Biol.* 2009;16(10):1080–1085. doi: 10.1038/nsmb.1679
7. Middleton RE, Warren VA, Kraus RL, et al. Two tarantula peptides inhibit activation of multiple sodium channels. *Biochemistry.* 2002;41(50):14734–14747. doi: 10.1021/bi026546a
8. Gui J, Liu B, Cao G, et al. A Tarantula-Venom Peptide Antagonizes the TRPA1 Nociceptor Ion Channel by Binding to the S1–S4 Gating Domain. *Curr Biol.* 2014;24(5):473–483. doi: 10.1016/j.cub.2014.01.013
9. Maatuf Y, Geron M, Priel A. The Role of Toxins in the Pursuit for Novel Analgesics. *Toxins (Basel).*

2019;11(2):131. doi: 10.3390/toxins11020131
10. Souza Monteiro de Araujo D, Nassini R, Geppetti P, De Logu F. TRPA1 as a therapeutic target for nociceptive pain. *Expert Opin Ther Targets*. 2020;24(10):997–1008. doi: 10.1080/14728222.2020.1815191
11. Dormer A, Narayanan M, Schentag J, et al. A Review of the Therapeutic Targeting of SCN9A and Nav1.7 for Pain Relief in Current Human Clinical Trials. *J Pain Res*. 2023;16:1487–1498. doi: 10.2147/JPR.S388896
12. Moore SJ, Cochran JR. Engineering knottins as novel binding agents. *Methods Enzymol*. 2012;503:223–251. doi: 10.1016/B978-0-12-396962-0.00009-4
13. Fitches EC, Pyati P, King GF, Gatehouse JA. Fusion to snowdrop lectin magnifies the oral activity of insecticidal ω-Hexatoxin-Hv1a peptide by enabling its delivery to the central nervous system. *PLoS One*. 2012;7(6):e39389. doi: 10.1371/journal.pone.0039389
14. Yang S, Pyati P, Fitches E, Gatehouse JA. A recombinant fusion protein containing a spider toxin specific for the insect voltage-gated sodium ion channel shows oral toxicity towards insects of different orders. *Insect Biochem Mol Biol*. 2014;47(100):1–11. doi: 10.1016/j.ibmb.2014.01.007
15. Monfared N, Ahadiyat A, Fathipour Y, Mianroodi RA. Evaluation of recombinant toxin JFTX-23, an oral-effective anti-insect peptide from the spider Selenocosmia jiafu venom gland proteome. *Toxicon*. 2022;217:78–86. doi: 10.1016/j.toxicon.2022.08.003
16. Matsubara FH, Meissner GO, Herzig V, et al. Insecticidal activity of a recombinant knottin peptide from Loxosceles intermedia venom and recognition of these peptides as a conserved family in the genus. *Insect Mol Biol*. 2017;26(1):25–34. doi: 10.1111/imb.12268
17. Costa S, Almeida A, Castro A, Domingues L. Fusion tags for protein solubility, purification and immunogenicity in Escherichia coli: the novel Fh8 system. *Front Microbiol*. 2014;5:63. doi: 10.3389/fmicb.2014.00063
18. Berlec A, Strukelj B. Current state and recent advances in biopharmaceutical production in Escherichia coli, yeasts and mammalian cells. *J Ind Microbiol Biotechnol*. 2013;40(3–4):257–274. doi: 10.1007/s10295-013-1235-0
19. Klint JK, Senff S, Saez NJ, et al. Production of recombinant disulfide-rich venom peptides for structural and functional analysis via expression in the periplasm of E. coli. *PLoS One*. 2013;8(5):e63865. doi: 10.1371/journal.pone.0063865
20. Anangi R, Rash LD, Mobli M, King GF. Functional Expression in Escherichia coli of the Disulfide-Rich Sea Anemone Peptide APETx2, a Potent Blocker of Acid-Sensing Ion Channel 3. *Mar Drugs*. 2012;10(7):1605–1618. doi: 10.3390/md10071605
21. Logashina YA, Solstad RG, Mineev KS, et al. New Disulfide-Stabilized Fold Provides Sea Anemone Peptide to Exhibit Both Antimicrobial and TRPA1 Potentiating Properties. *Toxins (Basel)*. 2017;9(5):154. doi: 10.3390/toxins9050154
22. Lyukmanova EN, Mironov PA, Kulbatskii DS, et al. Recombinant Production, NMR Solution Structure, and Membrane Interaction of the Phα1β Toxin, a TRPA1 Modulator from the Brazilian Armed Spider Phoneutria nigriventer. *Toxins (Basel)*. 2023;15(6):378. doi: 10.3390/toxins15060378
23. Berkut AA, Peigneur S, Myshkin MY, et al. Structure of Membrane-active Toxin from Crab Spider Heriaeus melloteei Suggests Parallel Evolution of Sodium Channel Gating Modifiers in Araneomorphae and Mygalomorphae. *J Biol Chem*. 2015;290(1):492–504. doi: 10.1074/jbc.M114.595678
24. Shlyapnikov YM, Andreev YA, Kozlov SA, Vassilevski AA, Grishin EV. Bacterial production of latarcin 2a, a potent antimicrobial peptide from spider venom. *Protein Expr Purif*. 2008;60(1):89–95. doi: 10.1016/j.pep.2008.03.011
25. Paiva ALB, Matavel A, Peigneur S, et al. Differential effects of the recombinant toxin PnTx4(5-5) from the spider Phoneutria nigriventer on mammalian and insect sodium channels. *Biochimie*. 2016;121:326–335. doi: 10.1016/j.biochi.2015.12.019
26. Zhang H, Huang PF, Meng E, et al. An efficient strategy for heterologous expression and purification of active peptide hainantoxin-IV. *PLoS One*. 2015;10(2):e0117099. doi: 10.1371/journal.pone.0117099
27. Shulepko MA, Lyukmanova EN, Shenkarev ZO, et al. Towards universal approach for bacterial production of three-finger Ly6/uPAR proteins: Case study of cytotoxin I from cobra N. oxiana. *Protein Expr Purif*. 2017;130:13–20. doi: 10.1016/j.pep.2016.09.021
28. Andreev YA, Kozlov SA, Vassilevski AA, Grishin EV. Cyanogen bromide cleavage of proteins in salt and buffer solutions. *Anal Biochem*. 2010;407(1):144–146. doi: 10.1016/j.ab.2010.07.023
29. Rupasinghe DB, Herzig V, Vetter I, et al. Mutational analysis of ProTx-I and the novel venom peptide Pe1b provide insight into residues responsible for selective inhibition of the analgesic drug target $Na_V1.7$. *Biochem Pharmacol*. 2020;181:114080. doi: 10.1016/j.bcp.2020.114080
30. Vásquez-Escobar J, Benjumea-Gutiérrez DM, Lopera C, et al. Heterologous Expression of an Insecticidal Peptide Obtained from the Transcriptome of the Colombian Spider Phoneutria depilate. *Toxins (Basel)*. 2023;15(7):436. doi: 10.3390/toxins15070436
31. Dubovskii PV, Dubinnyi MA, Konshina AG, et al. Structural and Dynamic "Portraits" of Recombinant and Native Cytotoxin I from Naja oxiana: How Close Are They? *Biochemistry*. 2017;56(34):4468–4477. doi: 10.1021/acs.biochem.7b00453
32. Lyukmanova EN, Shenkarev ZO, Khabibullina NF, et al. N-terminal fusion tags for effective production of g-protein-coupled receptors in bacterial cell-free systems. *Acta Naturae*. 2012;4(15):58–64. doi: 10.32607/20758251-2012-4-4-58-64
33. Saez NJ, Cristofori-Armstrong B, Anangi R, King GF. A Strategy for Production of Correctly Folded Disulfide-Rich Peptides in the Periplasm of E. coli. *Methods Mol Biol*. 2017;1586:155–180. doi: 10.1007/978-1-4939-6887-9_10
34. Li J, Zhang H, Liu J, Xu K. Novel genes encoding six kinds of three-finger toxins in Ophiophagus hannah (king cobra) and function characterization of two recombinant long-chain neurotoxins. *Biochem J*. 2006;398(2):233–242. doi: 10.1042/BJ20060004
35. Clement H, Flores V, De la Rosa G, Zamudio F, Alagon A, Corzo G. Heterologous expression, protein folding and antibody recognition of a neurotoxin from the Mexican coral snake Micrurus laticorallis. *J Venom Anim Toxins Incl Trop Dis*. 2016;22(1):25. doi: 10.1186/s40409-016-0080-9
36. Lyukmanova EN, Shulga AA, Arsenieva DA, et al. A Large-Scale Expression in Escherichia coli of Neurotoxin II from Naja oxiana Fused with Thioredoxin. *Russ J Bioorg Chem*. 2004;30(1):25–34. doi: 10.1023/B:RUBI.0000015770.38602.e3

GENERAL RULES

Acta Naturae publishes experimental articles and reviews, as well as articles on topical issues, short reviews, and reports on the subjects of basic and applied life sciences and biotechnology.

The journal *Acta Naturae* is on the list of the leading periodicals of the Higher Attestation Commission of the Russian Ministry of Education and Science. The journal Acta Naturae is indexed in PubMed, Web of Science, Scopus and RCSI databases.

The editors of *Acta Naturae* ask of the authors that they follow certain guidelines listed below. Articles which fail to conform to these guidelines will be rejected without review. The editors will not consider articles whose results have already been published or are being considered by other publications.

The maximum length of a review, together with tables and references, cannot exceed 50 000 characters with spaces (approximately 30 pages, A4 format, 1.5 spacing, Times New Roman font, size 12) and cannot contain more than 16 figures.

Experimental articles should not exceed 30 000 symbols (approximately 15 pages in A4 format, including tables and references). They should contain no more than ten figures.

A short report must include the study's rationale, experimental material, and conclusions. A short report should not exceed 12 000 symbols (5–6 pages in A4 format including no more than 12 references). It should contain no more than three figures.

The manuscript and all necessary files should be uploaded to www.actanaturae.ru:

1) text in Word 2003 for Windows format;
2) the figures in TIFF format;
3) the text of the article and figures in one pdf file;
4) the article's title, the names and initials of the authors, the full name of the organizations, the abstract, keywords, abbreviations, figure captions, and Russian references should be translated to English;
5) the cover letter stating that the submitted manuscript has not been published elsewhere and is not under consideration for publication;
6) the license agreement (the agreement form can be downloaded from the website www.actanaturae.ru).

MANUSCRIPT FORMATTING

The manuscript should be formatted in the following manner:

- Article title. Bold font. The title should not be too long or too short and must be informative. The title should not exceed 100 characters. It should reflect the major result, the essence, and uniqueness of the work, names and initials of the authors.
- The corresponding author, who will also be working with the proofs, should be marked with a footnote *.
- Full name of the scientific organization and its departmental affiliation. If there are two or more scientific organizations involved, they should be linked by digital superscripts with the authors' names. Abstract. The structure of the abstract should be very clear and must reflect the following: it should introduce the reader to the main issue and describe the experimental approach, the possibility of practical use, and the possibility of further research in the field. The average length of an abstract is 20 lines (1 500 characters).
- Keywords (3 – 6). These should include the field of research, methods, experimental subject, and the specifics of the work. List of abbreviations.
- INTRODUCTION
- EXPERIMENTAL PROCEDURES
- RESULTS AND DISCUSSION
- CONCLUSION

  The organizations that funded the work should be listed at the end of this section with grant numbers in parenthesis.
- REFERENCES

  The in-text references should be in brackets, such as [1].

RECOMMENDATIONS ON THE TYPING AND FORMATTING OF THE TEXT

- We recommend the use of Microsoft Word 2003 for Windows text editing software.
- The Times New Roman font should be used. Standard font size is 12.
- The space between the lines is 1.5.
- Using more than one whole space between words is not recommended.
- We do not accept articles with automatic referencing; automatic word hyphenation; or automatic prohibition of hyphenation, listing, automatic indentation, etc.
- We recommend that tables be created using Word software options (Table → Insert Table) or MS Excel. Tables that were created manually (using lots of spaces without boxes) cannot be accepted.
- Initials and last names should always be separated by a whole space; for example, A. A. Ivanov.
- Throughout the text, all dates should appear in the "day.month.year" format, for example 02.05.1991, 26.12.1874, etc.
- There should be no periods after the title of the article, the authors' names, headings and subheadings, figure captions, units (s – second, g – gram, min – minute, h – hour, d – day, deg – degree).
- Periods should be used after footnotes (including those in tables), table comments, abstracts, and abbreviations (mon. – months, y. – years, m. temp. – melting temperature); however, they should not be used in subscripted indexes (T_m – melting temperature; $T_{p.t}$ – temperature of phase transition). One exception is mln – million, which should be used without a period.
- Decimal numbers should always contain a period and not a comma (0.25 and not 0,25).
- The hyphen ("-") is surrounded by two whole spaces, while the "minus," "interval," or "chemical bond" symbols do not require a space.

- The only symbol used for multiplication is "×"; the "×" symbol can only be used if it has a number to its right. The "·" symbol is used for denoting complex compounds in chemical formulas and also noncovalent complexes (such as DNA·RNA, etc.).
- Formulas must use the letter of the Latin and Greek alphabets.
- Latin genera and species' names should be in italics, while the taxa of higher orders should be in regular font.
- Gene names (except for yeast genes) should be italicized, while names of proteins should be in regular font.
- Names of nucleotides (A, T, G, C, U), amino acids (Arg, Ile, Val, etc.), and phosphonucleotides (ATP, AMP, etc.) should be written with Latin letters in regular font.
- Numeration of bases in nucleic acids and amino acid residues should not be hyphenated (T34, Ala89).
- When choosing units of measurement, SI units are to be used.
- Molecular mass should be in Daltons (Da, KDa, MDa).
- The number of nucleotide pairs should be abbreviated (bp, kbp).
- The number of amino acids should be abbreviated to aa.
- Biochemical terms, such as the names of enzymes, should conform to IUPAC standards.
- The number of term and name abbreviations in the text should be kept to a minimum.
- Repeating the same data in the text, tables, and graphs is not allowed.

GUIDENESS FOR ILLUSTRATIONS

- Figures should be supplied in separate files. Only TIFF is accepted.
- Figures should have a resolution of no less than 300 dpi for color and half-tone images and no less than 600 dpi.
- Files should not have any additional layers.

REVIEW AND PREPARATION OF THE MANUSCRIPT FOR PRINT AND PUBLICATION

Articles are published on a first-come, first-served basis. The members of the editorial board have the right to recommend the expedited publishing of articles which are deemed to be a priority and have received good reviews.

Articles which have been received by the editorial board are assessed by the board members and then sent for external review, if needed. The choice of reviewers is up to the editorial board. The manuscript is sent on to reviewers who are experts in this field of research, and the editorial board makes its decisions based on the reviews of these experts. The article may be accepted as is, sent back for improvements, or rejected.

The editorial board can decide to reject an article if it does not conform to the guidelines set above.

The return of an article to the authors for improvement does not mean that the article has been accepted for publication. After the revised text has been received, a decision is made by the editorial board. The author must return the improved text, together with the responses to all comments. The date of acceptance is the day on which the final version of the article was received by the publisher.

A revised manuscript must be sent back to the publisher a week after the authors have received the comments; if not, the article is considered a resubmission.

E-mail is used at all the stages of communication between the author, editors, publishers, and reviewers, so it is of vital importance that the authors monitor the address that they list in the article and inform the publisher of any changes in due time.

After the layout for the relevant issue of the journal is ready, the publisher sends out PDF files to the authors for a final review.

Changes other than simple corrections in the text, figures, or tables are not allowed at the final review stage. If this is necessary, the issue is resolved by the editorial board.

FORMAT OF REFERENCES

The journal uses a numeric reference system, which means that references are denoted as numbers in the text (in brackets) which refer to the number in the reference list.

Bibliographic descriptions of cited sources in the reference list should be formatted according to the requirements of the International Committee of Medical Journal Editors (ICMJE) and the AMA Manual of Style: A Guide for Authors and Editors (11th Edition).

Detailed formatting rules are available at: https://actanaturae.ru/2075-8251/pages/view/references

For users of specialized reference management software, the editorial board recommends the following resources:

- EndNote — download the Acta Naturae.ens style file; use the reference style JAMA: Journal of the American Medical Association (AMA 11th edition);
- Zotero — use the reference style American Medical Association 11th edition (brackets);
- Mendeley — use the reference style American Medical Association.

Examples of reference formatting:

1. Hisakata R, Nishida S, Johnston A. An adaptable metric shapes perceptual space. *Curr Biol*. 2016;26(14):1911-1915. doi: 10.1016/j.cub.2016.05.047
2. Sambrook J, Russell DW. *Molecular Cloning: A Laboratory Manual*. 3rd ed. CSHL Press; 2001.
3. Hogue CWV. Structure databases. In: Baxevanis AD, Ouellette BFF, eds. *Bioinformatics*. 2nd ed. Life Sciences Series. Wiley-Interscience; 2001:83-109.

The following e-mail addresses can be used to contact the editorial staff: actanaturae@gmail.com, tel.: (495) 727-38-60.